Ceramic Hardness

Ceramic Hardness

I. J. McColm
University of Bradford
Bradford, England

Springer Science+Business Media, LLC

To my late father, David McColm,
whose hard life fashioned a kind man

Preface

As the utilization of ceramic materials is developing at a great pace, so too is the science of ceramics improving the understanding we have about these high-technology materials. New and improved ways of examining and investigating monolithic ceramics and ceramic composites are also being developed and reported at a great pace in a wide-ranging area of the scientific and technical literature. This book has been written with the aim of increasing the awareness of the general materials worker of developments in modern ceramics and of bringing to a focus how much the study of their hardness can contribute to our understanding of them and lead to technical data that can be of considerable use in this fast-growing field. The readership will consist of materials scientists, metallurgists, and engineers moving into the new worlds of advanced ceramics and ceramic-containing composites.

Detailed works on hardness are to be found in the metallurgical area, where much of the theory and early applications were developed. This book does not overly stress this early development of theory and practice, but concentrates wherever possible on the ceramics and glasses. Thus Chapter 1 introduces the general subject area to those whose interest may have been blunted in the past by the emphasis on one area of materials. Subjects raised in the first chapter are developed more fully in later chapters. Chapter 2 focuses on some practical aspects of the most commonly encountered techniques. Chapter 3 is a truly ceramic chapter, for it is in the area of single-crystal examination that the technique has made its greatest contribution to developing theory and uses. Much of the style of this chapter derives from work and ideas of Professor C. A. Brookes of Hull University, who set out with me to write this book but unfortunately was not able, due to pressures of time and work, to continue. I am indebted to him for the early discussions we had.

Chapter 4 introduces the ideas that external factors can affect the hardness of ceramics and so conversely these can be studied via the techniques of hardness measurement.

Chapter 5 is an extensive view of the useful work that can be done when hardness measurements lead to cracked areas in ceramics. This is probably the most important recent development in the areas of both hardness and ceramic properties. Thus Chapter 5 contains many examples of the way that relatively simple experiments can lead to many important data on polycrystalline, single-crystal, and fiber-formed ceramics. The last chapter, Chapter 6, brings together the previous five chapters via a discussion of many important ceramic systems and tabulates hardness data from the literature for them. Chapters 5 and 6 make this book a particular fusion of ceramic science and hardness developments. Overall the attempt has been to maintain an interdisciplinary approach, in keeping with the author's earlier publications, and as a result it is hoped that the contents and style will suit the wide readership at which the book is aimed.

Many people have helped me in my endeavors, and without them what has been achieved would not have been. Among them I acknowledge particularly the work of my student Dr. I. Inwang in drawing many figures and providing experimental data, Miss M. Cobb for devoted typing, and the technical staff of the department of Industrial Technology of Bradford University, who together form a great team.

I. J. McColm

Bradford, England

Contents

CHAPTER 4 APPLIED LOAD, ENVIRONMENT, AND TIME AS EXTERNAL DETERMINANTS OF CERAMIC HARDNESS

CHAPTER 5 CRACKED INDENTS—FRIEND OR FOE? THEIR USE IN TOUGHNESS AND BRITTLENESS CHARACTERIZATION

CHAPTER 6 CERAMIC SYSTEMS: BONDING, MICROSTRUCTURES, HARDNESS VALUES, AND HARDNESS-DERIVED PROPERTIES

Introduction and Overview

1.1. HOW LONG IS A PIECE OF STRING?

When asking the above question one is often implying that a previous request for information is too open and has no precise answer. Indeed it should be the answer to a type of question frequently asked: "How hard is this ceramic, this rock or powder, etc.?"

The problem is even deeper than it first seems because our questioner, when asked "how long is a piece of string?" could make the rejoinder, "measure it and see." Everyone agrees that a length may be measured in meters, inches, or some multiple of these and that it does not matter which because both units are traceable to a *natural* standard, namely, the wavelength of a particular reproducible light source. The same is true for many other properties of materials, making it possible to agree on values because the conversion factor from one unit, obtained by a particular method of measurement, to another is known precisely.

Hardness stands outside this convenient framework; the hardness of a material is *not a unique property* but is a measure of the reaction of the material to the type of disturbing force imposed. Following from this, the hardness is a function of the test method, and the dynamic nature of the measuring process imposes a different pattern of stress on the sample for different load ranges. A wide variety of very different hardness test procedures has been developed:

1. *Scratch Tests*, in which it is simply observed whether one material is capable of scratching another (the Mohs test).
2. *The Ploughing Test*, in which a hard blunt material like diamond is loaded and pulled across a surface to make a groove. The width and depth of the groove are a measure of hardness (the Bierbaum test).
3. *The Cutting Test*, in which a sharp tool is used to remove a chip of standard dimensions.

4. *The Abrasion Test*, in which a specimen is loaded against a rotating disk and the rate of wear as determined optically or by weight loss is used as a measure of hardness.
5. *The Erosion Test*, a variation on the abrasion test, in which abrasive grains are fired onto the sample surface and the loss of weight in a given time is used as a measure of hardness.
6. *The Damping Test*, in which a pendulum with a very hard pointed pivot is set rocking on the sample surface and the time to decrease the amplitude of the swing by 50% is used as a measure of hardness (the pendulum test or Herbert test).
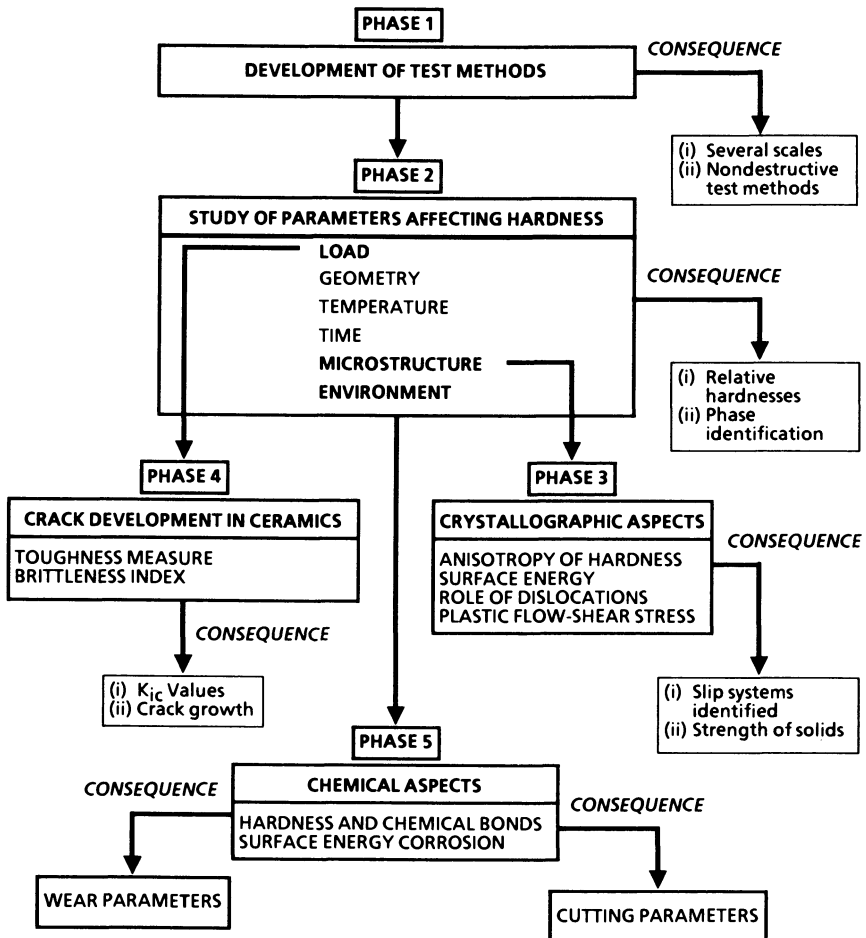
Figure 1.1. Flow chart showing the stages in the development of hardness science and hence the topics covered in the text.

7. *The Rebound Test*, a test easily adapted to measurements over wide temperature ranges whereby a ball is bounced on the sample surface and the height of the rebound is taken as a measure of hardness. (Shore's name is sometimes associated with this measure of hardness.)

8. *Static Indentation Tests*, by far the most widely used, the most widely analyzed, and the most generous in the breadth of data they supply. A ball, cone, or pyramid is forced into a surface and the load per unit area of impression is considered the material's hardness. Several types of such tests are well known: Brinnel, Vickers, Rockwell, and Knoop.

What emerges from the above is that no single unit of hardness can be defined such that a single linear hardness scale can be established.

Why not adopt the seemingly obvious course of finding or defining a reproducible *natural* standard suitable for establishing reference points on the practical scales which result from the various measuring techniques? No one reproducible natural standard exists that would provide unambiguous measurements across the very large range of values encountered in ceramic systems. For example, applied loads that produced clear, uncracked indents in the test material may be too small for some systems and would measure only very *local* surface properties. More important, a hardness test, while not destructive of the object in a macroscopic sense, is destructive of the local area tested and cannot therefore be repeated precisely.

After this salutary beginning, is it worthwhile pursuing the question of how hard a ceramic is? Yes, because the attempts at answering this question have followed several routes that shed light on ceramic development. Figure 1.1 is a flow chart of the development of the subject that should make it clear how the topics in this book are grouped for study.

1.2. CERAMICS OF PRINCIPAL INTEREST

Mitsubishi Heavy Industries announced plans in 1984 to begin mass production of ceramic turbines 40% lighter than conventional nickel alloy types. Made from "clay and air," these superior new materials come from an old source and they are formed by "traditional" thermal processes, but there all likeness to the popular conception of ceramics ends. It is impossible to visualize the traditional ceramic, made by heating earthy materials, withstanding the stresses, strains, and temperatures required in the Mitsubishi turbine. Then what are these new superceramics? In the case of the turbocharger they are silicon nitride, Si_3N_4, and silicon carbide, SiC, but are these the only possibilities? Development has required the solution of

problems in purity, powder technology, moulding and forming, machining, and ceramic-to-metal bonding which clearly, to the satisfaction of an industrial giant, have been overcome; if something as difficult as this can be accomplished, then it will be possible to make almost anything from ceramic materials. However, lagging somewhat behind has been the development of testing methods, particularly nondestructive methods, and it is here that hardness testing may be of growing importance, as Figure 1.1 indicates.

However, to return to the unanswered question in the above paragraph, what are superceramics? How should we limit our consideration and our compilation of data? These questions have been tackled in a previous book[1] in which, starting from Griffith's theoretical equation, an expression was developed that related the fundamental intrinsic properties of sublimation energy, density, Young's modulus, and molecular mass:

$$\sigma_{\text{th}} = \left(\frac{0.33 \Delta H_{\text{sub}} \rho E}{M}\right)^{1/2} \tag{1.1}$$

From equation (1.1), in order to achieve high modulus values and hence superior strength, a material must possess covalent bonds or, at second best, ionic bonds; both of these are common in ceramic materials. Besides this combination of chemical bonds, a suitable ceramic material must have a low molecular weight, thus relatively few materials need be discussed in this book, principally beryllium, boron, carbon, silicon, boron carbide (B_4C), silicon carbide (SiC), boron oxide (B_2O_3), silicon oxide (SiO_2) and glasses, magnesium oxide (MgO), aluminium oxide (Al_2O_3), zirconia (ZrO_2), boron nitride (BN), silicon nitride (Si_3N_4), and some refractory carbides and nitrides. Because of their considerable commercial importance, we must add to this list some "fine ceramics" that have assumed considerable importance in electronic and magnetic applications: gallium arsenide, germanium, borides, garnets, ferrites, and perovskites. These then will form the main focus of our numerical data, and sections will be devoted to each when we discuss applications.

Being ceramics, these materials are characterized, as has already been stated, by covalent or ionic bonding or combinations of these, with the result that much of the theory and many of the concepts of hardness have to be reviewed because they were developed principally for metals, in which weak nondirectional bonding lends itself to interpretation of data almost exclusively in terms of dislocation flow and easy plastic deformation. It is, however, interesting to see how far the conventional theories and concepts can be extended to ceramics. One aspect of hardness technique both unusual and extremely pertinent to ceramics is the question of brittleness.

The term "brittleness" has always loomed large in discussions of ceramics because it suggests serious problems which may be holding back the use of the engineering ceramics discussed in this text. Because of those

problems, the design and testing of ceramic systems is bounded by the desire to prevent the initiation and propagation of cracks as materials respond to two competing mechanisms of applied stress, namely, flow and fracture. In indentation hardness testing we have a *controlled* way of producing irreversible deformation together with crack patterns around and within the same sample volume of ceramic, enabling these two parameters to be determined, analyzed, and combined for each specimen into a measure of brittleness[2] since H_V, the Vickers hardness, is a measure of deformation and K_C is a measure of resistance to fracture. This leads to H_V/K_C being an index of brittleness. This index is of small predictive value stating as it does the seemingly obvious (see Table 5.2 ir Chapter 5, where toughness and hardness are discussed) but its derivation is an application of the hardness technique to ceramic systems that leads to the useful prediction of P^* and c^* as the maximum load and maximum associated flaw size that a ceramic system might sustain without starting a fracture process. In principle this useful design information can be obtained from a single indentation hardness determination, at least in a semiquantitative way which can nevertheless prove valuable. Thus part of Chapter 5 deals more fully with the brittleness index and its relationship to the grindability of ceramic powders.

This is one example of the wide scope for hardness measurements in the rapidly developing field of modern ceramic science and technology. The interlinking of hardness theory, hardness methods, strength, toughness, brittleness, wear, crystallography, structure, microstructure, and bonding to topics of current and future importance is the aim of the ensuing chapters.

1.3. CONCEPT OF HARDNESS

As already stressed, the concept of hardness has no precise definition and as a result possesses no recognized dimensions; some methods of measurement give it units of pressure and some units of time, while in others it is dimensionless. Even when the types of experiment to measure hardness seem on their face to be very similar—for example, the methods involving indentation of a crystal surface—the various hardness scales are not readily comparable. The reason for this situation is explained in Section 1.4 and Chapters 2 and 3 but can be briefly stated at this stage: In an indent test the measured hardness is a function of several parameters. This difficulty in turn has led to several models being used to interpret and quantify measured hardness values: tensile strength[3] and ease of plastic flow[4,5]; surface energy[6]; and chemical bond strength.[4,7,8]

The importance of each of these concepts and their role as rationalizing ideas in ceramic hardness studies are described in detail in this book, and the applicability and usefulness of each will be stressed. However, because

of the variable nature of hardness and the wide range of bond types encountered in ceramic systems, it is stressed that a variety of models should be considered before the applicability of any one is overemphasized. Briefly, then, what are the general parameters that affect a hardness test such as the indentation of a ceramic surface by a faceted diamond? First, but not necessarily most important, is *grain size*. It has been shown that in polycrystalline samples grain size has an important effect when it is of the same order as the indent diameter. A decrease in grain size is accompanied by an increase in hardness as the dislocations generated by the indenter are blocked by the grain boundaries. Figure 1.2 illustrates the practical problem
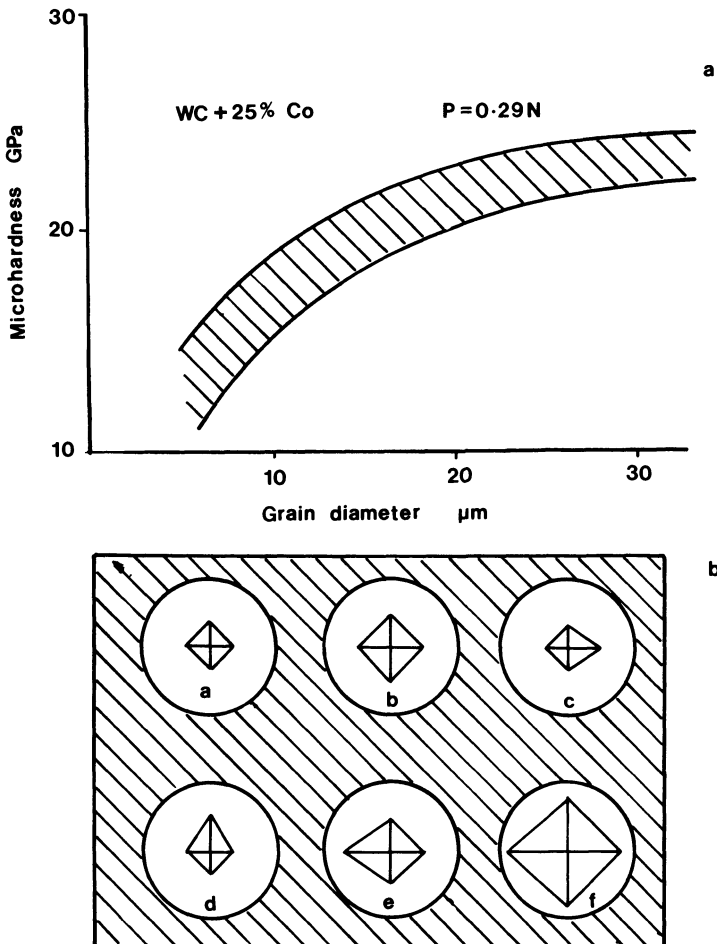
Figure 1.2. Grain size effects in microhardness testing. (a) Results from tungsten carbide cutting-tool compositions. (b) Apparent hardness changing as grain size to indent size decreases.

here. We can see immediately that a range of instrumentation is necessary to enable various load ranges to be used so that the indent–to–grain size ratio can be controlled. This in turn has led to the division of the subject into regions variously defined as macro- and microhardness depending on the load used.

Figure 1.3 emphasizes the arbitrary nature of the nomenclature in this type of hardness determination as well as the way in which load affects the determined hardness value.

The divisions into areas a, b, and c with their respective titles are arbitrary but commonly accepted as being near to the loads indicated. Only in area c with load in the range 3–10 kg is hardness independent of the applied load or sample microstructure. Area a shows the hardness value increasing as load diminishes, but great care is necessary in making determinations and interpreting results in this region when such small loads are applied. Variations in technique and microstructure can and do produce hardness values in area a that for one sample can range from 50% to 400% of the standard hardness value.

The need to control indent size according to the grain size of specimens leads to two areas of importance: What is hardness measuring if large loads are used with polycrystalline samples of fine grain size, and can load variation itself introduce problems as various parameters in the function that describes hardness become dominant?

Thus a second indentation-test parameter is the *applied load*. If the load is too light and the indenter impression is then shallow, the microhardness can be dominated by the ease with which dislocations can
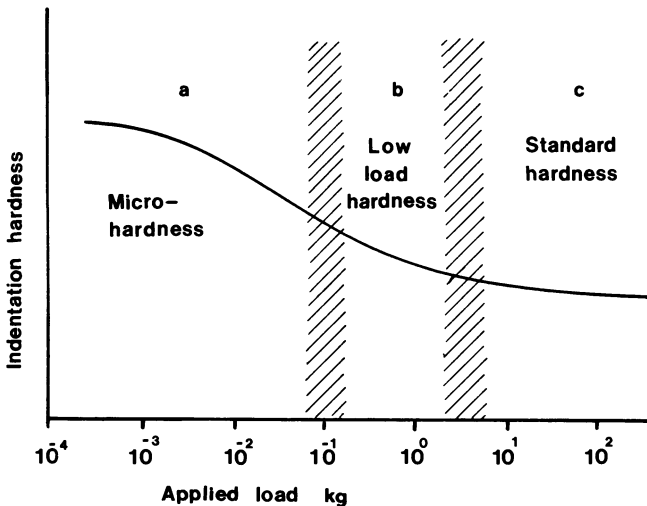
Figure 1.3. Range of load and hardness type in the indentation hardness method.

move in the near surface regions. Hence the nature of the surface will appear to be dominant in setting a hardness value for the material. This has been shown to be important in the effect that absorbed water has on reducing the measured values of hardness of ceramics such as SiC, MgO, and Al_2O_3 [9] when tests are made with small loads, for example, less than 100 g for MgO.

Here we see an important potential of hardness investigations because typically ceramics are used to take advantage of their "hard" surfaces. Furthermore they frequently have to be drilled, ground, or polished; hence, changes in their surface properties need to be monitored so that technical processes can be improved as ceramics become more widely used in engineering applications.

Once again, however, a warning note must be sounded because of the multivariable problem we are considering. If the indent is only shallow, then the nature of the surface itself and not just the surface environment is important. Surfaces can become hardened by the working and polishing needed to get a satisfactory area for testing. Such hardening could mask the environmental softening effect, and in order to study this aspect proper surface treatments should be used prior to hardness determinations. Chapters 2, 3, 4, and 6 deal more fully with these points.

Too great a load chosen for deep penetration to overcome or minimize the sample surface factors can produce erratic hardness results as brittle ceramics crack locally around the indent and energy is expended on crack propagation. Deliberate overloading has now been shown to be a nondestructive microscopic way of determining important properties of ceramic systems, and as such occupies the whole of Chapter 5. However, when a polycrystalline ceramic is not obviously cracked and the indented area extends over many grains, then other microstructural features become dominant. For example, equation (1.2) is found to relate hardness to porosity in sintered materials. [10]

$$H_x = H_0(1 - \theta)^2 \exp(-B\theta) \tag{1.2}$$

In equation (1.2), H_x is the measured hardness, H_0 is the hardness at zero porosity, and θ is the fractional porosity. Typically B is less than unity and for boron carbide, B_4C, it has the value 0.35 for θ in the range 0–1.0. The bifunctional dependence of hardness on porosity contrasts with equations used to relate ceramic porosity and strength, for example, equation (1.3),

$$\sigma = \sigma_o \exp(-b\theta) \tag{1.3}$$

which has been used to determine strengths of hydraulic cements for many years.

The mechanism of material flow beneath the indenter in the case of porous samples is referred to in Section 5.2.3, and the change in sample microstructure in the indented area is shown in Fig. 6.23 for a porous composite of β-Al_2O_3 + ZrO_2.

From all of the above we see that load selection is very important in determining the actual value of a measured hardness in this type of test, and as such it is dealt with in full detail in Chapter 4.

A third indentation test parameter of fundamental importance is temperature. In several studies of the temperature dependence of hardness, an activated process becomes apparent from Arrhenius-type behavior.[4] Calculation of the activation energies associated with thermal softening is characteristic of the activated processes governing plastic flow in crystals.[5,11] Thus, the role played by the crystal structure in determining micro- and low-load hardness values must be a major one since, apart from its effect on lattice energy, the actual arrangement of the ions in a ceramic crystal is important in determining the ease of plastic flow. This aspect of ceramic hardness and its potential applications is discussed in Chapter 3.

It should be noted at this stage that variations in micro- and low-load hardness observed as functions of indenter geometry and crystal orientation are in fact only reflections of different distributions of shear stress within the bulk of the crystal. In this respect, too, the variations in chemical bond type found in ceramics must be important since ionic bonding proves less of a barrier to plastic flow than the strictly directed covalent bonds.

When considering the hardness of ceramics, a fourth parameter is purity. It is known that aliovalent cation impurities are a potent source of solution hardening. For example, in MgO the solution hardening rate due to Fe^{3+} is an order of magnitude greater than that due to Fe^{2+} (Refs. 12 and 13); a closely related result is found for Ti^{4+} in Al_2O_3 when compared to Ti^{3+}.[14] The main thrust in the interpretation of solution hardening has, like much interpretation of ceramic hardness, involved dislocation theory; aliovalent cations are believed to form complexes with compensating lattice defects, which in turn cause elastic and bond distortions of the lattice, and then both these factors control the solution hardening rate by their interaction with crystal dislocations. Since many ceramic systems are solid solutions this aspect is important; it is dealt with in Chapter 3. However, we must return to our earlier warning and see that one type of explanation must not be overused because some ceramics show an impurity softening effect which is more readily rationalized through a chemical bond strength model; the solid solution hardness values of the dicarbides show this[15] as does the variation of hardness with carbon content in carbides and of β-boron as metals are dissolved in it.[7] These and many other aspects and examples are gathered together in Chapter 6 in sections dealing with each ceramic in terms of its structure, microstructure, uses, and values for

hardness, together with other properties that have been calculated for each material following the measurement of its hardness.

What we have just considered for one type of test procedure has parallels for others, but in each case the dominant function can be different. With respect to ceramic specimens the following test procedures, outlined here and described in Chapter 2, are most commonly encountered.

1.4. TYPES OF TEST

1.4.1. Static Indentation Tests

This group of tests has already been referred to in order to emphasize the multifunctional nature of hardness. There are several modes depending upon whether a ball, cone, or pyramid is forced into the ceramic surface. In all cases the load per unit area of impression is given as the measure of hardness. Results here are more variable than might seem necessary because different test methods use different unit areas. For example, in the *Brinell* test where a small sphere is used to indent the surface the hardness is calculated from the contact area, *not* the area in the plane of the surface which would seem to be a more directly measured and calculated variable. Thus

$$H_B = \frac{P}{\text{contact area}} = \frac{P}{\pi D[D - (D^2 - d^2)^{1/2}]} \qquad (1.4)$$

where P = applied load, D = sphere diameter, and d = diameter of the impression left in the sample surface.

Equation (1.4) has a different form and therefore a different hardness value is quoted when the area used is that projected onto the plane of the surface; this is then the Meyer hardness H_M.

$$H_M = \frac{P}{\text{projected area}} = \frac{4P}{\pi d^2} \qquad (1.5)$$

When a ball or spheroconical indenter is used but no indent area is calculated, then the Rockwell hardness is obtained. In fact the Rockwell indentation hardness is a depth of penetration value.

When a pyramid with apex of 136° is forced into the surface and the *contact area* is used to determine the stress, then the Vickers hardness H_V is obtained.

$$H_V = \frac{P}{\text{contact area}} = \frac{0.322P}{a^2 \sin 136°} = \frac{0.464P}{d^2} \qquad (1.6)$$

In this equation, $2a$ is the mean diagonal length expressed in microns of the diamond-shaped impression made in the indented surface and the load P is expressed in newtons.

Ceramics, because of their brittle nature or because they may be present as thin surface coatings in an engineering application needing to be tested, have dictated the development of a blunter indenter producing shallower impressions. When the pyramid has at the apex two angles, one of 172.5° and the other of 130°, a Knoop impression is made in a surface. This has the characteristic of one long diagonal, seven times longer than the short diagonal. Knoop hardness is not directly comparable to Vickers hardness because the projected area and *not* the contact area has always been used to determine the stress.

$$H_K = \frac{P}{\text{projected area}} = \frac{2P}{d_l^2(\cot 172.5° + \tan 130°)} \tag{1.7}$$

In this expression for hardness, d_l is the length of the long diagonal of the indent.

Because it is sometimes advantageous to have an indenter that more closely reflects the symmetry of the plane being indented, a triangular-based pyramidal indenter was developed during the late 1950's; it is the Berkovich indenter. This indenter has an angle of 65° between the vertical axis and each of its three faces which penetrate the surface. Equation (1.8) allows hardness values to be calculated when a_B is measured as the perpendicular distance from an apex to the opposite base of the triangular indent shape produced on the surface.

$$H_B = \frac{1.732P}{a_B^2} \tag{1.8}$$

where P is expressed in newtons and a in microns.

As anisotropy measurements and toughness determinations of ceramic systems have become more necessary, the indentation type of hardness measurement has become more popular, as Chapters 3 and 5 show.

Each of these methods is subject to restrictions, some of which will be made clear in Chapter 2, on the design of apparatus and application of the stress; but when these restrictions are conformed to, the hardness values obtained, although not obviously directly comparable, are related through the general expression

$$H_x = C\sigma_y \tag{1.9}$$

where C is the constraint factor and σ_y is the uniaxial flow stress.

1.4.1.1. Constraint Factors

Hardness values are related to flow stress by a *constraint factor*. It is easy to visualize this by considering a simple compression test because in such a test the whole specimen goes plastic due to the fact that there is no resistance to side flow with the specimen being only surrounded by air. In the indentation test the part of the specimen that flows is surrounded by elastic material and so side flow is restricted. Therefore a greater mean stress is required to cause plastic flow in hardness tests than in simple compression tests. In equation (1.9) C is called the constraint factor, approximating to 3 for Brinell, Vickers, and Knoop hardness.

Much theoretical consideration has been given to explain the origin and size of the constraint factor C. The common approach is given in terms of slip line field (SLF) theory, according to which plastic flow takes place in plain strain over a range determined by the displaced material, while at all other points the material is rigid. The SLF is a network of curves along which the shear stress or shear strain rate is a maximum; suitable flow patterns need to be consistent from the standpoint of velocities. Since 1920 various suitable flow patterns have been suggested and analyzed. For example, if a blunt 2-D punch is used to indent, as shown in Figure 1.4, the solid lines are directions of constant maximum shear stress. They constitute a set of orthogonal shear stress coordinates α, β.

Normal stress on the surface $\sigma_1 = 0$ since this surface communicates with air, but below the punch normal stress is σ_2' because the indented area communicates with the punch surface. The normal stress on the shear plane for any point within ABC will be $P_D = K$.
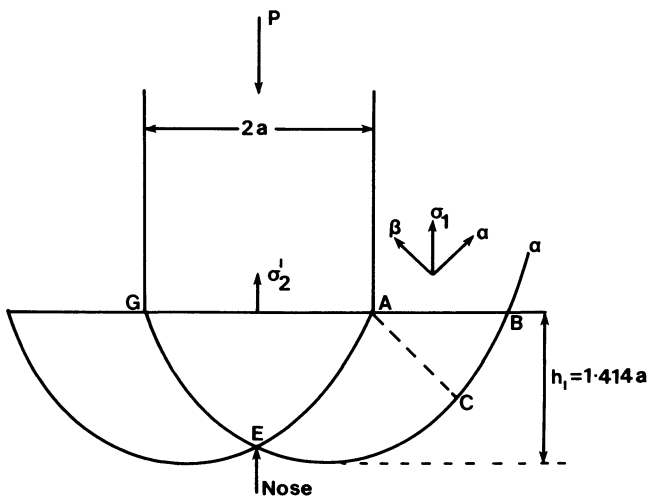

Figure 1.4. Two-dimensional blunt punch indenter.

From C to E the α line is curved; therefore there is no change in shear stress, but the normal stress will change according to equation (1.10)

$$P + 2\phi K = \text{constant} \tag{1.10}$$

where ϕ = angle between α and x axis.

At point C, $\phi = 90° = \pi/4$.

At point E, $\phi = 270° = -\pi/4$.

Hence $P_c + 2K\phi_c = \text{constant} = P_E + 2k\phi_E = k(1 + \pi)$.

Normal stress on the punch face in area AEG is given by

$$\sigma_2' = k + p' = 2k(1 + \pi/2) = 2k(2.57) \tag{1.11}$$

The corresponding mean stress on the punch for plane strain uniaxial compression is $2k$. Hence the constraint factor $C = (1 + \pi/2)2k/2k = 2.57$. The relation between the plane strain flow stress $2k$ and the axisymmetric (3-D) flow stress σ_y is $2k = 2\sigma_y/(3)^{1/2}$. Therefore the 3-D constraint factor will be

$$C = \frac{\sigma_2'}{\sigma_y} = \frac{(1 + \pi/2)2k}{(3/2)^{1/2}2k} = 2.97$$

Experimental values for many materials are around 3; therefore, good agreement exists.

For a perfectly elastic-plastic solid the theory of hardness indentation is relatively simple leading to the important conclusion expressed by equation (1.9), that the hardness or average pressure under an indenter is a constant factor of yield stress. In its simplest form, as shown above, $C = 3.0$, which is the *Tabor relationship*. This arises because $\frac{2}{3}$ the pressure under the blunt indenter is hydrostatic, the remainder being shear stress, and only this can produce the plastic flow necessary to leave a permanent indent. The effects of elastic deformation are considered unimportant and this obviously makes this constraint factor far from useful for engineering ceramics, which are far from perfectly elastic-plastic. Indeed, 43 years ago Westwood showed that C could be as large as 35 for single-crystal materials with alkali halide structures, while perspex or nylon materials have C values considerably below 3. As a result the constraint factor relating hardness to flow stress has received fairly constant attention in theory and in modelling the indentation process. This later aim is not easily achieved because the strain under an indenter is very complicated, involving considerable shear. However, Marsh in particular believed that elastic deformation in ceramic or glass systems was important and sought to bring this aspect out in the analysis.

Marsh recognized that in order to obtain a value for the flow stress of glass one is forced to work from indentation hardness tests since this is the only simple way to measure flow stresses for *macroscopically* brittle materials. This was in a sense learning from Tabor's model of the flat rigid indenter penetrating an elastic-plastic material. Such a material is sometimes called a Mises material. However application of Tabor's model to glass produces values for σ_y well below the observed brittle fracture stress and flow characteristics should be apparent in the breaking behavior of glass.

This was not the case. Marsh turned to Hill's analysis of a spherical cavity expanding under an internal pressure and *not* forcing the material to the surface as the rigid die model does because experimental observation shows the plastic zone to be hemispherical for a great range of materials. He had to introduce constraints to account for the inclusion of a flat surface to produce a hemisphere. For ceramic and glass materials with high values of σ_y/E Marsh derived semi-empirically the relationship

$$\frac{H_V}{\sigma_y} = C + kB \ln Z \qquad (1.12)$$

where C and k are constants and B and Z are functions of σ_y/E, respectively, and H_V is the Vickers hardness of the sample.

Equation (1.12) holds only when $B \ln Z$ is less than 4 and the constants were such that

$$H_V = 0.07 + 0.6 \ln \frac{E}{\sigma_y} \qquad (1.13)$$

Further development of Hill's expanding cavity model by Johnson, taking into account the shape factor associated with the different types of indenter, leads to equation (1.14).

$$H_V = \frac{2}{3}\left(1 + \frac{\ln E \cos \theta}{3\sigma_y}\right)\sigma_y \qquad (1.14)$$

where θ is the semi-angle of the indenter. This last equation allows values of hardness measured by indenters of various standard geometries to be correlated with a single parameter

$$H_x = \left(\frac{E}{\sigma_y}\right)\tan \beta \qquad (1.15)$$

where H_x is any type of hardness as determined by indentation methods using pyramids of general geometry and β is the angle of inclination of the indenter to the surface at the edge of the indentation. Below, Figure 1.6 shows that this angle might not be so simple to obtain. A more recent attempt to remove the empirical constants in Hill's approach concentrates on the fact that the plastic zone is hemispherical and the indentation pressure p is indenter shape insensitive. The volume V of the plastic hemisphere is directly equated to the plastic work of indentation which equals $p \, \Delta V$, where ΔV is the indent volume.

The parameter β is defined as b/r where b is the plastic zone radius and r is the radius of the indent for a spherical indenter and

$$\beta = \frac{b}{r} = \left(\frac{V}{\Delta V}\right)^{1/3} \tag{1.16}$$

For a wide-angle indenter, such as a Vickers pyramid,

$$\frac{b}{r} = \left(\frac{b}{a}\right) \frac{1.644}{\cot^{0.33} \Psi}$$

where $2a$ is the indentation diagonal and 2Ψ is the included angle between opposite faces. For the Vickers pyramid $\Psi = 68°$ and $r = 0.45a$. The indentation pressure p can be converted to hardness H_x by using the appropriate area term.

Hill's spherical cavity solution can then be adapted to give

$$\frac{E}{p} = \frac{4.5[(1 - \nu)\beta^3 - 0.66(1 - 2\nu)]}{1 + \ln \beta^3} \tag{1.17}$$

and

$$\frac{p}{\sigma_y} = 0.66\left\{1 + \ln\left[\frac{E/\sigma_y + 2(1 - 2\nu)}{3(1 + \nu)}\right]\right\} \tag{1.18}$$

Surface forces on the plane bisecting the spherical cavity generate shear stresses in the *plastic* hemisphere and these are added to those calculated for the symmetric solution in order to gain a quantitative picture of the stress at points on the surface, in the plastic zone, and in the elastic zone, both on indentation and on removal of the indenter. In order to do that the following equations can be used:

Under Load

a. Plastic zone

$$\frac{\sigma_r^{pl}}{p} = \left[\frac{3 \ln (r/a)}{1 + 3 \ln \beta}\right] - 1 \tag{1.19}$$

$$\frac{\sigma_t^{pl}}{p} = \left\{\frac{3[\ln(r/a) + \frac{1}{2}]}{1 + 3\ln\beta}\right\} - 1 \tag{1.20}$$

with σ_r^{pl} = radial stress at r', the distance from cavity center, in the plastic zone, and σ_t^{pl} = the tangential stress in the plastic zone for $\beta > r/a > 1$.

b. Elastic zone

$$\frac{\sigma_r}{p} = -\frac{\beta^3}{(r'/a)^3(1 + 3\ln\beta)} \tag{1.21}$$

$$\sigma_p^{el} = \frac{\beta^3}{2(r'/a)^3(1 + 3\ln\beta)} \tag{1.22}$$

These apply for $r'/a > \beta$ and el signifies the elastic zone.

On Removal of Load. The stresses in equations (1.19)–(1.22) are modified to become

$$\frac{\sigma_r^{pl(r)}}{p} = \text{Equation (1.21)} + \frac{1}{(r'/a)^3} \tag{1.23}$$

$$\sigma_p^{pl(r)} = \text{Equation (1.22)} - \tfrac{1}{2}(r'/a)^3 \tag{1.24}$$

$$\frac{\sigma_r^{el(r)}}{p} = \text{Equation (1.23)} + \frac{1}{(r'/a)^3} \tag{1.25}$$

$$\frac{\sigma_t^{el(r)}}{p} = \text{Equation (1.24)} - \frac{1}{2(r'/a)^3} \tag{1.26}$$

These are the residual stresses, hence the superscripts el(r), etc. This analysis shows that they are not negligible and play a dominant part in the production of fracture patterns around indents (see Chapter 5). To these cavity stresses have to be added the stresses caused by the flat surface needed to change the sphere to the hemisphere:

$$\sigma^s = \int_{\text{plastic}} dA \frac{\sigma_t^j}{p} g_{mm} + \int_{\text{elastic}} dA \frac{\sigma_t^k}{p} g_{mm} \tag{1.27}$$

j = plastic, k = elastic or residual plastic or residual elastic as necessary; $mm = xx$, xz, or zz and for a point force p applied at 000 acting in the

positive z direction,

$$\sigma_{xx} = pg_{xx}, \qquad \sigma_{yy} = pg_{yy}, \qquad \sigma_{zz} = pg_{zz}, \qquad \sigma_{xz} = pg_{xz}.$$

$$g_{xx} = \frac{z}{2\pi R^3}\left\{1 - 2\nu - 3\left(\frac{x}{R}\right)^2 - \frac{1-2\nu}{(R+z)^2}\left[R^2 - x^2 + \frac{R}{z}(R^2 - 2x^2)\right]\right\} \quad (1.28)$$

$$g_{yy} = \frac{z}{2\pi R^3}\left\{1 - 2\nu - 3\left(\frac{y}{R}\right)^2 - \frac{1-2\nu}{(R+z)^2}\left[R^2 - y^2 + \frac{R}{z}(R^2 - 2y^2)\right]\right\} \quad (1.29)$$

$$g_{zz} = -\frac{3z^2}{2\pi R^5} \qquad\qquad\qquad\qquad\qquad\qquad (1.30)$$

$$g_{xz} = -\frac{3xz^2}{2\pi R^5} \qquad\qquad\qquad\qquad\qquad\qquad (1.31)$$

where $R^2 = x^2 + y^2 + z^2$ and $\nu =$ Poisson's ratio.

Analytic solutions of the integrals and calculation of the stresses at various points for indents of varying sizes and shapes lead to several common features: the peak tensions are at the elastic-plastic boundary; there is a rapid change to compression within the plastic zone and a linear decrease in tension into the elastic zone; and, for indenters with large Ψ, the residual stresses are *greater* than the peak stress at loading, so that these stresses are important as the load is removed. These predictions are consistent with observations made on many ceramic crystals.

A plot of the σ_{yy} component of the tangential stress, normalized by the hardness, against distance in the x direction shows pictorially in Figure 1.5 the small effect on surface stress different-sized indents have and the tensile nature of the stress with residual values exceeding load stresses.

Experimental comparisons between the Vickers hardness H_V and the parameters in equation (1.15) as determined by bend tests, etc., give values of H_V in the range $6-12\sigma_y$, and not the $4.5\sigma_y$ predicted by equation (1.15). The difference is due to factors such as the strain rate, $\dot{\varepsilon}$ being very fast in hardness tests; the total strain, with values around 8% in hardness tests in the region around the indent shape compared to 1% in compression tests before macroscopic bursting; and the true nature of the ceramic material. For example, for the covalent structures found for diamond, silicon, germanium, quartz, silica, and glasses the room-temperature hardness may be a result not of normal plastic flow processes as found in metals and more
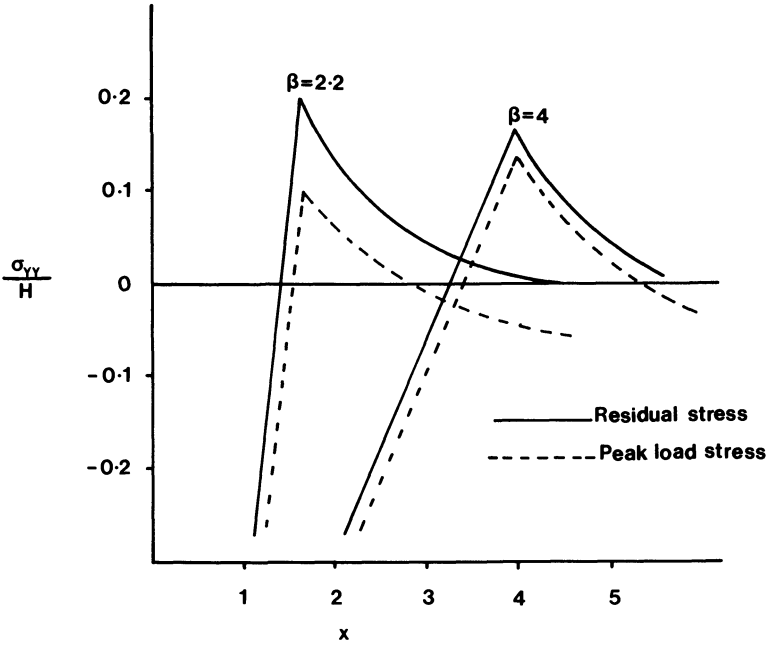
Figure 1.5. Tangential stress at the surface of a ceramic for different indent sizes. These stresses cause radial fracture.

ionic solids such as alkali halides, but of a critical stress-dependent mechanism. Such mechanisms include pressure-dependent semiconductor-to-metal transition-stress softening; athermal flow over the extremely strong Peierls barriers of these solids; densification under the indenter leading to a changing hardness as the penetration increases; the formation of cracks beneath the indenter; and stress-induced hardening. These parameters, especially densification for glasses and crack formation for general ceramic systems, have been included in analyses in extensive work to develop the hardness technique for finding toughness values for such materials.

Ceramics which, when indented, undergo the mechanisms listed above, with the exception of cracking, can be grouped as Mohr–Coulomb materials for which five parameters—E, σ_y, ν, $\dot{H}$, and α—are needed to calculate hardness. Here E, σ_y, and ν have their usual meaning while $\dot{H}$ is the stress hardening rate and α is the densification factor. Clearly if indentation causes densification then α and $\dot{H}$ must be closely linked.

Yield in Mohr–Coulomb materials follows a criterion which is the sum of stress terms and the Mises criterion:

$$f = \alpha(\sigma_x + \sigma_y + \sigma_z) + (1 + \alpha)(\tfrac{1}{2})^{1/2}$$
$$\times [(\sigma_x - \sigma_y)^2 + (\sigma_y - \sigma_z)^2 + (\sigma_z - \sigma_x)^2 + 6\tau_{xy}^2]^{1/2} \qquad (1.32)$$

This yield criterion would need to be used in any extended calculation of H_x or indentation shape, which explains why empirical and semiqualitative work is the order of the day in this field and approximate constraint factors are used.

The availability of computer time and the borrowing of the finite element method from architectural design has seen the growth of calculated hardness values for some ceramic materials.[16]

1.4.1.2. Indent Shapes

By advancing from Mises materials with the inclusion of different degrees of densification and stress hardening the prediction of indent cross-section is possible. When $|\alpha|$ and $\dot{H}$ are small, <0.1, the piled-up indent of the Tabor model arises. For α around -0.2 and $\dot{H}$ up to $0.2E$ the flat surface expanded cavity indent occurs. Densification with $\alpha = -0.33$ which implies a contribution to deformation by this mechanism of 45%, the remainder being from flow processes, produces the rosette-like indent observed in many glassy ceramics. Large values ascribed to $\dot{H}$ produce the partially piled-up cross section shown in Figure 1.6(d) along with the other schematic representations. Shapes (c) and (d) in Figure 1.6 are most commonly encountered in ceramic materials.

Flow patterns in the surface around indents and their significance are dealt with in Chapter 3. The development of surface and subsurface crack patterns is the subject of Chapter 5. Changes of shape with time and temperature—that is, the relaxation and creep of indentations—are covered in Chapter 4. All the indentation methods can be adapted to make studies at high and low temperatures and with various degrees of atmosphere control with the result that in a quantitative sense indentation has massively

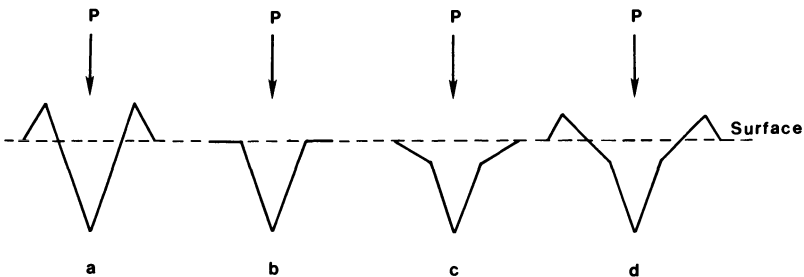**Figure 1.6.** Schematic representation of indent shapes for materials with different constraint factors. (a) Mises material with Tabor constraint. (b) Mises material with Hill constraint or Mises–Coulomb material with $\alpha \approx -0.2$, $\dot{H}$ $0.2E$. (c) Mises–Coulomb material with no stress hardening but about 45% densification, typical of glass. (d) Little densification but large values of $\dot{H}$.

outgrown all other hardness test methods which have to a large extent become comparative methods only.

1.4.1.3. Theoretical Hardness

So far for the method involving indentation we can see that the generalization in equation (1.33) applies:

$$H = \frac{P}{\text{Area}} \tag{1.33}$$

Now, taking area down to the fundamental cross-sectional area of one structural unit—atom, ion, or molecule—we might find a way to define and determine a fundamental hardness for any material. Figure 1.7 shows the model we might use.

In Figure 1.7, on the atomistic scale shown, the area of indent $= r_e^2$ and so we have one part of equation (1.33). To get the second variable from the figure we see that after time t atom B is moved by P until it reaches a position such that r between A–B and B–C is increased sufficiently to produce an opposition force to P and cause a new equilibrium. In this process we have shortened the distance between B and D to r_2 and caused a repulsive force to dominate in the shortened bond directly beneath the indenter. Thus we need an expression to represent the potential energy between the structural units so that we can redefine the new energy for the system.

Several expressions have been defined which have a form combining attractive forces with shorter-range repulsive forces, for example, the Lennard–Jones 6–12 potential:

$$V = 4\varepsilon \left[\left(\frac{\sigma}{r} \right)^{12} - \left(\frac{\sigma}{r} \right)^{6} \right] \tag{1.34}$$
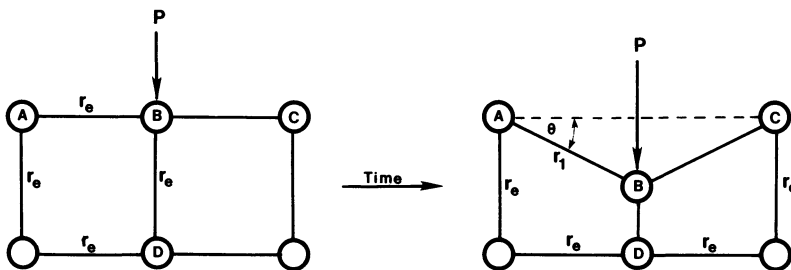

Figure 1.7. Atomistic representation of hardness indentation process.

A more general expression of this type is given as

$$V = \frac{V_e}{m-n}\left[m\left(\frac{r_e}{r}\right)^n - n\left(\frac{r_e}{r}\right)^m\right] \qquad (1.35)$$

In equation (1.35) the first term in the bracket is the repulsion force, important when $r < r_e$; m and n are constants related to bond type which will reflect the ionic, covalent, or mixed ionic-covalent bonding in the ceramic systems considered in this book. V_e is the equilibrium potential, r_e is the distance at which $V = 0$, and r is the distance r_1, r_2 as shown in Figure 1.7.

To generalize further the terms z/b_1 and z/b_2 need to be introduced into equation (1.35) to allow for structural variations by accounting for the number of type A atoms and type D atoms in Figure 1.7; hence z is the coordination number of the structure and

$$V = \frac{V_e}{m-n}\frac{z}{b_1}\left[m\left(\frac{r_e}{r}\right)^n\right] - \frac{V_e}{m-n}\frac{z}{b_2}\left[n\left(\frac{r_e}{r}\right)^m\right] \qquad (1.36)$$

Ignoring the repulsive part of equation (1.36) for the stretched bonds and ignoring the attractive part for the compressed bonds we can find dv/dr_1 and dv/dr_2, which when combined will give the force of interaction for the system. Resolving the stretching force vertically and combining it with the compression force (P in Figure 1.7) the second part of equation (1.33) will be found.

First considering the bond stretched from r_e to r_1, the first term in equation (1.36) is ignored, so that

$$V = -\frac{V_e z n}{(m-n)b_2}\left(\frac{r_e}{r_1}\right)^m$$

$$\frac{dV}{dr_1} = -\frac{V_e z n}{(m-n)b_2}\frac{(-m)}{r_e}\left(\frac{r_e}{r_1}\right)^{m+1}$$

$$= \frac{V_e z}{(m-n)}\frac{nm}{b_2 r_e}\left(\frac{r_e}{r_1}\right)^{m+1}$$

For the angle θ in Figure 1.7 this force resolves in the P direction as

$$\frac{dV}{dr_1} = \frac{V_e z}{(m-n)}\frac{nm}{b_2 r_e}\left(\frac{r_e}{r_1}\right)^{m+1}\left(\frac{r_e - r_2}{r_1}\right) \qquad (1.37)$$

Similarly the repulsive force as r_e decreases to r_2 can be found.

$$V = \frac{V_e}{(m-n)} \frac{z}{b_1} m \left(\frac{r_e}{r_2}\right)^n$$

$$\frac{dV}{dr_2} = \frac{V_e}{(m-n)} \frac{zm}{b_1} \frac{(-n)}{r_e} \left(\frac{r_e}{r_2}\right)^{n+1}$$

$$\frac{dV}{dr_2} = -\frac{V_e zmn}{(m-n)b_1 r_e} \left(\frac{r_e}{r}\right)^{n+1} \tag{1.38}$$

Combining equations (1.37) and (1.38) with respect to the action of P,

$$P = \frac{V_e znm}{(m-n)b_2 r} \left(\frac{r_e}{r_1}\right)^{m+1} \left(\frac{r_e - r_2}{r_1}\right) + \frac{V_e zmn}{(m-n)b_1 r} \left(\frac{r_e}{r_2}\right)^{n+1}$$

$$P = \frac{V_e znm}{(m-n)r_e} \left[\frac{1}{b_2} \left(\frac{r_e}{r_1} - \frac{r_2}{r_1}\right)\left(\frac{r_e}{r_1}\right)^{m+1} + \frac{1}{b_1}\left(\frac{r_e}{r_2}\right)^{n+1}\right] \tag{1.39}$$

Now, substituting equation (1.39) and the area of indent into equation (1.33), we have an expression for theoretical hardness:

$$H = \frac{V_e znm}{(m-n)r_e^3} \left[\frac{1}{b_2} \left(\frac{r_e}{r_1} - \frac{r_2}{r_1}\right)\left(\frac{r_e}{r_1}\right)^{m+1} + \frac{1}{b_1}\left(\frac{r_e}{r_2}\right)^{n+1}\right] \tag{1.40}$$

Given V_e and r_e we might be able to use this expression, but what about r_1 and r_2? It is worthwhile making substitutions for these terms to arrive at a more easily envisaged and easily used expression. Assuming average bond lengths at equilibrium, then

$$r_e^2 = \frac{V_m}{N_o K} \tag{1.41}$$

Here V_m is the molar volume, N_o is Avogadro's number, and K is a structure factor related to the coordination number z. For a surface atom,

$$V_e = \frac{U_L}{z N_o W} \tag{1.42}$$

where U_L is the lattice energy, z is the coordination number, and W is the number of atoms per formula unit.

In order to obtain expressions for r_1 and r_2, since we have equation (1.40) we need to find the ratios r_e/r_1 and r_e/r_2. To do this we analyze the model further. As the indenter displaces atom B, r_1 increases and the restoring force dV/dr_1 increases. This can continue only until a maximum force is developed and the bond breaks, hence dv/dr_1 will be zero. Thus, differentiating equation (1.35) twice,

$$\frac{d^2V}{dr^2} = \frac{V_e nm}{(m-n)r_e^2}\left[(n+1)\left(\frac{r_e}{r_1}\right)^{n+2} - (m+1)\left(\frac{r_e}{r_1}\right)^{m+2}\right]$$

$$\therefore \quad 0 = (n+1)\left(\frac{r_e}{r_1}\right)^{n+2} - (m+1)\left(\frac{r_e}{r_1}\right)^{m+2}$$

and

$$\left(\frac{r_e}{r_1}\right)^{n-m} = \frac{m+1}{n+1}$$

so that

$$\frac{r_e}{r_1} = \left[\frac{m+1}{n+1}\right]^{1/(n-m)} \tag{1.43}$$

To find r_e/r_2 we can make use of the fact that at equilibrium V in equation (1.35) will be zero, and the repulsive parts of extended bonds and the attractive parts of shortened bonds can be ignored.

$$V = 0 = \frac{r_e}{m-n}\left[m\left(\frac{r_e}{r_2}\right)^n - n\left(\frac{r_e}{r_1}\right)^m\right]$$

since $m = n$,

$$0 = m\left(\frac{r_e}{r}\right)^n - n\left(\frac{r_e}{r}\right)^m$$

and

$$\frac{r_e}{r_2} = \left[\frac{n}{m}\left(\frac{r_e}{r_1}\right)^m\right]^{1/n}$$

substituting from equation (1.43):

$$\frac{r_e}{r_2} = \left(\frac{m+1}{n+1}\right)^{-1/(n-m)} = \left(\frac{n+1}{m+1}\right)^{1/(n-m)} \tag{1.44}$$

$$\frac{r_e/r_1}{r_e/r_2} = \frac{r_2}{r_1} = \left(\frac{m+1}{n+1}\right) \tag{1.45}$$

Putting equations (1.41)–(1.45) into the theoretical hardness equation (1.40) gives rise to the general equation

$$H_{\text{th}} = \frac{nmU_LK}{(n-m)V_m}\left(\frac{1}{b_2}\left\{\left(\frac{m+1}{n+1}\right)^{(m+1)/(n-m)}\left[\left(\frac{m+1}{n+1}\right)^{1/(n-m)} - 1\right]\right\}\right.$$
$$\left. + \frac{1}{b_1}\left(\frac{n+1}{m+1}\right)^{(n+1)/(m+1)}\right) \tag{1.46}$$

Equation (1.46) suggests that four properties control the hardness of a material:

- The bonding, through values of n and m.
- The structure, through b_1 and b_2.
- The lattice energy.
- The molar volume of the material.

The direct dependence on lattice energy and inverse dependence on molar volume have been qualitatively inferred in the past.

An example of a special ceramic, silicon, which has a cubic structure reveals a similarity between this approach and the findings of theoretical strength calculations: for silicon, $V_m = 12.045 \times 10^{-6}\,\text{m}^{-3}$ per atom and $U_L = 488.2 \times 10^3\,\text{J}$ per atom. It has a face centered cubic (fcc) structure with $K = 0.7$, $b_1 = 1.5$, $b_2 = 1.0$, and $m = 3$, $n = 6$. These values substituted in equation (1.46) predict a theoretical hardness of $400\,\text{GN m}^{-2}$, about 80 times greater than the observed hardness. It could be argued that application of equation (1.46) depends on the structure of the material in that the hardness of a material with an open structure is determined by the extension of the bonds with little contribution from compression. This implies that equation (1.46) can be considered in two parts, the first dealing with extension and the second with compression. Silicon therefore can be thought to be dominated by the first term whereby its hardness would be approximately $14\,\text{GN m}^{-2}$, which is still two to three times larger than experimental values (see Table 6.16).

Dense, close-packed structures such as the metals have would involve using only the second term in the brackets in equation (1.46).

The theoretical strengths of materials are consistently shown to be one to three orders of magnitude greater than real strengths; thus, researchers have concentrated on the defects that lead to this discrepancy. Clearly

similar considerations would be worthwhile in hardness studies. Where this approach is tried, it will be highlighted in the text.

1.4.2. Damping Tests

A detailed description and analysis of this method is given in Chapter 2. The alleged similarity between this method and drilling processes together with the relatively unsophisticated type of apparatus, which can be readily made in the laboratory, makes this the next most used type of test on ceramic and glass systems. In 1923 Herbert introduced as the pendulum hardness sclerometer a steel ball pivoted on a mineral surface, but in this form the rolling friction rather than an indentation effect was being measured. Kuznetsov changed the design in 1929 to a single diamond point and related damping to hardness. Rebinder further developed the method with a two-diamond fulcrum and introduced the mathematical analysis. It has been demonstrated several times since then that there is a critical weight for a pendulum that depends on the material to be tested. The critical weight increases with hardness and the system is at its most sensitive at the critical weight. Although the energy of oscillation and subsequent damping can be calculated quite easily, the transfer of that energy to the surface of the solid ceramic becomes a source of theoretical development, dependent on the models used to describe the process. Such an analysis is given in Chapter 2. However, for all practical purposes the hardness obtained this way is used only in a relative way and to study changes within particular systems.

In this test hardness is usually defined by equation (1.47):

$$H_p = \frac{-A_0}{\left(\dfrac{dA}{dt}\right)_{t=0}} \tag{1.47}$$

Although this equation shows little resemblance to those defining indentation hardness, it has recently been shown that the major process contributing to a hardness value is material flow in the solid and not comminution. Thus, the two types of hardness are more closely related than at first might be thought. The relationship is found to be exponential when sclerometer hardness is compared to Knoop microhardness values for the range of minerals used as standards in the Mohs linear rank scale (see Figure 1.8). Using the same comparison, namely, the Mohs minerals, the relationship between surface energy and pendulum hardness is found to be exponential and given by equation (1.48), which produces a straight-line relationship between pendulum hardness and surface energy measured in ergs cm^{-1}

$$\ln H_p = 0.5066 + 0.9198 \ln \gamma \tag{1.48}$$

Pendulum hardness closely approximates the scale of the rank of Mohs minerals, which is also shown in Figure 1.8.

1.4.3. Rebound Tests

Rebound tests are used even less frequently than the two previous types of test and represent a bridge between indentation and damping. A sphere of very hard material or of the same composition as the test surface is dropped onto the flat surface and two parameters are measured, first the height of rebound and second the diameter of the surface impression. This method is most easily adapted to measure hardness at very high temperatures because the contact time of ball and surface is extremely short and negligible heating of the indenter occurs, making it easier to apply theoretical analysis to the process. Two values of hardness, height of rebound and area of indentation, can be found but it is the rebound height that is most easily determined as a function of temperature and is used for temperature versus hardness studies. Measurement of indent size at high temperature is greatly affected by indentation creep which will be discussed in Chapter 4.

1.4.4. Erosion Tests

Hardness is one parameter in erosion and cavitation behavior of solid surfaces and therefore can be extracted from the data such tests provide. However, it is more common to use hardness measurements as determined by the other methods to predict erosion behavior.

Erosion is a process frequently used to shape ceramics; consequently, it has often been investigated technologically rather than theoretically. It is the multiparticle impact of a *brittle* solid, and essentially two types of model have been researched, as will be shown in Figure 5.19.

The first of these considers elastic interactions only between the target and the streams of particles which produce ring cracks on the surface of the target. The ring cracks eventually intersect, and material is removed. This model does most closely suit the impingement of low velocity spherical particles. Clearly the Brinell static indentation test is most closely similar because overloaded Brinell spheres produce this type of damage (see 5.2.2).

The second model improves on the first one in the way that static indentation hardness test theory has advanced by introducing plastic defor-mation into this dynamic system as a parameter. Plastic deformation of the contact area between the particles and the target surface causes radial cracks to propagate outwards from the contact zone and subsurface lateral cracks to move outwards on planes nearly parallel to the surface. Here the parallel with overloaded Vickers static indent tests, which are discussed in detail in

Chapter 5, is obvious. Visual evidence for this being the dominant mechanism in erosion is frequently found when the impacting particles are angular and are harder than the target surface.

Attempts to calculate the erosion volume loss per impact for *isotropic* materials under highly idealized conditions involve the toughness parameter K_c and Vickers hardness H_V. A surprisingly wide divergence in the hardness dependence is predicted:

$$V \propto \frac{(\rho_p \rho_t G_p G_t)^{2/3}}{[(\rho_p G_p)^{1/2} + (\rho_t G_t)^{1/2}]^{8/3} \rho_p^{-19/12} R_p^{-11/3} V_p^{-19/6} K_c^{4/3} H_v^{1/4}} \quad (1.49)$$

or

$$V \propto \frac{(\rho_p \rho_t G_p G_t)^{2/3}}{[(\rho_p G_p)^{1/2} + (\rho_t G_t)^{1/2}]^{8/3} \rho_p^{-11/19} R_p^{-11/3} V_p^{-22/9} K_c^{4/3} H_v^{-1/9}} \quad (1.50)$$

Here V is the erosion volume loss per impact, ρ_p and ρ_t are particle and target densities, respectively, G_p and G_t are particle and target shear moduli, respectively, R_p is the particle radius, V_p is the particle velocity, K_c is the target fracture toughness, and H_v is the target hardness.

Equations (1.49) and (1.50) can be used to define erosion hardness but such values are clearly heavily dependent on the model chosen. In general hardness is expressed as volume removed or mass removed and detailed calculations are not often attempted.

1.4.5. Ploughing Tests

There is another form of dynamic test quite well suited to studies of anisotropy in ceramic hardness values—see Section 3.5.4—but the extraction of absolute hardness values is complicated by frictional dependence as well as pin shape such that only simple comparisons are attempted. As long ago as 1690 Huygens developed a scratch hardness technique and noted anisotropy for scratches in different directions. Mohs developed this in 1822 and showed the material property of hardness by demonstrating that the same mineral from different sources had the same hardness. Scratch hardness was developed using steel or diamond styli and hardness was expressed as the minimum weight required to produce a visible scratch. Mohs's minerals, beginning with gypsum and ending with corundum and diamond, enabled him to establish a linear scale between 1 and 10 with which to compare hardness. The scale, indicated in Figure 1.8, has continued in general acceptance except for the suggestion that the mineral chosen as Mohs's number 5, apatite, should be omitted because of the very obvious
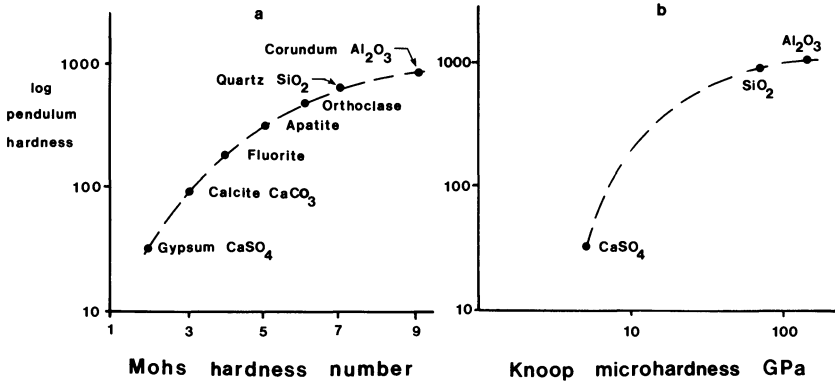
Figure 1.8. Relationships between (a) hardness of Mohs minerals and pendulum hardness and (b) Knoop microhardness and pendulum hardness.

anisotropy in its behavior. Apatite seems better placed at 4.5 on the linear scale.

More quantitative hardness scales have been sought for this method and expressions for hardness then reflect the shape of the slider; for example, using a square-based pyramidal slider with edge leading, the hardness is defined as

$$H_s = \frac{4P}{w^2} \tag{1.51}$$

where P is the normal load and w is the width of the groove. The units are $kg\,mm^{-2}$ to match the indentation method. If a conical slider is used, then

$$H_s = \frac{2.55P}{w^2} \tag{1.52}$$

The diameter of wear particles formed by sliding methods have been related to hardness through equation (1.53):

$$d = \frac{60{,}000\,W_{ab}}{H_V} \tag{1.53}$$

Here d is the wear particle diameter, H_V is the Vickers hardness of the mechanically weaker material, and W_{ab} is the work of adhesion that is found from a knowledge of specific surface work γ_π and interfacial energy between surface a and slider b, $^a\gamma_b$:

$$W_{ab} = (\gamma_\pi)_a + (\gamma_\pi)_b - {}^a\gamma_b \tag{1.54}$$

Thus a knowledge of hardness and tabulated values of surface energy make it possible to predict powder particle sizes from some milling processes.

The scratch hardness parabolic relationship between load and track width as predicted by equation (1.51) is seen in Figure 1.9 to be a reasonable approximation for polycrystalline samples of Al_2O_3, Si_3N_4, and ZrO_2.

A variety of modern designs exist for measurement of scratch hardness, all involving the movement of a loaded stylus over a brittle surface. Such devices produce wear tracks that are informative about the material and the processes leading to its deformation. Because of indentation plasticity the track is expected to show plastic grooving behind the stylus while indentation fracture may produce an array of median and lateral cracks (see Chapter 5) about the track. Interaction of the crack systems can result in debris from material removed as either whole grains or subgrain fragments, depending on the importance of intergranular strength. In the wake of the stylus tensile stress may be generated capable of producing cracks across the track width. A general ploughing action may produce very fine debris at the stylus tip which may be pushed out or further crushed by the stylus. Thus microscopic examination may be worthwhile and give some indication about deformation mechanisms and the importance of micro-structure, or both. Ploughing or scratch hardness measurements have an advantage over indentation methods in that the direction of sliding uniquely
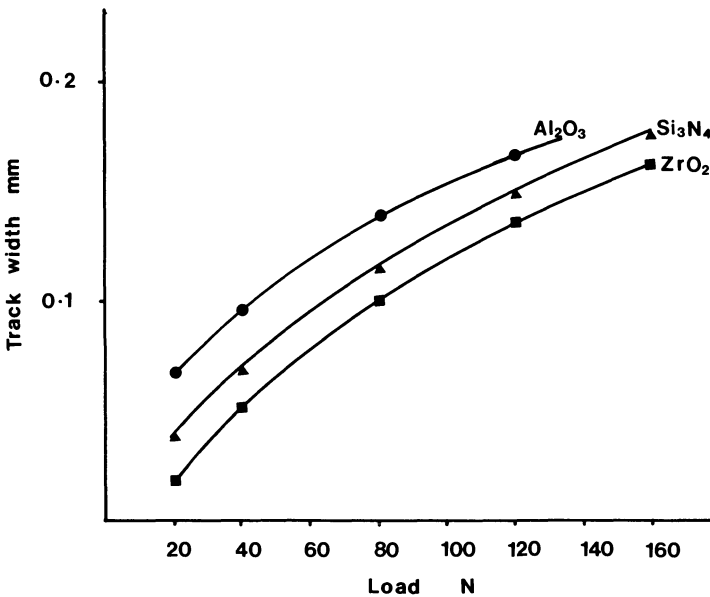

Figure 1.9. Scratch parameters—see equation (1.51)—for polycrystalline ceramics after single pass of 120° conical diamond.

defines the crystallographic direction of the measurements. To balance this advantage is the necessity of measuring the frictional forces set up by the process; Chapter 3 develops a model which attempts to do this.

1.5. AIMS

The methods outlined in Section 1.4 and in some cases described and discussed in more detail in the following chapters are the principal methods from which usable data can be extracted. Where available, results for the ceramic systems listed in Section 1.2 will be given in subsequent chapters of this book together with relevant bonding and structural information that may influence the hardness values of individual systems.

The remainder of the book will then concern the application of hardness methods to determine the following information on ceramic systems:

1. Flow properties and slip systems operating at different temperature ranges, including anisotropy of these systems and its effect on creep behavior.
2. Mechanical properties of ceramic systems which include yield stress, Young's and shear moduli, fracture toughness parameters, and determination of compressive zones at surfaces.
3. Definition and determination of a brittleness index.
4. Crack initiation and propagation.
5. Chemical effects present at ceramic surfaces and stress–corrosion susceptibility.
6. Erosion susceptibility and general ceramic grindability.
7. Critical flaw size analysis at ceramic surfaces.
8. Discussion of a number of ceramic systems in terms of preparation, structure, microstructure, and the hardness of such systems.

REFERENCES

1. I. J. McColm, *Ceramic Science for Materials Technologists*, Leonard Hill, Blackie, Glasgow (1983).
2. B. R. Lawn and D. B. Marshall, *J. Amer. Ceram. Soc.* **62**, 437 (1979).
3. D. M. Marsh, *Proc. Roy. Soc. London Ser. A* **279**, 420 (1964).
4. G. M. Schwab and A. Krebs, *Planseeber. Pulvermetall.* **19**, 91 (1971).
5. D. L. Kohlstedt, *J. Mater. Sci.* **8**, 777 (1973).
6. M. V. Swain, R. M. Latanision, and A. R. C. Westwood, *J. Amer. Ceram. Soc.* **58**, 372 (1975).
7. S. P. Denker, *J. Less Common Metals* **14**, 1 (1968).
8. J. J. Gilman, in *The Science of Hardness Testing and its Research Applications*, J. H. Westbrook and H. Conrads, eds., American Society for Metals (1973), p. 51.
9. J. H. Westbrook and P. J. Jorgensen, *Trans. Met. Soc. AIME* **233**, 425 (1965).

10. V. S. Kirillov, V. I. Kovalenko, V. G. Marinin, I. T. Ostapenko, and V. P. Podtykan, *Sov. J. Superhard Mater.* **5**, 21 (1983).
11. M. S. Kovalchenko, V. V. Dzhemelinskii, V. N. Skuratovskii, and Y. G. Tkachenko, *Inorg. Mater.* **9**, 1525 (1973).
12. G. W. Groves and M. E. Fine, *J. Appl. Phys.* **35**, 3587 (1964).
13. M. Srinivasan and T. G. Stoebe, *J. Appl. Phys.* **41**, 3726 (1970).
14. B. J. Pletka, T. E. Mitchell, and A. H. Heuer, *Phys. Status Solidi* **39**, 301 (1977).
15. I. J. McColm, *J. Less Common Metals* **78**, 287 (1981).
16. M. Imaoka and I. Yasui, *J. Non-Cryst. Solids* **22**, 315 (1976).

Some Aspects of Method

2.1. INDENTATION HARDNESS

From the introductory review in Chapter 1 and from the great preponderance of data to be reported in Chapters 3 to 6, it can be seen that for ceramic hardness studies the vastly dominant technique is that of static indentation. Now some practical aspects of indentation hardness measurements will be considered. Figure 1.3 shows that in a seemingly arbitrary way indentation hardness values and measurements have been determined by the range of the applied load. However, the ranges are not altogether arbitrary because the apparatus needed to make the measurements is characteristic of each of these three zones. Since many of the scientific uses of this technique lie in the microhardness regime 0.0098 N to 1.96 N and the low-load regime 1.96 N to 9.81 N, it is worthwhile concentrating on equipment and techniques necessary for measurement in these ranges. The generally high hardness values of ceramics and the complexity of equipment and technique needed to obtain and measure very small indents means that, in general, low-load hardness work is encountered rather than the microhardness ranges, although the distinction will always remain arbitrary, depending upon the materials under examination, which can lead to indents of greatly different size with a given load. It is after all the difficulties associated with measuring the size of the resultant indent trace and any cracks that may be present that determine to a large extent whether the equipment needed is for micro-, low-load, or macrohardness. In general we can make the following broad classifications among loads, equipment and expertise.

2.1.1. Loads

2.1.1.1. Microhardness

Loads 0.0098 N to 1.96 N characterize this domain, but most work concentrates in the range 0.049 N to 0.49 N where characteristic Vickers

diamond imprint diameters are in the range 3×10^{-6} to 50×10^{-6} m. This implies that satisfactory apparatus must include a high-quality microscope with numerical apertures better than 0.6 and magnification better than 500×. This in turn necessitates the employment of highly skilled workers who have learned microscope techniques in such a way that they are well versed in the causes of errors and are able to minimize them. In fact practitioners must be able to make a full appraisal of all sources of error in the technique from sample to sample; they must also be able to prepare specimens to high metallographic and mineralogical standards. Thus for routine work this range of hardness measurements, which is intended to probe in a scientific way the nature and behavior of ceramic systems, is not recommended.

Equipment and technique for this range of hardness study tend to be purpose-built with workers in different laboratories developing their own. However, all must have in common a first-class commercial microscope as part of the apparatus.

2.1.1.2. Low-Load Hardness

This domain is characterized by a load range from 1.96 N to 98.1 N with most work being accomplished up to 9.8 N. The higher loads are used in the now important work of developing cracked indents which is the substance of Chapter 5. Vickers diamond impressions in this range are from 50×10^{-6} to 200×10^{-6} m in diameter. This reduces the demands on the microscope quality, and commonly magnifications in the range 100× to 500× and numerical apertures from 0.2 to 0.6 are sufficient. A good technical staff in the habit of making careful measurements is able to do these tests, making this a very useful nondestructive testing method capable of yielding a great range of scientific and technical data on ceramic systems.

2.1.2. Equipment

2.1.2.1. Load Application

All indentation equipment contains some mechanism for applying the load to the surface. For the commonest technique, the static hardness test, it is inherent in the apparatus that the load be applied incrementally and not instantaneously. These two methods of load application produce fundamentally different values for the hardness of any sample. When the load is applied incrementally, then the indentation is in equilibrium with the load throughout the test.

An estimate of the difference caused by measuring hardness at instantaneous load application and at infinitely slow application of load can be made as follows for the commonly encountered Vickers indenter. From equation (1.6) the Vickers hardness is defined as $H_V = 0.4636\, P/d^2$ where P is the final load in newtons, or

$$\frac{P}{H_V} = \frac{d^2}{0.4636} \tag{2.1}$$

and the indent diagonal will be

$$d^2 = 0.4636 P/H_V \tag{2.2}$$

If the final load is applied instantaneously the force opposing the penetration will rise from zero at the surface to a maximum sufficient to stop the downward motion at $d_f = 2a_f$, where d_f is the final indentation diagonal length. The rest position will be at a depth h below the surface when the work done by the load P is equal to that necessary to form the pyramidal hole. For a ceramic system several components of this work may be important, but for the sake of simplicity assume that it is the plastic work done by P; this will be H_V times the indentation volume

$$\text{work done} = H_V \tfrac{1}{6} d_f^2 h \tag{2.3}$$

where h is the height of the pyramid—i.e., the depth travelled by the penetrator—and d_f is the indentation diagonal. Since h is the distance moved by the load P, the work done can be put as hP and

$$hP = H_V \tfrac{1}{6} d^2 h \tag{2.4}$$

Hence

$$\frac{P}{H_V} = \frac{d_f^2}{6}$$

or

$$\frac{6P}{H_V} = d_f^2 \tag{2.5}$$

Hence from equations (2.2) and (2.5) the indentation diagonal will be 12.9 times as long as in the static loading case, implying a much lower hardness than the accepted static value.

These two cases are extremes, and since the load has a finite rate of application to the surface and below, there will be a variable error in the hardness value obtained depending upon load, sample hardness, and rate of application of the load. For the Vickers method an expression relating these variables can be obtained that enables the order of the errors to be assessed and so to see how important load application really is in a hardness determination.

First an empirical expression between the load P and the depth of penetration h is assumed

$$P = Kh^n \tag{2.6}$$

In equation (2.6) K and n are constants characteristic of the ceramic under study. Now if h_o is the correct depth with no loading time effects, then the work done to achieve this depth is

$$W_o = Pdh_o \tag{2.7}$$

Substituting equation (2.6) and integrating gives

$$W_o = \frac{K}{n+1} h_o^{n+1} \tag{2.8}$$

Now the depth measured, h_1, will be greater than h_o and so we can write

$$W_1 = \frac{K}{n+1} h_1^{n+1} \tag{2.9}$$

Two terms can be seen to make the difference in work done from W_o to W_1: work done by the final load P_o and the kinetic energy of the indenter, respectively

$$W_2 = P_o(h_1 - h_o) \tag{2.10}$$

$$W_3 = \tfrac{1}{2}mv^2 \tag{2.11}$$

In equation (2.11) m is the mass of the indenter and v is the velocity it was given.

The work done is the sum of these, and so W_1 in equation (2.9) equals the sum of the work found in equations (2.8), (2.10), and (2.11):

$$W_1 = \frac{K}{n+1} h_1^{n+1} = \frac{K}{n+1} h_o^{n+1} + P_o(h_1 - h_o) + \tfrac{1}{2}mv^2 \tag{2.12}$$

Using equation (1.6) and equation (2.4) it is possible to express equation (2.12) as

$$v^2 = \frac{2.72 P_o^{3/2}}{m(n+1) H_{v_o}^{1/2}} \left[\left(\frac{H_{v_o}}{H_{v_1}} \right)^{(n+1)/2} - (n+1) \left(\frac{H_{v_o}}{H_{v_1}} \right)^{1/2} + n \right] \quad (2.13)$$

This final expression can be used to assess the effect a chosen load application velocity v in μm s^{-1} will have on H_{v_o}/H_{v_1}, the measured hardness as compared to the "absolute" hardness. Since the specimen hardness and applied load appear in the expression, a variable error is predicted. Figure 2.1 shows that this error is serious for hard materials like ceramics in the microhardness range of measurement when $n = 2$ and an indenter mass of 100 g is assumed.

Figure 2.1 shows that for ceramic systems where hardness values in excess of 9.81 GPa are commonly encountered the apparatus for "static" hardness measurements in the low-load regime has only to be capable of applying the load to the surface at rates slower than 250 μm s^{-1} to introduce just modest errors in the determination of ceramic hardness, while load application rates slower than 50 μm s^{-1} are needed for any microhardness apparatus.

Once full load application has been achieved, how long should that load be applied? In mainly plastic systems such as most metals this question is important because creep mechanisms may be triggered that lead to a
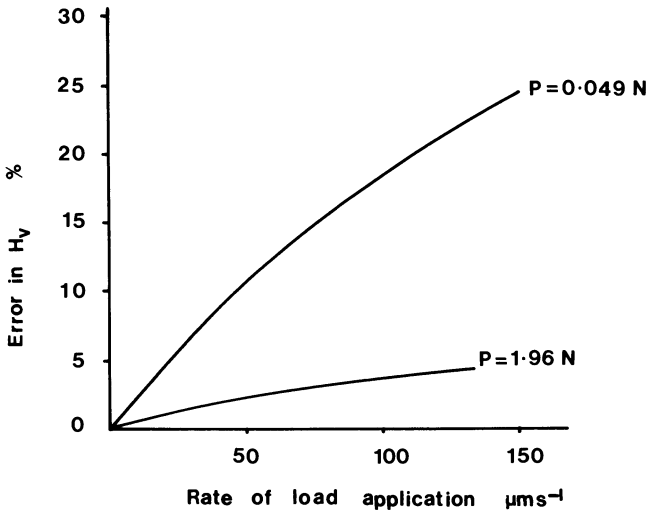

Figure 2.1. Error in the Vickers hardness value as a function of rate of application of load for a ceramic of hardness $H_V = 9.81$ GPa.

growing indent size—i.e., to a lower hardness value. By the same consideration sufficient time is needed for the indent to be correctly developed by the flow processes in the plastic region of the sample just around the indenter tip. For samples as hard as the average ceramic, a dwell time from 15 to 30 s is sufficient to produce "correct" well-developed indents with negligible creep effects. The size of these indents should be measured without undue delay after unloading because the stress generated on unloading (see Chapter 5) can in some combinations of sample hardness and temperature produce a creep that gives an incorrect indent diameter.

Time under load should not exceed the times recommended above because a more serious problem can develop if the sample or penetrator is subjected to vibration during load application. This is particularly true if really low microhardness-range loads are applied where the inclusion of kinetic energy from the vibrational source into the equation of penetrator motion, equation (2.12), leads to a deeper indent and an apparent reduction of the hardness value. Even for ceramic systems examined in the real microhardness region, great care has to be taken to isolate the apparatus from all sources of vibration, even in some cases from sound waves.

This leads us to another essential requirement of the load application mechanism which as well as having a controlled rate of load application must produce no lateral component in the movement of the penetrator; all movement must be absolutely vertical. Thus equipment that ensures purely vertical motion is to be preferred. Direct vertical load application to the penetrator via a regulated, timed movement through an oil dashpot that incorporates a leaf spring to counteract any horizontal tendency has the advantage of maximum load control. It does require that the microscope's objective lens and the indenter be interchangeable parts of a rotating microscope head, and is of course a complication. Several good instruments are built to this principle; Figure 2.2 shows one such instrument. Many others of this type are available, all of which are preferable to the older machines that employ a balance beam mechanism.

2.1.2.2. The Indenter

For ceramic work, diamond invariably is the chosen indenter material because of its absence of plastic deformation, its exceptional hardness (see Table 6.16), and its smooth surface with low coefficient of friction and high modulus. Some choice is left in the shape in which the diamond is cut because each shape is particularly suited to some applications.

For hardness determinations of ceramics the indenter used is always of the pyramid type and not the blunt spherical type. The reasons for this are developed in Sections 1.4.1.1 and 5.2.2 where the stresses developed beneath indenters of these shapes are analyzed and the crack patterns found
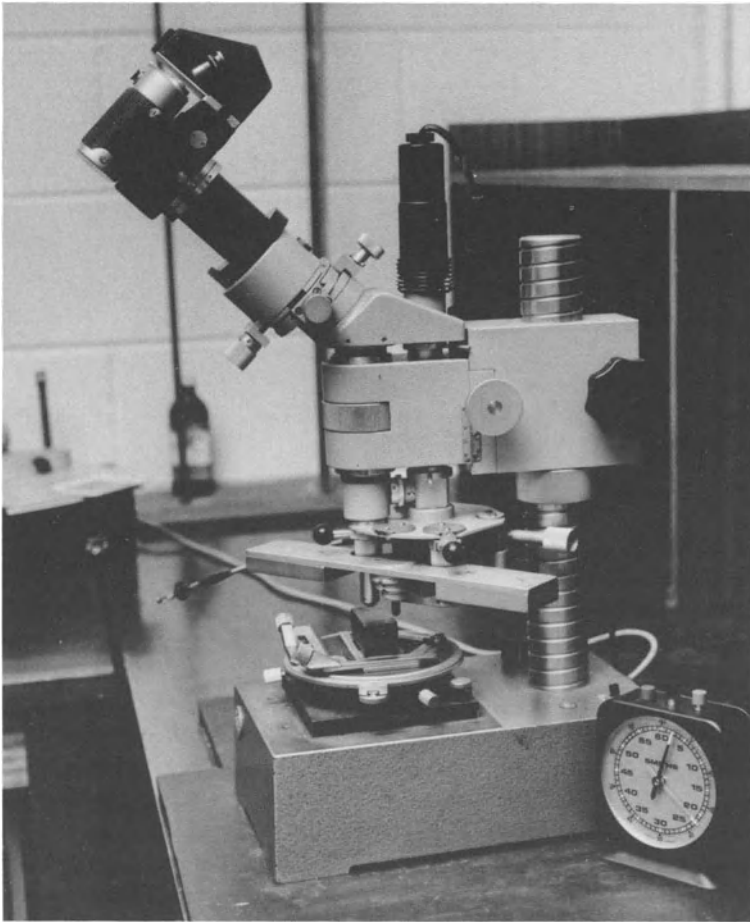
Figure 2.2. Typical Durimet micro- and low-load hardness apparatus as supplied by Leitz.

around overloaded indents are discussed. The main reason is a practical one arising from the fact that ceramics are brittle and, since the surface stresses on the loading cycle with a spherical diamond are tensile, cracking can occur during this stage. With pyramid indenters, as Sections 1.4.1.1 and 5.2.2 show, only on unloading are tensions generated at the surface. Thus to a large extent ring cracking and surface spalling can be avoided. Spalling and surface disruption occur at much smaller loads with spherical indenters.

   2.1.2.2a. Berkovich.   This is a triangular pyramid with a true point since only three sides have to meet. The point at which the three triangular faces meet can be polished very fine and so made small relative to the area

of any indent. This last quality is important for real microindentation work where this diamond indenter is sometimes used. The threefold symmetry of the indent base is useful when indentation techniques are used to examine anisotropy and crystal flow systems, as in Section 3.6. The angle between the vertical loading direction and each of the diamond faces is 65°, and hardness values are calculated according to equation (1.8). Berkovich diamonds are cut with an angle of 142° between any two of the planes along the line of join so that surface areas of indents are the same as the Vickers indent for the same depth of penetration. This means that isotropic hardness values are the same for a given material when probed by the Berkovich and the Vickers indenter.

  2.1.2.2b. Knoop. This is a more commonly encountered indenter shaped to emphasize anisotropy effects and to probe the surface layers of ceramics. With four faces as shown in Figure 2.3 this must be a chisel type of indenter because four planes cannot meet at a point. Skilled cutting and polishing does make the chisel edge small so that the indenter can be used easily and accurately in low-load hardness ranges and sometimes in the microhardness range. Figure 2.4c emphasizes the chisel edge and shows how the length affects errors in hardness. Two angles are involved: 172.5° between the faces that form the long axis and 130° between the faces that form the short axis. Such a geometry of the indenter gives a long axis able to be measured more precisely because of its length, for very small penetration depths, as Figure 2.5 shows. This figure also contrasts the depth obtained by a Vickers or a Berkovich indenter with that caused by a Knoop indenter.
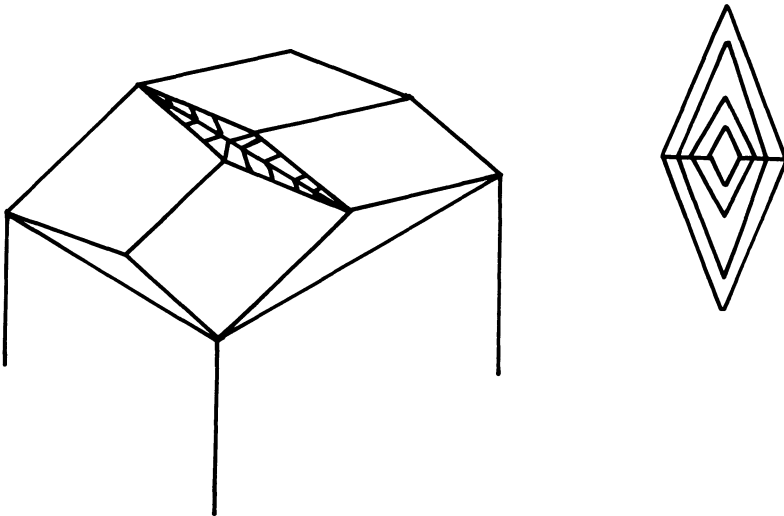

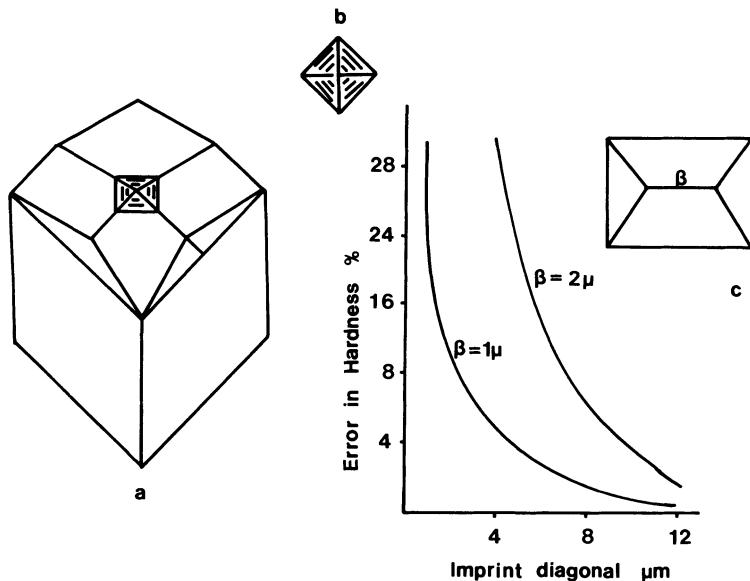**Figure 2.3.** The cut of a Knoop diamond indenter and the resultant indent trace.

Figure 2.4. (a) The cut of a Vickers diamond. (b) The shape of the surface imprint. (c) Effect on hardness of the chisel edge length resulting from four triangular faces being cut on the diamond.
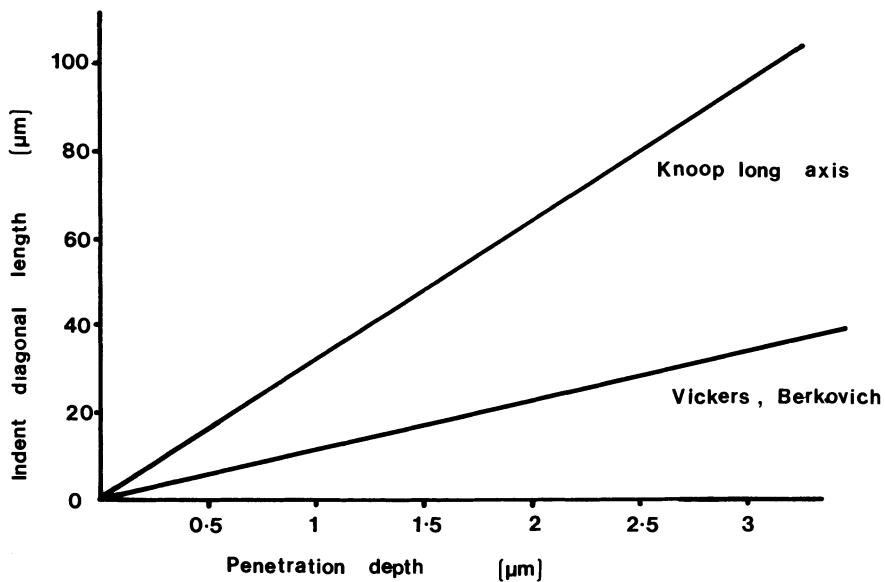

Figure 2.5. Penetration depth achieved by various indenters.

2.1.2.2c. Vickers. This diamond, the indent shape it makes, and the effect the unavoidable chisel edge makes on hardness values are shown in Figure 2.4. Cutting is done to get angles between two adjacent faces equal to 136° which produces an angle of 68° between any of the four facets and the vertical direction of the applied load.

Any error in the cutting of the interfacet angles introduces an error into the measured hardness of $20 \Delta\alpha$ if equation (1.6) is used to find hardness, where $\Delta\alpha$ is the deviation from 136°. Consequently, angle cut errors around 1° are not too serious, especially compared to the error introduced by not grinding the diamond to the smallest chisel edge possible, as Figure 2.5 shows. In the case of chisel edge length, β, this is clearly a most serious error when microhardness measurements are being attempted.

2.1.3. Expertise

2.1.3.1. The Indent

Whichever indenter is used, the major difficulty of the method when applied to ceramic systems is the measurement of the indent dimensions because the edges of the indents are not always easy to define on surfaces often showing poor contrast.

The angle of incident light, its wavelength, and the edge effects of the indent after removal of the indenter all conspire to introduce uncertainty into this measurement. An exaggerated example is shown as Figure 2.6 where edge effects of the indent on the original flat surface produce varying angles of reflected light, causing an uncertainty in the observation of points O and O', the distance between which is the correct indent diagonal $2a$. Contrast is improved by increasing the numerical aperture of the objective lens of the optical system, and as a result the error in measurement is decreased as shown in Figure 2.7.
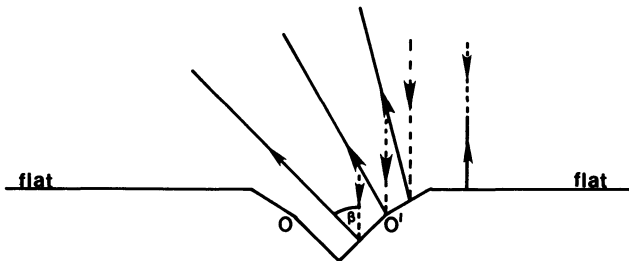

Figure 2.6. The uncertainty in the determination of indent diagonal length caused by the indent edges being made to deviate from 180°, causing variation in the angles of reflected light.
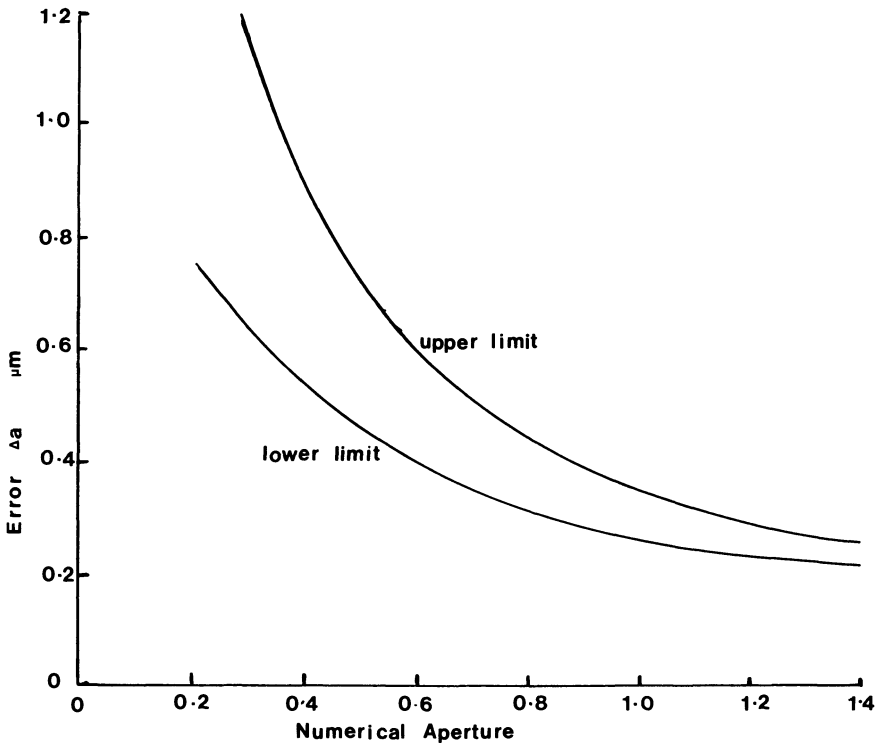
Figure 2.7. Errors in diagonal length resulting from the use of objective lens of small numerical aperture.

Another uncertainty entering the measurement of diagonal length is anisotropic elastic recovery of the indent leading to curved edges, barrelling, and pincushioning. While being often evident in single-crystal work (Chapter 3) these effects can also be seen in micro- and low-load hardness of polycrystalline samples. Figure 2.8 sketches these effects for indents made on a (100) plane of a cubic crystal showing slip lines on the crystal face. The two shapes in Figure 2.8 are extreme cases and all intermediate shapes can occur depending on the indenter's orientation and the individual crystal orientation in a polycrystalline sample.

Grain boundaries can contribute to poor shape along with poorly prepared sample surfaces, as emphasized in Figure 2.9. While misshaping from surface polishing and grain boundary interference can be corrected and allowed for, the errors arising from pincushioning and barrelling may be fundamental. The effect of elastic retraction on the measured length of the diagonals and thus on the hardness has not been clearly resolved. Empirical corrections have been proposed in order to obtain the true value of the
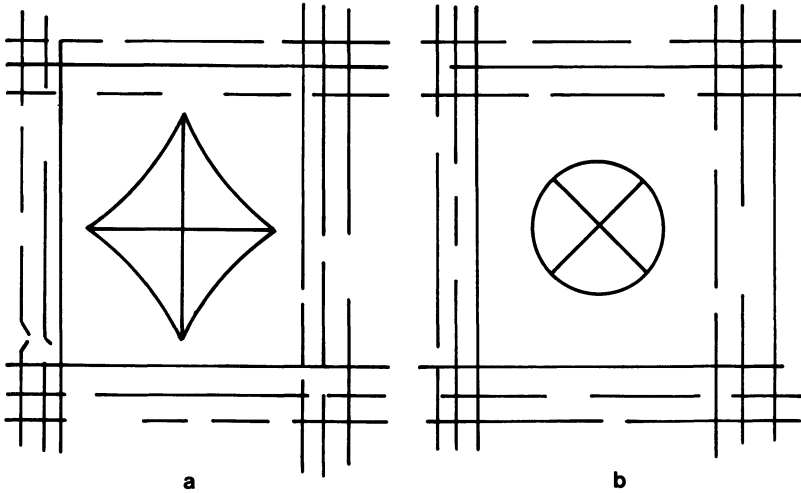
Figure 2.8. Pincushion and barrel indents caused by anisotropic recovery when indenter diagonals are (a) at 90° to the slip lines and (b) at 45° to the slip lines.

diagonals by adding on a constant distance c regardless of the load used to obtain an indent

$$P = a(d + c)^2 \tag{2.14}$$

Hence

$$H_V = \frac{2 \cos 22° P}{(d + c)^2} \tag{2.15}$$

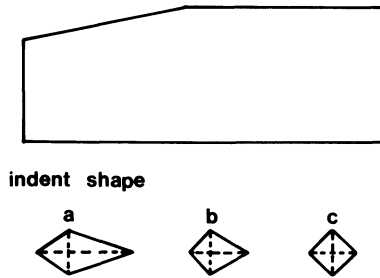The importance of this correction diminishes in the low-load and macrohardness regions, as Figure 2.10 indicates.

indent shape

Figure 2.9. Influence of surface slope on indent shape.
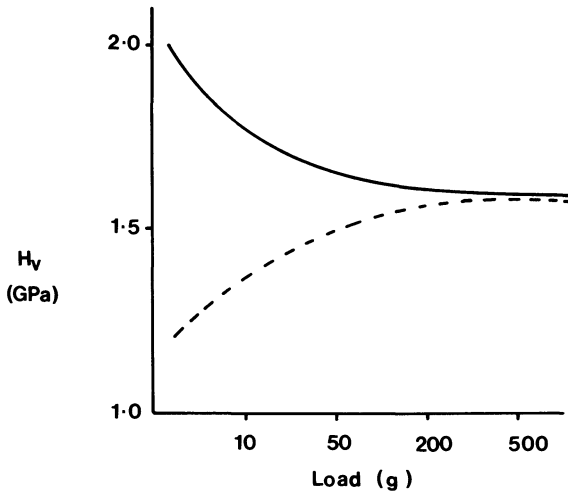
Figure 2.10. Vickers hardness as a function of applied load when calculated from measured diagonals (solid curve) and when 1.2 μm is added to the measured diagonal (dotted curve).

2.1.3.2. Sample Preparation

The sketches in Figure 2.9 emphasize the care that has to be taken once a route is decided upon by which to prepare the surface of the sample. Mechanical polishing is inevitable and can have a pronounced effect not only on surface shape but on surface properties. This latter aspect is covered more fully in parts of Chapters 3, 4, and 5.

Polishing to an optical finish is usually necessary, especially if crack types and lengths are to be studied. Obtaining this type of finish does have implications with respect to obtaining a hardness value from indent diagonal lengths; without such a polish indent edges are indistinct and hard to resolve, introducing real experimental difficulties and errors. But when obtained by purely mechanical means surfaces stresses do introduce errors, particularly in the microhardness regime. Figure 2.11 emphasizes the polishing effect on hardness because it shows a series of experimental Vickers hardness curves obtained for a soft metal, aluminum, using the same indenter and each time indenting the same grain of metal. Clearly the more mechanically violent the treatment from the polishing agent—i.e., emery > alumina or magnesia > electrolysis—the harder the sample appears to be even when indent depths of 10 μm are achieved. Work hardening is involved because the curve of hardness against depth of penetration from a sample that is re-annealed after the normal mechanical polish and then finally electro-polished has only a small slope, as Figure 2.11 shows.

This effect of work-hardened layers is not very serious as far as hard ceramic systems are concerned unless the crystal structure of the ceramic
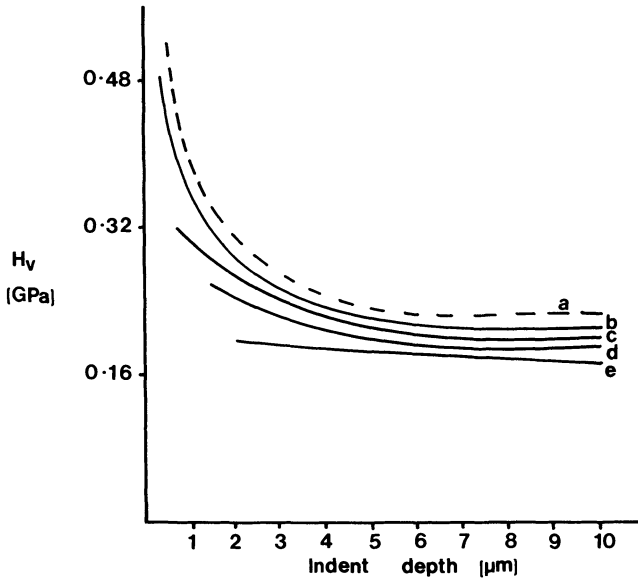
Figure 2.11. The effect of surface preparation on the measured Vickers hardness of aluminum metal as a function of indent depth. (a) Emery paper polish. (b) Fine emery, 10 minutes. (c) Fine alumina polishing cloth. (d) Electropolished. (e) Annealed after polish.

does lend itself to a degree of work hardening. It is therefore most in evidence for rock salt halides, and cubic materials like magnesia. The depth to which the effect can be found is, however, nowhere as great as in the metal surfaces because the microcrystals produced by the mechanical working of the ceramic surface are brittle compared to metal microcrystals and they are lifted by the polishing agent. Strong washing of the surface completes the removal of much of these submicroscopic crystals. Chemical attack in the multitude of grain boundaries introduced by the formation of the submicron crystals also aids their removal from ceramic systems when carefully washed with solvent spray. This process also reduces the depth of the work-hardened layers.

2.2. HARDNESS FROM PENETRATION DEPTHS

Depth of penetration has been used to assess the hardness of ceramic materials used for medical and dental work. Wallace hardness numbers quoted for dental cements based on gypsum ($CaSO_4 \cdot \frac{1}{2}H_2O$) are penetration depths expressed in multiples of 10^{-5} inches when a 136° pyramid diamond penetrates under loads up to 300 g. An obvious reason for this change in technique is that the surface cannot be mirror polished if "real" situations

are of interest. For typical gypsum-based dental cements allowed to set against a glass slide, values in the range 7.0 to 9.2×10^{-5} inches—i.e., 7.0 to 9.2 Wallace hardness—are reported.[1] In fact the long-established Rockwell indentation hardness is a depth of penetration value. First a light load is applied to the indenter and then, without removing this minor load, a heavy load is applied at a controlled rate. The Rockwell hardness number obtained is related to the additional depth to which the large load drove the indenter into the sample. The higher the number the shallower the indentation and so the harder the material is. Typically the small load is 10 N with a 60-to-150 N major load, but if near surface hardness is of importance these are changed to 3 N and 15-to-45 N. One scale point on a Rockwell hardness scale corresponds to an incremental increase in penetration depth of 2.03 μm. Depending upon the size of the indenter ball or cone and the major load applied, a series of scales is used designated Rockwell A through Rockwell V. The method is widely used in metallurgical laboratories but, with the exception of cemented carbides, is not often encountered in ceramics.

It is from these developments that a renewed interest in using penetration depths, as opposed to indent trace diagonal length with all the problems set out in Sections 2.1.3.1 and 2.1.3.2, has arisen.[2,3] Another reason for this renewed interest is the prospect of following the indentation process throughout the loading and unloading stages[4] in order to test the models proposed for the process. Some of these models are discussed in Chapter 5.

For conical smooth indenters the depth of penetration and the applied load are related by equations that pertain to different descriptions of material behavior, for example :

For elastic materials:

$$P = \frac{2Eh^2 \tan\theta}{(1 - \nu^2)\pi} \qquad (2.16)$$

For rigid-plastic materials:

$$P = K_p h^2 \qquad (2.17)$$

In these equations K_p is a function of mechanical properties of the material and the indenter geometry, E is Young's modulus for the material, ν is its Poisson's ratio, and θ is the indenter cone angle.

Equations (2.16) and (2.17) can be combined as

$$P = (K_p + K_e)h^2 \qquad (2.18)$$

In equation (2.18) we acknowledge the fact that most materials behave as though each was a combination of elastic and plastic extremes. Figure 2.12 is a series of sketches of the curves expected from equations (2.16), (2.17), and (2.18) and it permits the definition of some important points:

- Point O   is the surface of the specimen.
- Point A   is where maximum load and penetration are achieved.
- Point B   is where contact between indenter and top surface is lost.

Thus OC is the maximum penetration depth of the indenter while OB, in Figure 2.12(c), is the residual depth of the indent after elastic recovery. The areas enclosed by the curves are the work done in loading and recovery. This means from Figure 2.12 that

- OACO   = work W needed to create the indent.
- ACBA   = elastic work on recovery W_E.
- OABO   = final work invested in the indent volume W_I.

$$W_I = W - W_E \qquad (2.19)$$

For ceramic systems the ratio W_I/W is indicative of the elastoplastic nature of the solid and has been reported by Loubet[5] for magnesia and alumina as a function of the distances OB/OC—i.e., maximum and residual penetration depths.

Data for the two ceramics mentioned are shown in Figure 2.13.

In order to use this method to study ceramics, the equipment usually has to be of a self-made, one-off type, involving displacement and load transducers connected to recording equipment.[5] A simple outline sketch of the principles involved is shown in Figure 2.14.

The technique shown in Fig. 2.14 has been developed recently[4] for making extremely fine-scale hardness measurements on a quantitatively comparative basis. Instead of measuring the diameter of the indent the apparatus plots a continuous graph of the distance moved by the diamond
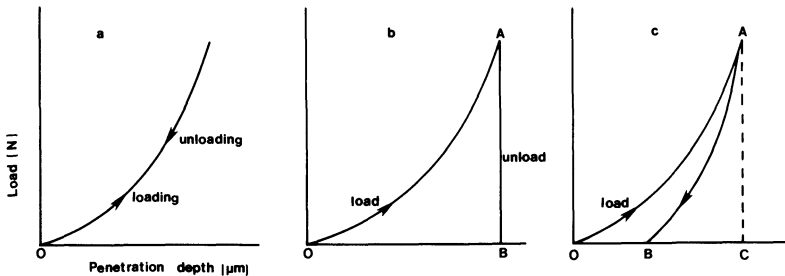

Figure 2.12. Indentation curves of (a) elastic materials, from equation (2.16), (b) rigid-plastic materials, from equation (2.17), and (c) experimentally determined curve, from equation (2.18).
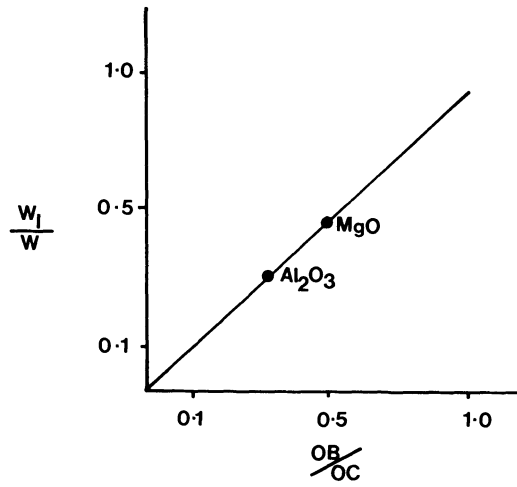
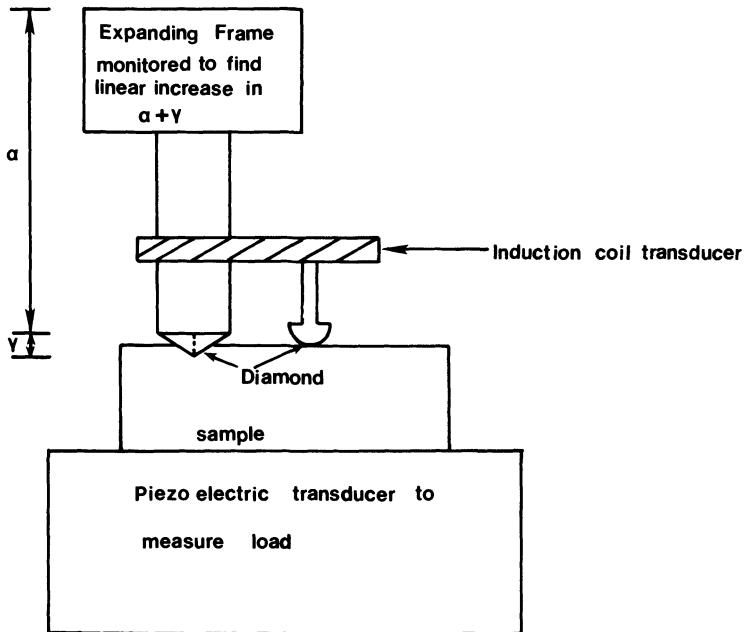**Figure 2.13.** Elastoplastic behavior data taken from Loubet.[5]

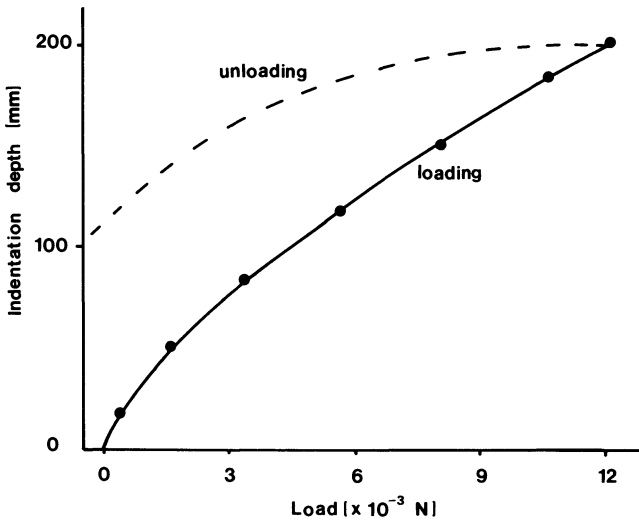**Figure 2.14.** Sketch of equipment needed to monitor indentation depth and applied load simultaneously.

Figure 2.15. Loading and unloading curves for a Lancaster micro-indentation test of a 2-μm-thick film of TiN.[4]

into the specimen as the load is increased. Because changes in distance as small as 1 nanometer can be detected, it is possible to use the equipment for detailed investigation of surface films as thin as 50 nm. The depth is measured during the complete loading-and-unloading cycle to give data on the elastic recovery of such surfaces. Figure 2.15 is an example of a loading-and-unloading cycle on penetrating into a 2-μm-thick layer of TiN, and it shows that a considerable proportion of the deformation should be ignored when calculating the hardness. The recoverable, elastic portion, 0.34 in the case shown, can be used to calculate Young's modulus for the film material. Calibration is achieved with a standard silicon sample.

Further development of the indentation depth measurement method seems to be imminent when semiconducting diamonds are cut to the Vickers geometry and used to indent conducting specimens.[6] At the moment the samples tested have been metals, but many special ceramics like TiC, TiN, SiC, and MWO_3 are electrically conducting and could be investigated. The method involves sensitive measurement of electrical resistance as a function of indenter load.

2.3. PENDULUM HARDNESS

This method of hardness measurement goes back to 1923 when a commercial pendulum hardness sclerometer was first marketed by E. G. Herbert[7]; the technique was further developed by Kuznetsov in 1929.[8]

The apparatus consists of a pendulum supported on a diamond or hardened ceramic tip. The center of gravity of the pendulum is arranged so that it is below the point of support, and the pendulum is in a state of equilibrium. When the pendulum is displaced from equilibrium it performs a damped oscillatory motion that decays back to equilibrium at a rate related to the hardness of the surface. What contributes to the rate of decay we shall discuss further below. At this point it is possible to see the versatility of the technique when chemically reactive species need to be studied because it is possible to immerse the pendulum fulcrum to a 1–2 cm depth in inert fluid as long as the same fluid and the same depth are used in the study of successive samples. A recent study of the hardness of some reactive ceramic carbides shows an example of this versatility.[9,10] The equipment, as described by Westwood,[11] is on the whole simple and inexpensive to construct, worthwhile therefore having in a laboratory interested in ceramic hardness. This is particularly true when it is realized that the experimental arrangement lends itself to studying the effect of chemical additives on the apparent hardness and drilling capability of surfaces. (Later chapters give some examples.) It could well be used to quickly determine the long-term corrosive effects of liquid environments on ceramics, ceramic alloys, and ceramic composites.

The energy U of the oscillatory motion was found by Kuznetsov to be proportional to the square of the amplitude a as well as to the mass of the pendulum. If the amplitude a_1 of the initial oscillation of the pendulum decreases to a_2 after time t or after n oscillations the energy

$$U = A(a_1^2 - a_2^2) \tag{2.20}$$

is transferred to the solid.

The pendulum is positioned at a different spot on the surface on each occasion and given an initial displacement to an amplitude a_1; in each case the test is concluded when the amplitude decreases to a_2. In this way the period t or the number of oscillations is related to the energy-absorbing processes beneath the pendulum point. In the early development of the technique, these processes were believed to involve the production of new surface energy on the material as new surface was constantly produced by comminution. This is once again, as shown in Chapter 1, the problem inherent in hardness determination: What are we measuring? More recently consideration[12] has been given to analyzing the energetics of the process, and we will discuss these below, but in the meantime it is sufficient to see that hardness is being measured and to consider a little further the quantification of the process. From the values of the successive amplitudes it is possible to calculate the logarithmic decrement λ which can be used to determine the damping:

$$\lambda = \ln\left(\frac{a_n}{a_n + 1}\right) \tag{2.21}$$

where a_n is the amplitude of the nth oscillation.

It is possible to express the oscillation amplitude a by the formula

$$a = a_o \exp - (xn + yn^2) \tag{2.22}$$

where n is the number of oscillations and x and y are constants for any given crystal. However for the practical purpose of *relative* hardness measurement it is sufficient to plot curves showing the amplitude as a function of the number of oscillations or to determine the value of the amplitude for any chosen nth oscillation. The correct design of a pendulum such that the center of gravity is only slightly lower than the point of support on the surface enables a user to read the size of the amplitude of oscillation directly from a suitable scale.

Rebinder[13] proposed that hardness H_p should be expressed by a quantity inversely proportional to the relative initial attenuation of the amplitude of oscillation A in time t:

$$H_p = \frac{-A_o}{\left(\dfrac{dA}{dt}\right)_{t=0}} \tag{2.23}$$

Figure 2.16 shows how the amplitude decreases with time. The elapsed time at point C, expressed in seconds, is obtained by drawing the tangent to the
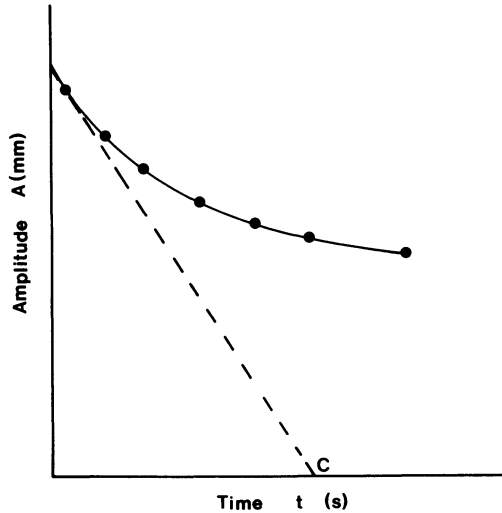

Figure 2.16. Curve of amplitude decrease with time showing hardness in seconds at point C.

curve at $t = 0$; hardness is determined by Equation (2.23). In the simplest case of damping with a constant logarithmic decrement, H_p does not depend on the units used for measuring A and can be regarded as a constant during the period of the damped oscillation process

$$\frac{dH_p}{dt} = 0 \quad \text{or} \quad \frac{1}{A}\frac{dA}{dt} = -\frac{1}{H_p}$$

and $dA/A = -dt/H_p$ which on integration gives

$$\int_{A_o}^{A} \frac{dA}{A} = -\frac{1}{H_p}\int_{0}^{t} dt$$

or

$$\ln A_t - \ln A_o = \frac{-t}{H_p} \tag{2.24}$$

and

$$A_t = A_o \exp\left(\frac{-t}{H_p}\right) \tag{2.25}$$

Thus from equation (2.24) we arrive at

$$H_p = \frac{t}{2.303(\log A_o - \log A_t)} \tag{2.26}$$

which expresses the hardness in units of seconds. Hardness determined in this manner should be a constant along the entire curve.

In reality the reduction in amplitude A towards the end of damped oscillations is slower than calculated from equation (2.25). In practice hardness is found to be independent of the initial amplitude A_o within the range 25–50 mm of displacement. Hence H_p is an arbitrary measure of the rate of pendulum damping which is in turn related to the energy absorbing processes beneath the fulcrum.

A typical pendulum sclerometer consists of a horizontal metal beam with a long, very light aluminum wire pointer above the fulcrum which serves as a Vickers diamond pyramid with a 136° angle. Stabilizing weights are suspended rigidly below the ends of the horizontal beam. The total weight is adjustable so that the diamond can be made to clearly indent the surface and not just rest on it, as in Figure 2.17. Only when a clear indent like that shown as Figure 2.18 can be obtained will the results become reproducible. The period of oscillation is about 1 second and the amplitude is measured after 60 seconds. It is best to enclose the whole in a transparent
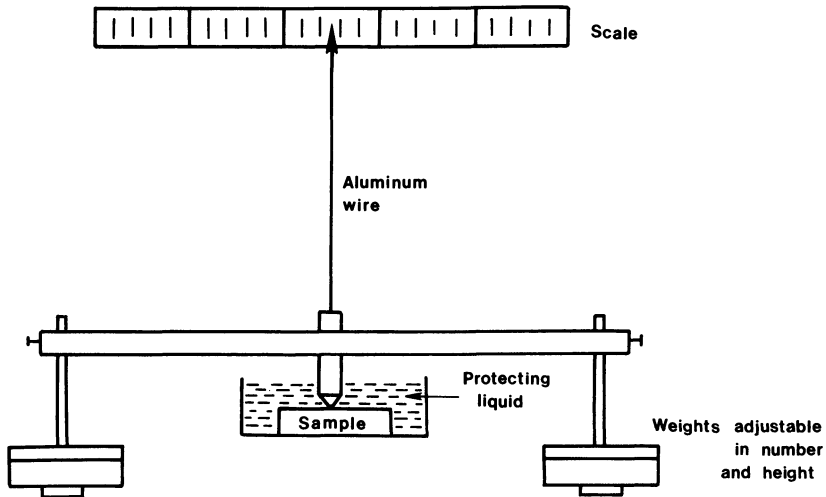
Figure 2.17. Pendulum sclerometer.

plastic box to minimize the effects of air currents. A centimeter scale fixed near the top of the box can be used to record the amplitudes A_o and A_t so that hardness can be found from equation (2.26).

   The units of hardness obtained by this method are clearly those of time but are often expressed as arbitrary and therefore mask what the process is actually measuring. Since Herbert's early work, where the depth of penetration and degree of disintegration were seen to increase with the decreasing surface energy of the material, it has been tacitly assumed that the process is measuring the surface energy of the solid and that therefore hardness and surface energy are synonymous in this context. The appearance of the area tested is dominated by the powdered debris and looks like a brittle surface after it has been drilled; therefore it is not surprising to find

Figure 2.18. Indented and comminuted surface beneath pendulum fulcrum on a surface of $Ho_{0.9}La_{0.1}C_2$.

that wear and fracture behavior have been assumed to dominate the hardness function. It was not until 1979,[12] when the process was analyzed with a view to determining the importance of different energy-absorbing processes in the determination of hardness by this method, that it was revealed how similar the Vickers hardness method and the pendulum hardness method are. Previously a simple numerical relationship between pendulum hardness and Vickers hardness had been claimed but not justified. The 1979 work is interesting in that it presents a numerical analysis of experimental data as justification for the conclusion that despite appearances the method is able to give little direct information on fracture processes; rather it shows that such processes are related to plastic or viscous flow in the solid. This conclusion may seem surprising at first, particularly since it was reached by making a detailed analysis of the pendulum hardness of soda–lime–silica glass samples; Marsh much earlier worked hard to justify the concept of plastic flow in glasses subjected to indentation by the Vickers method.

It is possible to list mechanisms for energy dissipation in the pendulum test and then through a series of assumptions and measurements calculate the energy absorbed by each process and compare it to the energy dissipated in a test, typically in the range 10^{-3}–10^{-2} J. The following have been considered by Fox[12]

1. Fracture and production of new surface.
2. Plastic flow under the pendulum pivot.
3. Energy absorbed moving and distorting the product debris around the pivot.
4. Effect of surface electric charge on the viscous flow of liquid through the debris.
5. Catalytic activity of freshly generated fracture surfaces.

In this list, (4) and (5) apply only to pendulum tests conducted on surfaces covered by liquid, protective or otherwise; (3) is probably a serious problem only when the debris is mixed with a liquid.

Considering the mechanisms listed above it is perhaps easiest to visualize (1) if we are dealing with an ideally brittle solid, for then the energy consumed is equal to total new surface area produced multiplied by the specific surface energy. Three components are present in this assessment. First, as Figure 2.18 shows, the pivot makes an indent similar to a Vickers diamond. Therefore there is the same projected area. Second, depending upon the load, there will be production of the median vent crack into the solid whereas the lateral vent cracks are not produced until the load is removed. Therefore, rocking the pendulum produces only one set of cracks which produce new surface. And, finally, as the pivot rocks and to some extent precesses, crushed debris is produced.

Lateral vent cracking, estimated in Ref. 12, seems unusual since it occurs only on removal of the pendulum and therefore does not contribute to the absorption of energy. However, the median and lateral vents are related as shown in Figure 5.5; thus the estimate obtained by Fox and Freeman and shown in Table 2.1 can be used.

Crushed debris was estimated by scanning electron microscope examination as 20% of the 5×10^{-14} m^3 of damaged volume. Depending on the geometrical shape assumed for each particle—and on the surface energy, which for glass can be taken as 4.0 J m^{-2}—a limit for the energy absorption is given as 1×10^{-7}–3×10^{-7} J.

Hence the total energy absorption attributed to these processes is around 3×10^{-7} J, which is surprisingly low since this has always been assumed to be the major factor in pendulum amplitude attenuation and the reason the process has been thought to be analogous to drilling ceramics.

Do mechanisms (3) plus (4), both of which involve debris, make up for the lack of energy absorption in (1)? Apparently not, since analyzing the process shows that energy would be absorbed by the viscous flow of any liquid–debris slurry between the pendulum pivot and the sample surface in a way directly related to the liquid's viscosity. The routine calculation of increased viscosity of a liquid with suspended solids shows that the viscosity would increase by no more than a maximum of 3.5 times but more likely about two times. Thus the buildup of energy absorption by this process would only double the viscous drag that the liquid exerts from the outset, and this is very small. It is feasible that the broken debris will possess a surface charge and the flow of liquid through such a charged bed of solid may be significantly impeded by what is known as the electrokinetic effect. Calculations based on debris particles of diameter 100 nm show this effect to be such as to change liquid viscosities by less than 2%. Thus this effect too can be neglected completely.

The cutting action of the pendulum pivot does produce new surface, and it is possible that this freshly generated surface may absorb energy to act as a catalyst for chemical processes taking place at its surface, mechanism

Table 2.1. Energy Absorption Processes in Pendulum Attenuation When Energy Lost Is Around 4×10^{-3} J

Mechanism	Energy absorption (J)
Fracture and surface production	Up to 3×10^{-7}
Plastic flow beneath fulcrum	2.5×10^{-4}
Movement of debris	Negligible
Viscous flow of liquid	Negligible
Catalytic activity of new surfaces	Values around those for plastic flow

(5) in the above list. Mechanical energy transferred this way could be thought of as lowering the activation energy barrier for appropriate reactions. Clearly the nature of the ceramic will determine any reaction, but for a glass surface the hydrolysis of the Si—O—Si network[14] and hydroxylation of bonds already broken by the pendulum in the tip of cracks and affecting their advance has been shown to be a very important chemical reaction. It is difficult to see how the energy consumed by such processes can be estimated, but Fox assumes it will be equal only to that absorbed when freely available water reduces the viscosity of the glass and so increases the pendulum damping as the fulcrum has to move in a high-viscosity, liquid-like layer instead of rocking on an elastic surface. One approach to quantification is to assume that the hydrolysis at the crack tip makes it possible for the pendulum to drive the crack forward. This is equivalent to saying that the energy absorbed will be a fraction of the activation energy for crack propagation, and we can try to estimate it in this way. This is the least satisfactory area of current analyses, but it has the advantage of allowing correlations to be made between pendulum hardness and the chemical nature of the environment. For example, peak hardness is found for surface covered in alcohols of different carbon-chain lengths, peaking at C_6-C_7, but this factor was also related to the partial pressure of water above the alcohol. The particular dependence on chain length has no obvious explanation but shows that changes in crack propagation behavior as suggested above cannot explain the observed maximum in hardness but indicates that friction may be important.

In the original list of energy absorbing processes contributing to pendulum damping there remains only (2) to consider; hopefully it will account for the bulk of the energy adsorbed. It is relatively easy, having chosen glass for the analysis, to base the consideration on material movement by viscous flow under the rocking action of the pivot. The schematic geometry is shown in Figure 2.19.

Assume that the average velocity of the material movement $= \frac{1}{2}$ the maximum velocity, which occurs when $\theta = 0$. Also assume that the average velocity over the area of contact of indenter and sheared layer can be used in the calculation. At the point of contact of specimen and indenter the velocity is zero and has a maximum in the direction $\phi/2$ when $\theta = 0$. This later value is given by

$$V_i = \frac{r_i \dot{\theta}_{max}}{\sin \phi} \tag{2.27}$$

where ϕ is determined by the geometry of the diamond. If it is a Vickers diamond and if $r_i = 25 \times 10^{-6}$ m with θ max = 1.1 rad s^{-1}, the energy absorbed per swing can be estimated as
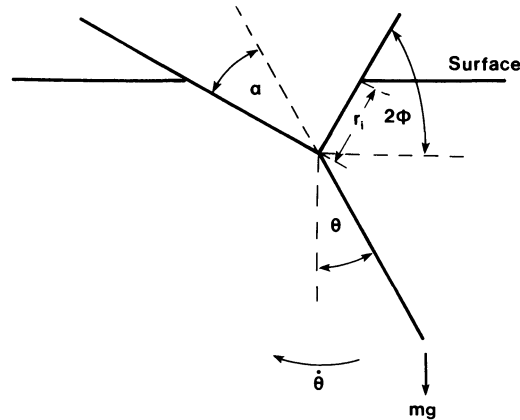
Figure 2.19. Schematic representation of diamond rocking into sample surface.

$$U = f \times \tfrac{1}{2}r_i\phi = \tfrac{1}{4}\eta V_i \times \text{area per swing} \qquad (2.28)$$

In equation (2.28) the area is easy to estimate; V_i can be found from equation (2.27) and the dimensions given. However, the value of η is not so easy to substitute because typical values of η for dry glasses at room temperature are in excess of $10^{20}\,\mathrm{nm^{-1}\,s^{-1}}$, which would imply a far too large absorption, giving damping in one swing. Viscosities drop considerably in the presence of sufficient water but taking the somewhat unrealistic value of $10^8\,\mathrm{nm^{-1}\,s^{-1}}$ used by Fox from the values found for $Na_2SiO_3 \cdot 3H_2O$ surfaces saturated with water gives a value of $2.5 \times 10^{-4}\,\mathrm{J}$ for a hardness test of 100 swings; this will be a low estimate but is closer to the energy absorbed by the sample from the pendulum than that estimated for purely brittle failure of an elastic solid as in mechanism (1) above.

Accepting the assumptions of this analysis leads to the results in Table 2.1 and a view that pendulum hardness is mostly a function of plastic or viscous flow and stress-aided corrosion processes. Hence the method can be used to study the interaction of these two processes. It clearly shows that once again an apparently simple technique must be carefully controlled to get usable and comparable data and that apart from comparisons within one study careful specification of conditions, etc., must be given to make interwork comparisons strictly valid.

2.4. SCRATCH HARDNESS TESTS

Section 1.4.5 describes the early origins of this test and contains equations that can be used to quantify it more usefully than the early scratch

hardness (Mohs) numbers. In practice, for scratch tests two types of loading condition can be applied, fixed load and fixed depth.

For single-phase ceramics or a pseudohomogeneous specimen where second-phase crystallites have small dimensions compared to the size of the groove produced by the stylus, both loading conditions are equivalent. However, they must be distinguished when the material contains large grains of a hard second phase because the load must be increased to prevent the stylus point from rising over the hard particles.

Prasad and Kosel[15] have described a fixed-depth scratch tester; Figure 2.20 is a diagram of such an apparatus taken from their paper. In such an apparatus the specimen is moved by hand horizontally relative to the stylus and care is taken in constructing the specimen mounting block to ensure that it maintains the specimen surface parallel to the direction of movement and at an angle of 90° to the stylus tip. Constant-depth conditions are achieved by using the two outer load arms to carry most of the applied load. Thus if the stylus encounters a hard second-phase particle and tries to rise over it, the outer frame is lifted which causes the normal load on the stylus to increase sharply.

In a scratch test the loaded stylus applies a compressive stress to the surface beneath the stylus if it is a cone, which is a common configuration, and a tensile stress at the free surface adjacent to the indentation caused by the stylus; these aspects are enlarged upon in Sections 1.4.1.1 and 5.2.2.

When a hard sphere is pressed on a flat surface, deformation of the surface occurs which is initially purely elastic. But as the load increases a critical point is reached where the elastic limit of the softer material is exceeded and plastic deformation begins. As the load continues to increase the mean pressure over the contact area increases up to the limit, where the material around the hard sphere is totally plastic and any further increase in load increases the dimensions of the indentation but produces no change in the mean pressure. By deforming the ceramic as it advances, the stylus develops a shearing force to break bonds between upper and lower layers of material to produce debris. The shearing force has a maximum value at the lip of the indentation. If a stylus of end radius R indents a distance h into a ceramic of hardness H_s for a stylus load L, then the shearing force F per unit area due to the deformation can be determined from the triangle of forces abc in Figure 2.21. The critical shearing force F_c at which debris is evident is the measure of the material's strength. Thus

$$F = H_s \tan \theta \qquad (2.29)$$

and

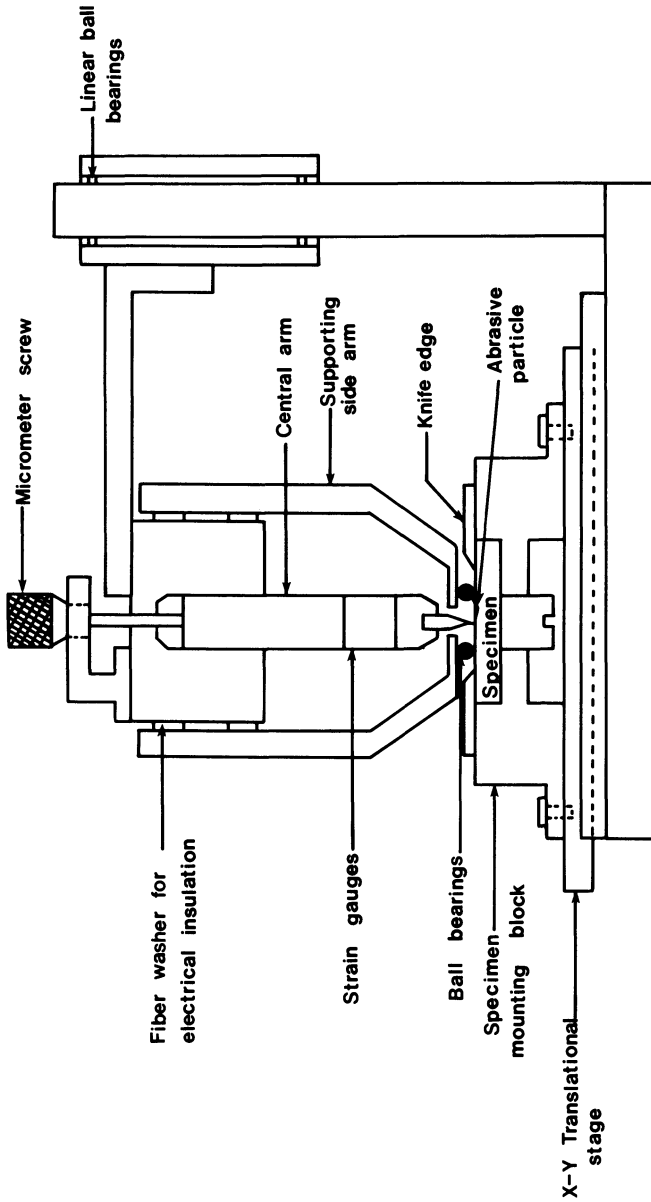$$H_s = \frac{L}{2\pi Rh} = \frac{L}{\pi A} \qquad (2.30)$$

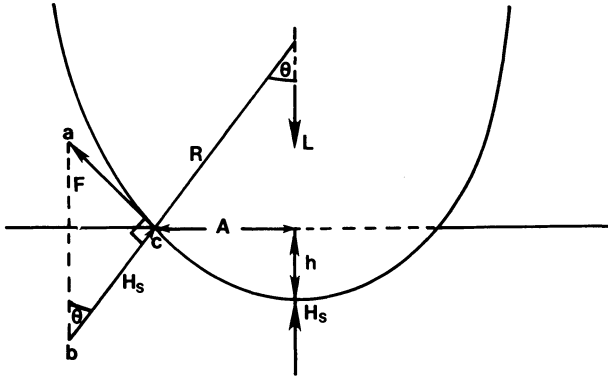**Figure 2.20.** Fixed-depth scratch test apparatus. After Prasad and Kosel.[15]

Figure 2.21. Scratch-test forces.

so that

$$F_c = \frac{L_c A}{\pi A^2 (R^2 - A^2)} \qquad (2.31)$$

and if $R \gg A$, then

$$F_c \approx \frac{L_c}{\pi A R} = \frac{2L_c}{\pi b R} \qquad (2.32)$$

Thus

$$\sigma_A = \frac{2KL_c}{\pi b R} \qquad (2.33)$$

where b is the scratch width that produces visible debris. A coefficient K is commonly included with a value between 0.2 and 1.0 to allow for assumptions in the derivation relating F_c with strength σ_A.

Because ceramics are generally hard, plastic deformation is relatively limited and a Griffith type elastic energy balance may be applicable. If a balance between bond energy ΔE and stored elastic energy is assumed, then

$$\Delta E = \frac{\sigma^2 h}{2E} \qquad (2.34)$$

where h is the penetration depth, E is Young's modulus, and σ is the compressive stress in the top layers of material ahead of the indenter. The total stress will be the sum of the applied stress and the intrinsic stress. The applied stress σ_a can be written

$$\sigma_a = \frac{(10\mu - 1)}{4\pi} L^{1/3} \left[\frac{3E_s}{4KR} \right] \qquad (2.35)$$

where μ is the coefficient of friction between stylus and surface, R is stylus radius, K is a parameter determined by Hertzian theory which equals 0.84 for a hard ceramic and a diamond stylus, and $E_s = 600\,\text{GP}_a$.

Equation (1.52) can be used to predict the size of debris particles formed in scratch hardness testing. Figure 1.9 contains some typical scratch widths obtained at different loads for three important ceramics.

Extension of scratch hardness technique to include scratching velocity and temperature control can allow conclusions to be drawn about the mechanism of the scratching process. The typical range over which the scratching velocity must be varied to extract new data is 1×10^{-8} to $1 \times 10^{-3}\,\text{ms}^{-1}$. In general, increasing the velocity results in a decrease in the scratch width which from equation (1.52) indicates a parabolic increase in H_s, the scratch hardness. The time t^* needed for the indenter to move a distance equal to track width d can be used as a kinetic parameter

$$t^* = \frac{d}{V} \qquad (2.36)$$

where V is the scratch velocity and d the track width. One can obtain t^* as a function of load P or H_s and temperature. From equations (1.51) and (2.36) we can write

$$(t^*)^2 = \frac{4P}{H_s V^2} \qquad (2.37)$$

The dependence of $\ln t^*$ on H_s and on $1/T$ leads to linear expressions such as

$$t^* = t_o \exp\left(\frac{E^*}{RT}\right) \qquad (2.38)$$

where E^* is the scratching activation energy as defined by a slope of the plot of $\ln t^*$ versus $1/T$. Values of E^* have been compared to energies

obtained by studying the penetration velocity of a standard Vickers hardness diamond over a range of temperatures:

$$\frac{dh}{dt} = \frac{dh_o}{dt} \exp\left(\frac{-E_v}{RT}\right) \tag{2.39}$$

and close agreement of values E_v and E^* can be taken as evidence for the same mechanisms being operative in indentation hardness and in scratch hardness.

REFERENCES

1. E. C. Combe and D. C. Smith, *Brit. Dental J.* 117, 237 (1964).
2. V. V. Gasilin and V. V. Kunchenko, *Zavod. Lab.* 46, 353 (1984).
3. C. H. Lee, S. Masaki, and S. Kobayashi, *J. Mech. Sci.* 14, 417 (1979).
4. H. Montagu-Pollack, *Interceram.* 36, 37 (1987).
5. J. L. Loubet, J. M. Georges, O. Marchesini, and G. Meille, *Trans. Amer. S.M.E., J. Tribology* 106, 43 (1984).
6. H. J. Goldsmid, V. R. Howes, and C. A. Baird, *J. Mater. Sci. Lett.* 6, 1043 (1987).
7. E. G. Herbert, *Engineer* 135, 390 (1923).
8. V. D. Kuznetsov, *Surface Energy of Solids*, H.M. Stationery Office, London (1957).
9. D. R. Bourne and I. J. McColm, *14th Rare Earth Research Conf., North Dakota State Univ.* Plenum, New York (1979), p. 291.
10. I. J. McColm, *J. Less Common Metals* 78, 287 (1981).
11. A. R. C. Westwood, N. N. Macmillan, and R. S. Kalyoncu, *J. Amer. Ceram. Soc.* 56, 258 (1973).
12. P. G. Fox and I. B. Freeman, *J. Mater. Sci.* 14, 151 (1979).
13. P. A. Rebinder, *Proc. 6th Physics Conf.*, Moscow State Press, Moscow (1928), p. 29.
14. I. J. McColm, *Ceramic Science for Materials Technologists*, Leonard Hill, Glasgow (1983), p. 197.
15. S. V. Prasad and T. H. Kosel, *Proc. Int. Conf. on Wear of Materials, Vancouver, B.C.*, ASME, New York (1985), pp. 59-66.

Chapter 3

Hardness of Ceramic Single Crystals

3.1. INTRODUCTION

The outstanding achievements of dislocation theory when applied to the mechanical properties of materials make it the natural source for workers in the materials hardness area to turn to when seeking to rationalize collected data. This has been particularly true when hardness anisotropy has been observed and then considered theoretically.

Anisotropy in general is defined as the variation in the properties of a crystal as its orientation is changed with respect to the sensing (or measuring) device.

The degree of anisotropy of a property may be negligible, but this is not usually the case in indentation hardness measurements on ceramic crystals. Later we will consider the phenomenological aspect of hardness anisotropy to demonstrate that, whatever the ramifications of the theoretical models, the nature of anisotropy is consistent and reproducible for a wide range of ceramics. Then we shall consider the models based on a resolved shear stress analysis and discuss their implications in terms of the role of plastic deformation and indentification of active dislocation slip systems.

Theoretical and experimental properties of dislocations are well understood for well-defined states of stress and simple deformations,[1] and so basic groundstates are available. However, the complex stress states present within the small volumes beneath indenters and scratch hardness and pendulum hardness testers are far from well understood. What then is the chance of applying dislocation theory to the understanding of the hardness behavior of ceramic single crystals, or rather, one might ask, why has its application been so successful and so dominant? The reason is that even for complex stress states the positions of dislocations and the ways they interact can be observed using a combination of techniques on single-crystal

samples. Using hardness indentation methods together with dislocation etch pit observation, X-ray diffraction topography, and scanning electron micro-scopy, all of which give distributions of dislocations around an indent on a cleared surface of a single crystal, it is possible to obtain a semiquantitative understanding of hardness. Dislocation distributions revealed by the above techniques do then offer some explanation of the anisotropy of hardness, the extent of plastic flow, and the onset of cracking.

Models with varying degrees of sophistication have been developed from combinations of these techniques over the past 30 years. One ceramic in particular, single-crystal MgO, has been intensively studied by these techniques throughout this time, and as a result good descriptions of cracking, hardness anisotropy, elastic recovery, and load hardness depen-dence exist.[2-4] Aspects of this and other work are the substance of this chapter, while MgO is specifically dealt with in Section 6.2.2.

3.2. INDENTATIONS AND DISLOCATIONS

Typically around indents in single-crystal faces series of slip lines are visible as shown in Figure 3.1 and Figure 6.23. These are sketched on Figures 2.8 and 3.4. Such glide bands contain systems of loops lying in several
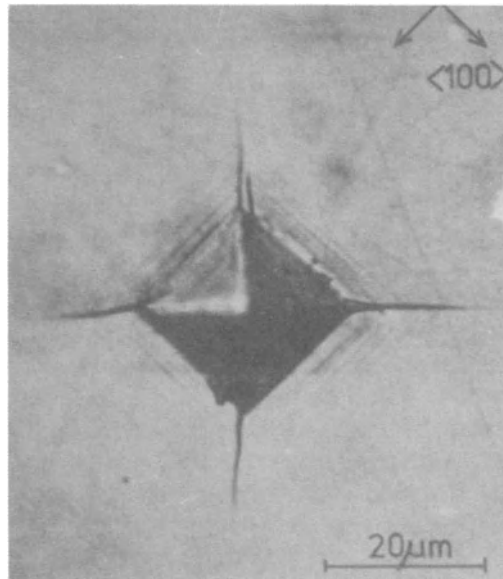
Figure 3.1. Cracked Vickers indent on a (001) plane of the perovskite $Na_{0.75}WO_3$ showing slip lines parallel to the indent edges. After McColm and Wilson.[5]
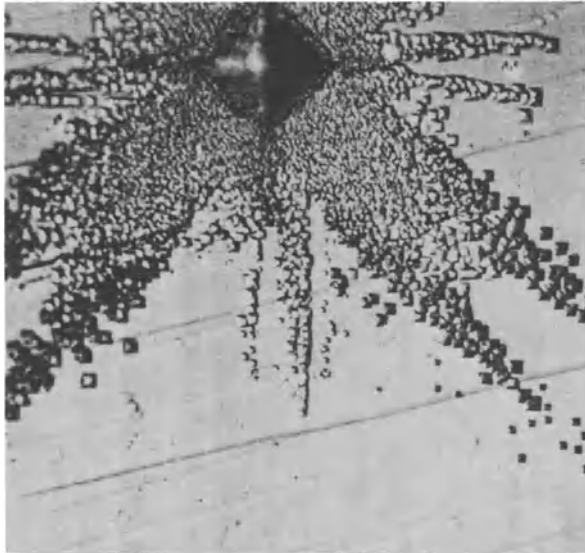
Figure 3.2. Dislocation rosette pattern around etched indent.

closely spaced parallel slip planes. Where they emerge at surfaces they must have edge or screw dislocation character as Figure 3.3 shows and can be revealed by etching as shown in Figure 3.2.

In Figure 3.3 the motion of the slipped area is such that at point C it is perpendicular to the Burgers vector (that is, the distance AB) and this part of the dislocation loop is of purely edge character. At point E the loop is parallel to AB in the sense of its movement and is therefore purely screw in character. At other points, such as D, the dislocation is of mixed character. Figure 3.3 contains the conventional symbol ⊥ at the point C where the
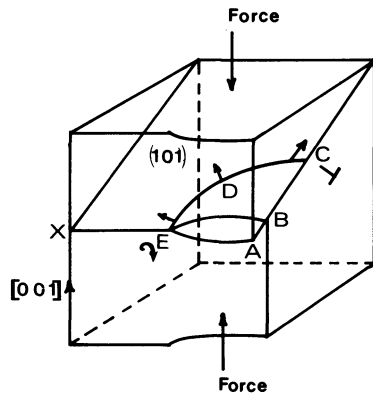
Figure 3.3. A dislocation loop CDE on a (101) slip plane showing edge dislocation at C, screw dislocation at E, and mixed character dislocation at D. AB is the slip step or Burgers vector.

edge dislocation is shown emerging at the surface. This denotes an arrange-
ment in the crystal such that the horizontal line represents the slip plane
and the vertical line the position of an incomplete plane of atoms known
as the half-plane. Clearly then a symbol ⊤ denotes a dislocation with the
extra half-plane below the slip plane; this dislocation is of opposite sign
to ⊥ (negative and positive, respectively). They will move in opposite
directions in response to a stress, and will if they meet on a given slip plane
cancel each other out. Both have been formed by extra material, the result
being that they contain misorientation-producing compressive and tensile
forces around them. Because etching is a chemical reaction and is therefore
activated, this "extra energy" around the dislocation helps to overcome
activation energy and aids the corrosion process at the site of ⊥ or ⊤. Thus,
still concentrating on Figure 3.3, any etching technique that revealed the
presence of dislocations emerging on surfaces would then indicate the type
of dislocation. For our example in Figure 3.3, etch pits found in ⟨110⟩
directions would be edge dislocations while rows in ⟨100⟩ directions would
be screw dislocations. Since the stress indicated in Figure 3.3 is compressive,
analogous to the penetrating diamond of an indentation test, it would force-
ing the screw dislocation out at point × making the crystal shorter—i.e., generat-
ing a compressive strain. In fact a glide band, like those shown in Figures
3.1 and 6.23, contains many loops like that shown in Figure 3.3 lying in
several closely spaced parallel slip planes. These lead to the rows of disloca-
tions revealed by any suitable etching technique. In practice, when the area
around an indent is etched the rows of dislocations that are revealed form
patterns referred to as "rosettes." An enlarged view of one side of such a
rosette is shown as Figure 3.2 and a sketch indicating the type of dislocation
contributing to such patterns is given as Figure 3.4.

The distribution of dislocations such as that in Figure 3.2 around
low-load hardness indentations made on cleavage faces, for example, (001)
planes of single crystal MgO, has been helpful in allowing interpretation
of the actual fine detail of the indent shape. Figure 3.4 shows the dislocation
distribution produced from the activity of the ⟨101⟩ {10$\bar{1}$} slip system when
the indenting Vickers diamond has its diagonals lined up along the ∓[110]
and +[1$\bar{1}$0] directions. This sketch emphasizes the troughs, equal in width
to the indentation, formed when one might instinctively expect the displaced
material to form a raised area around the indent. The existence of a trough
can be understood by considering how initial dislocations on the primary
system are forced to move by new ones following behind as the indented
volume increases; slip on [01$\bar{1}$](011) and [0$\bar{1}$$\bar{1}$](0$\bar{1}$1) systems requires that
the downward displacement vectors are along orthogonal ∓[100] directions
in a direction parallel to the stress. That is, the system has a screw orientation.
In Figure 3.4 the indent trace is shown as having curved sides caused by
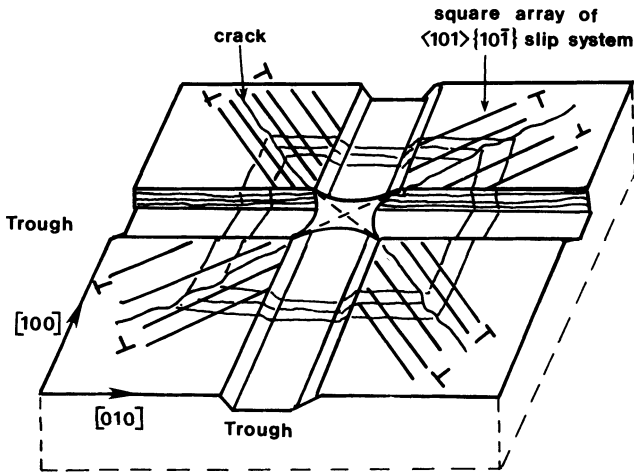the greater elastic recovery at the center areas of the troughs. Such recovery

Figure 3.4. Indent on (001) of MgO crystal showing the troughs spreading along the $\mp[100]$ and $\mp[010]$ directions.

is small but important because it is variable depending upon the indenter orientation relative to active slip systems. For example, an important secondary slip system in the rock salt structure is $\langle 101 \rangle \{10\bar{1}\}$ which is more interactive with the $\mp[110]$ and $\mp[1\bar{1}0]$ directions than with the $+[100]$ and $+[010]$ directions, along all of which the troughs lie. Because the dislocations of the square array $\langle 101 \rangle \{10\bar{1}\}$ are interactive with those generated by the primary system, Palmqvist cracking along the indenter diagonal directions $\mp[110]$ and $\mp[1\bar{1}0]$ occurs. The square array of $\langle 101 \rangle \{10\bar{1}\}$ slip systems operates to produce outward surface displacements from the indenter and so material, beginning from the tips of the indent diagonals, is raised along the $\pm[110]$ and $\mp[1\bar{1}0]$ directions, emphasizing the depths of the troughs along $\pm[100]$ and $\mp[010]$.

The discussion of dislocations so far shows that the combination of a ceramic single crystal, a micro- or low-load indenter, and a suitable chemical etchant can prove valuable in identifying operative slip systems in the complex stress patterns generated by the indentation process. Observation of hardness anisotropy on the crystal faces, allied to a satisfactory theory, will also aid in identification of the active slip systems as Section 3.6 shows.

3.3. INDENTATION CRACKS AND DISLOCATIONS

Overloading a pyramid indenter so that it produced cracks around the indent was for many years thought to be undesirable when making hardness measurements. Observation and analysis of such cracks, which is the subject

of Chapter 5, has more recently led to much greater use of the hardness indentation technique in the study of ceramic materials. Hence crack production and measurement has become important. The earliest publications on cracks emanating from indents on single-crystal faces attributed their production to the interaction of dislocations.[6,7] Towards the end of Section 3.2 the production of troughs in $\langle 100 \rangle$ directions along with raised material in $\langle 110 \rangle$ directions was analyzed, but it was not emphasized that such a situation implies extremely large strains at the indent diagonals that have to be accommodated on (110) planes. Cracking on the planes depends on there being limited deformation systems in the structure to satisfy the strain fields imposed by the indenter as it pushes beneath the (001) plane.

Analysis has to be done to come to some conclusions; pairs of adjacent slip systems are considered—for example, $[10\bar{1}](101)$ and $[0\bar{1}1](011)$—and the movement of half loops from the center of each plane to the line of intersection of the planes is considered. For (011) and (101) the direction of the line of intersection is given by

$$\begin{vmatrix} u & v & w \\ 0 & 1 & 1 \\ 1 & 0 & 1 \end{vmatrix}$$

hence

$$u = k_1 l_2 - k_2 l_1 = 1 - 0 = 1$$
$$-v = h_1 l_2 - h_2 l_1 = 0 - 1 = -1 \qquad = [111]$$
$$w = h_1 k_2 - h_2 k_1 = 0 - 1 = -1$$

The combination of $a/2[10\bar{1}]$ and $a/2[0\bar{1}1]$ Burgers vectors, when the slip planes (101) and (011) intersect, gives

$$\frac{a}{2}[10\bar{1}] + \frac{a}{2}[0\bar{1}1] = \frac{a}{2}[1\bar{1}0]$$

Thus we have an $a/2[1\bar{1}0]$ Burgers vector for a dislocation with line vector along $[11\bar{1}]$. Such a vector is contained within a plane given by

$$\begin{vmatrix} h & k & l \\ 1 & 1 & 0 \\ 1 & 1 & 1 \end{vmatrix}$$

whence

$$h = 1 - 0 = 1$$
$$-k = -1 - 0 = -1 \qquad = (112)$$
$$l = 1 + 1 = 2$$

Hence the (112) plane contains the dislocation which now has to be analyzed as to its sessile nature in terms of edge and screw components. The unit $a/2[10\bar{1}]$ dislocation has the partials $a/3[11\bar{1}] + a/6[1\bar{2}\bar{1}]$, of which the first term represents a screw component and the second an edge component. Similarly the unit $a/2[0\bar{1}1]$ has screw and edge components with the possibility, from their sign, of annihilation of the screw components. Thus annihilation of this component of the pair $a/2[10\bar{1}]$ and $a/2[0\bar{1}1]$ produces a lowering of energy for the system and subsequent dislocations following along meet this stabilizing effect and so pile up. Dislocation pile-up generates stress which can be sufficient to nucleate a crack. In this sense the merging of dislocations produces cracks around indents, but analysis of the slip directions is needed to gauge the plane of importance.

Slip along $[\bar{1}01]$ and $[0\bar{1}1]$ directions leads to components in the (001) plane that are orthogonal, which implies a tensile strain in this place. Steady penetration by the indenter causes the tensile strain between $[0\bar{1}0]$ and $[100]$ on (001) to build up and so, depending on the modulus, a steadily increasing tensile stress can be thought of as searching for a flaw to propagate unless the strain is relieved. Cross-slip of the pile-up dislocations to relieve the strain is hindered by annihilation of the easily moved screw components, and slip on alternative deformation systems does not occur at strains, that is stresses, below those that produce the cracking on (110).

From the above example it can be seen that a complex system needing careful analysis is present in each case, but the underlying fact is that the type of dislocation and their interactions are intimately concerned with the stress-strain field imposed by the geometry of the indenter. The implication of this is that hardness anisotropy is an obvious manifestation of dislocation interactions and indenter facet geometry. Simplified interpretations of this have been sought, of which the Brookes Resolved Shear Stress model, given in Section 3.6.1, is an important development.

The second implication of the mechanism involving crack nucleation and propagation, as so far outlined, is that the presence of any cracks associated with an indent means a lowered hardness value for the material. Furthermore, increased $\{1\bar{1}0\}$ radial cracking that occurs with increased load must mean a bigger error in hardness values as indentation pressure is deflected into the crack nucleation and propagation mechanisms. This supports the intuitive position stated at the opening of this section.

3.4. DISLOCATIONS AND ABSOLUTE HARDNESS

For single crystals, since slip systems are so clearly dominant in the way they interact with indenter facet geometry in determining the observed hardness, some attention should be given to the role of composition, since dislocation movement is sensitive to the size and type of the atoms of any impurities present. In general the lowest hardness for uncracked specimens is found in crystals of highest purity. At the limit the yield properties of a pure single crystal should be capable of providing values for absolute hardness in a way different from the analysis of this property in Section 1.4.1.3. Such an analysis is not easily accomplished but can be simplified through Gerk's[8] suggestion that predictive values can be approached in terms of crystal work-hardening characteristics. For ceramics of rock-salt structure like MgO, because of slip on favorably aligned slip planes, the initially small value of the generated shear stress on indentation does not increase significantly with the increasing strain. Eventually the easy slip is hindered as the large strains bring into operation other slip planes by cross-slip or invocation of secondary systems. This leads to dislocation multiplication, and so the shear stress seems to be linearly dependent on strain:

$$\tau = \frac{G\gamma}{125} \tag{3.1}$$

In equation (3.1) G is the elastic shear modulus and γ is one-half the engineering shear strain. This depicts a material for which the stress is proportional to the tensorial strain even though a plastic strain results in the vicinity of an indenter.

For indentation into wholly elastic solids, equation (3.2), derived later as equation (6.9), relates the hardness to indenter face angles, Young's modulus, and Poisson's ratio, which analyses in Chapter 1, like that leading to equation (1.15), also show

$$H = \frac{E \cot \psi}{2(1 - \nu^2)} \tag{3.2}$$

Using the general relationship that shear modulus $= E/2(1 + \nu)$ and the fact embodied in equation (3.1), that for work-hardening material the modulus is approximately $G/125$, equation (3.2) becomes

$$H = \frac{G(1 + \nu) \cot \psi}{125(1 - \nu^2)} \tag{3.3}$$

For ceramics, taking $\nu \approx 0.25$ and a cone angle of 68° to represent the pyramidal angle of a Vickers diamond, the relationship between H and G becomes:

$$H = 4 \times 10^{-3} G \qquad (3.4)$$

and equation (3.4) allows prediction of indentation hardness. This equation can be compared to equation (1.46) in which the material parameters of molar volume, lattice energy, bond type, and structure predict theoretical values of hardness greater than those observed. Equation (3.4) in practice predicts hardness values that are considerably lower than the measured values because, as Figure 4.12 shows, the relationship is approximately

$$H = 8 \times 10^{-2} G \qquad (3.5)$$

The fact that some correlation exists is strong evidence for the dominance of dislocation interaction in determining the hardness properties of single crystals.

3.5. HARDNESS ANISOTROPY

For the reasons developed in Chapters 2 and 5, we would not usually recommend the use of spherical or conical indenters for hardness measurements in materials with a marked tendency to brittle behavior because of the circumferential tensile stress, or where a significant amount of pile-up, controlled by discrete slip planes, may cause distorted indentations. Consequently, in this part of Chapter 3, we shall be concerned only with pyramidal indenters such as the Knoop, Vickers, and Berkovich indenters as well as the pentagonal indenter, which was designed with the advantages of the pyramidal indenters in mind but so as to offset the intrinsic anisotropy of crystals. Here we shall identify the orientation of a given indenter with respect to its facets, as sketched in Figures 2.3 and 2.5, rather than its diagonals.

3.5.1. Knoop Indentations

Most studies of anisotropy have been performed with this indenter since its almost two-dimensional shape and the fact that the projected area of the indentation is based on the measurement of the long diagonal only permit an unambiguous identification of its orientation. Thus the crystallographic direction of a given impression corresponds to $\langle uvw \rangle$ which is

parallel to the long diagonal and, in the absence of the sense effect encountered in some III–V electroceramics as polarity and described below in Section 3.6, this will lead to consistency in studies of anisotropy. Ideally, however, the indenter should have a symmetry which reflects that of the indented plane, and we should bear in mind that because this indenter has twofold symmetry it is best suited to those planes of two-, four-, and sixfold symmetry (e.g., {001}; {110}; {0001}, respectively) but not those with threefold symmetry, such as {111}.

The graphs obtained in Knoop hardness anisotropy investigations are typically like those in Figure 3.5. They are usually obtained by taking the
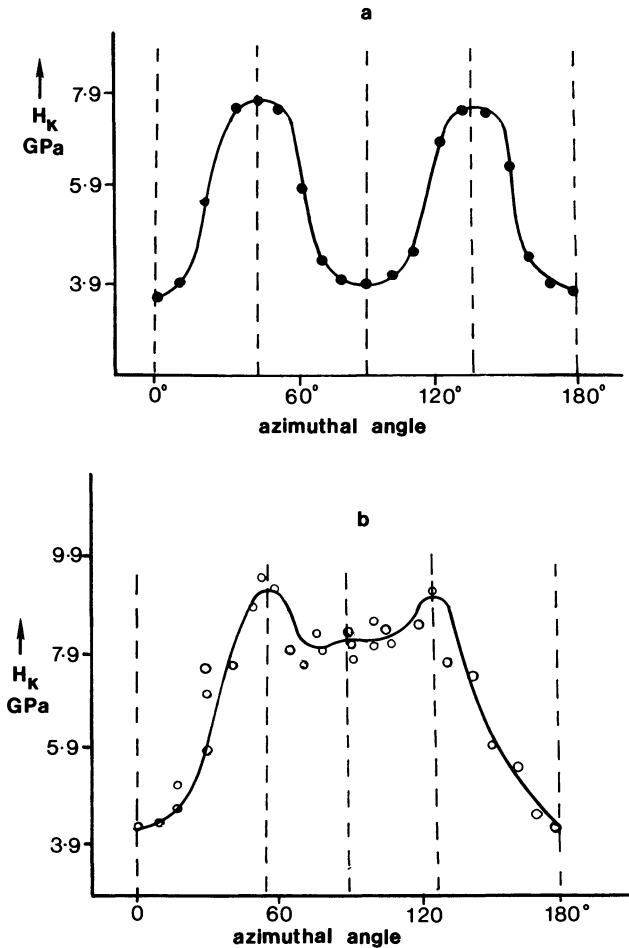
Figure 3.5. Anisotropy of hardness on (a) (001) planes and (b) (110) planes of magnesium oxide as revealed by a Knoop indenter. Replotted from Brookes *et al.*[9]

mean of 20 or more readings from each mirror symmetry position on either side of a low index direction such as $\langle 110 \rangle$ at small increments of angle—e.g., 0°, 15°, 30°, and so on up to 90°. This is to minimize systematic errors caused by deviations of the polished surface from that chosen (e.g., $\{100\}$) or the indenter's rotation axis not being at 90° to the polished surface.

3.5.1.1. Cubic Crystals

A typical plot illustrating the way in which the indentation hardness of a specific crystal plane varies with direction on that plane is given in Figure 3.5(a). These results are for a cleaved (001) plane of magnesium oxide indented at room temperature with a normal load of 4.9 N. Results for a chemically polished (110) plane, but otherwise the same experimental conditions, are shown in Figure 3.5(b). The nature of the anisotropy shown for (001)—i.e., a maximum hardness in $\langle 110 \rangle$ and minimum hardness in $\langle 100 \rangle$—is typical of all cubic crystals with a primary slip system of the type $\{110\}\langle 110 \rangle$, as Figure 3.6 confirms. However, within this class of crystals, the degree of anisotropy will vary significantly. For example, on the (001) plane of MgO results in the hardest and softest directions differ by a factor of two—approximately 4 GPa and 8 GPa in $\langle 100 \rangle$ and $\langle 110 \rangle$, respectively—while the difference for these two directions in, say, lithium fluoride is only about 10%.

Other examples of cubic crystals with these slip systems and, therefore, this characteristic of anisotropy, include nickel oxide, NiO; manganese oxide, MnO; ReO_3; bronze-type perovskites, M_xWO_3; and the transition metal carbides and nitrides.
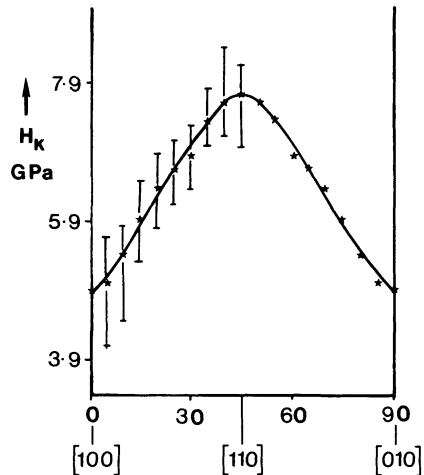
Figure 3.6. Knoop hardness anisotropy observed on the (001) plane of $Na_{0.69}WO_3$ using a load of 1.96 N at room temperature. After McColm and Wilson.[5]

The anisotropic behavior of cubic crystals with {001}⟨110⟩ slip systems is the converse of those in the above category. This effect is shown in Figure 3.7 where results on a mechanically polished and chemically etched (001) plane of zinc blende type InP, indented at room temperature with a load of 0.49 N, are replotted from work reported by Brazen.[10] Here the ⟨100⟩ directions are hardest and the ⟨110⟩ directions are softest with a degree of anisotropy amounting to some 15%. Other ceramic crystals of this type include the fluorite structure materials UO_2 and CaF_2.

Ceramics with cubic F structures and {111}⟨110⟩ slip systems exhibit the same hardness anisotropy as fluorite structure solids with {001}⟨110⟩ slip systems in the sense that the hardest directions on {100} are ⟨100⟩ and the softest are ⟨110⟩. Thus in order to determine which system is operative, a combination of the analysis given in Section 3.6.1 and other techniques, such as slip line analysis, is necessary. Ceramics with the diamond cubic structure have this slip system, and the parallel of their hardness anisotropy with that of fluorites can be seen by comparing the results for cubic boron nitride, BN, with the InP data in Figure 3.7.

It is interesting to note that the behavior of diamond itself is directly comparable with that of cubic BN, but in this case the absolute hardness is very dependent on the type of diamond being indented. For example, at room temperature Type I diamonds are softer than Type II. In this respect it should be noted that Type I is the more common (approximately 98% of all natural diamonds) and contains relatively high levels of nitrogen, as platelets in Type Ia and at substitutional sites in Type Ib, while Type II normally contains the greater density of dislocations. In very recent work,
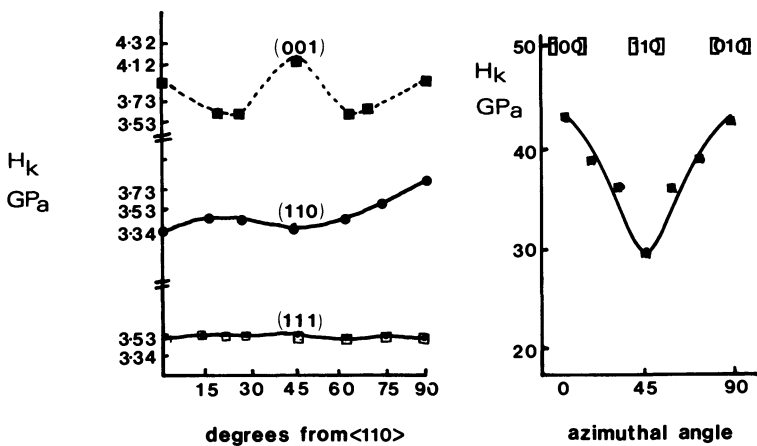
Figure 3.7. Knoop hardness anisotropy observed on specific planes of InP and cubic BN crystals. Note that 45° from ⟨110⟩ is equivalent to [100]. Data are represented from Brazen[10] and Brookes.[11]

it has been shown that the degree of anisotropy in synthetic diamonds of Type I is reduced and eventually entirely removed with increasing concentrations of nitrogen impurities.

This somewhat esoteric example does serve to introduce the critical role that sample purity and previous mechanical handling can have in masking, or even changing, any anisotropy of hardness in a crystal.

A clear demonstration of composition affecting the extent of anisotropy of hardness in a cubic system is shown in Figures 6.26 and 6.27, where filling of the A sites in the ABO_3 perovskite structure, when A is sodium and B is tungsten, leads to enhanced anisotropy on (001) in the $\langle 110 \rangle$ and $\langle 100 \rangle$ directions. Hardness increases substantially in the $\langle 110 \rangle$ direction as the sodium content increases, while the $\langle 100 \rangle$ hardness remains unchanged. Extrapolation of the data to hypothetical cubic WO_3 indicates that there would be zero anisotropy at room temperature. On the same diagram some results for cubic ReO_3 are given, and since this is equivalent to ABO_3 with completely empty A sites, the fact that this crystal does show almost zero anisotropy of hardness on (001) is interesting. In an electronic sense ReO_3 could be regarded as $Na_{1.0}WO_3$ but does not show the anisotropy expected for this, showing that the anisotropy is a structural effect involving atoms at the A sites. The {011} planes in the Na_xWO_3 crystals show more complex anisotropy, with hardness increasing in the sequence $\langle 100 \rangle$ to $\langle 21\bar{1} \rangle$ to $\langle 11\bar{1} \rangle$ which equals $\langle 01\bar{1} \rangle$, and the degree of anisotropy increasing as the sodium content increases from 28% for $Na_{0.51}WO_3$ to 38% for $Na_{0.6}WO_3$ as more A sites are filled.

Another example of composition having an influence on hardness anisotropy of cubic crystals is in the germanium system. This is a recent revelation[12]: Lack of obvious hardness anisotropy on germanium crystal planes was something of a puzzle since anisotropy is apparent in cubic BN and diamond, both of which are isostructural with germanium. Anisotropy in hardness on {100} was found only above a threshold temperature of about 100°C for n-type, 250°C for intrinsic, and 380°C for p-type crystals. This shows a two-parameter effect of composition and temperature; the n-type crystal contained 5.5×10^{18} As atoms cm^{-3} and the p-type contained 2.3×10^{19} Ga atoms cm^{-3}. The hardness anisotropy shown in Figure 3.8, after Roberts et al.,[12] is the type expected, by analogy with BN, CaF_2, and InP, to arise from {111}$\langle 1\bar{1}0 \rangle$ slip on an {001} plane.

One particular type of cubic structure, the zinc blende structure found in several important compound ceramic semiconductors such as GaAs and InP, has been known to exhibit a particular type of composition hardness anisotropy first noted more than 40 years ago when it was christened *hardness polarity*. This effect is seen on (111) and ($\bar{1}\bar{1}\bar{1}$) faces of the group III–group V ceramics, of which GaAs is the most investigated. The hardness difference is ascribed initially to the fact that these two planes are formed either by
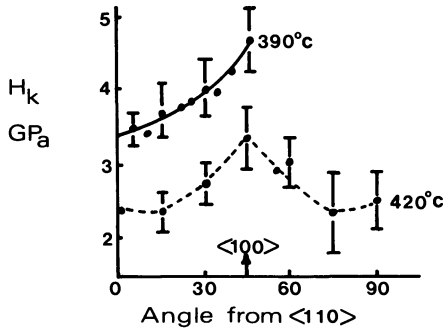
Figure 3.8. Knoop hardness versus indenter angle for n-type germanium at two temperatures. After Roberts et al.[12] This anisotropy is like that in Figure 3.7.

group III atoms or group V atoms, and generally it has been found that the planes formed by group III elements are up to 25% harder than those formed by group V elements.[13,14] Much more recent and detailed work[15] has shown that this type of anisotropy is also composition or impurity dependent and can be reversed when p-type dopants are added to GaAs instead of the n-type. Figure 3.9, re-presented from reference (15), clearly demonstrates this and further shows the effect of temperature on hardness anisotropy, particularly for n-doped material.

The fact that the structure formed from tetrahedral covalent atoms can be viewed as a three-dimensional array of puckered, six-membered rings easily explains why atoms of opposite types appear on (111) and ($\bar{1}\bar{1}\bar{1}$), as Figure 3.10 shows, but this explanation of hardness polarity overlooks the fact that penetration beneath the surface requires a more complex three-dimensional interaction between structure and penetration stress below the surface. On the face of it, this deeper interaction with the structure would be expected to obscure a purely surface polarity effect. It was this deeper question that recently led to a more sophisticated description of hardness anisotropy of the zinc blende structure by Hirsch and coworkers.[15] Outlines of this new work are given in Section 3.6.2.

As shown already, measuring Knoop hardness at elevated temperatures has been necessary to reveal anisotropy of this property in zinc blende cubic structures. In practice, when Knoop hardness tests are done at elevated temperatures on specific crystal planes over a full 360°C range more information about ceramic slip systems can be extracted. The results presented in Figure 6.24 for TiC, a ceramic with the rock-salt structure, are an impressive demonstration of this. A change in hardness anisotropy in this material, with its mixed bonding involving ionic, covalent, and metallic elements as described in Section 6.4.1, can be understood by assuming that one or another of the contributions to the total binding forces predominate in different temperature regimes. Thus at temperatures up to 220°C the anisotropy shown in Figure 6.24 is consistent with slip on $\{110\}\langle1\bar{1}0\rangle$ systems
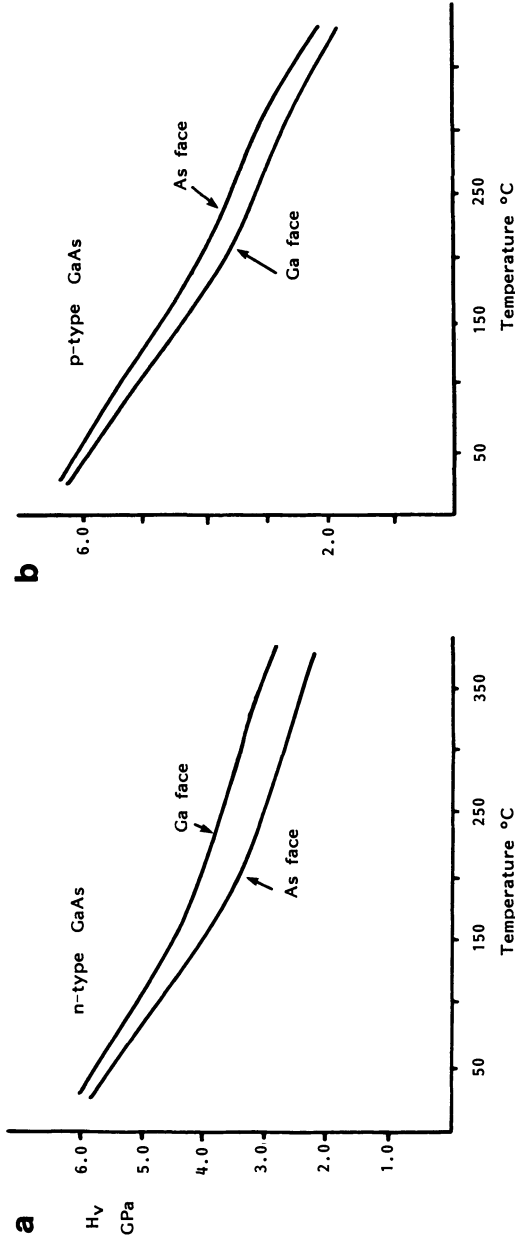
Figure 3.9. Vickers hardness using load of 0.98 N as a function of temperature for (a) 10^{18} cm^{-3} n-type GaAs and (b) 10^{18} cm^{-3} p-type GaAs. Taken from results in reference (15).

Raised As layer

Raised Ga layer
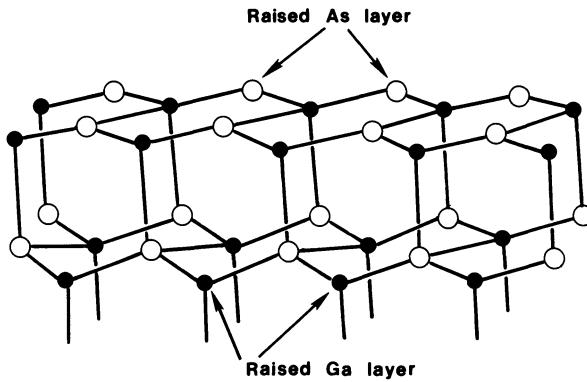
Figure 3.10. Sketch of the zinc blende structure emphasizing the appearance of As or Ga surfaces on (111) faces.

because the maximum hardness on {001} planes lies in [110] and minimum values we found in [100]; here ionic and covalent components in bonding predominate. As the temperature is increased, anisotropy becomes much less evident and, where definitely established, appears to indicate slip on either {110}⟨1$\bar{1}$0⟩ or {111}⟨1$\bar{1}$0⟩ systems. At sufficiently high temperatures— that is, above 600°C—the anisotropy is completely reversed, leading to an expectation of slip on either (111)⟨110⟩ or (001)⟨110⟩ systems. Supplementary evidence from etch pit rosettes and slip step patterns on the (001) surface combine to suggest the {111}⟨1$\bar{1}$0⟩ assignment. Dominant in the bonding at higher temperatures is the metallic component, so that the change to anisotropy patterns associated with more plastic crystals is to be expected.

Radiation damage can, in some samples, introduce a degree of plasticity; for example, in diamond the overall hardness is reduced after irradiation but there are no data showing what this does to the Knoop hardness anisotropy. We can, however, note that radiation damage in MgO increases the overall hardness but does not affect the anisotropy, a fact that seems to be general for the rock-salt structure.[16]

The work in reference (16), demonstrating the hardening effect of radiation, introduces a note of caution in ascribing the same type of hardness anisotropy to crystals having the same slip systems, because there is reported data for all, even nonceramic, rock-salt materials NaCl and KCl, which show the hard direction on (001) to be [100], not [110]. These anomalous data emerge from very soft crystals, NaCl (1.91 GPa) and KCl (0.92 GPa), which do have {110}⟨110⟩ slip systems; some attempt at interpretation is made in Section 3.6.1.

From the selection of experimental results so far presented and more fully collected in Table 3.1, it can be seen that rotating the long-axis direction

of the twofold symmetry Knoop indenter on single-crystal planes commonly found as facets of cubic ceramic crystals reveals limited classes of hardness anisotropy. Furthermore, this property is susceptible to the effects of temperature, impurity, and mechanical damage from radiation in ways reminiscent of those changes known to occur in dislocation density and mobility in crystals, linking again dislocation theory and hardness variation.

3.5.1.2. Hexagonal Crystals

An illustration of the planes and directions of interest is given in Figure 3.11. The anisotropy in the hardness of hexagonal ceramic crystals follows the pattern established for hexagonal metals in that the phenomenon is more pronounced on the prism planes than on the basal planes; Figure 3.12 demonstrates this for Al_2O_3. Again the observation of anisotropy is greatly influenced, as the results in Figure 6.13 and Table 3.2 show, by factors such as temperature that alter dislocation mobility. Composition variation within the same structure, as was the case for cubic crystals, can influence the sense of the hardness anisotropy as the (0001) results for Na^+-β-Al_2O_3 compared to other M^+-β-Al_2O_3 crystals shown in Table 3.2. The β-Al_2O_3 study[17] shows that for $\{01\bar{1}0\}$ the hardness in the [1000] direction is greater than the hardness in all other directions, which is a pattern of behavior also found for α-Al_2O_3. On the other hand, the relative hardness and the sense of anisotropy of hardness on (0001) depends on the composition of the mirror plane at 90° to the c-axis; for Na^+-β-Al_2O_3, as Figure 3.13 shows, the hardness in direction [11$\bar{2}$0] is greater than all other values of hardness, which is again like α-Al_2O_3, while for Ag^+, K^+-β-Al_2O_3, etc., the hardest direction is [10$\bar{1}$0], as in SiC.
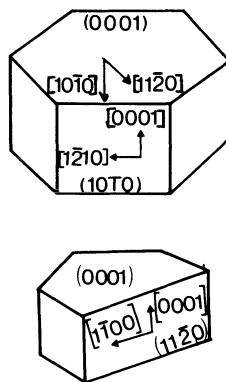
Figure 3.11. Planes and directions of importance in Knoop hardness anisotropy studies of hexagonal crystals.

Table 3.1. Knoop Hardness Results from Cubic Single Crystals

Crystal	Plane indented	Slip system	Temperature (°C)	Knoop hardness (GPa)								Notes
				[100]	[110]	$[21\bar{1}]$	$[11\bar{1}]$	$[01\bar{1}]$	$[22\bar{3}]$	$[12\bar{3}]$	$[02\bar{3}]$	
MgO	(100)	$\{110\}\{1\bar{1}0\}$	25	4.41	7.35							
NiO	(100)	$\{110\}\{1\bar{1}0\}$	25	4.12	5.25							
MnO	(100)	$\{110\}\{1\bar{1}0\}$	25	2.47	2.80							
	(110)		25	2.47	—	—	2.82	2.82				
ReO_3	(001)	$\{110\}\{1\bar{1}0\}$	25	5.45	5.68							
$\text{Na}_{0.515}\text{WO}_3$	(100)	$\{110\}\{1\bar{1}0\}$	25	4.66	6.94							
	(011)		25	4.47	—	6.06	6.72	6.80				
$\text{Na}_{0.691}\text{WO}_3$	(100)	$\{110\}\{1\bar{1}0\}$	25	4.92	7.67							
	(011)		25	4.44	—	5.64	7.05	7.52				
$\text{Na}_{0.707}\text{WO}_3$	(100)	$\{110\}\{1\bar{1}0\}$	25	4.82	7.81							
	(032)		25	5.22	—	—	—	—	7.44	7.34	7.44	
$\text{Na}_{0.8}\text{WO}_3$	(100)	$\{110\}\{1\bar{1}0\}$	25	5.37	7.94							
(MnZnFe) Fe_2O_4												Load = 3 N
	(100)			6.18	5.50							
	(011)			6.18	5.50				5.89			
	(111)					5.69	—	5.69				
	(211)						5.40					

Ge	(100)	$\{111\}\langle 1\bar{1}0\rangle$	390	4.6	3.5				n-type
			420	3.1	2.3				
Diamond	(100)	$\{111\}\langle 1\bar{1}0\rangle$	25	103.0	91.0				Type II 3.63 [210]
InP	(100)	$\{111\}\langle 1\bar{1}0\rangle$		4.22	3.98				
	(110)			3.92	3.35	3.46	3.35		
	(111)			—	3.51	—	—	3.57	
BN	(100)	$\{111\}\langle 1\bar{1}0\rangle$		43.0	30.0				
	(111)			—	39.45	41.5			
$VC_{0.84}$	(001)	$\{111\}\langle 1\bar{1}0\rangle$ two systems	196	20.02	21.10				
			25	18.25	18.25				
VC	(111)	$\{111\}\langle 1\bar{1}0\rangle$	300	13.52	10.78				
			350	13.69	11.19				
			350	13.72	10.78				
Nb_6C_5	(100)	$\{111\}\langle 1\bar{1}0\rangle$	25	23.46	21.59				Max at 15° from [100] = 24.6 GPa
	(100)								
TiC	(110)	$\{110\}\langle 1\bar{1}0\rangle$	25	20.01	26.95				
	(100)		25	19.31	23.03				
	(100)		600	10.0	8.5				
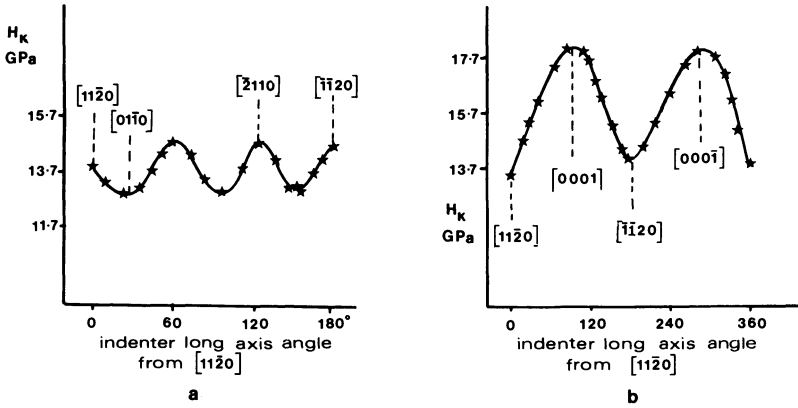
Figure 3.12. Anisotropy of Knoop hardness observed on (a) (0001) plane and (b) (1Ī00) plane of Al_2O_3. Redrawn from reference (9).

Hence in broad terms, as was the case for cubic crystals, it is possible to divide the results in Table 3.2 into two classes and assign them to a probable slip system. For example, the hardness anisotropy on {01Ī0} SiC planes is the converse of that found in Al_2O_3{01Ī0}—e.g., values of 20.27 and 27.00 GPa for ⟨0001⟩ and ⟨11Ī0⟩, respectively, compared to 17.7 and 13.7 GPa for these directions in Al_2O_3{01Ī0}. More detailed work by Sawyer et al.[18] shows, however, that not only is anisotropy most marked in the sequence {0001}<{1Ī00}<{11Ī0}, but a peak in hardness occurs on (1120) about 60° from [0001] as shown in Figure 3.14. Likewise, beryllium[19] shows zero anisotropy on the basal plane but 30% on {11Ī0} where [0001] is the softest direction, [11Ī0] is intermediate in hardness, and the maximum lies midway between these directions. The diboride crystals that have been examined by slip line analysis and to some extent by hardness indentation,[20,21] the detailed SiC work, and the β-alumina crystals that have been examined suggest that the two classes of behavior arise to a first approximation from the operation of the two basic slip systems {0001}⟨11Ī0⟩ and {1Ī00}⟨1120⟩.

Note the possible significance of the slip direction here, i.e., ⟨11Ī0⟩ for both {0001} and {10Ī0} systems; for {0001} slip, dislocations will be moving parallel to the indented surface when indenting the basal plane, and for (1010) slip only screw dislocations will be emerging onto the indented plane. On the (10Ī0) indented surface, edge dislocations will emerge for {10Ī0} slip but only screw dislocations for basal slip.

The more detailed work and wider analysis given by Sawyer, outlined in Section 3.6.1, suggest that the details of a hardness orientation curve are
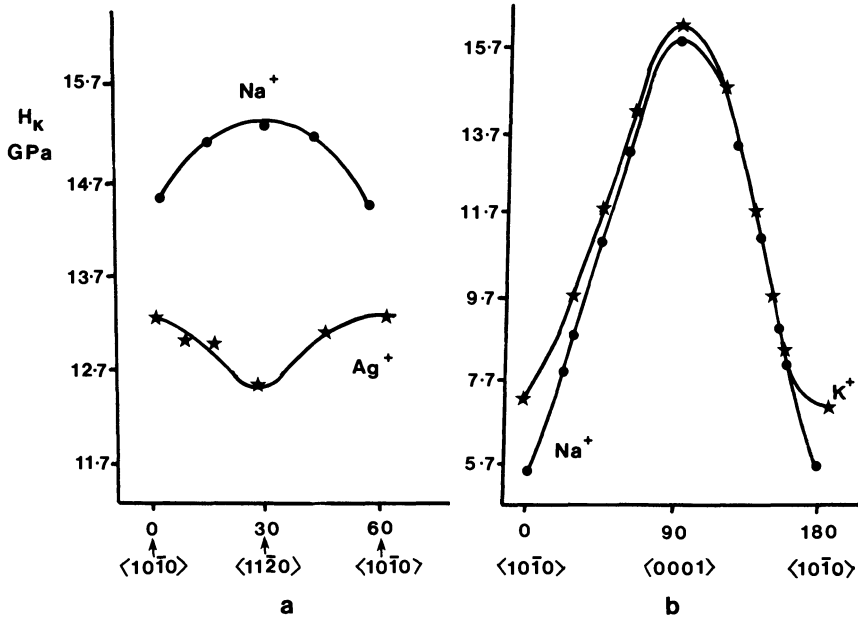
Figure 3.13. Hardness anisotropy for (a) (0001) plane of Na^+-β-Al_2O_3 and Ag^+-β-Al_2O_3, (b) ($11\bar{2}0$) planes of Na^+-β-Al_2O_3 and K^+-β-Al_2O_3. Redrawn from reference (17).
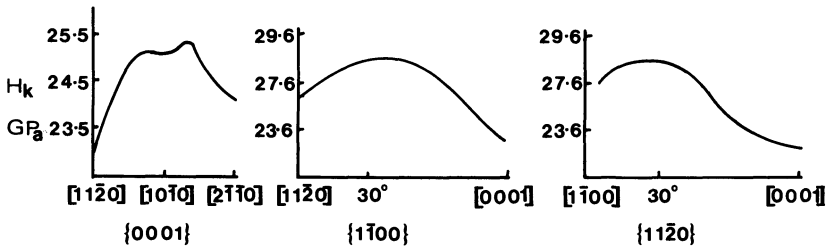
Figure 3.14. Knoop hardness anisotropy on three sets of planes of SiC as observed by Sawyer *et al.*[18] with 4.9 N load.

important. Hence full curves must be plotted instead of measuring hardness with the Knoop diamond long axis only placed along two principal directions on any given plane, as is more common. Furthermore, a greater range of planes should be investigated. When this is done the division into an α-Al_2O_3 and a SiC group arises because only one of the two slip systems operates for α-Al_2O_3 but a combination of both the slip systems for other hexagonal crystals. Adewoye and Agu[22] have taken this further and used the anisotropy curves they found for beryl, reproduced as Figure 3.15, to

Table 3.2. Knoop Hardness Data for Hexagonal Single Crystals

Crystal	Plane indented	Slip system	Knoop hardness (GPa)				Notes
			[0001]	[11$\bar{2}$0]	[01$\bar{1}$0]	⟨1$\bar{1}$00⟩	
Al$_2$O$_3$	(0001)	{0001}⟨11$\bar{2}$0⟩	—	13.7	12.7		
	(1$\bar{1}$00)		17.7	13.7			
Na$^+$-β-Al$_2$O$_3$	(0001)	{0001}⟨11$\bar{2}$0⟩	16.19	15.21	14.52		
	(11$\bar{2}$0)				5.74		
Ag$^+$-β-Al$_2$O$_3$	(0001)		15.70	12.56	13.35		
	(11$\bar{2}$0)				5.74		
K$^+$-β-Al$_2$O$_3$	(0001)		15.70	12.76	14.23		
	(11$\bar{2}$0)				7.46		
Tl$^+$-β-Al$_2$O$_3$	(0001)			12.27	13.54		
NH$_4$-β-Al$_2$O$_3$	(11$\bar{2}$0)		14.96		6.87		
Be	(0001)		Zero anisotropy				Max hardness of 1.26 GPa in between [11$\bar{2}$0] and [01$\bar{1}$0]
	(11$\bar{2}$0)		0.88	1.08			
SiC	(0001)	{$\bar{1}$100}⟨11$\bar{2}$0⟩		23.06	25.03		Cusp at [0110] max to side of [0110] = 25.12 GPa
	{01$\bar{1}$0}	{$\bar{1}$100}⟨11$\bar{2}$0⟩ + {0001}⟨11$\bar{2}$0⟩	22.57				Max of 29.4 GPa 60° from [0001]
	{11$\bar{2}$0}	{0001}⟨11$\bar{2}$0⟩	21.59	—	26.50		Max of 28.95 GPa 60° from [0001]. All done at 4.91 N

Material	Plane	Slip system					Remarks
TiB_2	(0001)	$\{0001\}\langle11\bar{2}0\rangle$	—	28.86	25.98		This Al_2O_3 behavior lasts until 250°C
	(10$\bar{1}$0)		38.68	32.04			Above 250°C
	{11$\bar{2}$0}		38.10				
ZrB_2	(0001)	$\{10\bar{1}0\}\langle\bar{1}210\rangle$	—	21.36	25.69	28.90	
	{10$\bar{1}$0}		19.63				
	{11$\bar{2}$0}		19.63				
HfB_2	(0001)	$\{10\bar{1}0\}\langle\bar{1}210\rangle$ +	—	23.09	21.94	23.96	
	{10$\bar{1}$0}		23.96	21.36			
	{11$\bar{2}$0}		23.96	22.80			
$Be_3Al_2Si_6O_{18}$	(0001)	$\{0001\}\langle11\bar{2}0\rangle$ $\{1010\}\langle\bar{1}210\rangle$ $\{1010\}\langle\bar{1}210\rangle$ + $\{0001\}\langle1\bar{2}10\rangle$ + $\{10\bar{1}0\}\langle0001\rangle$	—	5.54	5.94	24.53	Load = 19.4 N
	(1010)		6.53	—	6.33		Max at 60°C from [0001] = 7.26 GPa, min at 55° from [0001] = 6.30 GPa
				6.33			
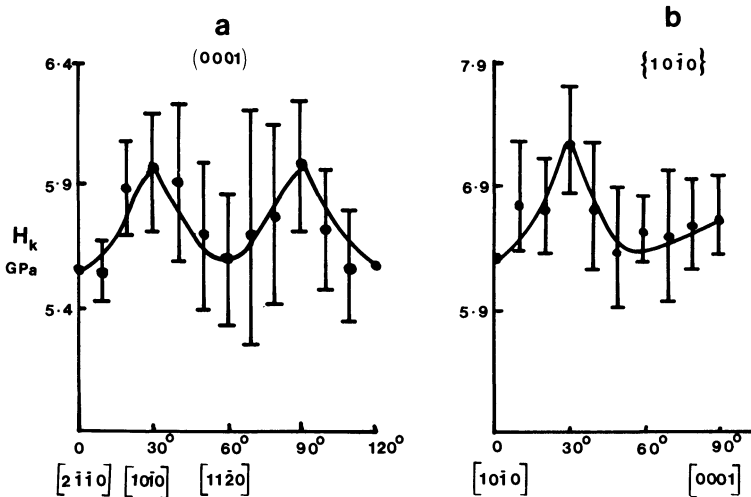
Figure 3.15. Knoop hardness anisotropy on (a) (0001) and (b) $\{10\bar{1}0\}$ planes of beryl, $Be_3Al_2Si_6O_{18}$, from reference (22).

conclude that the SiC-like maximum in hardness at 60° from [0001] together with the minimum somewhat optimistically noted between 50° and 60° from [0001] on ($10\bar{1}0$) planes, is controlled by three slip systems: $\{10\bar{1}0\}\langle1\bar{2}10\rangle$, $\{0001\}\langle1\bar{2}10\rangle$, and $\{10\bar{1}0\}\langle0001\rangle$.

This third class of anisotropy arises because c/a for beryl is 0.988, making $b = \langle0001\rangle$ viable, along with $b = \langle2110\rangle$. Here then is a case where choice of slip system is important in reproducing the detail of an anisotropy curve and not the general pattern of such a curve as achieved in the critical resolved shear stress analysis (CRSS) of Section 3.6. In fact, choice of slip systems is not so easy with hexagonal systems; for example, in the case of α-Al_2O_3 all the 17 possible slip systems listed in Table 3.3, since they have in varying degrees been observed experimentally, have to be considered. Basal slip has the lowest CRSS, but it is no easy task to rank the other slip systems in terms of their CRSS because, with anisotropic ionic materials in particular, the assumption that the self-energy of a dislocation increases as the square of the Burgers vector does not always hold true; Burgers vectors for α-Al_2O_3 are given in Table 3.4, but as pointed out above in the case of beryl, the effect of the c/a ratio must be taken into account when considering the differences shown in Table 3.4.

3.5.1.3. Other Crystals

There are few results pertaining to crystals other than cubic or hexagonal ones. If the marked anisotropy reported for V_2O_5 is typical, then

the Knoop indentation technique is a good way to explore their slip behavior and indeed to orient them for other studies. As Table 3.5 shows, anisotropy factors up to 8.8 occur in the orthorhombic structure of V_2O_5.

The order of hardness is $H_{(001)} < H_{(010)} < H_{(100)}$. Microscopic observation shows slip lines parallel to [100] on (010) planes, as is perhaps not

Table 3.3. Experimentally Observed
Dislocation Slip Systems in
α-Al_2O_3

Slip plane	Slip system
(0001)	$(0001)\frac{1}{3}\langle11\bar{2}0\rangle$, $(0001)\langle10\bar{1}0\rangle$
$(10\bar{1}0)$	$\{10\bar{1}0\}\frac{1}{3}\langle\bar{1}2\bar{1}0\rangle$
$(11\bar{2}0)$	$\{11\bar{2}0\}\frac{1}{3}\langle\bar{1}101\rangle$, $\{11\bar{2}0\}\frac{1}{3}\langle2\bar{2}01\rangle$,
	$\{11\bar{2}0\}\langle\bar{1}100\rangle$, $\{11\bar{2}0\}\frac{1}{3}\langle1\bar{1}02\rangle$
$(01\bar{1}2)$	$\{01\bar{1}2\}\frac{1}{3}\langle2\bar{1}\bar{1}0\rangle$, $\{01\bar{1}2\}\frac{1}{3}\langle01\bar{1}1\rangle$,
	$\{01\bar{1}2\}\frac{1}{3}\langle20\bar{2}1\rangle$
$(10\bar{1}1)$	$\{10\bar{1}1\}\frac{1}{3}\langle\bar{1}2\bar{1}0\rangle$, $\{10\bar{1}1\}\frac{1}{3}\langle1\bar{1}01\rangle$
$(2\bar{1}\bar{1}3)$	$\{2\bar{1}\bar{1}3\}\frac{1}{3}\langle1\bar{1}01\rangle$, $\{2\bar{1}\bar{1}3\}\langle01\bar{1}0\rangle$
$(2\bar{1}\bar{1}2)$	$\{2\bar{1}\bar{1}2\}\langle01\bar{1}0\rangle$, $\{2\bar{1}\bar{1}2\}\frac{1}{3}\langle10\bar{1}2\rangle$
$(4\bar{2}\bar{2}3)$	$\{4\bar{2}\bar{2}3\}\langle01\bar{1}0\rangle$

Table 3.4. Shortest Burgers
Vectors in α-Al_2O_3

b	Size of unit b (nm)
$\frac{1}{3}\langle11\bar{2}0\rangle$	0.475
$\frac{1}{3}\langle1\bar{1}01\rangle$	0.512
$\frac{1}{3}\langle20\bar{2}1\rangle$	0.698
$\langle10\bar{1}0\rangle$	0.822
$\frac{1}{3}\langle21\bar{3}1\rangle$	0.844
$\frac{1}{3}\langle10\bar{1}2\rangle$	0.908

Table 3.5. Knoop Hardness of Orthorhombic V_2O_5 for
Load of 0.15 N[a]

Plane	Knoop hardness (GPa)			Anisotropy factor
	[100]	[010]	[001]	
(100)		4.86	1.72	2.8
(010)	0.98		3.53	3.6
(001)	0.59	4.51		8.8

[a] From reference (23).

surprising when the structure is examined: each vanadium atom is inside a pyramid of five oxygen atoms with V–O distances varying from 0.158 to 0.202 nm. Edge sharing of the VO_5 pyramids forms zig-zag chains along the [001] direction. These chains are linked at an apex to form sheets parallel to the (010) plane. A sixth oxygen atom situated at 0.278 nm from a vanadium atom produces bonding between planes of the (010) type, and this is the weak link in the structure, permitting easy cleavage between (010) planes. Thus on the (010) face, for example, when the indenter is aligned along [001] it is parallel to the VO_5 chains, while the [100] direction is parallel to the weak oxygen bridges; hence easy cleavage and slip in this direction leads to the very low hardness values. Similarly on (001) the measurement in [100] is in effect along the cleavage direction while the hard direction [010] is perpendicular to it.

Two tetragonal silicides, WSi_2[24] and $MoSi_2$[25], have been shown from slip patterns and by the dislocation etch pit technique to have (100)[001] primary slip, but different secondary slip systems, and to exhibit Knoop hardness anisotropy with the hardest direction being along [001] on the (100) plane. In the case of $MoSi_2$, along [011] on the (001) plane, H_K is 12.76 GPa, falling to a minimum of 10.79 GPa along [010], giving an anisotropy factor of 1.18. Table 3.6 contains the observed hardness values for these two tetragonal ceramics.

The difference in behavior due to having different secondary slip systems active in these two tetragonal silicides appears to be slight. First, WSi_2 has a more obvious anisotropy factor, 37% on (100); second, there is a reversal in the order of hardness on (101) when [100] is the softest direction for WSi_2 but hardest for $MoSi_2$.

3.5.2. Vickers Indentations

Two ambiguities concerning its orientation with respect to the indented crystal plane make this indenter less convenient than the Knoop. For good reasons, the Vickers hardness number is based on the average length of the two diagonals formed by the square-based indenter. If the orientation of the indenter is determined by the alignment of these diagonals, then both can lie in the same family of directions only when indenting (100) surfaces. For example, if one diagonal is aligned with [001] on a (110) surface, then the other is parallel to the [1$\bar{1}$0] direction. Furthermore, it is only on (001) planes that the symmetry of the indenter matches that of the indented surface so that the resultant indentations will be square. On other planes, indentations tend to be distorted as the result of pile-up due to emerging dislocations and slip steps. Mainly for this reason, anisotropy in Vickers hardness measurements on planes other than (001) is rarely reported.

Table 3.6. Knoop Hardness Anisotropy of Some Tetragonal Special Ceramics

Material	Plane									Known slip systems
	Direction — Knoop hardness (GPa)									
	(100) [010]	(100) [011]	[001]	[010]	(001) [011]	[100]	[010]	(101) [101]	[100]	
WSi$_2$	11.48	12.56	15.70	13.54	14.43	12.66	13.50	13.74	12.17	{100}⟨100⟩ (010)[001]
MoSi$_2$	8.93	9.91	10.87	12.27	12.76	10.89	11.09	11.38	12.46	{100}⟨001⟩ {110}⟨001⟩
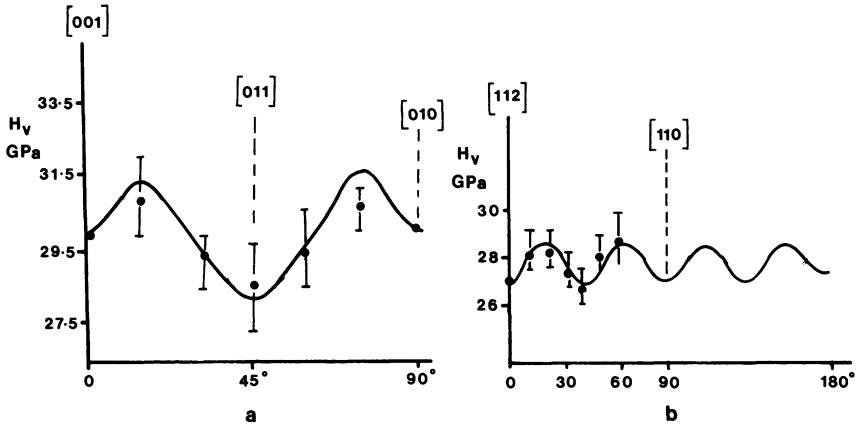
Figure 3.16. Anisotropy of Vickers hardness for (a) (001) plane of $NbC_{0.8}$ and (b) (111) plane of $VC_{0.088}$. After Kumashiro and Sakuma.[26]

Likewise there are few, if any, studies of anisotropy using the Vickers diamond on noncubic crystals.

Figure 3.16 and Tables 3.7 and 3.8 show that the anisotropy is of the same nature as that observed for Knoop indentation hardness measurements in that $\langle 110 \rangle$ and $\langle 100 \rangle$ are the hard and soft directions, respectively, for crystals which slip on $\{110\}\langle 110 \rangle$, and similar behavior is exhibited by those cubic crystals with $\{110\}\langle 111 \rangle$, $\{112\}\langle 111 \rangle$, and $\{123\}\langle 111 \rangle$ systems. Again, analogously to the Knoop measurements, the converse is found for $\{100\}\langle 0\bar{1}1 \rangle$ and $\{111\}\langle 1\bar{1}0 \rangle$ systems.

Generally, Vickers hardness anisotropy on planes other than (001) is less evident, while hardness values on all planes have higher values than those obtained when using a Knoop indenter on the same material. As a result of the somewhat uncertain revelation of hardness anisotropy characteristics by the Vickers diamond, some investigations have been made quoting average H_V values for given planes and comparing these values with anion and cation distribution and packing densities. For example, some inverse spinels[27]—synthetic magnetite and synthetic Mn–Zn ferrite, $Fe^{3+}_{(tet)}(Fe^{2+}Fe^{3+})_{2(oct)}O_4$—have been reported to show $H_{(111)} > H_{(100)} > H_{(110)}$ in the range 5.28, 5.14, and 4.95 GPa, respectively, while $Fe^{3+}_{(tet)}(Mn^{2+}, Fe^{2+}, Zn^{2+}, Fe^{3+})_{2(oct)}O_4$ reverses the hardness order; i.e., $H_{(110)} > H_{(100)} > H_{(111)}$ in the range 6.33, 6.18, and 5.79 GPa, respectively. Anion and cation packing densities are the same in both cases, and so the increased hardness and the change in planar order arise from composition variation in the octahedral sites. For some noncubic crystals, ranges of hardness value for (001) planes that imply a hardness anisotropy have been quoted, but they have not been substantiated by listing any specific direc-

Table 3.7. Oriented Vickers Hardness Measurements on Some Perovskite Single-Crystal Planes

Load (N)		Vickers hardness (GPa)					
		{001}					
	Composition	$Na_{0.75}WO_3$		$Na_{0.601}WO_3$		$Na_{0.515}WO_3$	
	Diagonals along	$\langle 100 \rangle$	$\langle 110 \rangle$	$\langle 100 \rangle$	$\langle 110 \rangle$	$\langle 100 \rangle$	$\langle 110 \rangle$
0.49		10.80	7.84	12.05	9.10	8.61	7.38
0.98		9.56	7.11	10.60	6.93	8.19	7.11
1.96		7.25	6.11	7.59	6.26		5.87
2.94		7.02	5.64	—	5.95		6.07
4.90		5.74	5.28	—	6.02	—	—

Load (N)		Vickers hardness (GPa)					
		{011}					
	Composition	$Na_{0.75}WO_3$		$Na_{0.601}WO_3$		$Na_{0.515}WO_3$	
	Diagonals along	[100] and [0$\bar{1}$1]	[1$\bar{1}$1] and [2$\bar{1}$1]	[100] and [0$\bar{1}$1]	[1$\bar{1}$1] and [2$\bar{1}$1]	[100] and [0$\bar{1}$1]	[1$\bar{1}$1] and [2$\bar{1}$1]
0.49		10.49	9.19	9.36	7.20	8.34	8.43
0.98		8.77	7.38	8.54	7.11	7.04	6.27
1.96		8.18	6.37	7.32	6.21	6.98	5.89
2.94		6.91	5.83	6.72	5.99	6.11	5.50
4.90		6.44	5.59	6.10	—	5.95	—

Table 3.8. Vickers Hardness on (001) Plane of Some Cubic Crystals and Slip Systems Independently Identified

Crystal	Slip system	Temperature (°C)	Vickers hardness (GPa)	
			[100]	[110]
NiO	{110}$\langle 110 \rangle$	25	5.18	6.25
TiC	{110}$\langle 110 \rangle$	25	25.48	34.30
VC	{111}$\langle 110 \rangle$	350	18.03	16.61
$(MnZnFe)Fe_2O_4$	—	20	6.18	6.18

tional hardness values.[28] Thus for MoB_2, WB_2, and CrB_2 maximum and minimum hardness values on (001) are 24.24–21.30 GPa, 22.18–20.51 GPa, and 22.47–20.37 GPa, respectively. These hardness values are very similar even though MoB_2, being hexagonal, has a different crystal structure from

that of WB_2 and CrB_2. Some ranges of hardness values that imply anisotropy on (001) and {010} planes in hexagonal, tetragonal, and orthorhombic borides are given in Table 6.24. In the case of the different boron units, see Table 6.23; the mean H_V values are surprisingly similar.

3.5.3. Berkovich Indentations

From what has been observed in previous sections, it is obvious that the Berkovich indenter is suited to indenting only planes of three- and sixfold symmetry—i.e., the {111} planes of cubic crystals and the (0001) planes of hexagonal crystals. Nevertheless, its use is favored for indentations in these planes of the ultrahard ceramic solids, such as diamond and cubic boron nitride, since it is easier to avoid a chisel tip on repolishing a blunted indenter with three facets than one which has four facets and a natural chisel edge. Because it has no chisel tip, the Berkovich indenter is favored for measurements using very low loads when indent diagonals will be small and the errors, shown in Figure 2.4(b), that arise from the presence of a chisel edge do not then occur.

Because this is not a commonly encountered indenter and because of the restricted type of plane that it can usefully investigate, there are very few results from which to draw conclusions. However, for cubic crystals the difference between those having {001}⟨011⟩ slip systems and the other types is evident in the symmetry of the hardness anisotropy curves as it was in the case of the Knoop indenter and the Vickers diamond.

It is interesting to observe that indentations of similar orientation but opposite sense—e.g., [$\bar{1}\bar{1}2$] and [$11\bar{2}$]—yield different hardness values and have different fracture characteristics, as Figure 3.17 shows. Such observations serve to emphasize the fact that hardness measurements reflect bulk and not surface properties even though this whole area of work emphasizes
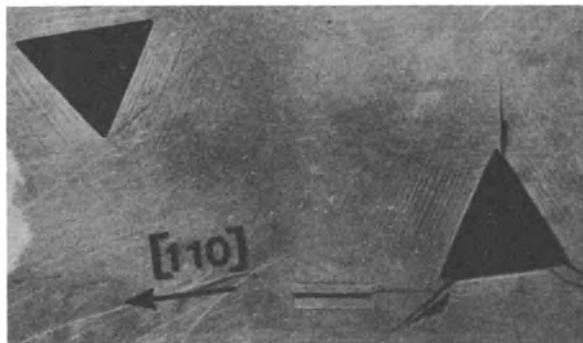
Figure 3.17. Berkovich indentations on (111) plane of CaF_2 which has an {001}⟨110⟩ slip system. Scale bar: 10 μm. From reference (29).

planes of indentation and hardness in directions along such planes. In Figure 3.17 the orientation of the facets of this indenter with respect to the (111) plane indented is the same for both indentations. However, there is a difference in orientation when compared to the resolved shear stresses developed on the active slip systems in the bulk of the solid. Such an effect clearly leads to crack formation in the soft directions while no radial cracks form for the harder orientation.

3.5.4. Scratch Hardness Anisotropy

Because the direction of sliding uniquely defines the crystallographic direction of measurement on a crystal plane, and since Section 2.4 concludes that the same mechanisms are operative in scratch hardness as in indentation hardness, it is surprising to see that the scratch method is so little used in hardness anisotropy investigations. Furthermore, one would expect a greater anisotropy factor to emerge from the different method of calculating hardness; see, for example, equation (1.51), where just the groove width is used for calculating hardness and not the total or projected area as in indentation hardness. An important reason for this lack of use is that the frictional forces must also be measured. This is particularly true if resolved shear stress calculations are to be made in order to predict the shape of the hardness anisotropy curve for any plane on which sliding occurs, in terms of possible slip systems that could operate. Thus the resultant stress axis has an angle of inclination determined by the coefficient of friction through equation (3.6)

$$\mu = \tan \theta \qquad (3.6)$$

The effect this has on developing predictive equations is discussed in Section 3.6.1 where resolved shear stress models are considered.

That the method can reveal hardness anisotropy in nonmetallic materials, even if neither example might be considered to be a ceramic in the accepted sense, is shown in Figure 3.18. In order to achieve these results the temperature had to be elevated so that untorn grooves were produced.[30] The two materials used, LiF and CaF_2, are examples of the two types of slip system mainly encountered in cubic ceramics, as Table 3.1 shows, and clearly they are the converse of each other, as Fig. 3.18 clearly shows. This method is worthy of development.

3.5.5. Avoiding Directional Hardness Anisotropy

In routine hardness measurements, the phenomenon of anisotropy is irksome and there would seem to be a need for an indenter which overcomes
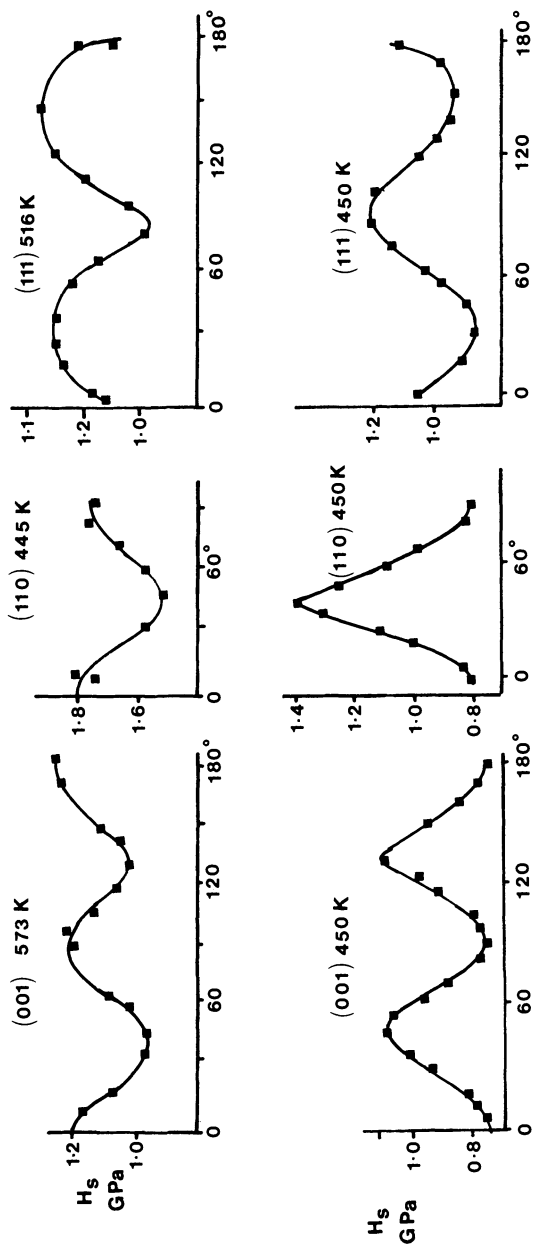
Figure 3.18. Scratch hardness H_s on planes of (top) CaF_2 and (bottom) LiF. The load in both cases was 7.85 N on a leading-edge diamond stylus. The temperatures are as shown. After Brookes and Green.[30]

this effect so that a single representative hardness value may be determined for a specific plane of a given crystal. This could be particularly useful for measurements on ceramic crystals, where the degree of anisotropy is most marked, and therefore of greatest interest to mineralogists and gemologists. In this way the convenient technique of indentation hardness could help to identify crystal faces before subsequent experiments were conducted involving single crystals.

A conical or spherical indenter would seem to solve the problem in the first place, but as the analysis in Section 5.2.2 in particular shows, these geometries, when used on brittle crystal faces, readily produce ring cracks at the loads required to make an indentation, and they are therefore not suitable. Given the disadvantages of indenters based on cones and spheres the intrinsic anisotropic properties of crystalline solids may be overcome by using a fivefold symmetrical indenter (i.e., an inverted pyramid having a regular pentagonal base) since this represents the smallest number of facets with a symmetry not shared by crystal structures.

Because this is a very uncommon indenter there exist very few results relevant to ceramic systems; NiO(100) planes indented with this diamond at a load of 4.9 N show an absence of anisotropy in contrast to both the Knoop and Vickers diamond indenters.

3.6. THEORETICAL MODELS FOR HARDNESS ANISOTROPY

The most striking feature of the collected data in the tables in this chapter and in Chapter 6 on anisotropic indentation hardness values for crystalline ceramics is its dependence on the relevant active slip systems. This has been extended by observation to encompass materials beyond ceramics. Thus, the nature of anisotropy for a soft, face-centered cubic metal may be the same as for hard, covalent cubic crystals like diamond, since they both have $\{111\}\langle 1\bar{1}0\rangle$ slip systems. Consequently it is natural that, in order to develop a universal model, we should first look for explanations based on mechanisms of plastic deformation.

3.6.1. Resolved Shear Stress Models

3.6.1.1. The Brookes–O'Neill–Redfern Model

The most consistently successful models for explaining and predicting the nature of anisotropy in indentation hardness have been those based on adaptations of the Schmid–Boas resolved shear stress criteria. Thus slip is initiated when the critical resolved shear stress (τ_e) is reached for the most favorably oriented slip system. Then:

$$\tau_e = P/A \cos \phi \cos \lambda \qquad\qquad (3.7)$$

where P is the load applied along the axis of a cylindrical element of cross-sectional area A, λ is the angle between the slip direction and the stress axis, and ϕ is the angle between the stress axis and the normal to the slip plane (SN) as defined in Figure 3.19. As plastic deformation takes place, the slip plane will usually rotate about an axis (AR) which lies in the slip plane and is normal to the operating slip direction. Under uniaxial stress conditions, and for certain crystallographic directions of the stress axis, it is possible that the resolved shear stress is zero on all the operative slip systems. Such conditions obtain when the stress axis lies in a $\langle 111 \rangle$ direction of a crystal with $\{110\}\langle 1\bar{1}0 \rangle$ slip systems. Then, even though subjected to a compressive load, the material is incapable of plastic deformation. The following considerations show that these conditions will never obtain during indentations since the direction of the stress axis will vary from one position beneath the indenter to another. Nevertheless, the Schmid–Boas equation can form the basis for an analysis of anisotropy in the hardness of crystals when two further points have been accepted. First, the angle between the axis of the stress responsible for deforming the crystal and the surface of indentation must be determined. Values of λ and ϕ, for a given orientation, can then be calculated. Secondly, it must be recognized that the available slip planes, unlike those submitted to a unidirectional stress, are not free to rotate about a number of axes governed only by the slip directions in those planes. The indenter facets and the hinterland of material, which is only elastically deformed, will both influence the choice of active slip system. However, there will generally be a tendency for material between these two regions to be displaced, during the indentation process, from within the bulk onto the surface of the crystal, as sketched, for example, in Figure 3.4. Consequently, a slip system which allows rotation about an axis parallel to an indenter facet will be more favorably oriented for slip than one whose axis of rotation is normal to that facet.
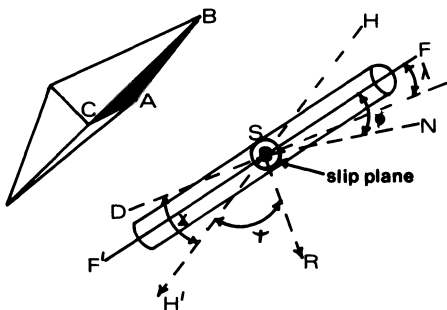
Figure 3.19. Representation of a cylindrical element of material adjoining an indenter facet, in this case ABC. HH′ is an axis drawn parallel to the facet ABC. The direction SN is a slip-plane normal. SD is the slip direction and SR is the axis of rotation. FF′ is the tensile axis. ϕ, λ, ψ, and γ are angles determined by the indenter-to-specimen orientation, which in this case is governed by facet ABC.

Daniels and Dunn in 1949 first proposed a model developed for the Knoop indenter along these principles. They chose a tensile stress axis, FF in Figure 3.19, parallel to the steepest slope of each indenter facet, and then modified equation (3.7) by including a constraint term, $\cos \psi$, to allow for the restricted rotation of slip planes during indentation. The diagram in Figure 3.19 shows the angles λ, ϕ, and ψ for one cylindrical element adjoining a given indenter facet. Initial slip on the primary slip plane—i.e., that subjected to the maximum resolved shear stress—causes that plane to rotate about an axis AR. Daniels and Dunn concluded that the constraint is minimal when the axis of rotation is parallel to the indenter facet—i.e., along the direction HH' in Figure 3.19. In this case, the angle $\psi = 0$ and the constraint term is unity. They further suggested that the constraint is a maximum when $\psi = 90°$ and that there is no slip because rotation of the slip planes cannot occur. Thus, their equation for effective resolved shear stress τ_e was developed:

$$\tau_e = F/A \cos \lambda \cos \phi \cos \psi \qquad (3.8)$$

Clearly, values of F and A cannot be unambiguously defined in a hardness test. Nevertheless, the product of the cosine factors may be used to demonstrate the relative magnitude of resolved shear stresses for indentations in various crystallographic directions on a given crystal plane. An averaging method, described later, was used to obtain mean values τ_e' for the calculations based on the product of the geometric terms in equation (3.8). In essence, the hardness should be inversely proportional to the mean effective resolved shear stress. The correlation between τ_e' and Knoop hardness, for (001), (110), (111) surfaces of iron-3%-silicon-alloy single crystals assuming $\{11\bar{2}\}\langle 111 \rangle$ slip systems, was good.

Later, anomalous results were obtained by Daniels and Dunn for the hexagonal crystal zinc. Modifications to this model were suggested by Feng and Elbaum[31] and Garfinkle and Garlick.[32] Instead of considering a tensile force parallel to the indenter facets as the effective deformation force, these authors preferred to use a compressive force normal to the facets. However, their analysis gave little agreement with experimentally established anisotropy in the hardness of crystals. Furthermore, dislocation etch-pit studies on MgO later demonstrated that slip was obtained under conditions where $\psi = 90°$, which is in direct contradiction to the constraint term in the model.

By developing the constraint term, with particular respect to the displacement of material in the slip direction, Brookes, O'Neill, and Redfern[9] improved the correlation between hardness values and the resolved shear stress calculation. Moreover, they extended the applicability of this approach to the complete range of crystalline solids. They proposed that

the minimum constraint is obtained only where the slip direction and HH′ in Figure 3.19 are coincident and ψ is automatically 90°. If the angle between the slip direction and HH′, designated as γ, exceeds zero degrees, then the slip plane can rotate even though ψ is 90°. On the other hand, the minimum constraint is obtained when the axis of rotation SR and HH′ are coincident; i.e., when γ must always be 90°. Thus the modifying function which reduces the effective resolved shear stress, due to rotational constraint, is $\frac{1}{2}(\cos\psi + \sin\gamma)$. The complete form of the effective resolved shear stress equation is then

$$\tau'_e = \tfrac{1}{2}(F/A) \cos \lambda \cos \phi \,(\cos \psi + \sin \gamma) \qquad (3.9)$$

A computer program can be used to calculate complete resolved shear stress curves, based on equation (3.9), for cubic and hexagonal crystals having the common sets of slip systems noted in Tables 3.1, 3.2, and 3.8. Each facet of the Knoop indenter has to be dealt with separately and complete sets of curves calculated. The mean τ'_e curve is obtained from the mean values of the envelopes (maximum τ'_e values) at each indenter orientation. The inverted form of this curve is shown in Figure 3.20 because those directions having the lowest effective resolved shear stress will be the hardest. Because F and A cannot be unambiguously defined, the product of the cosine factors and the rotational constraint term is used to demonstrate the probable hardness anisotropy of crystals. As was quickly seen, this method, despite its first-order nature, was very good at predicting the form of hardness anisotropy of ionic and covalent ceramic materials as well as metals and alloys. The extent of anisotropy—i.e., the anisotropy factor—was not approachable in this theory.
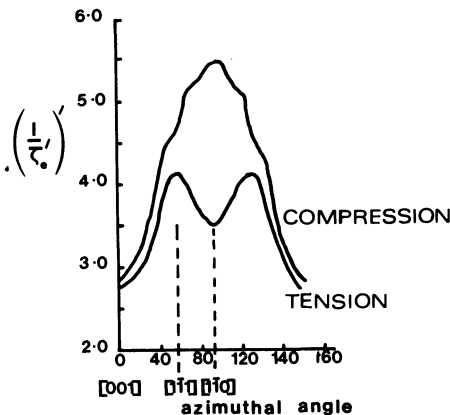
Figure 3.20. Reciprocal of the cosine and rotational constraint terms of equation (3.9)—that is, the effective resolved shear stress—on (110) plane of MgO using either compressive or tensile forces with the slip system {110}⟨1$\bar{1}$0⟩.
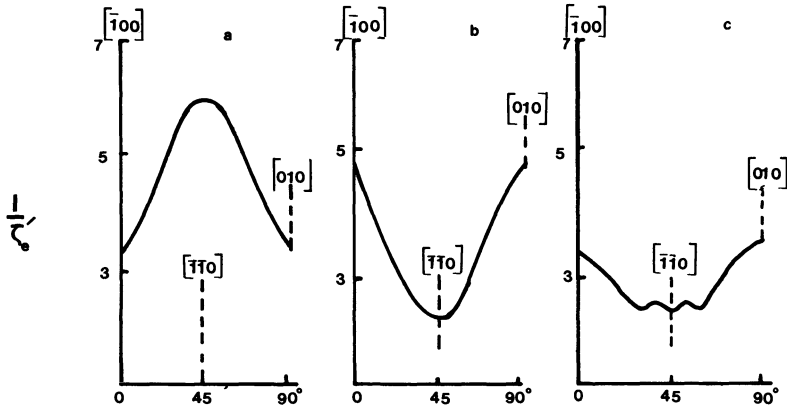
Figure 3.21. Reciprocal mean effective resolved shear stress curves for Knoop indentation calculated for (001) planes of a rock-salt cubic crystal using (a) $\{110\}\langle1\bar{1}0\rangle$, (b) $\{001\}\langle1\bar{1}0\rangle$, (c) $\{111\}\langle1\bar{1}0\rangle$ slip systems.

Comparison of Figure 3.20 with Figure 3.5(b), where hardness anisotropy on a (110) plane of MgO is recorded, verifies that the tensile model reflects the measured anisotropy more closely than the compressive model. However, it should be pointed out that it is generally the case that there is no significant difference in the nature of anisotropy as predicted after choosing either one of these two axes.

The inverse mean effective resolved shear stress curves for a Knoop indenter for common slip systems on low index planes of cubic and hexagonal systems are sketched in Figures 3.21 to 3.27.

Because these curves closely parallel the results obtained in real systems, as shown in Figures 3.5, 3.6, 3.7, 3.8, 3.12, 3.13, 3.14, and 3.15, the types of observed anisotropy in Knoop hardness have been used to study plastic
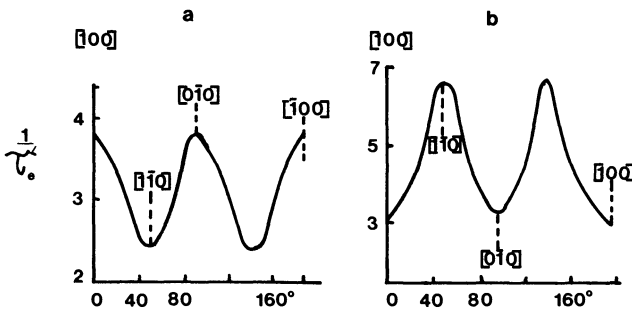
Figure 3.22. Reciprocal mean effective resolved shear stress curves for Knoop indentation calculated for (001) planes of a fluorite cubic crystal for (a) $\{001\}\langle1\bar{1}0\rangle$ and (b) $\{110\}\langle1\bar{1}0\rangle$ slip systems.

[$\bar{1}\bar{1}0$]

$\dfrac{1}{\tau'_e}$
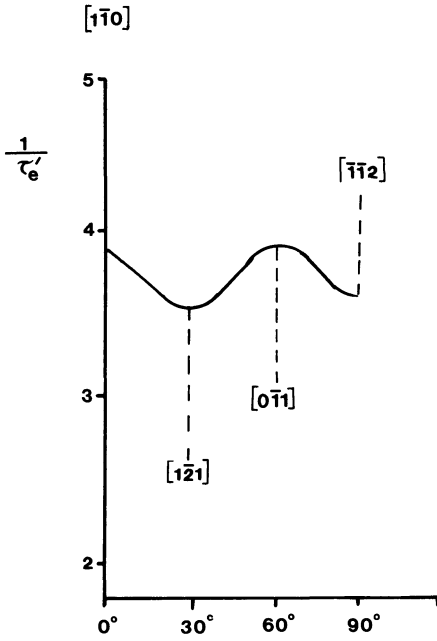
Figure 3.23. Reciprocal mean effective resolved shear stress curves for Knoop indentation calculated for (111) planes of a fluorite cubic crystal for the {110}⟨1$\bar{1}$0⟩ slip system.
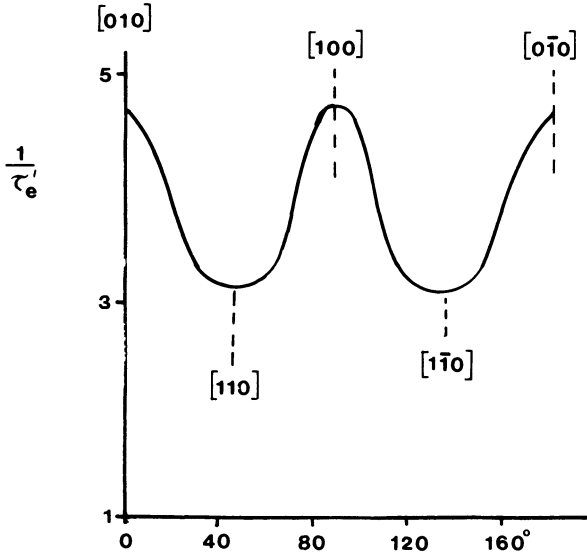
Figure 3.24. Reciprocal mean effective resolved shear stress curves for Knoop indentation calculated for (001) planes of diamond cubic crystals for the {111}⟨1$\bar{1}$0⟩ slip systems.
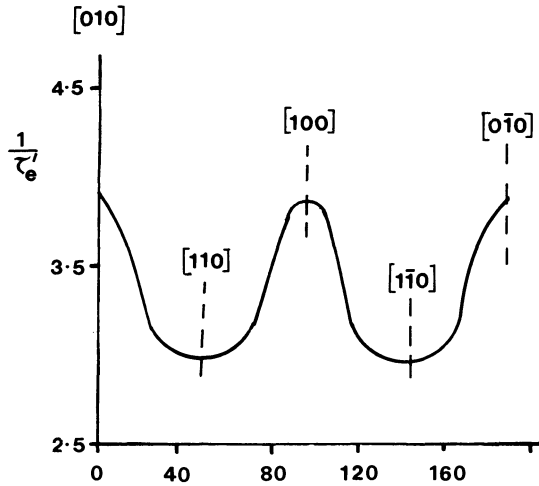
Figure 3.25. Reciprocal mean effective resolved shear stress curves for Knoop indentation calculated for (001) planes of cubic I crystals for $\{110\}\langle 1\bar{1}1 \rangle$ slip systems.

flow and identify operative slip systems in what are largely regarded as brittle materials—i.e., the ceramics. Despite the fact that the mean effective resolved shear stress model makes no attempt to consider anything other than equal resolved shear stresses on different planes, considers only one (i.e., the primary slip system), and ignores work-hardening effects, all the categories of crystal examined by the technique show easily recognizable hardness anisotropy behavior that can be interpreted simply. These observations are responsible for the universal belief that anisotropy in hardness is controlled by mechanisms of bulk plastic deformation in the small volume of subsurface layers between indenter facets and the large mass of elastic material.

The major anomaly occurs not in hard ceramic systems, like those of interest in this book, but within the soft rock-salt halides with $\{110\}\langle 1\bar{1}0 \rangle$ primary slip. Examination of the anomaly, which makes H_K along [100] greater than H_K along [110] for NaCl and KCl, compared to the expected converse for MgO and LiF, etc., has led to a series of different explanations: for example, indentation creep—i.e., a time effect when the indenter is left too long in contact with the surface—or the use of more sophisticated models, involving several slip systems operating simultaneously with extension to include work-hardening effects. However, when this is done the great benefit of simplicity inherent in the ERSS model is lost.

Examination of Figure 3.21 shows that one of the three slip systems can be easily identified from Knoop hardness measurements, namely, the $\{110\}\langle 1\bar{1}0 \rangle$ system, but because in actual practice the anisotropy factors can
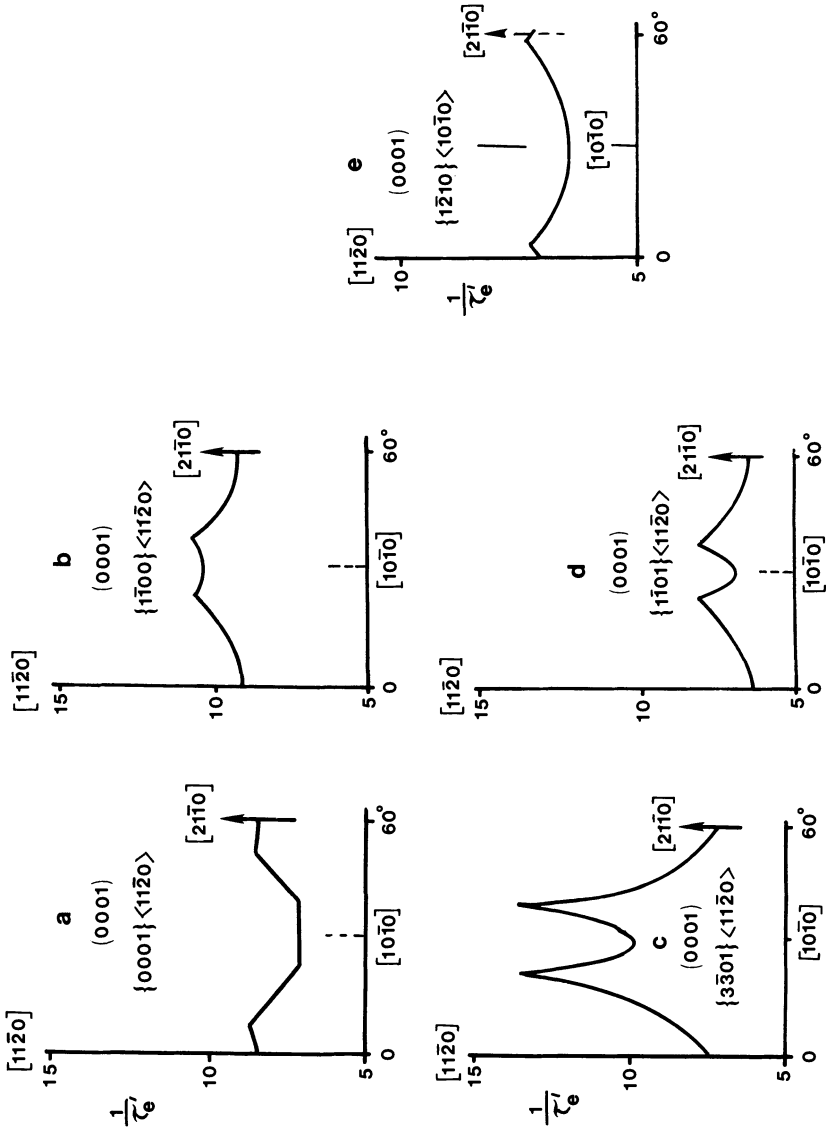
Figure 3.26. Reciprocal mean effective resolved shear stress curves for Knoop indentation calculated for (a) {0001}⟨112̄0⟩, (b) {1̄100}⟨112̄0⟩, (c) {3̄301}⟨112̄0⟩, (d) {1̄101}⟨112̄0⟩, (e) {1̄21̄0}⟨101̄0⟩ slip systems on (0001) planes of hexagonal crystals.
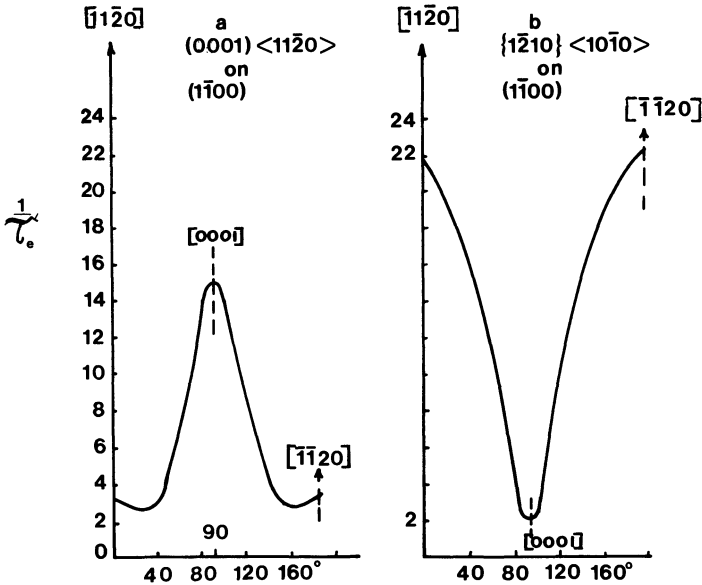
Figure 3.27. Reciprocal mean effective resolved shear stress curves for Knoop indentation calculated for (a) $(0001)\langle 11\bar{2}0\rangle$ and (b) $\{1\bar{2}10\}\langle 10\bar{1}0\rangle$ slip systems on the prismatic $(1\bar{1}00)$ plane of hexagonal crystals.

be quite small and experimental variation large, it may not be possible to distinguish between the $\{001\}\langle 1\bar{1}0\rangle$ and $\{111\}\langle 1\bar{1}0\rangle$ systems shown in that figure. This emphasizes the statement made at the opening of this chapter, that other techniques used in conjunction with hardness greatly help with slip system analysis. Scratch hardness when analyzed by the mean resolved shear stress method is one helpful method, as the anisotropy predictions in Figure 3.28 show.

3.6.1.2. Resolved Shear Stress and Scratch Hardness

Here again, after making very similar sweeping simplifications to those used for the indentation model, it is possible to produce a powerful tool in the analysis of hardness anisotropy and slip-system identification. The following assumptions and simplifications can be compared to those in Section 3.6.1.1.

1. Anisotropy is determined only by the primary slip system.
2. The absolute magnitude of the effective resolved shear stresses need not be known. This is occasioned by the fact that the actual area supporting the applied load cannot be determined unambiguously.
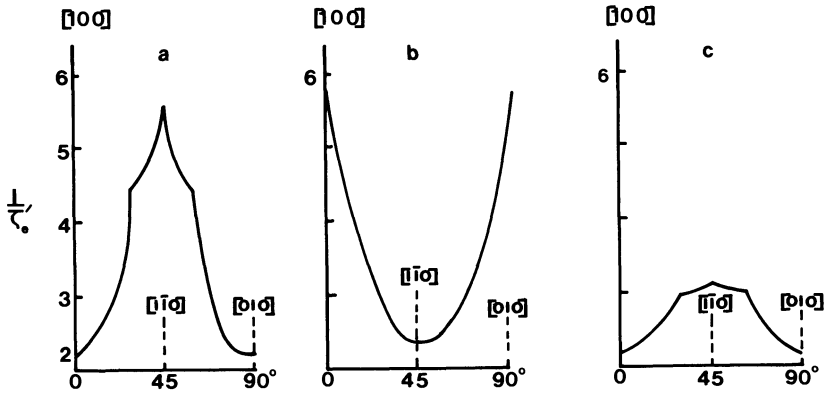
Figure 3.28. Reciprocal mean effective resolved shear stress curves for scratch hardness on a (001) plane of a cubic crystal calculated for (a) {110}⟨1$\bar{1}$0⟩, (b) {001}⟨1$\bar{1}$0⟩, and (c) {111}⟨1$\bar{1}$0⟩.

3. The interaction of displaced material and slider shape is ignored.
4. Work hardening is ignored.
5. The Schmid–Boas equation will give the distribution of the resolved shear stresses as a function of sliding direction.
6. The frictional force F and normal load P can be resolved into a resultant P' inclined at an angle θ to the vertical axis of the slider.
7. Angle θ is related to the coefficient of friction μ through equation (3.6).
8. The axis P' represents the principal compressive axis of stress.
9. Only the resolved shear stresses in a small element of the ceramic in front of the slider and at 90° to the P' axis are considered. This produces a reasonably uniform tensile stress at right angles to the P' axis and lying in the plane of P', P, and F.
10. As slip occurs on the primary system, rotation of the slip plane occurs about an axis at 90° to the slip direction as contained in that plane. Thus it can be seen that the axis of rotation might be parallel to, or at right angles to, the direction of sliding. When the rotation axis is normal to the sliding direction and parallel to the deformed surface, then slip will result in slip steps at right angles to the sliding direction, causing material pile-up in front of the slider. This makes sliding harder and results in a thinner groove, producing a greater measured hardness. Conversely, if the axis of rotation is still parallel to the deformed surface, but now also parallel to the sliding direction, the pile-up of material will be parallel to the groove, making sliding easier and producing a softer direction with respect to hardness. In this way the geometry of the

slip system, the crystallographic plane, and the direction of slip combine to produce a modification in a resolved shear stress.

11. To generalize this situation it is necessary to define an angle ω between the axis of rotation for the slip system of interest and an axis lying in the surface being investigated and normal to the sliding direction on that surface, say, XY.

This leads to an expression for the effective resolved shear stress τ_e:

$$\tau_e = \frac{P''}{A} \cos \phi \cos \lambda \tfrac{1}{2}(1 + \sin \omega) \tag{3.10}$$

In equation (3.10), P'' is the force at 90° to the P' axis, which, as point 9 above states, is tensile; A is the area supporting the force; ϕ is the angle between the direction of P'' and the slip-plane normal; λ is the angle between the P'' direction and the slip direction; and ω is defined above in point 11.

According to equation (3.10), when the axis of rotation of the slip system is parallel to the axis drawn at 90° to the sliding direction that lies in the plane of sliding, i.e., XY, then $\sin \omega = 0$. This produces a decreased penetration and therefore an increased hardness. At $\omega = 90°$ to XY, the slip system rotation axis will be normal to the surface axis XY, the effective resolved shear stress is maximized, leading to a maximum penetration, and this direction will be the softest.

For each angle of sliding relative to XY a value for τ_e from equation (3.10) is calculated for a given slip system, and then the mean effective resolved shear stress τ'_e is found. The reciprocal of τ'_e is a measure of the relative hardness in that particular direction and can be used to model scratch hardness anisotropy. Figure 3.28 compares the mean resolved shear stress curves for three slip systems operating when a (001) plane of a cubic crystal is scratch tested; clearly plastic deformation due to the $\{100\}\langle 0\bar{1}1\rangle$ system can be separated from others by scratch testing in the way that $\{110\}\langle 1\bar{1}0\rangle$ is recognizable in Figure 3.21 by indentation testing.

It is obvious by now that the mismatch of symmetry between the Knoop indenter and $\{111\}$ planes is a weakness when exploring hardness anisotropy of such planes. However, since scratch hardness does not suffer from such a mismatch, the resolved shear stress curves for the (111) plane in cubic crystals with the three commonly found slip systems shown in Figure 3.29 may be useful in anisotropy and slip system investigations. Clearly more detailed anisotropy is predicted but the small anisotropy factors implied in the scale of Figure 3.29 must be remembered. Generally speaking, only the main features of the predicted curves have ever been established and experimental uncertainty makes it unlikely that the fine detail will be found.
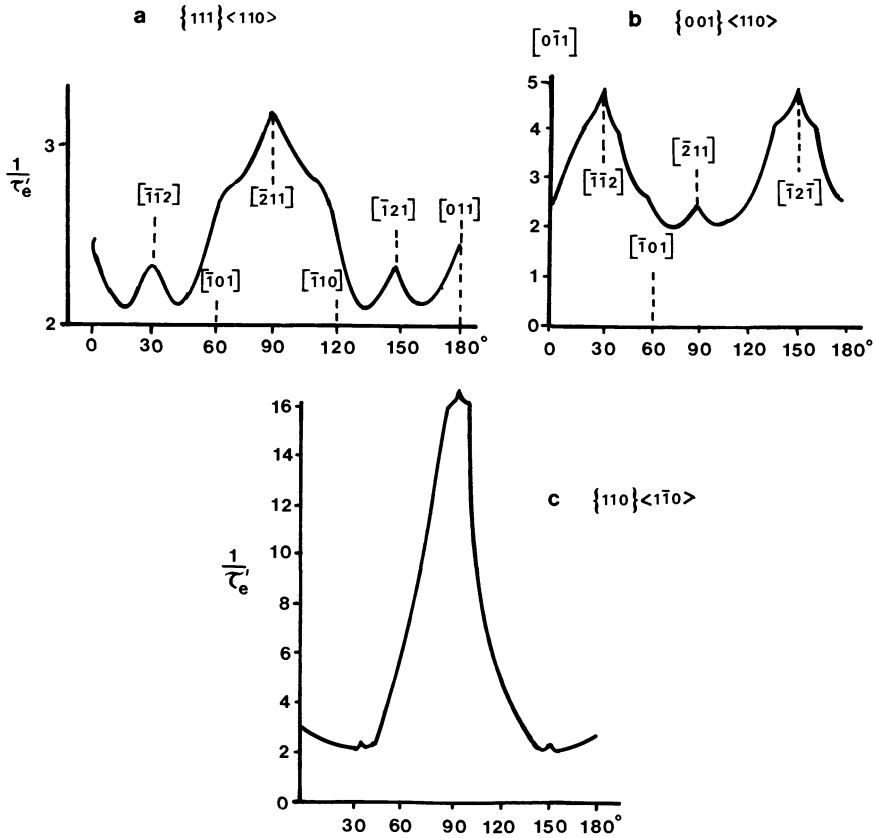
Figure 3.29. Reciprocal mean effective resolved shear stress curves for scratch hardness of a cubic crystal (111) plane calculated for (a) $\{111\}\langle1\bar{1}0\rangle$, (b) $\{001\}\langle1\bar{1}0\rangle$, and (c) $\{110\}\langle1\bar{1}0\rangle$ slip systems.

3.6.1.3. The Effect of Multiple-Slip Systems

The effect ascribed to more than one slip system operating has already been recorded in Table 3.2 where results for TiB_2, ZrB_2, and HfB_2 are listed. In fact the slip systems listed in Table 3.2 for these three borides were derived from a resolved shear stress model analysis by Nakano *et al.*[33] which may of course be making a somewhat circular argument. Using the Brookes equation, (3.9), Nakano *et al.* were able to calculate, as the reciprocal of the angular functions, the values given in Table 3.9, which can be used to establish expected Knoop hardness inequalities such as these for the $(0001)\langle11\bar{2}0\rangle$ slip system operating:

- (0001) plane $H[11\bar{2}0] > H[10\bar{1}0]$
- (0001) plane $H[11\bar{2}0] \gtrsim H[1\bar{2}10]$ on $(10\bar{1}0)$ plane

Table 3.9. Reciprocal τ'_e Values for Two Hexagonal Slip Systems

	Plane indented					
	(0001)		(10$\bar{1}$0)		(11$\bar{2}$0)	
			Knoop long-axis direction			
Slip system	[10$\bar{1}$0]	[11$\bar{2}$0]	[0001]	[1$\bar{2}$10]	[0001]	[1$\bar{1}$00]
(0001)$\langle$11$\bar{2}$0$\rangle$	2.65	3.02	17.39	2.99	15.42	2.69
{10$\bar{1}$0}$\langle$1$\bar{2}$10$\rangle$	18.07	6.39	2.19	44.18	2.63	31.06

- (10$\bar{1}$0) plane $H[0001] > H[1\bar{2}10]$
- (10$\bar{1}$0) plane $H[0001] > H[0001]$ on (11$\bar{2}$0) plane
- (11$\bar{2}$0) plane $H[0001] > H[1\bar{1}00]$
- (11$\bar{2}$0) plane $H[1\bar{1}00] > H[10\bar{1}0]$ on (0001) plane

and these for the {10$\bar{1}$0}$\langle$1$\bar{2}$10$\rangle$ slip system operating:

- (0001) plane $H[10\bar{1}0] > H[11\bar{2}0]$
- (10$\bar{1}$0) plane $H[1\bar{2}10] > H[0001]$
- (10$\bar{1}$0) plane $H[1\bar{2}10] > H[1\bar{1}00]$ on (11$\bar{2}$0) plane
- (11$\bar{2}$0) plane $H[1\bar{1}00] > H[0001]$
- (11$\bar{2}$0) plane $H[0001] > H[0001]$ on (10$\bar{1}$0) plane.

Because the observed hardness values for TiB$_2$ are in accord with the inequalities of the first group and the hardness values of ZrB$_2$ are in accord with the inequalities of the second group, the hardness was assumed to be dominated by the slip system causing such inequalities. HfB$_2$ was not clearly covered by either set of inequalities, leading to the prediction that both sets of slip systems could act in HfB$_2$ depending on the orientation of the long axis of the Knoop diamond.

A closer look at the simple model by which SiC was examined has shown that even though the Brookes model is surprisingly good, it can be tested, and even when it is found satisfactory more than one operating slip system can be detected.[18] Sawyer noted that the rotational constraint term in equation (3.9) is not unique and is one of the simplest that can be chosen to fulfill the requirements that $CF = 1$ when $\psi = 0$ and $CF = 0$ when $\gamma = 0$. Thus the suggestion was made that a variety of constraint terms should be used in equation (3.9) and the anisotropy predictions compared. If the model is unstable in its prediction of anisotropy as the constraint factor changes, it should be applied with caution. Using the constraint factors given in equations (3.11)–(3.13) for some of the possible slip systems in hexagonal crystals operating on a (0001) plane, the stability of the model was shown for basal, {0001}$\langle$11$\bar{2}$0$\rangle$ slip and prismatic, {1$\bar{1}$00}$\langle$11$\bar{2}$0$\rangle$ slip but

not for pyramidal, $\{1\bar{1}01\}\langle11\bar{2}0\rangle$ slip; this is shown in Figure 3.30 where some of Sawyer's calculations are given.

$$\text{Rotational constraint factor (2)} = 0.5[\cos^{0.25}\psi + \sin^{0.25}\gamma] \quad (3.11)$$

$$\text{Rotational constraint factor (3)} = 0.5[\cos^{4}\psi + \sin^{4}\gamma] \quad (3.12)$$

$$\text{Rotational constraint factor (4)} = 0.5[\cos^{4}\psi\,\sin^{0.25}\gamma] \quad (3.13)$$

The important point that can now be made is that if a variety of constraint factors show stable predictions, then any observed experimental deviation in anisotropy pattern can be taken as real and mechanisms to account for the difference can be sought after. In seeking explanations of the deviations already shown in Figure 3.14 it was noted that on prism planes $\{1\bar{1}00\}$ and $\{11\bar{2}0\}$, while the lowest hardness was found with the indenter's long axis parallel to [0001], the maximum hardness was found at some 60° from [0001]. This could not be simulated by any slip system acting in isolation. However, when the two most probable slip systems, $\{1\bar{1}00\}\langle11\bar{2}0\rangle$ and $\{0001\}\langle11\bar{2}0\rangle$, were considered jointly, an approach to the observed anisotropy could be made. The $\{1\bar{1}00\}$ was used as an example which showed that when the indenter was along [0001] the reciprocal f value for $\{1\bar{1}00\}\langle11\bar{2}0\rangle$ slip is low and the value for $\{0001\}\langle11\bar{2}0\rangle$ is slightly higher. Thus $\{1\bar{1}00\}\langle11\bar{2}0\rangle$ appears to be preferred. Since the $1/\tau_e'$ values are nearly equal, the critical resolved shear stress for $\{1\bar{1}00\}$ slip is less than that for
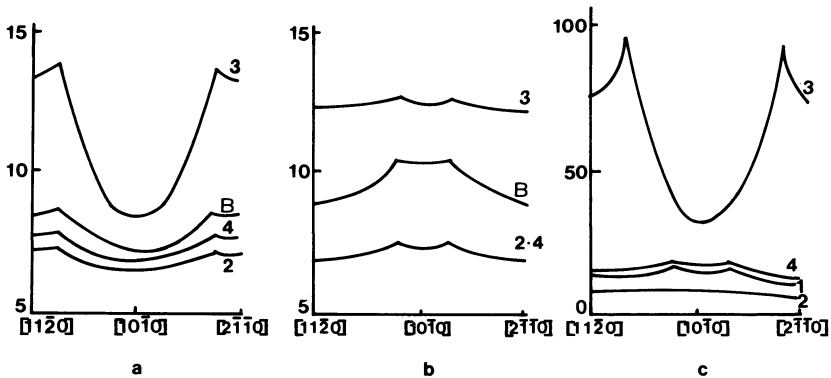
Figure 3.30. $1/\tau_e'$ plot for the (001) plane for the slip systems (a) $\{0001\}\langle11\bar{2}0\rangle$, (b) $\{1\bar{1}00\}\langle11\bar{2}0\rangle$, (c) $\{1\bar{1}01\}\langle11\bar{2}0\rangle$. Lines labelled B, 2, 3, or 4 correspond to the use of constraint factors according to Brookes, equation (3.11), equation (3.12), or equation (3.13), respectively, in equation (3.9) for the calculation of τ_e'. Note the larger scale for (c). The plots in (a) and (b) show the consistency of prediction for (0001) Knoop hardness anisotropy while plots in (c) show inherent instability in the model.

{0001} slip. If this continued to be the case hardness would increase until the indenter lay 80° from [0001]. Thus the decrease in hardness that is observed between 60° and 90° from [0001] implies, since the constraint-factor test is good, that another system must be activated.

Further calculation shows that, for indenter orientations in the neighborhood of [11$\bar{2}$0], the {0001}$\langle$11$\bar{2}$0$\rangle$ slip system has a $1/\tau'_e$ factor around 10 while the $1/\tau'_e$ factor for {1$\bar{1}$00}$\langle$11$\bar{2}$0$\rangle$ slip is about 30; and, since the effective resolved shear stress is proportional to the inverse of these numbers, the {0001}$\langle$11$\bar{2}$0$\rangle$ system feels a much higher stress, which presumably is sufficient to activate it. In this way the controlling slip system changes from {1$\bar{1}$00}$\langle$11$\bar{2}$0$\rangle$ to {0001}$\langle$11$\bar{2}$0$\rangle$ on {1$\bar{1}$00} planes as the indenter is rotated, the changeover occurring around 60° from [0001]. A natural implication of two systems becoming possible around the changeover point is that both will act, and work hardening due to multiple slip may then be responsible for the observed hardness peak, such as that in Figure 3.14(b). Because the two slip systems discussed so far have no intersecting reactions, new glissile dislocations satisfying relationships implicit in equations like those in Section 3.3 have to be formed. Even more recently, as already discussed in Section 3.5.1.2, the hardness data for beryl[22] have been used to postulate tranfer of slip control to three systems consecutively as the indenter orientation from [0001] increases.

These methods are now strongly suggesting a work-hardening function to account for anisotropy peaks as dislocations lock; this feature becomes the dominant one in the most recent developments of hardness anisotropy theory that finally move away from the resolved shear stress models.

3.6.2. Plastic Zone Modeling

The benefits of simplicity inherent in the resolved shear stress models were lost when Hirsch and co-workers,[15] examining the plastic zone beneath (111) and ($\bar{1}\bar{1}\bar{1}$) faces of GaAs indented by a Vickers diamond, carefully sectioned the crystals and found that hemispherical symmetry of the plastic zone is not evident. Hagan has shown the hemispherical symmetry but only for noncrystalline solids. This demonstration pointed to the fact that the plastic zone is anisotropic and the realization that a new model must be developed based on the stresses caused by a straight punch. From such an analysis the hardness is seen to be related to the degree of work hardening in different regions of the plastic zone, in turn leading to an explanation of hardness anisotropy and plastic recovery after indenter withdrawal. At least it does this for diamond-type cubic crystals; other, more complex systems have yet to be tackled.

In choosing GaAs for the original work an extra complication is introduced because it is known that dislocations in III–V compounds have

different mobilities depending on whether the extra half-planes end on rows of group III or group V atoms. Both polarity of hardness and hardness anisotropy are likely to be related to this difference in dislocation velocity and how it is linked to the stress field under the indenter through the possible slip systems. Looking for these links does produce a newer theory of hardness and hardness anisotropy. Thus, by introducing an apparent complication, in the end more experimental confirmation of the model was forthcoming than would have been found had a simpler system been chosen.

The two types of dislocations in GaAs, which are believed to exist and move in the glide configuration, are denoted as follows:

- As(g), when the extra half-plane ends with arsenic atoms on the glide plane.
- Ga(g), when the extra half-plane ends with gallium atoms on the glide plane.

For the family of planes {111}, each of the above dislocations having Burgers vector $\frac{1}{2}\langle 1\bar{1}0\rangle$ has been shown to be dissociated and to glide between the narrowly spaced planes of the volume formed by the {111} family in the zinc blende structure.

Thus it is possible to define with respect to a (111) surface a polyhedron described by the {111} family. It is, in effect, a tetrahedron. However, closer inspection requires the definition of two tetrahedra relative to a direction normal to, say, the (111) plane, which of course would be the direction of indentation if a (111) surface or a $(\bar{1}\bar{1}\bar{1})$ surface was indented. The slip plane tetrahedra are mirror images; i.e., the triangular base of the tetrahedron lies on (111) or $(\bar{1}\bar{1}\bar{1})$ and the apex is then below the surface, or of course the apex can be a (111) or $(\bar{1}\bar{1}\bar{1})$ atom with the triangular base lying beneath the surface. These two glide polyhedra are sketched in Figure 3.31.

In relation to Figure 3.31, the extra half-planes of the dislocations As(g) and Ga(g) can be inside or outside the tetrahedron depending on which tetrahedron they glide on. If the (111) surface, because of the kinked ring structure shown in Figure 3.10, is made up of As atoms, the Ga(g)
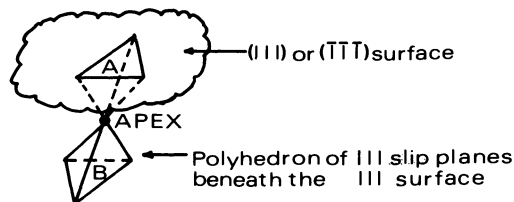
Figure 3.31. Sketch from a (111) surface showing the opposite sense of the two {111} slip tetrahedra. A denotes an internal apex tetrahedron and B an external apex tetrahedron.

dislocations glide on the tetrahedron with the internal apex, A in Figure 3.31, and the extra half plane will be inside tetrahedron A. Conversely, As(g) dislocations will have their extra half plane outside as they glide on tetrahedron B. The argument is reversed if the $(\bar{1}\bar{1}1)$ surface is considered, which must now be a face composed of Ga atoms.

The significance of these two tetrahedra of slip planes, as shown in Figure 3.31, is that relative to an indenter penetrating a {111} face, dislocations can move on slip planes that are converging (tetrahedron A) or diverging (tetrahedron B), or in fact parallel to the surface being indented, since each tetrahedron has a face parallel to that surface. Immediately Hirsch *et al.* were able to suggest tests that might confirm such a situation because Ga and As {111} faces can be detected by their selective etching behavior towards bromine in methanol. Furthermore, a solution of HF and H_2O_2 in water is able to reveal etch-pit rosettes and slip lines in the region of a Vickers indent. Then, by polishing to greater depths below the original surface and re-etching, it was possible to observe all three expected effects:

1. When slip occurred on the internal apex tetrahedron, the successive depths showed a slip line equilateral triangle around the Vickers indent that became smaller.
2. When slip occurred on the diverging tetrahedron, B, the slip line triangle became larger.
3. On the surface, dislocation rosettes appear along ⟨110⟩ directions, which indicates that they are traces of {111} planes.

With such clear evidence of anisotropic behavior within the plastic zone, it was natural to search for a new model that would predict correctly the pattern of slip. Three components in the model are necessary: knowledge of the slip system combinations enabling the indenter to penetrate the surface by plastic flow, knowledge of the shear stresses acting under the indenter, and dislocation mobilities.

Considering the first of these points a little further, the slip systems have to be ones that carry material into the crystal, not up to the surface, and so must have Burgers vectors inclined and parallel to the indentation surface.

The new theory makes use of old established work[34] by ignoring plasticity and modeling elastic stress fields around a long, flat punch of finite width subjected to a uniform pressure. Stresses are calculated with the variables shown in Figure 3.32 and the following equations:

$$\sigma_{xx} = -\frac{P}{2\pi}[2(\phi_1 - \phi_2) + \sin 2\phi_1 - \sin 2\phi_2] \qquad (3.14)$$
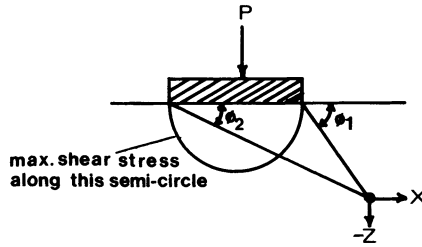
Figure 3.32. Coordinate system for calculation of a stress field from a long flat punch. After Nadai.[34]

$$\sigma_{zz} = -\frac{P}{2\pi} [2(\phi_1 - \phi_2) - \sin 2\phi_1 + \sin 2\phi_2] \tag{3.15}$$

$$\sigma_{xz} = \frac{P}{2\pi} (\cos 2\phi_1 - \cos 2\phi_2) \tag{3.16}$$

$$\sigma_{yy} = \nu(\sigma_{xx} + \sigma_{zz}) \tag{3.17}$$

Equations (3.14)–(3.17) enable the principal stresses in the XZ plane to be found, and these can then be used to calculate the resolved shear stresses along slip planes and Burgers vectors of interest; these are the 12 $\{111\}\langle 1\bar{1}0\rangle$ types. Clearly, the calculation has to be done for various orientations of surface and indenter at a range of depths below the surface. A computer program is essential, and the results appear as a map of systems with the highest resolved shear stresses and contours of these maximum values. A small portion of the mass of work necessary is shown in Figure 3.33 which is taken from one of the papers by Hirsch and his co-workers. General analysis of Figure 3.33 shows that, for a long punch indenter, which
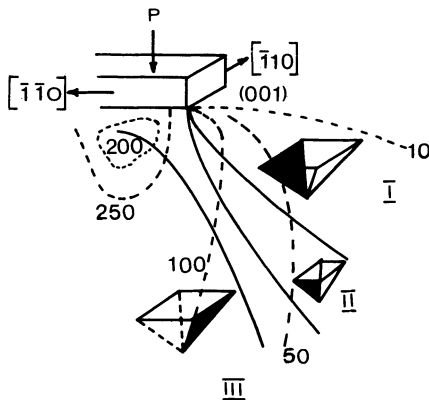
Figure 3.33. Part of a map showing the most highly stressed slip systems beneath and to the sides of a long punch indenter oriented along [110]. The filled faces on the polyhedra are the most highly stressed slip systems in the three regions I, II, and III separated by the solid lines. The arrows indicate the direction of slip showing convergence in III, rosette in II, and divergence in I. Dotted lines with numbers are contours of maximum resolved shear stress. After.[12]

approximates to a Knoop diamond, aligned with its long and short directions along two of the ⟨110⟩ directions on a (001) plane, three distinct areas are denoted:

1. Directly beneath the indenter, slip polyhedra shown as type A in Figure 3.31 are active and slip is converging.
2. Outside the volume covered by the indenter, the slip is diverging with the extra half-planes above the slip plane. It should be noted here that the diagram shown in Figure 3.33 is for an indentation into a (001) plane, not a (111) plane as shown in Figure 3.31, and so the inverted slip tetrahedron, B, is not obvious. To make the point more clearly, the diagram of indentation of a (111) surface is shown as Figure 3.34.
3. In a narrow zone separating 1 and 2 above, slip parallel to the surface is favored; this is known as rosette slip.

It can be seen that these predictions are in accord with the observations of the slip lines and are therefore encouraging. However, when the relative values of the resolved shear stress contour lines are considered as a function of azimuthal angle there appears to be only a slight dependence on orientation and so no reason to distinguish between, say, [010] and [110]. Thus, to explain hardness anisotropy on this model, the work-hardening behavior of the slip patterns rather than the stresses on the slip system have to be invoked. This is where the model is substantially different, because up to this point resolved shear stress considerations and calculations have been used. As Figure 3.33 shows, the near surface slip away from the indenter is divergent and into the crystal, while the slip beneath the indenter is into the crystal and convergent. A diagram for the [010] orientation would show the same convergent slip beneath the indenter, but slip away from the indenter is all of the parallel rosette type. Thus anisotropy between these
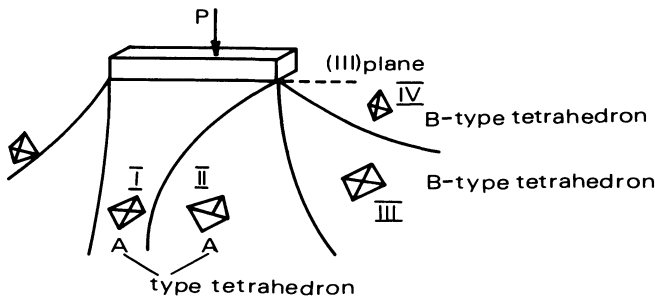
Figure 3.34. Sketch map of slip systems under and around a long punch indenter on a (111) plane aligned along the [211] direction. In region I the slip planes and directions are $(11\bar{1})[\bar{1}0\bar{1}]$, $(1\bar{1}1)[\bar{1}\bar{1}0]$; in region II $(11\bar{1})[0\bar{1}\bar{1}]$, $(1\bar{1}1)[0\bar{1}\bar{1}]$; in region III $(111)[\bar{1}01]$, $(111)[\bar{1}10]$; and in region IV $(11\bar{1})[\bar{1}10]$, $(1\bar{1}1)[\bar{1}01]$.
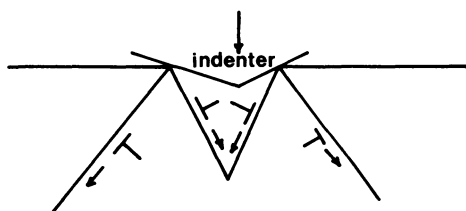
Figure 3.35. Simplified model showing dislocations moving on diverging and converging slip planes beneath an indenter.

two directions must arise from the slip outside the indenter volume. When the indenter is along the $\langle 110 \rangle$ directions, the hardness is lower, at least when the temperature is raised sufficiently to reveal the anisotropy, because of the greater slip activity on the low work-hardening diverging slip systems.

The dominant role in anisotropy played by the divergent slip systems in the near-punch regions is supported by the fact that there is a predictable [110]:[110] asymmetry of hardness in GaAs. Using the simplified model of flow shown in Figure 3.35 and the fact that As(g) and Ga(g) dislocations have different velocities, the following interpretation arises. The dislocations along the intersecting, converging slip planes are of opposite type to those on the diverging planes. Thus the orientation where the faster dislocation type moves on the diverging planes will move material more effectively, and so the Knoop hardness will be low. When the indenter is now put at 90° to this orientation the fast type of dislocation will move on the converging planes, leading to greater dislocation interaction, and the slower dislocations will not move material so efficiently on the diverging planes. Hence in this orientation both mechanisms will lead to high Knoop hardness.

So far all experimental observations on the diamond cubic solids GaAs, Ge, and Si are in agreement with the predictions of this model.

REFERENCES

1. A. H. Cottrell, *Dislocations and Plastic Flow in Crystals*, Oxford University Press, Oxford (1965).
2. R. W. Armstrong and C. C. Way, *J. Amer. Ceram. Soc.* **61**, 102 (1978).
3. A. S. Keh, *J. Appl. Phys.* **31**, 1538 (1960).
4. K. C. Yoo, R. G. Rosemeier, W. L. Elban, and R. W. Armstrong, *J. Mater. Sci. Letters* **3**, 560 (1984).
5. I. J. McColm and S. J. Wilson, *J. Solid State Chem.* **26**, 223 (1978).
6. A. S. Keh, *J. Appl. Phys.* **31**, 1538 (1960).
7. A. H. Cottrell, *Trans. AIME* **212**, 192 (1958).
8. A. P. Gerk, *J. Mater. Sci.* **12**, 735 (1977).
9. C. A. Brookes, J. B. O'Neill, and B. A. W. Redfern, *Proc. Roy. Soc.* **A322**, 73 (1971).
10. D. Brasen, *J. Mater. Sci.* **11**, 791 (1976).
11. C. A. Brookes, R. M. Hooper, and W. A. Lambert, *Phil. Mag.* **A47**, L9 (1983).
12. S. G. Roberts, P. D. Warren, and P. B. Hirsch, *J. Mater. Res.* **1**, 162 (1986).

13. H. C. Gatos and M. C. Lavine, in *Progress in Semiconductors* **9**, 1, A. P. Gibson and R. E. Burgers, eds., Heywood, New York (1965).
14. K. Maeda, O. Ueda, Y. Murayama, and K. Sakamoto, *J. Phys. Chem. Solids* **38**, 1173 (1977).
15. P. B. Hirsch, P. Pirouz, S. G. Roberts, and P. D. Warren, *Phil. Mag.* B**52**, 759 (1985).
16. Y. S. Boyarskaya, D. Z. Grabko, and E. I. Purich, *J. Mater. Sci. Letters.* **14**, 737 (1979).
17. J. Thery, *Mater. Res. Bull.* **18**, 481 (1983).
18. G. R. Sawyer, P. M. Sargent, and T. F. Page, *J. Mater. Sci.* **15**, 1001 (1980).
19. T. Tsuya, *J. Nucl. Mat.* **22**, 148 (1967).
20. K. Nakano, H. Matsubara, and T. Imura, *J. Less Common Metals* **47**, 259 (1976).
21. F. W. Vahldiek and S. A. Mersol, *J. Less Comm. Metals* **55**, 265 (1977).
22. O. O. Adewoye and J. I. Agu, *J. Mater. Sci. Letters* **6**, 953 (1987).
23. A. M. Lejus, D. Ballutaud, C. R'Kha, and J. Livage, *Mater. Res. Bull.* **15**, 95 (1980).
24. S. A. Mersol, F. W. Vahldiek, and C. T. Lynch, *Trans. Met. Soc. AIME* **233**, 1658 (1965).
25. F. W. Vahldiek and S. A. Mersol, *J. Less Common Metals* **15**, 165 (1968).
26. Y. Kumashiro and E. Sakuma, *J. Mater. Sci. Letters* **15**, 1321 (1980).
27. S. B. Wen and H. K. Liu, *J. Mater. Sci. Letters* **6**, 1057 (1987).
28. S. Okada, T. Atoda, I. Higashi, and Y. Takobushi, *J. Mater. Sci.* **22**, 2993 (1987).
29. C. A. Brookes, in *Science of Hard Materials*, R. K. Viswanadham, D. J. Rowcliffe, and J. Gurland, eds., Plenum, New York (1983).
30. C. A. Brookes and P. Green, *Proc. Roy. Soc.* **A368**, 37 (1979).
31. C. Feng and C. Elbaum, *Trans. Met. Soc. AIME* **212**, 47 (1958).
32. M. Garfinkle and R. G. Garlick, *Trans. Met. Soc. AIME* **242**, 809 (1968).
33. K. Nakano, T. Imura, and S. Takeuchi, *Jap. J. Appl. Phys.* **12**, 186 (1973).
34. A. Nadai, *Plasticity*, McGraw-Hill, New York (1931), p. 247.

Applied Load, Environment, and Time as External Determinants of Ceramic Hardness

4.1. INDENTATION SIZE EFFECT

In Chapter 1 applied load and sample grain size were highlighted as two variables affecting the determination of "absolute" hardness values for ceramic materials; Figures 1.2 and 1.3 emphasize the point. The load variation of hardness is better called the *indentation size effect*, ISE, because this emphasizes the volume dependence of hardness when this property is determined by a pyramidal indenter.

Clearly all indents made with a pyramidal indenter should have the same shape regardless of their size. Thus, since we take pressure used to make this shape to be a measure of hardness—see equations (1.6) and (1.7)—we would expect hardness to be the same and there to be no load effect. Therefore when hardness increases as the applied load decreases, as shown in Figure 1.3, it must be because the volume of material used to yield is smaller and the mechanism for yielding is dependent on a volume term which becomes more significant as the indent size decreases. The most obvious development of this idea is that the shallow near-surface volume of the deformation zone can become a significant fraction of the total affected volume when a very small load is used to make the indent. Thus, work hardened layers, surface compressed layers, ion-implanted layers, and the possibility of chemical reactions between the atmosphere and the surface can dominate the yielding mechanism to produce nonstandard hardness values. Conversely we can say that these phenomena could be studied by measuring the ISE of a ceramic.

However, it is not simple to use ISE as a probe, unless large single-crystal material is available, because microstructure, and in particular grain-

size effects, can overlay and produce a multivariable dependence. Several investigations have shown a dependence of hardness on grain size like that shown in equation (4.1) when grains are very large compared to indent size

$$H_x = \frac{K}{d^{1/2}} \qquad (4.1)$$

In equation (4.1) K is a constant and d is the grain diameter.

The relationship in equation (4.1) has a familiar form, being the same as the Hall–Petch relationship for fracture stress or yield stress–grain size dependence. Through this connection the dominance of flow mechanisms in establishing hardness values is once again emphasized.

However, not all work shows the simple relationship of equation (4.1), but when examined more closely, those investigations that do not follow equation (4.1) usually involve tests where the indent size and the grain size are comparable, and grain boundaries may then be important. Since the ISE exists in correctly chosen grain-size–indent-size regimes, we can accept that hardness increases as the load decreases, which means that from equations (1.6) and (1.7) there will be more complex relationships among applied load, hardness, and grain size.

As yet the real origins of the ISE have not been quantitatively modelled, but a general power law, like that in equation (4.2), is used to express the relationship between applied load and indentation diagonal

$$P = K_L a^n \qquad (4.2)$$

Equation (4.2) is sometimes called Meyer's law or the log–index relationship. The material constant K_L is the load required to make an indentation of 1×10^{-6} m. Since all sensible hardness determinations involve indentations larger than $1\ \mu$m, then K_L is usually an extrapolated material parameter, useful for comparisons but having only limited physical significance.

It is the value of n in equation (4.2) that is used to express a measure of the ISE of a material. Equation (1.6) gives the relationship of Vickers hardness to load, and for there to be no dependence of hardness on indentation size, n in equation (4.2) must equal 2. When hardness changes as the half diagonal a decreases, then clearly the relationship between P and a is not simple and n will not equal 2. Deviations from $n = 2.0$ are then a measure of the ISE effect and for a given ceramic, variations in n will be a measure of microstructural variations, surface layers, surface chemistry, or mechanochemical effects.

It is not easy to examine equation (4.2) numerically, so it is usually expressed as equation (4.3)

$$\ln P = \ln K_L + n \ln a \qquad (4.3)$$

Thus corresponding values of $\ln P$ and $\ln a$ are plotted and a straight line is fitted to the data from the slope of which n can be found.

If a single crystal or a polycrystalline sample with large grain sizes such that indent sizes are always small relative to the grain size, is used to determine n from equation (4.3), a straight line will result in a plot of $\ln P$ versus $\ln a$. When a microstructure exists with grain sizes smaller than the indent impressions, so that the yielded volume sweeps through several boundaries, a second line will be apparent in the plot which will produce a different intercept value, that is a different K_L, because the grain boundaries are influencing the yield stresses. The slopes can be so similar for these two lines that experimental methods do not easily reveal the difference. However, between two particular load values there will be a nonlinear transformation, as Figure 4.1 shows. It is the transition effect and the different K_L values so produced that highlight a microstructural and, in particular, a grain-size effect in ceramic microhardness measurements.

Careful plots of the type shown in Figure 4.1 can be used to estimate grain sizes in ceramic samples as well as make investigators aware of when microstructure is playing a dominant role in determining hardness values.

An early study[1] involving MgO showed how important it is to establish good statistical procedures in this work so that the ISE effect can be properly unraveled from microstructural effects; the analyses developed allow n versus $\ln K_L$ plots to be made. Such plots can be used diagnostically to compare different forms of ceramic materials, and therefore the concepts leading to their development are outlined here.

Using one load, P_i, to make n indentations on the same sample, it is possible to look at the distribution of the measured indentation diagonals a_i. Experience shows that the experimental variation is close to a Gaussian distribution. This fact justifies the use of a least-squares fit for $\ln a$ versus $\ln P$ data and equation (4.4) will be a minimum for the best fit line.
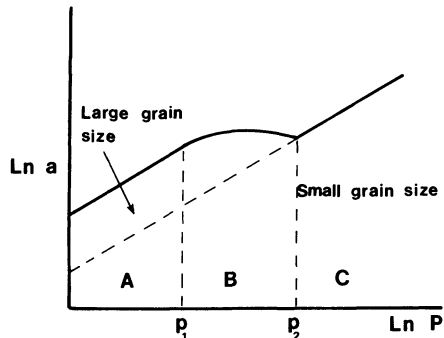
Figure 4.1. Plot of $\ln a$ versus $\ln P$ showing transition zone B where grain size and indent size are comparable.

$$s' = \sum_{i=1} [\ln a_i - \ln \bar{a}_i] \tag{4.4}$$

In equation (4.4) $\bar{a}_i$ is the mean of the indent half diagonal sizes.
    From equation (4.3) we can write

$$\ln \bar{a}_i = -\frac{\ln K_L}{n} + \frac{\ln P_i}{n}$$

which is written in a shorter form as

$$\ln \bar{a}_i = A + B \ln P_i \tag{4.5}$$

Now s' in equation (4.4) is minimized with respect to A and B by differentiating and setting equal to zero

$$\frac{\partial s'}{\partial A} = 0 \tag{4.6}$$

and

$$\frac{\partial s'}{\partial B} = 0 \tag{4.7}$$

    The solution of the simultaneous equations (4.6) and (4.7) provides the best-fit values of $-\ln K_L/n$ and $1/n$. Variances and covariances can also be calculated which set the shape and inclination of the confidence ellipses drawn in Figure 4.2. Ellipse size is taken to include two standard deviations.
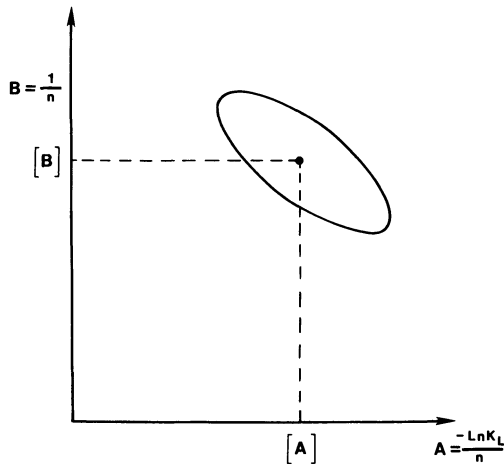
Figure 4.2. Variance, covariance, and confidence ellipse for an [A], [B] value of equation (4.5).

Because A and B are, respectively, $-\ln K_L/n$ and $1/n$, the ellipses can be transformed into ellipsoids by plotting n against $\ln K_L$ and when this is done a feature of the plots is the wide separation of the ellipsoids for different materials, while for any one material, microstructural variations show up as smaller separations. These trends are demonstrated in Figure 4.3, taken from reference (1), where it can be seen that such plots are useful for characterizing unknown samples of ceramics by using the hardness indentation technique alone.

The ellipsoids in Figure 4.3 show the effect of bonding on strength because $\ln K_L$ can be taken as a relative measure of absolute hardness and lower values are found in the order SiC, Si_3N_4, MgO, and LiF. These features are discussed under the relevant section dealing with these materials in Chapter 6.

It is particularly noticeable that when indents are made that are approximately the same size as the grain size in a ceramic such as MgO, then the material hardens as the grain size is increased. This is in contrast to the trend for metallic systems, from which equation (4.1) was obtained. The probable explanation for this weakening effect of the grain boundaries in ionic ceramic oxides is the sharp contrast between ionic bond strength and grain-boundary cohesive forces compared to the similarity between weak metallic bonds and metal grain-boundary forces. Thus in ceramics the yielded volume sweeping through several grain boundaries encounters less resistance relative to the situation in metallic systems.

It is this example, taken from magnesia, and the way it contrasts with the general behavior of metallic systems in its ISE properties, that shows
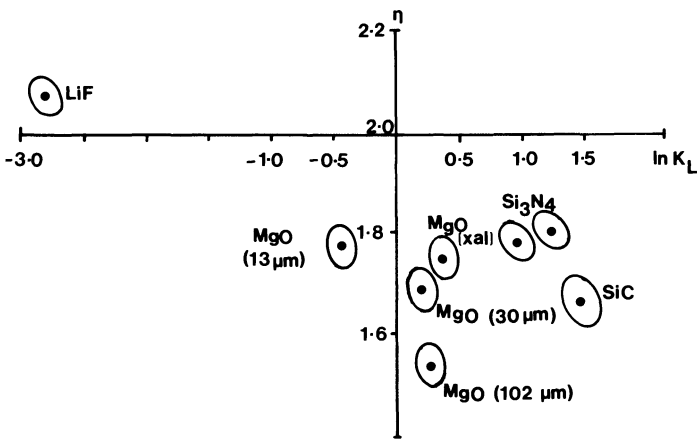
Figure 4.3. Confidence ellipsoids for some ceramics. The grain size effect is shown for MgO where the MgO becomes softer with decreasing grain size, shown in brackets in μm alongside the ellipses.

us that microstructural effects must be removed or standardized before using a simple comparison of ISE indices to draw conclusions about ceramic systems. However, the following general relationships hold for the *low-load* hardness region, as defined in Figure 1.3:

- $n < 2$ the measured hardness will increase as the applied load is decreased;
- $n = 2$ hardness is constant with load;
- $n > 2$ measured hardness decreases as the load decreases.

4.1.1. Indentation Size Effect and Surface Layers

Since 1973 evidence has been accumulating for machining-associated plastic flow in ceramics which can result in work-hardened surface layers. Such layers decrease in depth with increasing bulk hardness of the ceramic and so small loads will be necessary to reveal their presence by the hardness technique. Table 4.1 gives early data underlining this effect in rutile and Table 6.18 contains K_{IC} values measured by the hardness method using equation (5.48) as a function of depth below the surface by using a range of loads with a Vickers indenter in conjunction with a careful polishing technique.

The depth of material removed from a surface is obtained from the geometry of a Vickers indent via equation (4.8)

$$d = 0.286(a_1 - a_2) \qquad (4.8)$$

In equation (4.8), d is the depth of surface removed by a polishing operation and a_1 and a_2 are the Vickers indent impression half diagonals before and after polishing the surface. Data in Table 6.10 are very recent and suggest that toughness can be four times greater at the surface of sialon after it is bombarded with fine-grained Al_2O_3 particles.

Table 4.1. Surface Hardening of Rutile Caused by Machining and Revealed through the Hardness Technique[a]

Treatment of {100} surface	Knoop hardness ($GN\,m^{-2}$)		
	Load 0.98 N	Load 1.96 N	Load 4.90 N
Diamond ground	12.66 ± 0.59	9.32 ± 0.39	9.41 ± 0.29
Sanded (240 SiC grit)	11.38 ± 0.29	8.92 ± 0.20	9.61 ± 0.25
Gas polished	8.83 ± 0.29	8.83 ± 0.34	8.53 ± 0.20

[a] After Becher.[2]

It follows from this that there will be a need to consider theoretically how a composite effect of surface layer with hardness H_1 on a substrate with hardness H_2 will affect the ISE and in particular the exponent n. A simple approach is developed later in this chapter.

Surface alloying can be effected in glasses and ceramics which, if the general picture seen for most materials and particularly for metals is followed, will result in increases in hardness as solute solid is added to solvent solid. However, there is evidence being accumulated even in the field of metals that alloying additions can cause softening. The explanation of these contrasting effects is a source of controversy and two kinds of explanation dominate. In one kind, extrinsic explanations, attempts are made to adhere to wholly dislocation-based mechanisms where the scavenging effect of the solute are said to alter the number, strength, and distribution of obstacles to dislocation movement. In the other kind, intrinsic explanations, the phenomenon is related to the intrinsic property of electronic structure, changes in which lead to electronic band structure changes which strengthen or diminish the filled bonding levels. This represents an alternative to the dominant dislocation theories and should be considered further, not least for the relatively simple picture that is presented. Because such a range of bond types is encountered in ceramics, particularly in the area of special ceramics, the intrinsic explanation is developed in the relevant results sections where some Vickers and some pendulum hardness results for carbides do show a solid solution softening effect, and an electronic bond structure explanation seems simple and adequate. In approaches like those referred to above hardness is plotted against a function containing a statement of electron orbitals such as equation (4.9)

$$\Omega = c^{1/2}\Delta V \qquad (4.9)$$

In equation (4.9) c = concentration of the alloying material in mol% and ΔV = difference in numbers of outer s and d electrons between solute and solvent.

As Figure 4.4 shows, a hardness minimum occurs at a critical electron concentration in those cases where solid solution softening occurs, and simple relationships can be developed to predict the softening effect

$$\Delta H_V = s_1\Omega_t \qquad (4.10)$$

In equation (4.10)

$$\Omega_t = \frac{c_1\Delta V_1 + c_2\Delta V_2}{(c_1 + c_2)^{1/2}}$$
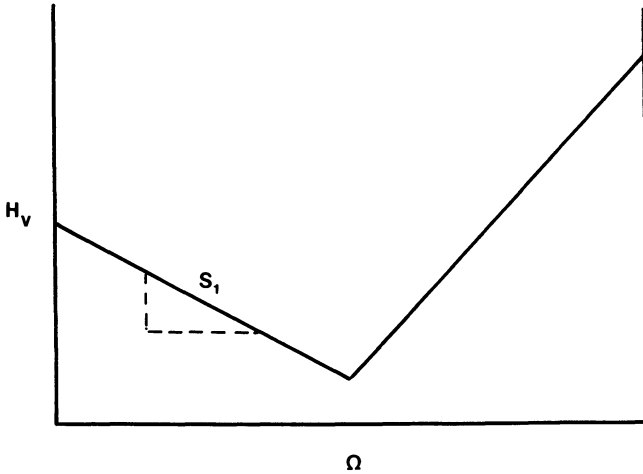
Figure 4.4. Schematic representation of solid solution softening versus an intrinsic electronic effect. After Gypen and Deruyttere.[3]

ΔH_V is the softening decrement and s_1 is the slope of the line. By using the ideas inherent in equations (4.9) and (4.10) one is applying the hardness technique to investigate chemical bonding of ceramic systems and the ISE to probe the nature of alloyed and enameled surfaces.

In more recent times, with the use of ion beams to clean the surfaces of ceramic substrates, implantation of ions into the surfaces has been brought about with consequent changes in the mechanical properties of such surfaces, and this can be probed in a nondestructive way by using the ISE following the development of a model such as that which follows.

Ceramics such as silicon and α-Al_2O_3 have been examined in recent studies because of their application as semiconductor and substrate materials and the fact that ion beam thinning and surface cleaning is often used. Ion beams consisting of Y^+ and N_2^+ have been used to change the surface properties.[4] In such an operation the sequence shown in Figure 4.5 occurs as the positive ion content builds up.

As the scheme in Figure 4.5 shows, contrasting effects are simultaneously produced. The induced stress is a biaxial compression which obviously works against the "pop-in" of lateral cracks, as described in Section 5.2(a), and diminishes the radial crack traces, Section 5.2.1. Both these events imply an increased K_{IC} value for the surface layer.

Immediately on bombardment, hardness will rise as a result of the compressive stress; simultaneously, an amorphous state begins to form and grow inwards from the surface. As the amorphous layer begins to predominate, a decrease in hardness occurs and barreling, Figure 2.8, around the indent begins to appear due to material pile-up. The change from hardening

Ions $\left(Y^+, N_2^+\right)$ + Substrate surface

Amorphous layer   Induced compressive stress

(a) Decreased hardness (changed ISE)   (a) K_{IC} changes

(b) Increased surface plasticity   (b) Fracture pattern around

                                                 indent changes
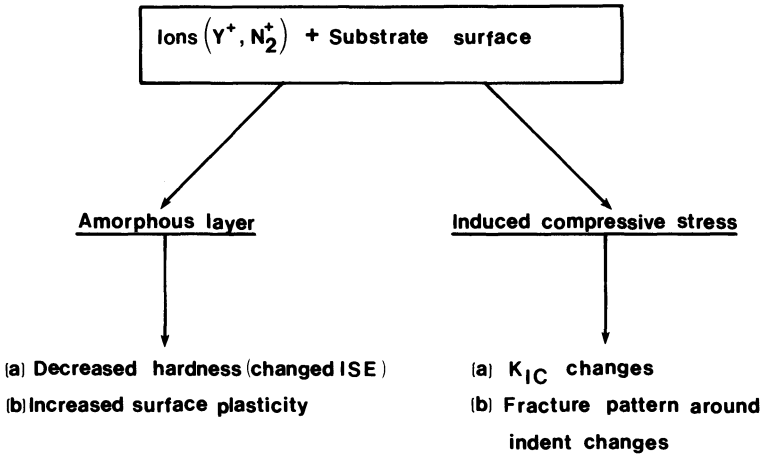
Figure 4.5. Sequence of events in ion-bombarded ceramic surfaces.

to softening is time dependent and can be affected by solid solution formation when metal cations are used for bombardment. As already stated, solid solution formation can promote hardening or softening depending upon the electronic structure of the substrate. Changes in toughness are shown in the results in Table 4.2, which were obtained using equation (5.40) to determine toughness. Toughness increases and the magnitude of the effect increases at lower loads as less of the unaffected substrate is involved in the indentation process. Results such as these show that the low-load hardness of the ion-implanted material is less than the low-load hardness of the conventionally prepared material with the hardness values converging at higher loads. Silicon, for example, has a strong ISE with $n = 1.7$, and the presence of a softer surface layer will produce a *smaller increase* in hardness as the load decreases until eventually specimens with thicker

Table 4.2. Toughness of Silicon and α-Al_2O_3 Before and After Ion-Beam Treatment[a]

	K_{IC} (MPa m$^{1/2}$)		
Material	1.96 N	4.9 N	9.81 N
Si	0.744	0.886	—
Si (Al^+ bombardment)	0.961	1.041	—
Al_2O_3	1.081	—	1.696
Al_2O_3 (Y^+ bombardment)	1.451	—	1.530

[a] After reference (4).

amorphous layers will show a softening in absolute terms. The implication is that the amorphous layer will have an ISE with $n = 2$, which is not unreasonable for a highly defective structureless layer with low yield stress. How the ISE index, n, varies in such a composite needs further consideration because the model of Mathewson[5] of composite layers of 2-mm thickness subjected to large loads through a spherical indenter does not provide a solution. Burnett and Page[6] have provided an empirical solution based on the simple law of mixtures because stress distributions are not known; Figure 4.6 shows the model used.

From Figure 4.6 a simple law of mixture gives

$$H_V^* = \frac{H_{V_1} V_1 + H_{V_2} V_2}{V_1 + V_2} \tag{4.11}$$

where H_V^* is the effective hardness. Assuming H_{V_1} and H_{V_2} are constant, equation (4.11) is reasonable. However, as V_1 and V_2 change with layer growth or with change in load on the indenter, there will be an obvious hardening ISE as V_1 decreases.

From equations (4.2) and (1.6) we can write

$$H_{V_1} = ka^{n-2}$$
$$H_{V_2} = ka^{n'-2} \tag{4.12}$$

and, using these expressions in equation (4.11),

$$H_V^* = \frac{ka^{n-2} V_1 + ka^{n'-2} V_2}{V_1 + V_2} \tag{4.13}$$

Equation (4.13) produces the observed experimental effect of H_V^* rising slightly for small indentation diagonal lengths before falling as the indent diagonal increases. Better agreement with observed hardness versus film thickness curves is achieved when $H_{V_1} V_1$ is replaced by $ka^{n-2} V_1^2 / V_1 + V_2$ in order to emphasize the substrate hardness.
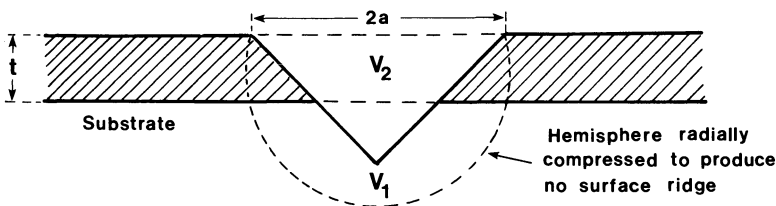
Figure 4.6. Model used to determine ISE for an amorphous layer growing on a hard substrate.
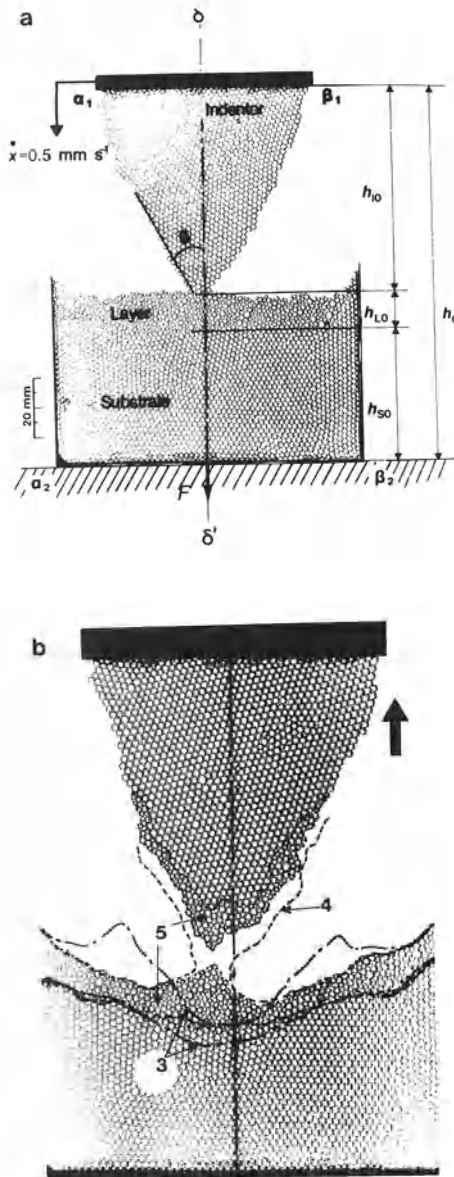
Figure 4.7. (a) The two-dimensional bubble raft model of the indentation process. (b)The amorphous layer disrupted and sticking to the indenter face. Taken from reference (7).

Assuming in the case of ion-bombarded silicon that $n = 2$, and for the substrate $H = 13$ GPa, and $n' = 1.7$, good agreement with the experimental curves is obtained if the hardness of the amorphous layer is taken to be 5.89 GPa. This is an interesting application of the indentation size effect that will stand further development since it provides information on very thin surface layers on semiconductor materials. However, there may be adhesion problems as a fascinating model of the indentation process using bubble rafts shows. This model appeared in *Nature*,[7] and not only does it provide a moving picture of the indentation process but it shows that when a crystalline substrate is coated with a softer amorphous layer, adhesion of the layer to the indenter and its subsequent rupture may be a problem. Using soap solution and capillaries to blow bubbles, a two-dimensional model of a crystalline indenter and substrate can be made in which the indenter face angle can be varied. When using a 60/40 ratio of the two capillaries, an amorphous layer can be produced on the substrate surface, as in Figure 4.7(a). Slowly moving the indenter into the substrate raft causes considerable plastic flow in the amorphous layer, but the substrate does not visibly yield until only a very small thickness of amorphous material lies under the tip of the indenter. It was noted that however deep the indentation was, the amorphous layer was never penetrated. On removal of the indenter raft the indenter tip has an adherent layer of the amorphous material, as shown in Figure 4.7(b). This is a significant demonstration.

Table 4.3. ISE Index Values for Knoop Hardness Measurements on Single Crystals

Crystal	Plane	Direction	Temperature (°C)	n
Si	(111)	[110]	25	1.54
			100	1.73
			200	1.80
			300	1.82
			400	1.83
MgO	(001)	[100]	25	1.85
		[110]	25	1.87
	(110)	[001]	25	1.96
		[1$\bar{1}$0]	25·	1.92
		[111]	25	1.81
Diamond	(001)	[110]	25	1.61
		[110]	25	1.49
TiB$_2$	(10$\bar{1}$0)	[$\bar{1}$2$\bar{1}$0]	25	1.69
Al$_2$O$_3$	(0001)	[10$\bar{1}$0]	25	1.80
	(11$\bar{2}$0)	[0001]	25	1.88
	(1$\bar{1}$00)	[0001]	25	1.87
	(1$\bar{1}$00)	[11$\bar{2}$0]	25	1.72

Several experiments with this bubble model confirmed the fact that the constraint factor, described in Section 1.4.1.1, is dependent on the angle at the indenter tip. By measuring the force transmitted to the frame at the bottom of the substrate raft, the tensile stress generated on indenter removal, and the rate at which these stresses decayed, were monitored and were shown to follow the theoretical paths calculated for the indentation process in Section 5.2.

4.1.2. Indentation Size Effect and Temperature and Orientation

In the case of ceramic materials, because they are generally hard, when single crystals are investigated with a Knoop indenter which, because of its shallow penetration, emphasizes the effects in the near surface layers and therefore may be reflecting the points made below, it is possible to discern a temperature and an orientation effect on the ISE. From the limited amount of data available a summary is made in Table 4.3. It appears that increasing the temperature raises the n index closer to the expected value of 2 while indenter orientation reveals the harder directions.

4.2. SURFACE ENVIRONMENT, CRACK-TIP CHEMISTRY, AND HARDNESS

Every ceramic has a "space-charge" region in the vicinity of the surface caused by the existence of surface defects. When the ceramic has ionic bonds, vacancies and interstitials are charged: The effective charge of a vacancy is opposite to that of the lattice ion in whose sublattice it is formed. For charge neutralization in the bulk, defects of opposite charge occur in compensating concentration. For example, MgO has as intrinsic defects equal numbers of cation and anion vacancies: that is Schottky defects. *At a surface* there is no such constraint because an excess of one type of vacancy may occur, producing a surface charge, while an excess of the opposite vacancy in the immediate subsurface layers maintains bulk behavior with respect to neutrality. That is, the surface is a *dipolar* space-charge region. This dipole produces an electrostatic potential in the bulk able to equalize the difference in vacancy formation energy for cations and anions sufficiently to ensure overall charge neutrality. It also produces a potential at the surface that can influence the energy required to move a dislocation, which itself has regions of charge imbalance, and in this way affect the apparent hardness. It is not a large step now to see that surface environment in terms of liquids, solutions, or gases can then affect the value of the surface potential and with it the hardness of the ceramic as measured by the methods discussed so far. Studies in this area rarely measure the

surface potential, but instead a related potential known as the zeta potential which is the potential at the slipping plane in a liquid double layer covering the solid.[8]

Added to a consideration of how surface chemistry affects dislocation energy, which is discussed below, must be questions concerning the processes occurring at the moment when mechanical treatment of solids causes flow or cracking. The process of bond breaking or decomposition of ceramics and inorganic compounds is a sequence of excitation processes summarized by the following three stages:

Ceramic bonds + energy → excited states

$$\xrightarrow{\text{(transform)}} \text{excited state products}$$
$$\downarrow$$
relaxation of the excited states
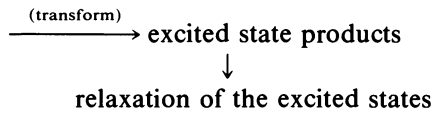
This model can be expressed as equation (4.14)

$$A \underset{k_2}{\overset{k_1}{\rightleftharpoons}} A^* \xrightarrow{k_3} B \qquad (4.14)$$

From equation (4.14) the rate can be written as

$$V = \frac{k_1 k_2}{k_2 + k_3}[A] \qquad (4.15)$$

Two cases can be discerned. First, when $k_2 \ll k_3$, equation (4.15) becomes

$$V = k_1[A] \qquad (4.16)$$

Second, when $k_3 \ll k_2$, equation (4.15) becomes

$$V = \frac{k_1 k_3}{k_2}[A] \qquad (4.17)$$

Equation (4.16) corresponds to limitation of the decomposition by the excitation step, while equation (4.17) corresponds to limitation by transformations in the excited state. Thermal decomposition is an example of the first case while photolysis is an example of the second.

Mechanochemical decomposition, which is of interest in the indentation or comminution of a surface in a chemical environment—i.e., the process of hardness determination—occurs via excitation of vibrational levels like thermal decomposition but, unlike what happens in thermolysis, during mechanolysis high-energy phonon states are excited first, as is not possible by thermal excitation alone. However, since the rate is limited by transformations in the excited state, the mechanochemical stability decreases with increasing cation radius because its probability depends on the free volume. Thus physical situations where better conditions exist for the removal of fragments produced by bond rupture, so that fractured bonds cannot recombine, lead to lower hardness; and in a series of similar ceramics the mechanochemical stability decreases as the molecular volume of the components increases, and hardness will be more influenced by atmosphere effects. According to the theoretical hardness equation, equation (1.46), the hardness itself is inversely proportional to the molar volume, indicating that softer ceramics are more susceptible to mechanochemical effects than hard ones. Vibration mill, rotating mill, and shock wave experiments, as well as environmentally sensitive hardness tests, show that mechanochemical stability coincides with the second above, in which $k_3 \ll k_2$. Thus the following broad generalizations apply: Predictions based on thermal equilibrium data may be of little use, the hardness of some ceramics may be affected by high-energy photons, such as those provided by light, and the mechanochemical effect will be more marked for softer ceramics containing larger-sized atoms.

Hardness determinations are often associated with crack production, and certainly when ceramic toughness is to be determined by the hardness technique cracks must be generated, so processes occurring at the moment of fracture of a solid at a crack tip are of interest. In brittle solids crack-tip velocity in the range of 1–3 km s^{-1} is common and therefore very high energy is involved along with excited states of very short life. This inevitably leads to nonequilibrium chemical consequences which will also be unpredictable from thermal equilibrium data. For example, thermolysis of nitrates produces oxygen through the activity of low-energy photons, while oxides of nitrogen are produced as cracks are made to propagate under an indenter on single-crystal nitrate samples; such a mode of decomposition requires higher-energy photons which must therefore be available at crack-tip energies.

Summarizing the above, it can be said that there are three ways the environment can be important in determining the observed hardness of a ceramic: first, through zeta potential, and hence surface potential control, by adsorption and chemisorption and hence affecting the energy required for slip through dislocation movement. This will be most obvious with ionic ceramics. Second, through mechanochemical processes as the combined

effect of stress and environment work to cause bond rupture leading to shear. The covalent ceramics may be more susceptible to this effect especially if high-energy photons are also available. Third, through crack propagation and changes in the growth rate of cracks during and after testing.

From an early stage in these studies a fourth, purely physical effect was also considered, namely, the change in friction coefficient caused by chemical lubrication between an indenter face and the surface as it is penetrated. Brookes and Atkins[9] showed in 1964 that the coefficient of friction μ can be altered by adsorption and that such a change could then alter the distribution of stress around an indenter. In this way many of the observed environmental effects on hardness could be explained. A gradual build-up of results from hardness, drilling, and wear experiments involving glasses and ceramics show, however, that friction may play a part, but only a part, with the first of the above processes providing the most comprehensive and predictive interpretation.

Some of the earliest data shown in Table 4.4 clearly demonstrate the softening effect of water. A consideration of results such as those in Table 4.4 led at an early stage of this work to two important conclusions: One was that dislocation motion in nonmetals is more obviously affected by *electronic* and *strain* interactions with point defects than by Peierls resistance. Chemisorption causes energy-band bending in the surface region, and this can alter the electronic core structure of dislocations or the state of ionization of point defects or both. The other was that direct comparisons of hardness values from one study to another should *not* be made unless specimen preparation, history, and measurement technique and conditions are known.

The two conclusions stated above have received little contradiction, only more detailed consideration, in the past 15 years.

Table 4.4. Knoop Hardness of Some Ceramics When Wet and Dry[a]

Ceramic	Hardness ($GN\,m^{-2}$)			
	Wet			Dry
	A Face[b]		B Face	A + B Faces
BeO	11.9		10.8	13.7
SiC	30.4		27.8	36.5
Ge		5.89		7.45
Si		8.14		11.0
Al_2O_3		24.0		26.5
SiO_2 quartz	11.5		10.1	12.2
Silica fused		5.39		7.11

[a] After Hanneman and Westbrook.[10]

[b] An A face terminates in the electropositive element; a B face terminates in the electronegative element: This is the hardness polarity effect encountered in Section 3.5 and shown in Figure 3.10.

For example, the way the hardness of a ZnO surface changes with surface potential has been examined by Westwood's group, who have been foremost in developing applications of the mechanochemical effects to the technology of drilling and cutting hard ceramics.[11] Zinc oxide was chosen as a model material because the relationships between surface potential and the near-surface electronic band structure are known—see Figure 4.8 taken from Westwood's work, and the ZnO crystal can be made into a working electrode in an electrolytic cell.

As the bias potential at a ZnO ($10\bar{1}0$) or (0001) surface was made to change from positive to negative, the hardness reached a maximum when the surface potential was slightly positive and not zero as the usual zeta-potential measurements lead one to expect. This effect is shown as Figure 4.9. From such a carefully controlled experiment it is possible to discern a more direct effect of chemical environment on observed hardness because H_V can be measured at the potential of maximum hardness while varying the solution pH in the range 8.5 to 12. It is then just possible to detect a maximum hardness at pH 9.5 which is the pH at the minimum dissolution rate of ZnO. The effect of strain energy around the hardness indentation on chemical dissolution will be a minimum at pH 9.5, and so there will be a smaller etching of the indent compared to say pH 8.5, which reflects as a measured increased hardness at pH 9.5 because the indentation diagonal will be smallest. However, this effect is only a small effect, hard to measure within normal experimental variation, compared to the surface charge effect, which produces a 12–15% increase in hardness.

Because the energy levels of semiconducting ZnO are known and the applied potentials also known, it was possible to see that the valence band and dislocation band in Figure 4.8 were not able to interact to change electron densities at applied voltages near the flat band level. However, the applied voltages could make it possible for the donor band, formed from interstitial Zn atoms, and the conduction band at negative applied potential to make electron transfers, and so a hardening mechanism for this material has been suggested based on charge exchange and dislocation disruption of the band system: First, one assumes a dislocation, by virtue of one or more mechanisms—e.g., because it is surrounded by a cloud of conduction electrons or interstitial zinc ions—distorts the conduction band in an upward direction. For flat band conditions when the dislocation moves, it is necessary only to move the band distortion in the conduction band and relatively unimpeded movement would be possible. Under the influence of positive surface charge, when the bands bend downwards as shown in Figure 4.8, the donor band cuts the Fermi level and some Zn^+ interstitials are neutralized. Now to move the dislocation, not only must the conduction band's upward distortion be carried, but electrons from the now-neutral donors must be excited through the gap to the conduction level to allow ionized Zn atoms to remain as the dislocation environment. Such transfers
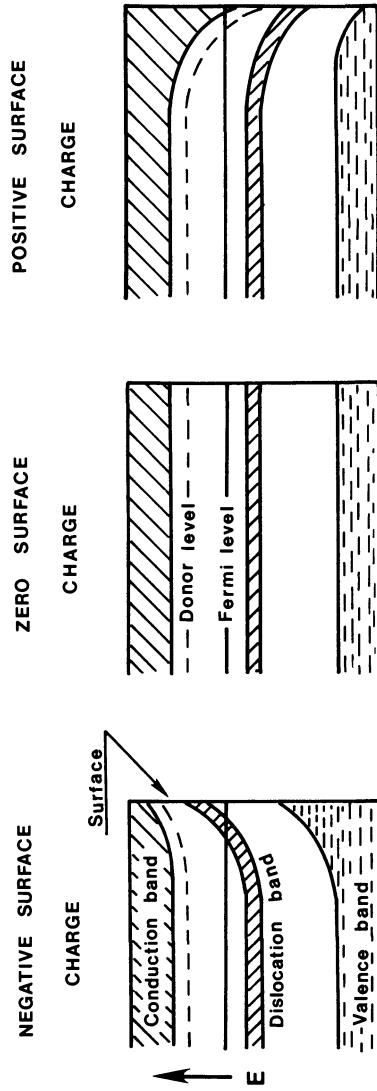
Figure 4.8. Schematic representation of band bending in n-type ZnO as a function of surface charge. After Westwood et al.[11]
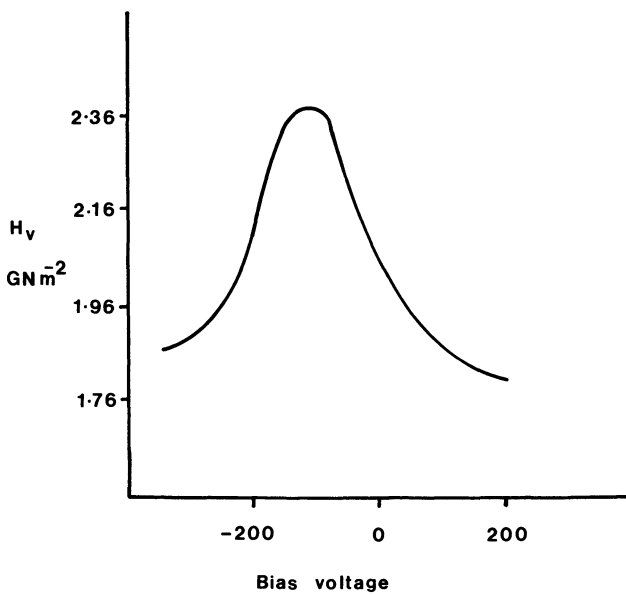
Figure 4.9. Vickers hardness of ZnO (0001) surface as a function of surface charge. After Westwood *et al.*[11]

require 50 MeV per donor; as a result dislocation movement is hindered and so hardness increases. Further downward bending of the bands produces a deeper neutralized layer of Zn^+ to Zn from Fermi band interaction, until all interstitial zinc is atomic. This includes the dislocation environment, and so movement of the dislocation is back to just moving the upward kink in the conduction band with it. Hence a softening is perceived. If the energy bands are bent upwards a similar argument applies except that the Zn^+ ions in the atmosphere of the dislocation are neutralized as the dislocation band intersects the Fermi band.

In this way the chemical effects at the surface that produce variations in energy band bending will produce a maximum in hardness.

These theories will be quite applicable to all forms of hardness determination and hardness related properties since dislocation movement is important in them all; see for example Section 2.3, where the mechanisms of energy absorption under a pendulum hardness diamond as it cuts into a ceramic surface are discussed.

There is not much to offer at present as an alternative approach to the above in explaining mechanicochemical effects and environment-sensitive hardness, but one attempt is emerging[12] where the zero of zeta potential is associated with a minimum concentration of charged species in the liquid at the surface as ions aggregate to form neutral species, leading to a greater

concentration of free hydrogen ions. It is then suggested that H^+ interaction with surfaces and cracks allows hydrogen to diffuse into the near surface region and change its mechanical properties.

A general conclusion has been reached that drilling rate is a maximum, wear rate a minimum, and hardness a maximum in any environment at a *pH* that produces a zeta potential equal to zero. Thus the isoelectronic point is important however it is achieved; Figure 4.10 is a visual demonstration of this viewpoint taken from the work of Swain *et al.*[13] Chemisorbed or weakly physisorbed species lead to differing effects; for example, weakly absorbed lauric acid does not shift the zeta potential from *pH* = 9.0 (fixed by strongly adsorbed OH^- and H^+ that between them determine the surface potential) while oleic acid is strongly chemisorbed and so the isoelectronic point moves to *pH* 7.5 and drilling rates and hardness are consequently affected.

From this we can see an application for Knoop or pendulum hardness in the practical field of cutting and drilling because they can be used as comparative test methods to examine surface additives. Indentation tests have to be conducted over time periods that are long compared to changes in drilling contact times, as discussed in Section 2.1.2.1.

It should be noted here that although two seconds seems a short time in terms of an indentation experiment, it is an extremely long time in terms
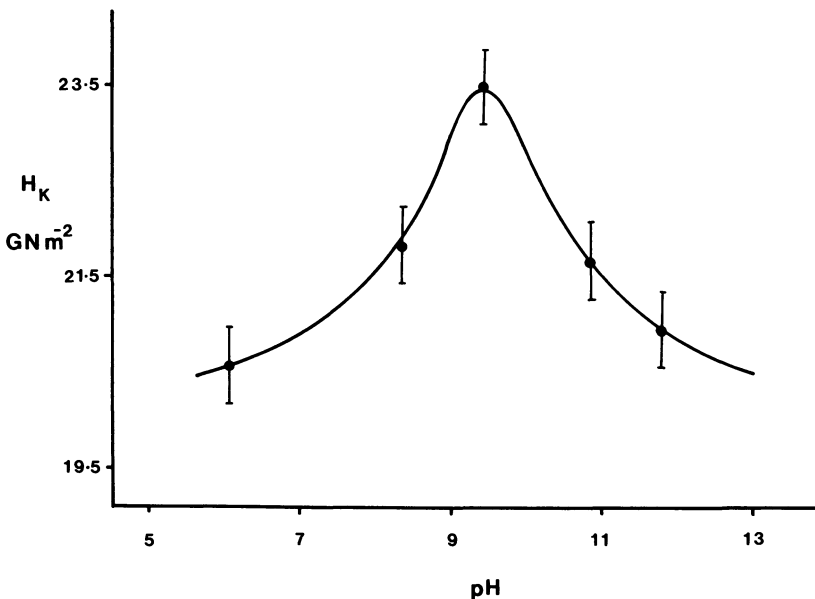
Figure 4.10. Knoop hardness of Al_2O_3 as a function of *pH*. Load = 0.98 N, t = 1000 s, long axis along $\langle 1\bar{2}10 \rangle$ on $\{0001\}$ planes.

of what is happening during erosion, drilling, wear, and crack propagation. Does this mean that these properties are insensitive to environment? Clearly the answer is no, because many experiments show them to be otherwise, but rather indentations made at times less than two seconds relax significantly because extended dislocations have not had time to be effectively pinned by mobile defects. This results in consistently high hardness as measured by the diagonal length. Chemical effects do occur in the short times available in crack-tip extension, etc., as we have already indicated.

It is not so easy to produce visual and numerical evidence for the mechanism of bond rupture, but chemical etching after indentation on ceramics like SiC can be used to provide some evidence. Chapter 3 explains how dislocation etch-pitting techniques have been used in conjunction with hardness tests to study dislocation distributions around indentations and to obtain information on slip plane identities and dislocation mobilities. The technique is useful in softer materials where the etch-pit rosettes are apparent some distance from the indent, but it is almost impossible to use with harder materials such as NbC, SiC, and other such covalent ceramics, because plastic deformation is highly localized beneath the indent and cannot be found by etching techniques. However, since the indent area has stored strain energy—see Section 5.2—it will itself change shape on etching in a way interpretable on the resolved shear stress model given in Section 3.6.1. The curve for Knoop hardness of single-crystal SiC on the (0001) plane shown as Figure 6.3 can be interpreted from the ERSS model as a single slip system of the $\{h\ o\ \bar{h}\ l\}\langle 11\bar{2}0\rangle$ type. Adewoye and Page[14] made normal shaped Knoop indents with the long axis along $[11\bar{2}0]$ and $[1\bar{1}00]$ directions which puts the short axis along $[1\bar{1}00]$ and $[11\bar{2}0]$, respectively, and gave the aspect ratio $l[11\bar{2}0]/l[1\bar{1}00]$ differences of 10.75 and 0.10. After etching at 400°C in molten Na_2O_2, the indents became either regular or elongated hexagons with aspect ratios 1.0 and 1.71, respectively. As the etching proceeds, material is removed parallel to the surface, and the indents would be expected to become steadily smaller, but due to the stored plastic energy around the indentation acting with the etchant, material is removed preferentially, resulting in indent shape change. Thus etching examines the stored energy as a function of anisotropy, and conversely this visual evidence shows the interaction of environment and stress that might influence observed hardness values.

In the example under discussion, because slip is controlled by flow in defined crystal planes as in Section 3.5, the new shape is quite crystallographic, and is related to the original indent, producing the quoted changes in aspect ratio. When the long axis was parallel to $[11\bar{2}0]$, preferential flow occurred in the long-axis direction, and so those members of the slip system family containing this direction had been most active, producing the lozenge-shaped indent after etching because most stress was stored in the slip

directions. When the long axis was along [1$\bar{1}$00], all $\langle$11$\bar{2}$0$\rangle$ were equally active, so equal amounts of stored strain reacted during etching and produced the regular hexagonal shape of the indent.

The effect of applied stress on crack tip propagation—that is, on crack tip chemistry—is so important in the area of fracture toughness determinations from hardness that a whole section, Section 5.11, is devoted to this and so the discussion is not repeated here.

4.3. ENVIRONMENTAL–TIME EFFECTS ON HARDNESS

The results shown in Figure 4.10 give a clear indication of the softening/hardening effect promoted by chemical environments changing the *pH* at the ceramic surface, but it should be emphasized that if the hardness is determined after a two-second indentation period it appears to be independent of chemicomechanical effects, so that the material appears to be harder; all values in the *pH* range 5–12 give a mean hardness for alumina of 23.5 GN m^{-2} if indentation is for only two seconds. This highlights the fact that there is a time dependency for ceramic hardness and the elastic solution to models for the indentation process such as equation (4.18), which should be compared to equation (3.3), represent a time-independent *minimum* which a solid approaches when the yield stress is *very small*.

$$H_x = \frac{2 \tan \beta \cdot G}{A} \qquad (4.18)$$

In equation (4.18), G is the shear modulus, β is the angle between the indenter face and the surface, ν in equation (3.3) is taken to be 0.5, and A is a dimensionless hardening constant.

For most ceramics, the yield stress is not small, the indentation process is controlled by the dynamic process of the growth of a plastic zone around the indent, and the hardness will obviously be time dependent. In the context of this chapter the time dependency will be markedly influenced by mechanicochemical effects on the dynamic processes which involve bond rupture.

With hardness tests conducted in a vacuum on the known covalent ceramics, the hardness is not obviously time dependent unless extremely long times of indentation are used. Under normal atmospheric conditions, and particularly when surface chemical reagents are added, it appears that the time dependency becomes more apparent with short time; tests lasting less than three seconds produce hardness figures of high value and with no apparent environmental effect. The environmental effect occurs in the range

3–1000 s when lower hardness values that show a marked *pH* dependency are obtained.

Another way to achieve the strongly time-dependent hardness range, preceding the achievement of the constant time independent minimum value of hardness predicted by equation (4.18), is to make hardness tests at elevated temperatures. As the test temperature increases above $\frac{1}{2}T_m$, where T_m is the melting point of the sample, the hardness rapidly decreases and becomes time dependent until a temperature is reached where the dislocation mobility becomes high, the yield strength becomes very low, and hardness approaches the constant, time-independent value. It may not be easy with some ceramics to achieve the constant hardness zone because elevated temperature may permit diffusional creep, when once again the hardness will become obviously time dependent, and hardness values *lower* than that predicted by equation (4.18) will be achieved.

In some systems, increasing the "dwell time"—that is, the time over which the full load is applied to the surface—results in an increase in the size of the indentation and hence an apparent reduction in the hardness of the material. This effect is called *indentation creep*.

There are three types of indentation creep:

Conventional creep. This type is observed for all crystalline materials when the temperature of the sample is raised above $0.4T_m$, where T_m is the melting point of the material. As the temperature increases, this form of creep increases, and hardness values become very sensitive to dwell time as equation (4.19) suggests

$$\frac{1}{H_x^3} - \frac{1}{H_{x_o}^3} = A \exp\left(\frac{-E}{3RT}\right)[t^{1/3} - t_o^{1/3}] \qquad (4.19)$$

In equation (4.19), H_x and H_{x_o} are the hardness values at times t and t_o, respectively; T is the absolute temperature, E is the activation energy of the creep process, and R is the gas constant. Linear plots of $\ln(\Delta H)^{-3}$ against $1/T$ at constant $\Delta t^{1/3}$ have a slope from which the activation energy for the process can be determined. When this is done for this type of creep, the activation energy is frequently found to be in close agreement with that obtained from conventional creep and self-diffusion measurements; for example, that for MgO is 460 kJ mol^{-1}, for SiC 527 kJ mol^{-1}, and for WC 460 kJ mol^{-1}, which strongly suggests that this type of indentation creep is controlled by a mechanism of lattice vacancy diffusion.

Anomalous indentation creep. This has been observed at room temperature in ceramic materials when light loads are used. It is called

anomalous indentation creep because the apparent softening on increasing the dwell time becomes *less* apparent at higher temperatures.

Low temperature creep.   By low temperature one is referring to temperatures up to $0.4T_m$ and so we are really talking about low homologous temperatures because, in an absolute sense, $0.3T_m$ could be quite a high absolute temperature for some ceramic systems. Surprisingly high rates of creep are observed for such low homologous temperatures as Figures 4.11 and 6.8 show; it is clear from Figure 4.11 that the effect is anisotropic. So far it has not been possible to anticipate this behavior on the basis of the models that relate to conventional creep mechanisms.

When the time-independent hardness range is achieved, either through environmental effects or by temperature increase, hardness is related directly to shear modulus as analysis in Section 3.4 shows, supported by the results shown in Figure 4.12.

The main purpose of this section has been to emphasize the fact that, in ceramic systems, if it is desired that the hardness technique is to be used as a probe of surface environment effects, then hardness determinations should extend over a suitably long period, which may be in the region of 15 minutes. Furthermore, for the use of hardness data in wear and erosion predictions, as in Section 5.7.2, it is critical that effective hardness values *relevant* to the contact conditions of environment, temperature, and size be used, rather than typical listed values obtained under arbitrary conditions.
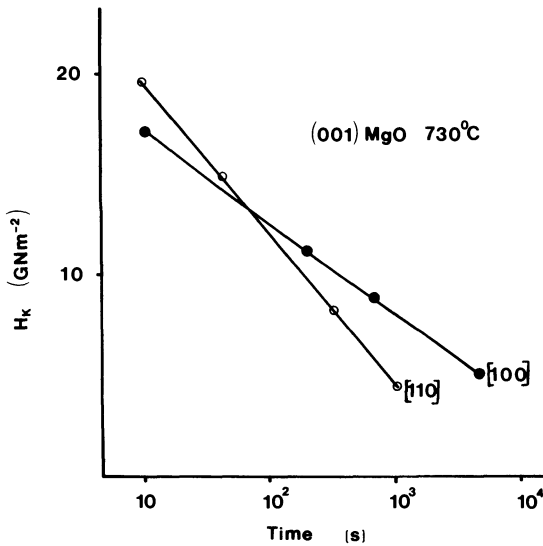
Figure 4.11. Anisotropic rates of indentation creep in magnesia. After Brookes.[15]
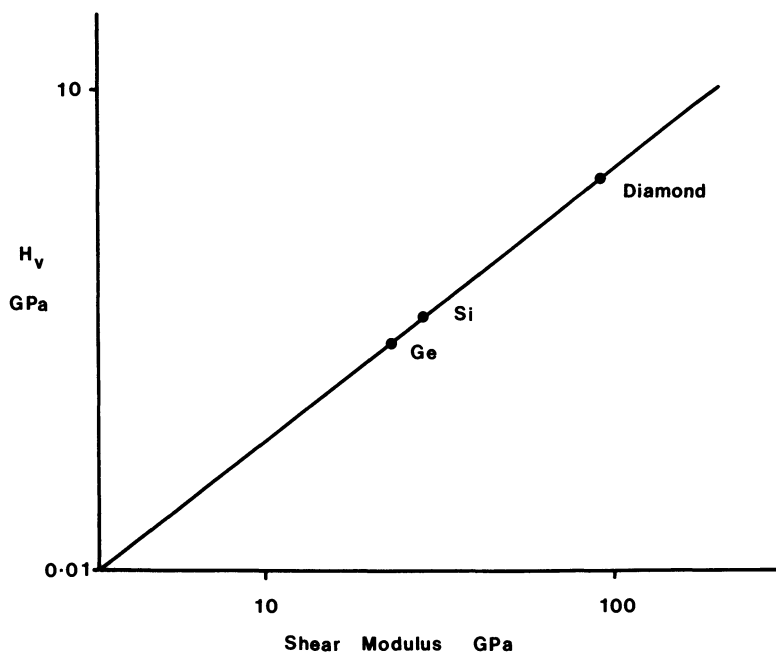
Figure 4.12. Time-independent Vickers hardness obtained at $T > \frac{1}{2}T_m$ for some covalent ceramics plotted against shear modulus. The straight line shows the predicted values using equation (4.18) with $A = 200$. After Gerk.[16]

REFERENCES

1. P. M. Sargent and T. F. Page, *Proc. Brit. Ceram. Soc.* **26**, 209 (1978).
2. P. F. Becher, *J. Amer. Ceram. Soc.* **57**, 107 (1974).
3. L. A. Gypen and A. Deruyttere, *J. Less Common Metals* **56**, 91 (1977).
4. P. J. Burnett and T. F. Page, *J. Mater Sci.* **19**, 3524 (1984).
5. M. J. Mathewson, *J. Mech. Phys. Solids* **29**, 89 (1981).
6. P. J. Burnett and T. F. Page, *J. Mater. Sci.* **19**, 845 (1984).
7. J. M. Georges, G. Meille, J. L. Loubet, and A. M. Tolen, *Nature* **320**, 342 (1986).
8. I. J. McColm and N. J. Clark, *Forming, Shaping, and Working of High-Performance Ceramics*, Blackie, Glasgow (1988), p. 67.
9. C. A. Brookes and R. G. Atkins, in *Plansee Proc.*, F. Benesowsky, ed., Metallwerk Plansee AG, Reutte Tyrol, Austria (1964), p. 712.
10. R. E. Hanneman and J. H. Westbrook, *Phil. Mag.* **17**, 73 (1968).
11. A. R. C. Westwood, J. S. Ahearn, and J. J. Mills, *Colloids and Surfaces* **2**, 1 (1981).
12. R. F. Cuthrell, *J. Appl. Phys.* **49**, 432 (1978).
13. M. V. Swain, R. M. Latanision, and A. R. C. Westwood, *J. Amer. Ceram. Soc.* **58**, 372 (1976).
14. D. Adewoye and T. F. Page, *J. Mater. Sci. Letters* **11**, 981 (1976).
15. C. A. Brookes, in *Science of Hard Materials*, R. K. Viswanadham, Q. J. Rowcliffe, and J. Curland, eds., Plenum, New York (1983) p. 181.
16. A. P. Gerk, *J. Mater. Sci.* **12**, 735 (1977).

Cracked Indents—Friend or Foe?

Their Use in Toughness and Brittleness Characterization

5.1. INTRODUCTION

Inevitably ceramics will become more widely used as they are made tougher through the application of developments in the following areas:

1. Achievement of zero porosity and maximum densities from the use of better characterized starting powders and improved sintering techniques.[1]
2. Utilization of the *transformation toughening* process available via zirconia. Such processes may involve any or all of the following four mechanisms:
   a. Microcrack generation around transformed particles.
   b. Stress-induced compression zones.
   c. Compressive surface layer formation.
   d. Agglomerate toughening.
   Discussion of these phenomena can be found in several sources.[2,3]
3. Development of duplex structure ceramics.
4. Manufacture of composites containing large volumes of fibrous or whisker ceramic materials.

A natural consequence of such progress will be the need to measure fracture toughness of ceramic materials more frequently in the routine characterization of products. Herein lies a major outlet for the technique of *hardness indentation* within the field of ceramic technology. The convenience of the microhardness indentation method has already been stressed, involving as it does the use of robust conventional equipment acting on only a small area of polished surface of a sample from which

many data points can be obtained. Now, if a load is chosen that causes cracks to occur around the indentation shape, a new microscopic method of studying toughness becomes available that does not in fact destroy the test specimen in the way that macroscopic fracture toughness tests do. In Figure 1.1, this aspect of development is shown as phase four arising from studies of the effects of changes in applied load on hardness.

This is an intriguing development because so far cracked indents have been seen to be a problem which must be avoided in precise hardness determinations, not because the energy used to propagate cracks is significant compared to the energy used to produce the plastic yield in the volume of the indent and beyond, but because cracks profoundly alter the stress state in surface and subsurface regions. Perhaps the most important reason why cracks are considered to be unfortunate in ceramic studies is that substantial surface disruption makes it impossible in many cases to define and measure the indent diagonals. In this chapter, however, we see a requirement for cracks around the indented area.

In general, for ceramic systems a load is easily found that generates a crack pattern around the indentation trace; see, for example, Figure 5.1. It was Palmqvist working with special refractory hard metal carbides and a Vickers diamond pyramid indenter in the period 1957-63[4] who particularly noted these cracks and did an empirical analysis which established the property of hardness as an important parameter in their formation. However, no great interest was aroused by them, but rather loads were recommended that avoided crack production, until several workers including Evans, Lawn, and Hagan from about 1972 began to analyze the crack formation in some detail. The work so far has culminated in relating crack dimensions, crack pattern, the load, and the toughness parameter K_{1C} to each other by
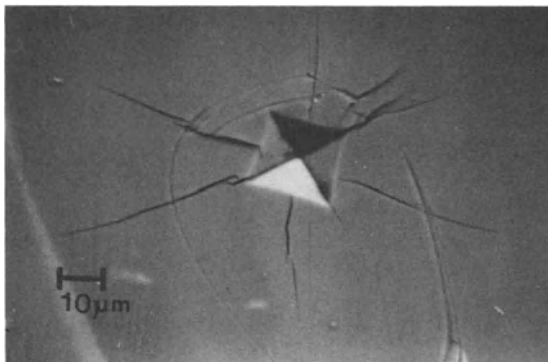
Fig. 5.1. Cracks developed around a Vickers indent on a scandium silicide ceramic showing median and lateral vent cracks. The lateral crack shows a marked anisotropy arising from the structure.

analyzing the sequence of operations occurring during an indentation load-
ing and unloading cycle. The major outcome of this analytical approach
has been a series of semi-empirical calculations dependent on data-curve
fitting exercises. Four material and experimental parameters are related in
all such work: hardness, Young's modulus, crack size on the *surface* of the
sample, and toughness (through K_{1C}).

As experience grows in the use of the method it is becoming more
apparent that sample microstructure plays a major role in influencing
toughness values obtained this way. For example, the indentation fracture
technique cannot be used to find *intrinsic* toughness values when the crack
runs between grains rather than by intragranular paths. Thus toughness
values found by the microhardness indentation method should not be quoted
without a clear statement of crack shape, crack path, and the general
microstructural features of the sample. These characteristics, together with
a clear statement of which of the several semi-empirical equations (see
Section 5.4) are used in the calculation, should always be considered.

Results obtained with different-shaped indenters cannot be compared
directly; the curves relating hardness and crack length for each indenter
shape are unique.

5.2. CRACK TYPES AND CRACK FORMATION

It is necessary to make a distinction based on the shape of the indenter
used to produce the cracks because the position and pattern of cracks are
dominated by surface flaws for blunt indenters, while such flaws are not so
important when sharp indenters are used. Therefore to study crack gener-
ation and subsequent propagation in ceramic systems and not the distribu-
tion and behavior of pre-existing flaws, work is best restricted to sharp
indenters of the Vickers or Knoop type. Conversely, blunt indenters such
as the Brinell ball give some indication of flaw distribution on surfaces.

5.2.1. Sharp Indenters

5.2.1.1. Median Crack

This is a penny-shaped crack (see Figure 5.2) formed beneath the
surface when the indenter is overloaded. Median cracks form directly below
the apex of the indenter in an area below the heavily deformed region.
Glasses and ceramics are classically brittle, and surprisingly low critical
loads will form this type of crack; for example, for a typical glass estimates
given below show this to be in the order of 0.2 N when a Vickers diamond
is used.
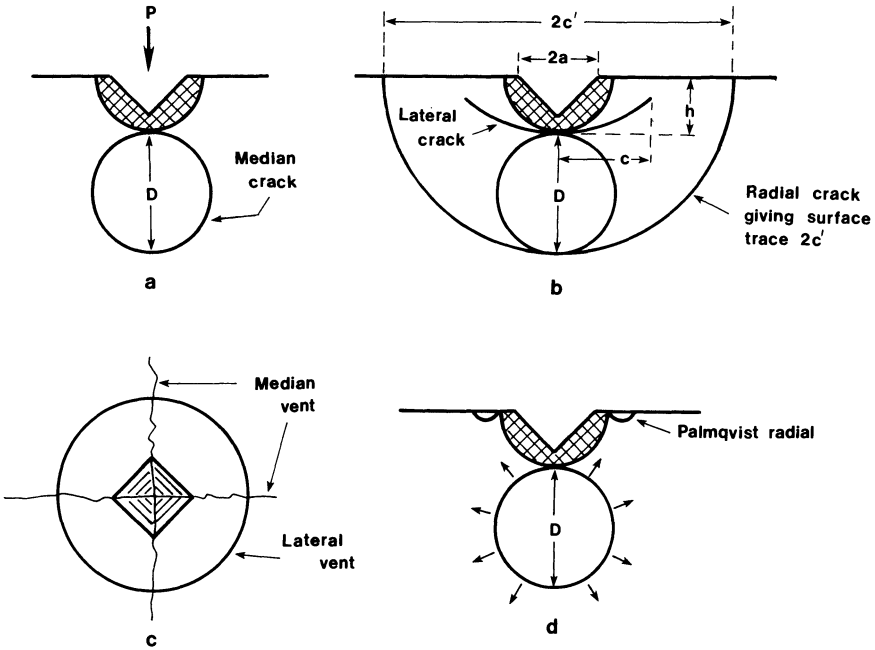
Figure 5.2. (a) Normal form of median crack with $P <$ critical load needed to cause "pop-in" and P still applied. (b) After unloading, residual tensile stress causes "pop-in" and development of radial crack as well as development of shallow lateral cracks on planes parallel to specimen surface. (c) Plan view of indented surface after indentation cracking. (d) Palmqvist crack formed before the median "pops in" as radial.

The component of the stress field characterized by one approach, that in Section 1.4.1.1, responsible for generating median cracks is σ_{yy} and can be estimated using equation (1.29) and relevant equations from (1.19) to (1.27). Such calculations show that peak values of tension are appreciably smaller than tangential tensile stress on the surface. The peak load stresses are smaller than the residual stresses when the load is removed; thus, medians are generated on loading once the critical load has been reached or on occasions when a just subcritical load is removed. The peak tension is at the boundary of the elastic–plastic zones. These features are shown in Figure 1.5.

5.2.1.1a. Nucleation of medians. Figure 5.2(a) shows the median crack as being nucleated in the interface between plastically deformed material and material which is just elastically strained. Despite there being clear visual evidence for this situation (see Figure 5.3), only limited attention has been given to understanding or modeling the initiation stage. This is unsatisfactory as far as the ceramics industry is concerned because all subsequent
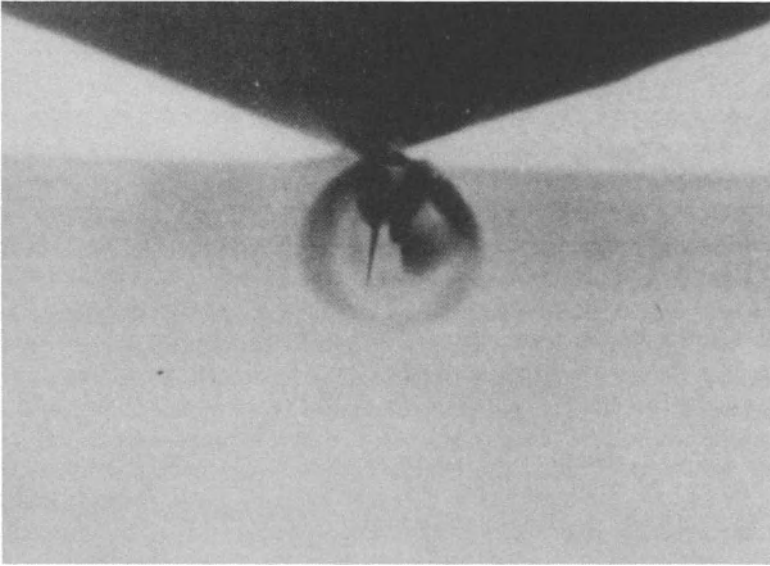
Figure 5.3. Median crack in transparent ceramic. After Lawn.[5]

erosion and degradation stem from the initial formation of the median crack on surface impaction. The following interesting and useful analysis of the nucleation stage of median crack formation is taken directly from the model developed by Lawn *et al.*[5,13] Figure 5.4 gives the characteristic dimensions and stress distribution used to develop the model.

A sharp indenter of the Vickers type at load P produces a plastic impression with characteristic surface dimensions $2a$ given by equation (1.6), repeated as equation (5.1) in the form that has load in kilograms

$$H_V = P/2a^2 \tag{5.1}$$

It is assumed that the resulting deformation produces the simple linear *tensile* stress field shown in Figure 5.4(a). Since the hardness of the material determines the dimension a, it can be seen that the maximum tensile stress developed is related to hardness, and σ_m in Figure 5.4(a) can be written as $\sigma_m \propto H_V$, i.e., σ_m is constant since hardness is a material property. Thus

$$\sigma_m = \theta H_V \tag{5.2}$$

where θ is a constant.
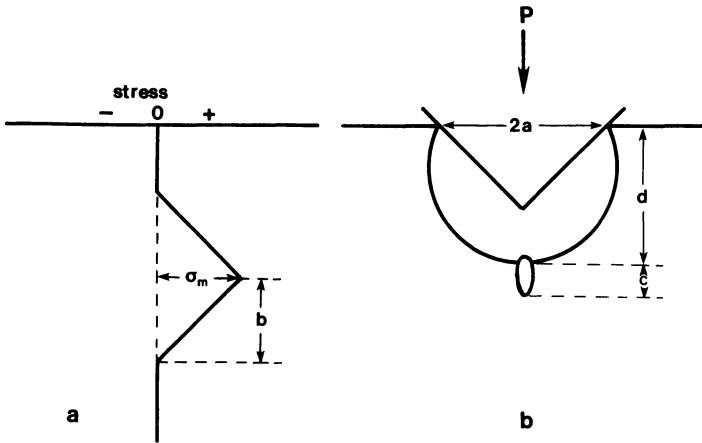
Figure 5.4. (a) The simplified stress profile assumed to be developed below the apex of the sharp indenter. (b) Median crack, half length c', nucleated at region of maximum stress on boundary between plastic deformation and normal, elastically strained material.

The volume over which the stress field acts is indicated in Figure 5.4 by the dimension b which must depend on the volume of material moved plastically as determined by the contact dimension a. Thus $b = \phi a$ where ϕ is another proportionality constant.

From equation (5.1), a is related to the material property of hardness, from which

$$b = \left(\frac{\phi^2}{2H}\right)^{1/2} P^{1/2} \qquad (5.3)$$

The stress field in the material below the surface can now be considered to be searching for a critical flaw, and the increased load needed to intensify the field to a level such that a penny-shaped flaw is developed can be examined.

By assuming a flaw shape, the stress intensity factor for loading it axially can be written as equation (5.4)

$$K = \frac{2}{(\pi c)^{1/2}} \int_0^c \frac{r \sigma_r \, dr}{(c^2 - r^2)^{1/2}} \qquad (5.4)$$

The simply defined stress field is now useful because the function σ_r in equation (5.4) can be inserted from Figure 5.4(a)

$$\sigma_r = \sigma_m(1 - r/b) \qquad \text{when } r = b$$

$$\sigma_r = 0 \qquad \qquad \text{when } r \leq b$$

These two conditions give two solutions from equation (5.4), when half crack length c is greater or equal to the region under the influence of the tensile stress b,

$$K = 2\sigma_m \left(\frac{c}{\pi}\right)^{1/2} \left[1 - \frac{1}{2}\left(1 - \frac{b^2}{c^2}\right)^{1/2} - \frac{1}{2}\left(\frac{c}{b}\right)\sin^{-1}\left(\frac{b}{c}\right)\right]$$

When the crack lies wholly in the tensile stress $c \le b$

$$K = 2\sigma_m \left(\frac{c}{\pi}\right)^{1/2} \left(1 - \frac{\pi c}{4b}\right)$$

For equilibrium under Griffith conditions $K = K_c$ and, using equations (5.2) and (5.3) to eliminate the difficult-to-determine terms σ_m and b, it is possible to obtain two relationships concerned with crack extension for the two sizes of crack defined above.

$$1 = \frac{2\theta H_v c^{1/2}}{\pi^{1/2} K_c}\left[1 - \frac{1}{2}\left(1 - \frac{\phi^2 H_v^{-1} P c^{-2}}{2}\right)\right]^{1/2}$$
$$- \frac{1}{2}\frac{2^{1/2} H_v^{1/2} c P^{-1/2}}{\phi}\sin^{-1}\left[\frac{\theta^2 H_v^{-1/2} P^{1/2} c^{-1}}{2^{1/2} P}\right] \qquad (5.5)$$

Equation (5.5) is for the crack contained within the stressed volume. When the crack is longer than the stressed zone a second equation is obtained:

$$1 = \frac{2\theta H_v c^{1/2}}{\pi^{1/2} K_c}\left(1 - \frac{2^{1/2}\pi H_v^{1/2} c P^{-1/2}}{4\phi}\right) \qquad (5.6)$$

As they stand these two equations are cumbersome and do not readily show a relationship between crack length and applied load. It has been possible to overcome this deficiency by making one substitution, equation (5.7), based on the relation of hardness, toughness, and crack length, and one, equation (5.8), based on the relation of hardness, toughness, and load:

$$c = \frac{4\theta^2 H_v c}{\pi K_c^2} \qquad (5.7)$$

$$P = \frac{8\phi^2 \theta^4 H_v^3 P}{\pi^2 K_c^4} \qquad (5.8)$$

Making these substitutions gives (5.5) and (5.6) in reduced forms:

$$1 = c^{1/2}\left[1 - \frac{1}{2}\left(1 - \frac{P}{c^2}\right)^{1/2} - \frac{1}{2}\left(\frac{c}{P^{1/2}}\right)\sin^{-1}\left(\frac{P^{1/2}}{c}\right)\right] \qquad (5.9)$$

and

$$1 = c^{1/2}\left(1 - \frac{\pi c}{4P^{1/2}}\right) \qquad (5.10)$$

It is possible to plot out the reduced flaw size function C and P through equations (5.9) and (5.10) to obtain an equilibrium curve; Lawn and Swain[5] have done this, and Figure 5.5 is taken from their work. The notable feature of such a curve is the minimum at $P = 28.11$ and $c = 2.25$ and its usefulness is in visualizing the process of median crack nucleation and subsequent extension. For example, if all flaws are very small so that $C \leq$ unity, the asymptote in Figure 5.5, it is impossible for any line of constant reduced flaw size, C, to intersect the equilibrium curve—this is region I—hence the flaw can never expand. The hardness value is here controlling the stress
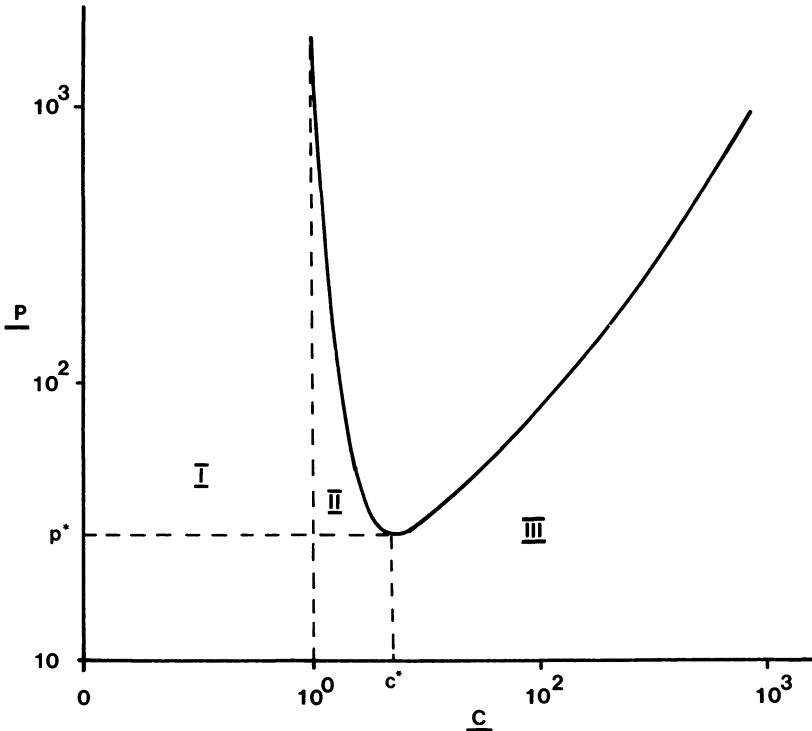
Figure 5.5. Equilibrium curve P versus C used to discuss the nucleation stage of median cracks.

distribution over the flaw length and preventing a load being achieved that causes the critical stress intensity factor to be achieved.

Flaws with reduced sizes corresponding to region II in Figure 5.5 behave such that a critical load will be achieved and spontaneously there is development of the median crack because intersection at increasing load is on the negative-slope branch of the equilibrium curve. For the large flaws, region III in Figure 5.5, increasing load for a given reduced flaw size leads to a critical reduced load that cuts the equilibrium curve on the side of positive slope, and stable growth occurs at increasingly reduced load, P.

This approach emphasizes the variability of nucleation being dependent upon the distribution of both flaw sizes and the flaw positions.

The approach does further highlight the fact that, because of the minimum shown in Figure 5.5, no flaw can extend at all to initiate the median crack unless a critical load P^* is exceeded. It is now possible to estimate critical loads sufficient to cause the formation of median cracks in brittle solids. This is done by using equations (5.7) and (5.8) and the minimum point at (2.25, 28.11) on the equilibrium curve.

$$\text{Critical load } P^* = \frac{34.67}{\phi^2 \theta^4} \frac{K_c^4}{H_V^3} \tag{5.11}$$

$$\text{Critical flaw size } c^* = \frac{1.767}{\theta^2 H_V^2} K_c^2 \tag{5.12}$$

Using equations (5.11) and (5.12) with $\phi = 1$ and $\theta = 0.2$ with hardness and toughness values from the relevant chapters in this text gives the values in Table 5.1. The interesting feature of Table 5.1 is the surprisingly small loads required to produce median cracks within ceramics when an impinging object has a sharp profile like that of a Vickers diamond. The model used

Table 5.1. Critical Loads Needed to Nucleate Subsurface Median Cracks in Some Ceramics

Material	P^* (N)[a]	C^* (μm)[b]
Si	0.003	0.2
SiO_2 (silica)	0.02	0.6
MgO	0.06	0.8
SiC	0.8	2
Al_2O_3	3	5
Si_3N_4	3	4
WC–Co	96	22

[a] From equation (5.11).
[b] From equation (5.12).

is a simple one, but more realistic stress distribution function would alter the estimate of P^* and C^* only by an order of magnitude. Using the stress distribution obtained from equations (1.17) to (1.27), the threshold loads and crack lengths for several ceramics are given in Table 5.2 for the three principle crack systems.

Equations (5.11) and (5.12) show us that to build in *resistance* to *flaw generation* in ceramic systems H_V must be decreased while increasing K_c. However, once a sample is flawed, the intrinsic toughness parameter alone is important.

5.2.1.1b. Median growth. Once nucleated in the interface region between plastically and elastically deformed material, in the way discussed above, the median crack extends downwards. In terms of the three principal normal stresses downward is σ_{33} in Figure 5.6 and is compressive everywhere. The crack maintains orthogonality with σ_{11}, which is everywhere tensile, and σ_{22}, which is a hoop stress, and is tensile in a cone of about 104° from the indenter and compressive between the surface and the 52° cone contour. Thus the crack will also expand outward in the σ_{11} direction as it remains orthogonal to the σ_{22} tensile stress. It is this orthogonality that develops the median crack into the enclosed full-penny configuration of Figure 5.2.

Table 5.2. Critical Loads for Generation of the Critical Sized Cracks on Radial, Median, and Lateral Systems

		Prediction		Observed	
Material	Crack type	P^* (N)	C^* (μm)	P^* (N)	C^* (μm)
Soda–lime–silica	Radial	0.4	1		
glass	Median	0.6	1.1	5.0	17
$\beta = 2.2^a$	Lateral	2.0	3		
Ge (crystal)	Median	0.014	0.16	0.02	0.25
$\beta = 2.5$					
SiC (polycrystal)	Radial	5	3		
$\beta = 2.8$	Median	14	4		
	Lateral	40	7		
Si (crystal)	Median	0.05	0.36	0.03	0.65
$\beta = 2.65$					
Si_3N_4 (polycrystal)	Radial	30	7		
$\beta = 2.8$	Median	80	12		
	Lateral	210	20		
Al_2O_3	Median	0.4	0.6	0.25–0.5	3
$\beta = 2.5$					

$^a\beta$ defines the indent size according to equation (1.16).
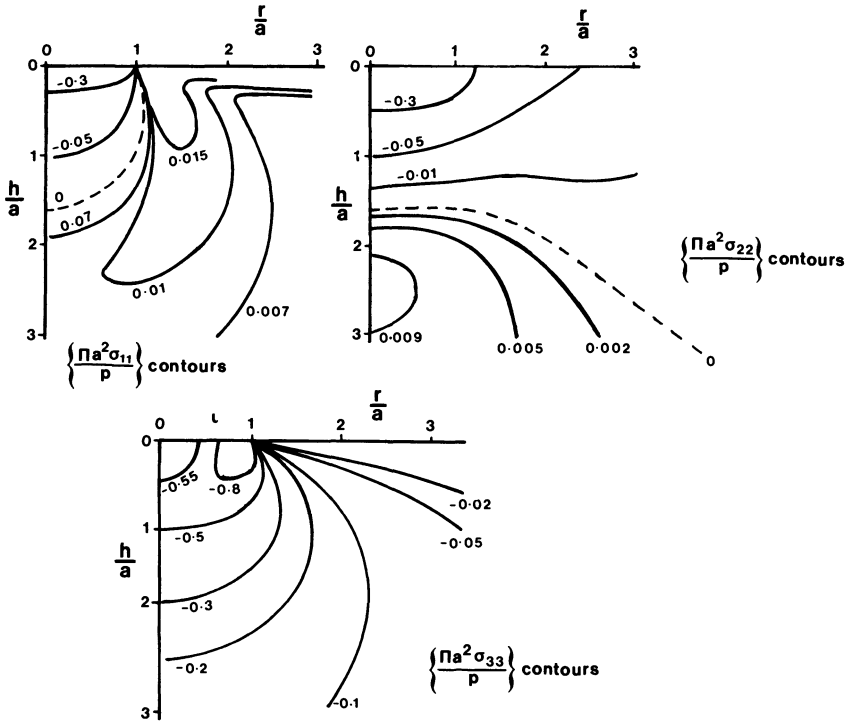
Figure 5.6. The three principal normal stresses in the volume beneath an indenter.

Constraint on the sideways expansion is exercised by the compressive volume of the σ_{22} hoop stress at angles less than 52°.

Depending on the symmetry of the indenter and on any anisotropy of the ceramic's mechanical properties, several intersecting cracks can move simultaneously. This fact must seem to be a major problem if crack depth as a function of load is to be used to investigate ceramic toughness. However, experimental observation shows that crack depth, $D + h$ in Figure 5.2.(b), is not sensitive to the number of cracks formed. At this stage the crack diameter D is a function of four parameters: the load, P; the hardness, H_x; Young's modulus, E; and the fracture surface energy, γ.

Different analyses and slight changes in the model lead to some minor variations being proposed for the relationship among these four parameters. Nevertheless, equation (5.13) is a generally accepted form of the function:

$$\frac{P^2}{D^3} = \frac{2\gamma E}{K_f} \tag{5.13}$$

In equation (5.13), K_f is a constant that is itself a function of *experimental* and *material* properties

$$K_f = f\left(\nu, \frac{H_x}{E}, \psi\right) \qquad (5.14)$$

In equation (5.14) ψ is the indenter half angle, ν is Poisson's ratio, H_x and E have the usual meaning, and the subscript f denotes the crack formation stage of the process. The constant K_f is an experimentally determined feature that makes the overall approach semi-empirical.

At this stage we can see a physical restriction because the penny-shaped median cracks are contained below the sample surface and can be measured only in transparent media. This would restrict the method to glasses and some large single crystals. Perhaps that is why at this stage the median crack is said to be "not well developed" since it remains within the sphere of influence of the nucleation zone immediately below the indenter.

Growth of the penny crack is achieved by increasing the load, and experiment has shown the growth to be stable as the load increases in accord with equation (5.15)

$$\frac{D}{a} \propto P^{1/6} \qquad (5.15)$$

Eventually D exceeds the deformed contact zone and, spontaneously at a critical value of P, breaks through to the surface. At this stage it is said that "pop-in" has occurred and the penny median becomes "well developed," changing its shape to a *halfpenny* when $D + h$ becomes c' in Figure 5.2(b).

5.2.1.2. Surface Trace of Median: The Radial Cracks

Also referred to as median vent cracks, these are caused to "pop-in" by exceeding a critical indenter load. It is the "pop-in" phenomenon that is important to the development of this subject in ceramic science because the halfpenny crack has the surface trace which allows opaque materials to be analyzed by recording the radial crack size as a function of increasing load. There is, however, the implication that the surface must be prepared carefully by polishing to an optical finish in order to see the radial cracks. If necessary, samples must be annealed to remove polishing stresses. Radial cracks are the result of surface tensile stresses, σ_{yy} in equation (1.29). Such stresses are at a maximum at the elastic–plastic boundary.

Observation and analysis, as in Section 1.4.1.1, both show that "pop-in" can occur at loads *less than* the critical load on *removing* the indenter. This is the result of residual tensile stresses, equations (1.23)–(1.26), acting as

the indenter is released on the contained median and translating it to the halfpenny radial crack. Observations in transparent samples and acoustic emission studies have shown this to occur. Residual *tensile* stresses (see Section 5.4.1) associated with the indented area are approximately $H_V/20$ in magnitude and these, especially in hard materials, are found to be sufficient to develop the trace system shown in Figure 5.2(c); they are larger, as Figure 1.5 shows, than the loading stress.

Whether the radial cracks are "popped-in" under load (P larger than critical load) or after removal of the indenter (P smaller than critical load), some general features emerge. First, critical load diminishes as ψ decreases. Second, indenters with small half angles (small ψ) produce multiple median formation. Finally, mutually intersecting medians may "pop-in" at different loads, implying that some mutual retardation can occur. Bearing these points in mind a wider angled indenter is preferable, which explains the general acceptance of the Vickers diamond for this work.

Once a median crack escapes the nucleation zone, then it is fruitful to consider the model in which a component of the applied load acts to wedge open the mouth region to which equation (5.16) applies. From Figure 5.2(a)

$$\frac{P^2}{(D+h)^3} = \frac{P^2}{(c')^3} = \frac{2\gamma E}{K_p} \tag{5.16}$$

Comparing equations (5.13) and (5.16), the change to surface trace size can be seen, together with the introduction of a new constant K_p, signifying the propagation stage of the process. K_p is a function of fewer variables, as equation (5.17) shows:

$$K_p = f(\nu, \psi) \tag{5.17}$$

Notably the properties of elasticity and hardness are not now involved, and as a result a theoretical analysis based on a center-loading, full-penny-shaped crack in an infinite solid has been applied to calculate K_p. The resultant expression is shown in equation (5.18)

$$K_p = \frac{(1 - \nu^2)}{\pi^3 \tan^2 \psi} \tag{5.18}$$

A theoretical curve for K_p against indenter half angle ψ is shown in Figure 5.7. It is possible to compare theory with observed results by using equation (5.16) and a material such as glass for which good values for γ and E have been found independently. Indenters can be sintered from tungsten carbide powder with a range of half angles. Figure 5.7 indicates divergence between theory and practice. To accommodate such divergence
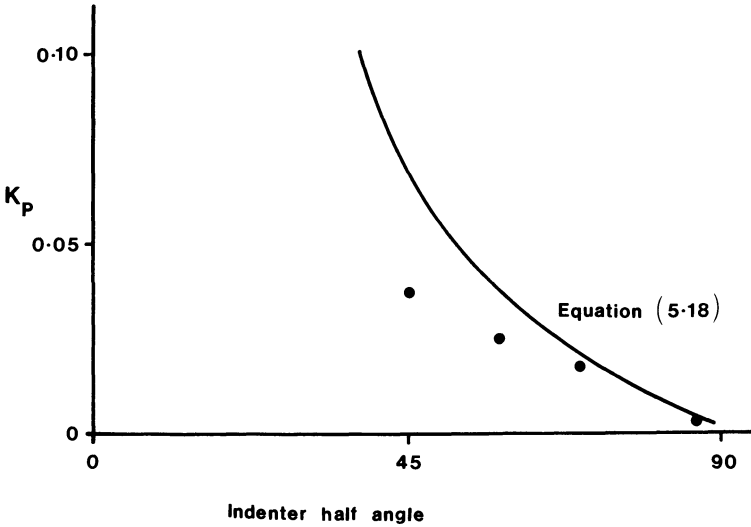
Figure 5.7. Median crack parameter K_p as a function of indenter half angle, equation (5.18) using $\nu = 0.2$. Glass indented with WC produces points shown as •.

it has been suggested that interfacial friction between sample and indenter is an important parameter with the result that equation (5.18) is changed to

$$K_p = \frac{(1 - \nu^2)}{\pi^3 \tan^2 \psi'} \qquad (5.19)$$

where $\psi' = \psi + \tan^{-1} \mu$ and μ is the coefficient of friction between indenter and sample. Since the real values of μ during indentation are difficult to measure or even estimate, this is another reason why models, theory, and experimental data are closely linked in this application of hardness techniques to ceramic systems.

5.2.1.3. The Lateral Vent Crack

These cracks are much shallower and are formed on *unloading* at the boundary between elastic, nonpermanently deformed material and the plastically deformed material close to the indenter; the interface between these two regions is the source of a stress field because material that has been plastically strained has a different stress–strain behavior than the normal material.

Analysis has shown that the component σ_{zz} of the stress field is tensile in character, acting parallel to the sample surface and at a maximum about $\beta/2$ below the surface; β is defined in equation (1.16). On unloading, the

stress is greater than on loading; thus it is able to propagate any nucleated cracks along directions or planes parallel to the surface. This gives rise to the name *lateral crack system*. Clearly if a critical load is exceeded these shallow cracks can be made to "pop-in" and produce surface traces. So far little analysis has been expended on the lateral vent system despite the fact that it is so close to the surface and can break through to it and is therefore a major source of material removal from ceramic surfaces (i.e., erosion and wear).

In all cases where direct observations can be made (that is, in transparent or translucent samples) the lateral cracks are seen to nucleate just prior to complete *unloading* of the indenter. Nucleation is followed by an initial unstable propagation to a stopped stage beyond the immediate indentation plastic zone. Finally as the indenter unloading continues the laterals propagate stably. The final crack length is always larger than the indentation diagonal. However the lateral crack length is variable with respect to radial crack length, being longer in some cases and shorter in others as shown by the circular contours in Figure 5.8.

Compared to the radial crack, the lateral is more susceptible to subcritical growth and slow growth on unloading due to atmospheric effects. This is to be expected from their near surface position and the fact that corrosive elements can penetrate down the radial traces to the laterals.

The presence of lateral cracks causes visible raising of the sample surface around the impression zone. Thus they are not constrained in the way that median cracks are. This lack of constraint makes the modeling and analysis much more difficult. Notwithstanding such difficulty, a recent analysis has been presented.[6] The basis of this analysis is given now.

The material above and below the lateral crack is distinguished by its different compliance; at depth $<h$ in the surface zone, Figure 5.2(b), the

<center>a   b</center>
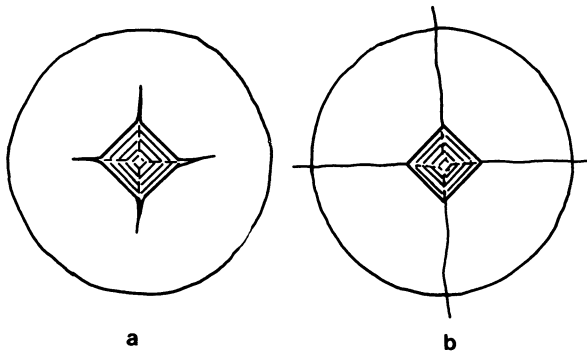
Figure 5.8. (a) Lateral crack much longer than radials. (b) Lateral crack system shorter than radials.

surface allows much movement, while material at depth $>h$ is more rigidly held. For this situation a linear compliance relation is assumed:

$$U_r = \lambda P_r \qquad (5.20)$$

In equation (5.20) U_r is the net load-point displacement, P_r is the residual tensile force exerted on unloading, and λ is given by equation (5.21) for a circular plate of material as defined by the extension of the lateral cracks being held rigidly at the edges.

$$\lambda = \frac{Ac^2}{Eh^3} \qquad (5.21)$$

In equation (5.21), A is a geometrical constant varying within the two extreme cases shown in Figure 5.8: When lateral length $>$ radial crack length $A = 3(1 - \nu^2)/4\pi$, implying no interaction between the two systems, and $A = \frac{3}{4}$ when lateral crack length $<$ radial crack length. The crack extension force is

$$\frac{P_r^2}{2} \frac{d\lambda}{dA'} \qquad (5.22)$$

A' in equation (5.22) is the crack area, πc^2 in Figure 5.2(b). For plane strain fracture the crack extension force is $K^2(1 - \nu^2)/E$.

Using this fact and equations (5.21) and (5.22), the stress intensity factor is then

$$K = \left[\frac{A}{2\pi} (1 - \nu^2) \right]^{1/2} \frac{P_r}{h^{3/2}} \qquad (5.23)$$

The residual tensile force P_r has to be modeled, and a precompressed linear spring acting through the center of the slipped material and indentation pyramid is chosen

$$\frac{P_r}{P_{r_o}} = 1 - \frac{U_r}{U_{r_o}} \qquad (5.24)$$

In equation (5.24), P_{r_o} is the force exerted by the spring in a fully compressed state when $U_r = 0$. Then U_{r_o} is the displacement in the fully relaxed state when $P_r = 0$.

Equation (5.20) can be used to replace the movement term U_r, which is otherwise not easy to determine, and use of equation (5.21) effects further simplification

$$P_r = \frac{P_{r_o}}{\left(1 + \dfrac{AP_{r_o}c^2}{EU_{r_o}h^3}\right)} \tag{5.25}$$

By obtaining expressions for P_{r_o}, U_{r_o}, and h in terms of material properties from the model and from the geometry shown in Figure 5.2(b), it has been possible to express the lateral crack size as a function of applied load

$$c = \left[\frac{B}{(A')^{1/2}}\cot^{5/6}\psi\left(\frac{E}{H}\right)^{3/4}K_c^{-1}H_v^{-1/4}\right]^{1/2}P^{5/8}\left[1-\left(\frac{P_o}{P}\right)^{1/4}\right]^{1/2} \tag{5.26}$$

In equation (5.26), P_o represents a threshold for the analysis, not to be confused with a threshold load necessary to initiate cracks.

$$P_o = \frac{D}{(A')^2}(\cot\psi)^{-2/3}\frac{K_e^4 E}{H_v^4} \tag{5.27}$$

In equations (5.26) and (5.27), B and D are dimensionless constants found from experiments using glass: $B = 2.5 \times 10^{-2}$, $D = 1.2 \times 10^3$.

The lateral crack length for large contact loads when $P \gg P_o$ is seen to depend on load as $P^{5/8}$ which is a useful approximation when considering the role of the lateral crack system in ceramic erosion and in making estimates of the effects of collisions on ceramic surfaces. Perhaps this is the field where this analysis will be most used in ceramic systems.

5.2.1.4. Palmqvist Cracks

These cracks are shown in Figure 5.2(d). They are shallow *radial* surface cracks lying within median planes (i.e., planes containing the axis of the indenter) extending out from the corners of an indentation. Clearly when the median crack "pops in," the Palmqvist cracks become part of the median–radial system described in Section 5.2.1.2.

There has been some discussion as to whether these cracks always precede the formation of the median crack in ceramics and therefore are evident before the penny median can become the halfpenny radial. An answer to this query is important because if they do always occur first, then surface flaws are important in their formation and subsequently in the mechanical failure, erosion, and wear of ceramic materials. Furthermore,

equation (5.11) will need to be modified as a more complex stress-field function is developed to explain their existence. Such a modification will only affect the constant multiplying the K_c^4/H_V^3 term in equation (5.11).

A model analysis using a more complex stress distribution which increases the slip length along which shear stress acts from $1.4a$, where a is half the indent diagonal length, to $1.577a$ if Palmqvist cracks first form without a prior median crack, gives a tensile stress acting across radial planes greater by a factor of about 13 than the tensile stress acting in the median plane. Thus the near surface plastic zone makes a bigger and more effective search for flaws than the median stress. This puts the model more in accord with the practical experience that surface flaws are dominant in strength degradation of glasses and ceramics under impact. The increased tensile stress, relative to the median crack model, leads to a prediction that the Palmqvist radial cracks will form before the median crack.

Acoustic emission studies and microscopy, used to examine Al_2O_3, SiC, Si, and Ge, do show that for these materials the first cracks formed on increasing the indenter load are the Palmqvist radials; this necessitates a change of the constant in equation (5.11) from 867 to 700 which in turn leads to lower critical loads at which strength-degrading flaws are produced; equation (5.12) requires no alteration.

5.2.1.5. The Effect of Temperature on Radial and Lateral Cracks

In Chapter 4, as equation (4.19) highlights, it is demonstrated that hardness is not a simple function of temperature because the mechanisms contributing to the movement of material change; at low temperatures hardness is only a weak function of temperature and athermal mechanisms are responsible for plastic deformation. At higher temperatures hardness decreases strongly with temperature increase as deformation occurs through a combination of dislocation glide and thermally activated dislocation climb. The change from regime I to regime II identifies a temperature T_c which is a material constant. It is however *not* a conventional ductile–brittle transition temperature but, not unexpectedly, it does have an effect on the radial and lateral crack size. As Figure 6.11 shows, there is a dramatic increase in radial crack size in the case of silicon in the range 300–400°C. The dramatic increase is due to an increase in the *residual* stresses because the increased temperature results in greater plasticity and hence an increased plastic–elastic zone boundary. This in turn produces an increase in the $(E/H_V)^n$ term in any of the equations developed to relate toughness, K_{IC}, to applied load, hardness, Young's modulus, and crack extent in Section 5.4.2. Thus following a temperature interval when the crack length shows no dependence on temperature, there is a regime in which a strong correlation between crack length and temperature exists, because while E is little

affected by temperature the hardness decreases sharply after T_c has been exceeded. A further consequence of the sharp decline in hardness after T_c is seen in equation (5.11) which then indicates that an increased critical load is needed to produce cracking as crack nucleation becomes more difficult at high temperatures.

Because crack lengths are used to determine K_{IC}, and because the equations are developed for crack systems of stated geometry, care is needed when considering individual ceramic systems tested at elevated temperature. For example, with GaAs low temperature cracks are deep, approximating to the halfpenny shape, but high temperature cracks are shallow. On the other hand in Ge the low temperature cracks are long and deep for a given load but the high temperature cracks are deep and *short* for the same load. Such differences arise from the geometry of slip as discussed in Chapter 3.

5.2.2. Blunt Indenters

The archetypal blunt indenter is the Brinel or Rockwell ball type (see Section 1.4) in which a spherical ball is centrally loaded as shown in Figure 5.9. When the ball is loaded past a critical value, ring cracks within the annulus region denoted as CB-B'C' on the figure are produced. Such cracks have a circular trace on the surface and a conical shape within the volume beneath the indenter, as shown in Figure 5.10. The conical shape arises as the crack deviates outward to avoid the compressive field below the indenter.

The pressure applied through the ball has three main consequences: It creates a depression; it produces some flatness on the ball face; and it
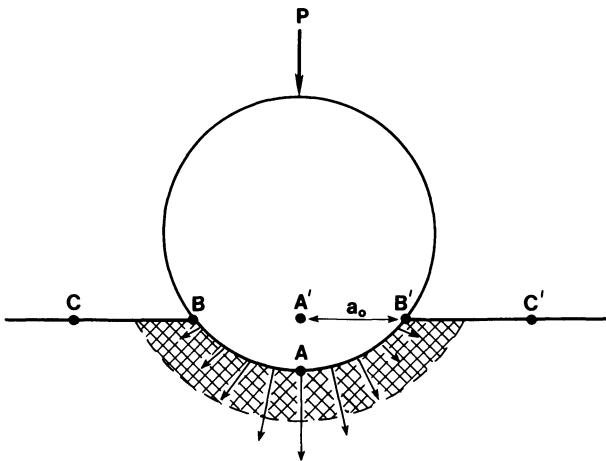
Figure 5.9. Spherical indenter on surface CC'.
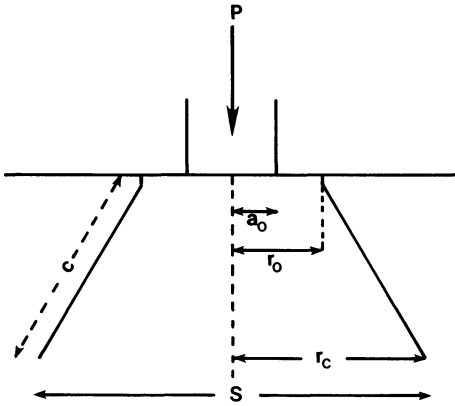
Figure 5.10. A well formed cone crack that is developed when either a ball or flat cylindrical punch is pressed into a ceramic surface with a pressure $P > P_c$.

causes tangential elastic displacements of the contact surfaces directed *radially inwards* towards the center of the contact circle.

Analysis of these elastic displacements leads to compression of the surface in the center of the contact region at A and the change of compression to tension on moving upward to the circumference BB'. The maximum tension occurs at the edge of the contact circle which has the radius a_o in Figure 5.9. The tension decreases outside the contact area toward the circle CC' according to the relationship

$$\sigma_a = \frac{(1 - 2\nu_1)P}{2\pi a^2} \tag{5.28}$$

where σ_a = the tensile stress at radial distance a, ν_1 = Poisson's ratio of the ceramic surface, P = load, and a = the distance from A' in Figure 5.9.

The tensile stress at a as expressed by equation (5.28) can be related to the radius of the indent impression a_o

$$\sigma_a = \frac{(1 - 2\nu_1)P_o a_o^2}{3_a^2} \tag{5.29}$$

In equation (5.29), a_o is the contact radius and P_o is the maximum stress applied, sometimes called the Hertz pressure.

Following the above analytical conclusions, because the maximum tensile stress occurs at the periphery of the indentation, circle BB', it would be expected that at some critical load a crack would nucleate and propagate around the circumference BB'. On a surface of glass or another amorphous material a ring crack is observed, but on highly anisotropic crystalline ceramics a less well traced crack is produced as the ring has a definite

polygonal appearance; with alumina, for example, such surface cracks are distinctly hexagonal. However, the *position* of such cracks on all types of material is some 20–30% further out from BB, falling within the region CB–B′C′.

There is no agreed explanation for the variable radius of the ring crack on ceramic and glass surfaces. A common belief is that a pre-existing surface flaw will reach critical proportions and nucleate the crack in which case $a > a_o$. To investigate this proposition the relationship between the load needed to cause cracking and the radius of the indenter has been examined by using the relationship between the radius a_o of the contact circle and sphere radius R

$$a_o^3 = \tfrac{3}{8}PR\left(\frac{1 - \nu_1}{G_1} + \frac{1 - \nu_2}{G_2}\right) \tag{5.30}$$

In the above expression, G and ν are shear modulus and Poisson's ratio, respectively, with the subscripts 1, 2 being used to distinguish between ceramic surface and indenter material, respectively.

Using equations (5.28) and (5.30), σ_a can be related to R

$$\sigma_a = \frac{(1 - 2\nu_1)P}{2\pi\left[\tfrac{3}{8}PR\left(\dfrac{1 - \nu_1}{G_1} + \dfrac{1 - \nu_2}{G_2}\right)\right]^{2/3}}$$

or, using a more compact form,

$$\sigma_a Y R^{2/3} = X P^{1/3} \tag{5.31}$$

Hence the critical load P_f to cause ring cracking is related through equation (5.31) to indenter radius

$$P_f \propto R^2 \tag{5.32}$$

A square dependence such as that in equation (5.32) is found only for large indenters with $R > 3.5$ cm.

For small-radius indenters a direct dependence is found

$$P_f \propto R \tag{5.33}$$

The relationship shown as equation (5.33) is sometimes called *Auerbach's*

law. It has been suggested that a statistical relationship between mean surface–flaw spacing and absolute size of stress field accounts for the change to Auerbach's law as R decreases.

It is common to use a ball made from different material than the surface under investigation and this feature has consequences that some investigators feel are important. The most significant parameter introduced in this situation is *friction* arising from differing elastic constants for specimen and indenter. On contact, material is displaced radially inward a distance proportional to $(1 - 2\nu)/G$. This slip is resisted by frictional traction acting radially outward on the more compliant surface and inwards on the surface showing less movement. This situation now modifies the radial tensile stress at points outside the contact circle by reducing it in softer material but *increasing* it in the harder less compliant material of larger modulus value. A steel ball indenting glass corresponds to the latter proposition, leading to ring cracks outside the contact zone periphery.

When the indenter is more compliant, the maximum stress in the sample is increased due to the frictional forces but remains at the edge of the contact circle. Smaller diameter secondary cracks are sometimes produced as the indenter ball is *unloaded* in cases where Young's modulus of the ball exceeds that of the surface under test. If, as suggested above, friction is an important parameter, then on unloading there will be a reversal in the direction of frictional traction at the edge of the contact circle which will produce an increase in stress nearer to the contact radius which can, if there is a critical sized surface flaw in the vicinity, give rise to the secondary ring crack.

A significant feature of a ball indentation test that makes ring–crack initiation and propagation difficult to analyze and observe is the fact that as the indenter is pushed into the surface it produces a contact circle of increasing radius. This can engulf an already formed crack, allowing the compressive stress field to work to close the surface trace of such a crack. Furthermore, the stress contours from the periphery must change and move as the contact radius increases. In order to counter this effect, work has been done using a cylindrical flat-end punch to have a constant radius of contact; this work has been considerably extended of late[7] by incorporating a stress field analysis found in earlier mathematical reports. A schematic representation of a well formed cone crack is given in Figure 5.10 for a blunt cylindrical punch. This schematic geometry is also expected for the more common ball indenter.

Development of this type of crack is discussed in terms of the dimensions c/a_o as defined in Figure 5.10. The crack is known as a *shallow ring crack* for $c/a_o < 10^{-1}$, and as a *cone crack* within the ceramic when $c/a_o > 10^{-1}$. A good analytical curve has been developed by Mouginot and Mangis[7] by plotting the variables $G/2\gamma$ against c/a_o where G is the

strain energy release rate and γ is the specific surface energy. In order to do that, G is found from equation (5.34)

$$G = \frac{1-\nu^2}{\pi}\left(\frac{1-2\nu}{2}\right)^2 \frac{P^2}{Ea_o}\left(\frac{a_o}{r_o}\right)^4 \frac{c}{a_o} \tag{5.34}$$

Depending upon Poisson's ratio, the applied load P, and the position where the crack nucleates on the surface, as defined by r_o in Figure 5.10, the curves have a general shape for a blunt cylindrical punch like that sketched in Figure 5.11. Such curves allow a discussion of ring and cone crack development along the following lines: equilibrium is conventionally defined as $G = 2\gamma$. Thus the equilibrium criterion is the dotted line in Figure 5.11, which cuts the curve with two maxima for a given critical load. On a branch of the curve with positive slope, the equilibrium is unstable, and vice versa on a branch of the curve with negative slope.

Consider a flaw existing at a position defined as c/a_o in Figure 5.10. It will have a length of, say, c_f. Let c_f/a_o correspond to point A in Figure 5.11; as can be seen, it is on the curve of positive slope and the equilibrium is unstable so that G will increase at constant load by using the elastic strain energy to make the crack spontaneously extend. This is denoted by
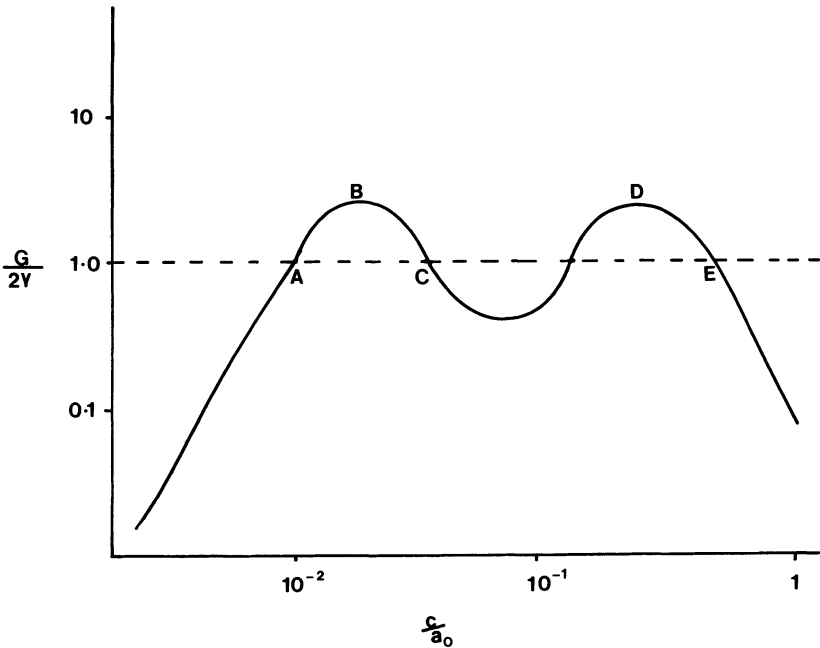
Figure 5.11. Strain energy release rate against c/a_o curve as derived from equation (5.34) for fixed values of ν, r_o/a_o. Points A–E are discussed in text.

an increasing c/a_o. After point B an increase in c/a_o is on the negative slope, so the crack slows down as it advances, eventually coming to rest on the equilibrium line at point C; now an increase in load is required to continue growth. Since $c/a_o < 10^{-1}$, a shallow surface ring has been formed. If P is increased, the whole of curve ABCDE is lifted to higher $G/2\gamma$ values and so stable growth down the negative slope curve can continue. At some critical load P^*, the minimum of the ABCDE curve will lie on the $G/2\gamma = 1.0$ line, so an increase of c/a_o will be spontaneous and accelerating since the slope of the curve for increasing c/a_o is positive up to the next maximum, point D. Then it will decelerate in stable growth to a point like E on the equilibrium line again. Now $c/a_o > 1$ and a well developed cone has followed from the initial shallow surface ring crack.

Equation (5.34) gives G in terms of cone edge length c and ring crack start radius r_o. It can be re-expressed in terms of cone base diameter s

$$G = D\frac{P^2}{Es^3} \tag{5.35}$$

Here D is a constant depending upon ν and cone angle; values from 5.7×10^{-3} to 2.15×10^{-2} have been estimated.

5.2.3. Indent Edge Cracks

Porous samples that densify beneath the indenter exhibit a crack pattern which is characteristic of such a microstructure; Figure 6.23 is an example of such a crack pattern which is a network of fine cracks along the sides of the indent. It is clear in Figure 6.23 that porosity is considerably reduced within the indented area and therefore compaction has occurred. The compaction mechanism is one of grain-boundary fracture and grain rearrangement.

A semilog plot of hardness versus the log of the pressure used to form the porous specimen is linear, suggesting that the hardness of a porous body can be estimated from a value of the compaction pressure used in sample forming.

As equation (1.2) predicts, porous ceramics have low hardness and, because of compaction and edge crack generation, such hardness is relatively temperature insensitive.

5.3. SUMMARY OF SEQUENCE OF EVENTS BENEATH A SHARP INDENTER

The description of the crack types in Section 5.2 has to some extent dealt with this sequence, but it is worthwhile considering the model process

again in a stepwise fashion. This is because it is these important concepts that have led to a series of semi-empirical calculations linked to experimental data-fitting exercises that produce a universal curve relating hardness, Young's modulus, crack size, and the toughness parameter K_{1C}.

STEP 1.	Loading produces a stress field.
STEP 2.	The stress field is seen as building up from a. the applied load, and b. the stress between the bulk of the sample around the indented area, which is only moving in accord with the elastic modulus and material which has flowed plastically from the indent volume. Since this will be present when applied load is removed, it is called the *residual stress.*
STEP 3.	The applied load as in (a) above causes a *tension* in the bulk material which has a maximum at the interface between the elastic body and the plastically deformed zone, in turn causing microcracking dependent upon the surface flaw population and the nucleation mechanisms of slip.
STEP 4.	Microcracks nucleated in Step 3 develop into a penny-shaped crack below the indenter and shallow Palmqvist cracks in the surface region. These are the *median* and *radial* cracks.
STEP 5.	In the surface the indenter causes compression, not tension; this acts in opposition to the residual stress.
STEP 6.	As the indenter is withdrawn, the surface compression decreases to zero.
STEP 7.	The residual stress now acts toward the surface and on it to produce cracks with surface traces that can be seen in the microscope on suitably polished surfaces; these are *radial cracks.*
STEP 8.	Radials and medians have combined to give semi-elliptical cracks, called *halfpenny* cracks, whose surface diameter is about twice the maximum depth.
STEP 9.	Fully developed radials are in mechanical equilibrium and have crack dimensions that are determined by K_{1C}; hence, this parameter can be measured.

As outlined, these steps in the loading–unloading cycle lead to three main applications of the indentation hardness technique that will be developed with examples in the remainder of this chapter.

First, there has been much analytical work on the residual stress fields, (see Section 1.4.1.1) in attempts to establish relationships that can be used to determine K_{1C}.

Second, the cracks developed at Step 8 are used as controlled flaws in macroscopic toughness determinations.

Third, the whole sequence is a good analogue of the formation of defects in ceramics and glasses following impact.

5.4. FRACTURE TOUGHNESS EQUATIONS

Evans and Charles[8] introduced the first relationship based on a dimensional analysis backed by experimental work to measure K_c by the double torsion technique and hardness with a Vickers diamond in the standard hardness macroindentation range shown in Figure 1.3. The ceramics studied were WC/Co, Si_3N_4, SiC, B_4C, sapphire single crystals, and spinel single crystals. An unfortunate choice of constraint factor for the diamond geometry was made which meant that this good semi-empirical beginning was later the source of some doubt and disagreement.

In general terms, the analysis showed that

$$\frac{K_c\phi}{H_Va^{1/2}} = F_1\left(\frac{c'}{a}\right) F_2\left(\nu, \mu, \frac{R_y}{a}\right) \tag{5.36}$$

where ϕ is the constraint factor (see Section 1.4.1.1), μ is the coefficient of friction between a material under test and the indenter, ν is Poisson's ratio, c is the radial crack extension as defined in Figure 5.2, a is the half diagonal of the indent trace (see Figure 5.2b), and R_y is the radius of the plastically deformed zone. F_1 and F_2 are empirically determined functions of the variables shown in parentheses. Experiments revealed that the c'/a function was more strongly related to $K_c\phi/H_Va^{1/2}$ than the F_2 function.

A good fit to experimental data was found if the F_2 function was

$$F_2 = \left(\frac{H_V}{E\phi}\right)^{0.4} \tag{5.37}$$

and a plot of $(K_c\phi/H_Va^{1/2})(H_V/E\phi)^{-0.4}$ against c'/a followed the experimentally determined points for the range of ceramics studied. When c'/a was large, the slope of the function was $-3/2$ which is what would pertain for a penny-shaped crack wedged by a force P at its center and so at the large crack extensions observed it is possible to use such a model and write for K

$$K = \frac{P}{(\pi c')^{3/2}} \tag{5.38}$$

Then, using equation (1.6),

$$\frac{K_c\phi}{H_V(a)^{1/2}} = 0.15S\left(\frac{c'}{a}\right)^{-3/2} \tag{5.39}$$

where S is a surface correction factor found experimentally to be 3.2. Using a constraint factor of 3.0, which has since been acknowledged as too large, and $S = 3.2$ the relationship for K_c becomes

$$K_c = 0.16 H_V a^{1/2}\left(\frac{c'}{a}\right)^{-3/2} \tag{5.40}$$

For ceramics in general, where no data for Young's modulus E exists, equation (5.40) can be used to determine K_c values at the 20–30% confidence level. When values for E are known, better toughness data can be obtained by using the full Charles and Evans equation

$$K_c = 0.0732\left(\frac{E}{H_V}\right)^{0.4} H_V a^{1/2}\left(\frac{c'}{a}\right)^{-3/2} \tag{5.41}$$

Naturally, following from the success of this original work, others have attempted to rationalize the approach and make it less empirical. Lawn and co-workers have provided justification for the approach and in the process found the H/E exponent in equation (5.37) by describing an approximate function relating plastic zone size to indent size. This approach leads to a dimensionless, independent constant that has to be calibrated by means of experimental data for chosen ceramics systems. In general, glass is chosen for this purpose.

5.4.1. Residual Stress

The residual stress in the vicinity of an indentation is complex and has not been modelled and computed with complete agreement, but recent attempts by both Chiang et al.[9] [see equation (1.17) and following] and Yoffe give residual stress fields near the surface of the material that have a compressive radial and a tangential tensile component decreasing as the third power of distance from the indentation center. The model applies to the elastic region and gives a value of the stress field at radius r

$$\sigma_r^{K(r)} = \frac{B(\Delta V)^2}{(r')^3} \tag{5.42}$$

ΔV is a reference volume equal to the radius of a hemisphere whose volume equals that of the Vickers indent. $\sigma_r^{K(r)}$ is the residual radial stress, and r' is the distance from the indent center. B is given by Chiang as 40 GPa. The tangential tensile stress is equal to $-\frac{2}{7}\sigma_r^{K(r)}$ when Poisson's ratio is taken as 0.25. As stated in Section 5.2.1.2, the residual tensile stresses associated with the indented area are about $H_V/20$ in magnitude.

Lawn, Marshall, and others have emphasized the fact that the residual stress term was not just a correction factor but played the important part in determining the final size of the radial crack system. However, like Evans and Charles, they developed the model of the plastic deformed zone acting to force open the penny-shaped median crack just beneath it, so that the basic equations to be used were still

$$H_V = \frac{P}{\alpha a^2}$$

$$K_c = \frac{P}{\beta (c')^{3/2}}$$

where α and β are constants; α is dependent on the indenter geometry and is 2.0 for the Vickers diamond, β is a complex geometrical constant incorporating interaction effects between the specimen-free surface and crack configurations that may not be as simple as the planar median system described in Section 5.2. The constant β has to be found by experimental calibration.

When $c' \gg a$, the cracks can be considered to be center loaded and the driving force characterized by separating out the residual stress as contributing to a residual stress intensity factor K_r for which the simple form is maintained

$$K_r = \frac{\beta_r P}{(c')^{3/2}} \qquad (5.43)$$

In equation (5.43), β_r is a constant that can be analyzed by modeling how the plastic impression is accommodated by the surrounding elastic matrix. All the several attempts so far show $\beta_r \propto (E/H_V)^n$; n was equal to 0.5 in Lawn's original work. The implication of β_r is that ceramics with weaker bonding, that is ionic and mixed ionic–covalent, will have lower values of E than the covalent types and be softer and so experience smaller residual driving forces. Thus they will be less susceptible to indentation and erosion cracking flaw generation.

When mechanical equilibrium has been achieved and the cracks show no movement either during the loading period or after the load has been removed, then

$$K_r = K_c = \frac{\beta_r P}{(c')^{3/2}} = \alpha_r \left(\frac{E}{H_V}\right)^{1/2} \frac{P}{(c')^{3/2}} \qquad (5.44)$$

Measurement of K_c by other methods gives the constant α_r in equation (5.44) as equal to 0.016 ± 0.004 which means that equation (5.44) can be used, when E/H_V and c' are determined at a known P, to obtain values for the fracture toughness of ceramics. Equally a plot of $(c')^{-3/2}$ against P has a slope $\alpha_r (E/H_V)^{1/2}/K_c$ and such a plot can be made if a series of indents at loads in excess of the critical load are made on the same surface.

5.4.2. Collected Equations

Following on from the Lawn analysis, all the subsequent relationships have the same two features: K_c is made proportional to $P(c')^{-3/2}$ by keeping the model which places the cracks in a center loaded position from the deformed zone-elastic zone interface. The ratio E/H_V appears in them all because the residual stress arises from deformation mismatch. A selection of these expressions is given below with a and c' defined according to Figure 5.2:

1. Evans and Charles[8] equations (5.40) and (5.41):

$$K_c = 0.16 H_V a^{1/2} \left(\frac{c'}{a}\right)^{-3/2}$$

or

$$K_c = 0.0732 \left(\frac{E}{H_V}\right)^{0.4} H_V a^{1/2} \left(\frac{c'}{a}\right)^{-3/2}$$

2. Lawn et al.[10]:

$$K_c = 0.028 \left(\frac{E}{H_V}\right)^{0.5} H_V a^{1/2} \left(\frac{c'}{a}\right)^{-3/2} \tag{5.45}$$

3. Evans[11]:

$$K_c = 10^4 \left(\frac{E}{H_V}\right)^{0.4} H_V a^{1/2} Y \tag{5.46}$$

where

$$Y = -1.59 - 0.34 \log\frac{c'}{a} - 2\,02\left(\log\frac{c'}{a}\right)^2 + 11.23\left(\log\frac{c'}{a}\right)^3$$

$$-24.97\left(\log\frac{c'}{a}\right)^4 + 16.32\left(\log\frac{c'}{a}\right)^5$$

4. Niihara *et al.*,[12] whose equation depends on the c'/a ratio; see also equation (5.53) for Palmqvist cracks:

$$K_c = 0.067\left(\frac{E}{H_V}\right)^{0.4} H_V a^{1/2}\left(\frac{c'}{a}\right)^{-3/2} \tag{5.47}$$

for $c'/a > 3.0$

5. Antis *et al.*[13]:

$$K_c = 0.016\left(\frac{E}{H_V}\right)^{0.5} P(c')^{-3/2} \tag{5.48}$$

6. Bhat[14]:

$$K_c = 1.59 \times 10^{-5} E^{0.4} P^{0.6} a^{-0.7}\left(\frac{c'}{a}\right)^{-0.36} \tag{5.49}$$

for $c'/a > 3$

Equation (5.49) is expressed in a form such that if P is measured in grams, a and c in microns, and E in $N\,m^{-2}$, then K_c can be found directly in $MPa\,m^{1/2}$.

7. Henshall and Brookes[15] have derived an equation for the Berkovich indenter starting from equation (5.41) and using a constraint factor of 2.57:

$$K_c = 0.0385\left(\frac{E}{H_B}\right)^{0.4} P(c'_B)^{-3/2} \tag{5.50}$$

In equation (5.50), H_B is the Berkovich hardness as defined by equation (1.8), P is the load in newtons, and c'_B is the length in meters of the surface crack as measured from the center of the isosceles triangular indent.

8. Shetty and Wright[16] are responsible for an experimentally determined equation that applies *only* to Palmqvist cracks. Working with WC/Co cermets that contained more than 5% by volume of cobalt, they observed that only Palmqvist cracks could be developed after the critical load P^* was exceeded, and further there was a simple linear relationship between surface crack length l' and load: $l' = (P - P^*)/4W$ from which W, the Palmqvist crack resistance constant, could be determined and used in equation (5.51) to determine toughness:

$$K_{IC} = \beta(H_x W)^{1/2} \tag{5.51}$$

In equation (5.51), β is a constant determined by the indenter geometry and material $\beta = 1/3(1 - \nu^2)(2^{1/2}\pi \tan \psi)^{1/3}$.

Thus for a Vickers indenter equation (5.51) becomes $K_{IC} = 0.089(H_V W)^{0.5}$, which in turn is

$$K_{IC} = 0.0445\left[H_V \frac{(P - P^*)}{l'} \right]^{0.5} \tag{5.52}$$

In this equation l' is the length of the Palmqvist crack.

9. Another expression dealing with the Palmqvist crack as opposed to the radial crack is equation (5.53), due to Niihara et al.[17] (for Palmqvist cracks only):

$$K_{IC} = 0.018\left(\frac{E}{H_V}\right)^{0.4} H_V a^{1/2}\left(\frac{l'}{a}\right)^{-0.5} \tag{5.53}$$

where l' is the measured trace of the Palmqvist surface crack. It must be emphasized that, since Palmqvist cracks are near surface phenomena, the specimen must either be very carefully and gently polished or an annealing procedure must be used to remove surface stress.

10. Mirazano and Moya[18] have produced more recent equations based on a more fundamental analysis involving the expansion of a spherical cavity modified by the creation of new surface and the shape of the indenter. It is an extension of Chiang's and Hill's analysis in Section 1.4.1.1. As long as c'/a is greater than 1.3 these equations can be applied *regardless of the crack type*:

$$K_{IC} = 0.09\left(\frac{c'}{a}\right)^{-1.08} f\left(\frac{E}{H_V}\right) H_V a^{1/2} \quad \text{for } \frac{c'}{a} \geq 2.8 \tag{5.54}$$

$$K_{IC} = 0.0136\left(\frac{c'}{a}\right)^{-0.5} f\left(\frac{E}{H_V}\right) H_V a^{1/2} \quad \text{for } \frac{c'}{a} \leq 2.8 \tag{5.55}$$

If H is expressed in GPa and a is in microns the answer will be in MPa m$^{1/2}$.

In the two equations (5.54) and (5.55) the function $f(E/H_V)$ is quite complex

$$f\left(\frac{E}{H_V}\right) = \frac{1}{1 - m}\left(\frac{1}{\Delta}\beta_{\exp}^2 - 1.5\right) \tag{5.56}$$

where β exp $= 1.35[E/\sigma_y(1 - \nu)]0.155$ with $\nu =$ Poisson's ratio and σ_y the yield stress; $\Delta = 0.66(1 + 3 \ln \beta_{exp})$ and m is a surface correction factor related to β_{exp} as Figure 5.12 shows and to hardness via equation (5.57)

$$\frac{H_V}{P - \dfrac{\sigma_r^s}{P}} = 1 - m \tag{5.57}$$

where σ_r^s is the radial stress at the expanding cavity interface.

All the equations so far listed, with the exception of equation (5.52), are based on analyses of wholly brittle monolithic ceramic systems. More recent considerations of the application of the indentation technique to the determination of K_{IC} parameters for cemented carbides containing ductile cobalt as a binder have resulted in the following two equations, which apply to Palmqvist cracks.

11. Peters[19]:

$$K_{IC} = 0.0132\left[\frac{E}{1 - \nu^2}\left(\frac{P}{4l'} + 86{,}300\right)\right] \tag{5.58}$$

In this equation ν is Poisson's ratio, P is the load in newtons, and l' is the average length of a Palmqvist crack measured from the Vickers
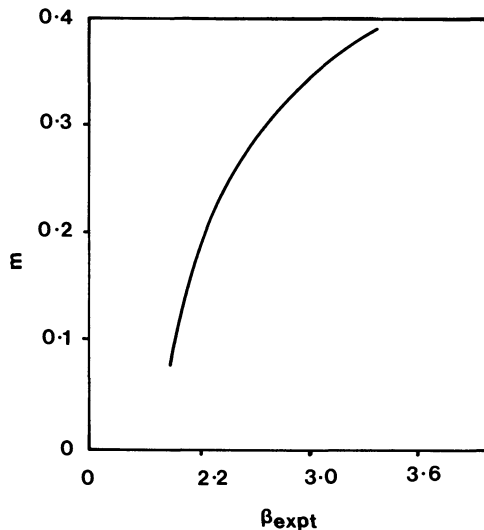
Figure 5.12. Correction factor due to free surface for equation (5.56).

indent corner. Put another way, $4l'$ is the total length of the Palmqvist crack around the indent.

12. Laugier[20]:

$$K_c = 2,150,000 \left(\frac{E}{H_V}\right)^{0.6} \left(1 + 0.012 \frac{E}{H_V}\right)^{-0.6} H_V^{-1.5} \qquad (5.59)$$

13. A method independent of crack type is the minimum load–crack nucleation method.[21] To operate this method the minimum load to nucleate cracks, P^*, has to be determined. By its nature this is a statistical method whereby about 20 indentations are made per load in a range from, say, 0.5 to 50 N. The number of indent corners where cracks appear are counted and expressed as a percentage of indent corners; the minimum load for crack nucleation, P^*, is the load of which 50% of corners project a crack, and then equation (5.60) can be used

$$P^* = 700 \left(\frac{K_c}{H_V}\right)^3 K_c \qquad (5.60)$$

This selection of "universal" equations, when applied to data from samples of the same material and therefore constant E, give for the same load a 100% variation in the calculated value of K_c. Such a variation represents the differences made in the final expressions by the assumptions used in the models to get the relationships as well as the quality of the calibration curves used to find the experimental constant α_r.

It is possible to use any of the expressions to find K_c at different loads, which usually results in a K_c versus P curve as sketched in Figure 5.13. The shape of the curve in Figure 5.13 is mostly controlled by microstructural features in the ceramic under test.

When a variety of samples are used there is some concern about the accuracy of the modulus value that is used in the equation chosen from those above. To some extent this can be overcome by using the technique *comparatively* to study, for example, the effect of a specific treatment or a change in microstructure, etc., on fracture toughness.

It must be re-emphasized that surfaces should have an optical finish to find crack length accurately and measurements should be made as fast as possible after indentation because ambient conditions can lead to corrosion growth of cracks and hence lower values of K_c as Section 5.11 clearly shows.

Samples studied should not be too soft, cracks should *not* interact and should develop correct halfpenny geometry (unless equations for Palmqvist cracks are chosen). Crack length must be in excess of the indent diagonal length to make the assumptions of the models leading to the above equations operative. Spalled surfaces should not be used; this problem can be corrected by adjustment of the load.
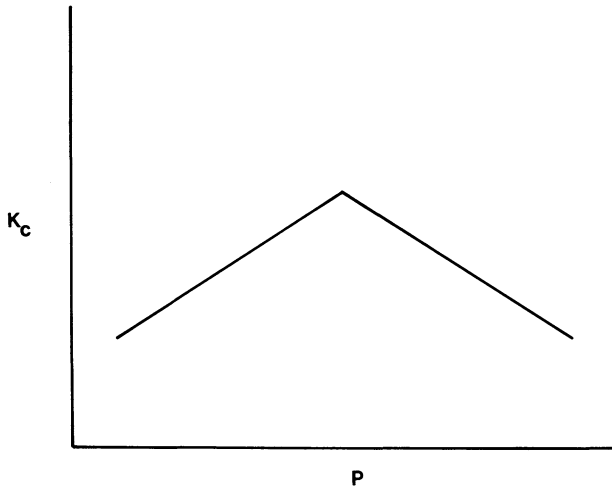
Figure 5.13. Load dependence of fracture toughness parameter.

Any surface compressive stresses must be annealed out unless of course one is trying to measure such a stress (see below). Finally, for polycrystalline samples the grain size must be small in comparison to the indentation size in order to generate a uniform crack pattern.

5.4.3. Determination of the Ratio H/E to Use in Toughness Determinations[22]

All of the requirements at the end of Section 5.4.2 arise from the nature of the models used to obtain equations (5.40) and (5.45)–(5.60), and efforts have been made to minimize their restrictions. A good example of this is the *in situ* determination of H/E by first indenting with a Knoop pyramid indenter using a load that does *not* produce a cracked indent. This method follows from the fact that on unloading there is some elastic recovery, related to E/H, in the depth of the indent. In order to determine the effect, low loads must be used in conjunction with surface analysis in a SEM.

The displacements of the shape when unloaded due to the elastic recovery in the zone immediately below the plastic zone in Figure 5.2 can be estimated by assuming an elliptical hole subject to a uniaxial stress

$$b - b' = \frac{\alpha x P}{E} \tag{5.61}$$

In equation (5.61), b is the short axis dimension under load, b' is the relaxed dimension when the indenter is removed, x is the long axis of the indentation under load, P is the load, and α is a constant.

Since P scales as H_K,

$$b - b' = \frac{\alpha' x H_K}{E} \qquad (5.62)$$

Dividing through by x

$$\frac{b - b'}{x} = \frac{\alpha' H_K}{E}$$

For a Knoop diamond, b/x is close to $\frac{1}{7}$ and b'/x' is then close to b'/x and it is possible to write

$$\frac{b'}{x'} = \frac{b}{x} - \alpha'' \left(\frac{H_K}{E} \right) \qquad (5.63)$$

If α'' is known, it is possible to find H_K/E from a measurement of the diagonals of a Knoop indentation. Using loads in the range 2–700 N for a series of materials of known E and H_K, a calibration curve emerges (see Figure 5.14) from which the slope $= \alpha'' = 0.45$.

The use of Figure 5.14 enables H/E to be determined for a ceramic material with an error $<10\%$. Then, armed with this value, a change of
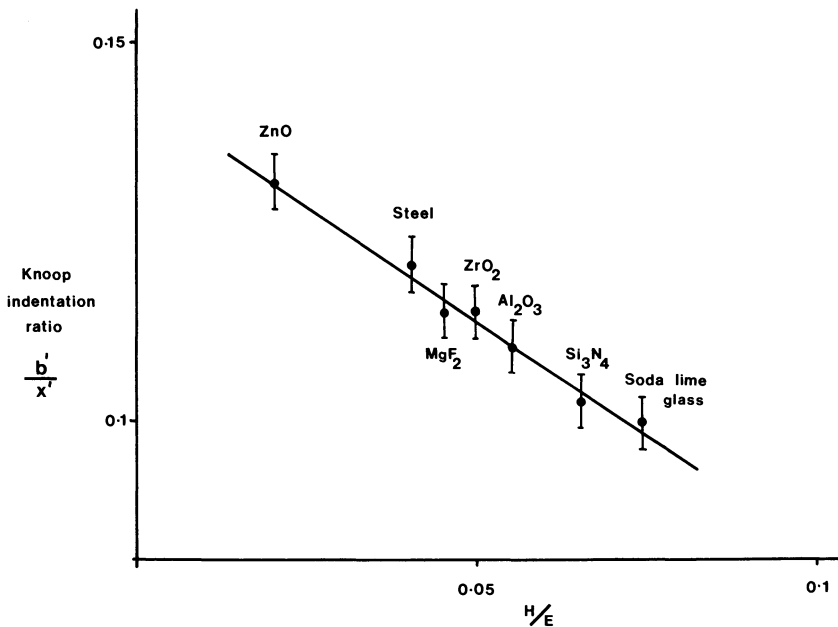
Figure 5.14. Determination of H_K/E from a noncracked indent in a Knoop hardness test.

diamond to Vickers geometry, and an increase in load to produce median trace cracks, a choice of equation from (5.40) or (5.45)–(5.60) gives rise to a fracture toughness value for the ceramic.

An alternative procedure to find H/E using the degree of elastic recovery on removal of a Vickers diamond has also been proposed.[23] The method is once again based on an analysis of the indentation process and in particular after two consecutive indentations at the same place using two different loads. The indent is first made using a load P_1 and on removal of the indenter the diagonal half length a_1 is measured. Due to elastic recovery the peak of the indent rises nearer to the surface and now, if a load $P_2 < P_1$ is used, the indenter penetrates only in an elastic manner but has to overcome the residual stress. Analysis of this situation with the knowledge that $\gamma_E = \pi/2$, where γ is the depth of penetration, that is, depth of tip below the contact perimeter and subscript E stands for the elastic only, second loading cycle, and the assumptions that $\nu = 0.25$ and γ_H, the original Z/a ratio, is a linear function of H/E, leads to

$$\left(\frac{Z_r}{a_1}\right)^2 = 0.08168\left[1 - 8.70\left(\frac{H_V}{E}\right) + 14.03\left(\frac{H_V}{E}\right)^2\right] \qquad (5.64)$$

Z_r = depth of first indent *after* elastic recovery; a_1 = half diagonal distance of indent after first load P_1. Thus the depth and diagonal length of a Vickers indent can be used to find H/E.

Finally, if a value of Young's modulus of the ceramic is needed to use in the toughness equations, a relationship suggested by Marshall *et al.*[22] can be used

$$E = \frac{0.45 H_K}{\dfrac{b}{a} - 0.1406} \qquad (5.65)$$

where a is the measured long axis length of the Knoop indent and b is the short axis length of the indent. To use equation (5.65) the Knoop hardness value for a load of 0.98 N has to be inserted.

5.5. ALTERNATIVE INDENTATION TECHNIQUES FOR FRACTURE TOUGHNESS

5.5.1. Residual Stress Method[24]

This approach to ceramic testing using hardness methods loses the advantage of the surface crack length versus load method because after

indentation the sample is tested to destruction in a bending mode. It can be argued that this approach measures the effective toughness of a ceramic since microscopic flaws which control the strength are frequently introduced by sharp contacts.

The big step forward in this method is the realization that the flaw propagation analysis can be made to include the residual strength term discussed in Section 5.4 and, in so doing, the microcrack size is replaced by the easily determined parameter, the normal load on the indenter.

In broad terms the argument is developed from Figure 5.15. In the arrangement shown in Figure 5.15 the lateral cracks experience no loading but the median or the radial cracks do, so that

$$K_a = \sigma_a (\pi c' \Omega)^{1/2} \tag{5.66}$$

In equation (5.66), Ω is a crack-geometry factor—that is, an experimental parameter which reflects the fact that the cracks are formed close to a free surface, that because of the demands of crystal structure the profile of the radian or median cracks may be noncircular, and that there is mutual interaction between radials and median cracks that are simultaneously formed.

The radial crack gives a surface trace, shown in Figure 5.2, equal to $2c'$. It is this flaw that now controls the strength of the indented bar, and failure will occur spontaneously from it at some critical experimentally applied stress; i.e., when $\sigma_a = \sigma_o$, then $K_a = K_c$ and (5.66) becomes

$$\sigma_o = \frac{K_c}{(\pi \Omega c')^{1/2}} \tag{5.67}$$

Equation (5.67) is telling us that the ceramic strength is controlled by the indentation flaw c', but two points must be remembered. First, the size of the radial c' may increase due to stress corrosion to a value c before the sample is loaded in tension to breaking. And, second, we must consider the residual crack driving force, arising from the permanently deformed
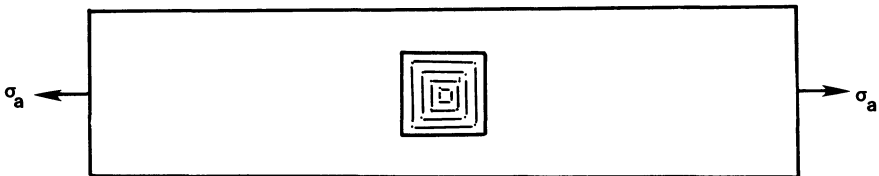
Figure 5.15. Beam to be tested has been indented so that the indentation has one set of edges parallel to the direction of applied stress.

indented area, which was expressed by equation (5.44). Thus the total stress intensity factor is the sum of two sources

$$K = K_a + K_r$$

From equations (5.66) and (5.44), this becomes

$$K = \sigma_a (\pi \Omega c')^{1/2} + \alpha_r \left(\frac{E}{H_V} \right)^{1/2} \frac{P}{(c')^{3/2}} \tag{5.68}$$

And, for growth under equilibrium conditions, $K = K_c$, hence

$$\frac{K_c}{(\pi \Omega c')^{1/2}} = \sigma_a + \alpha_r \left(\frac{E}{H_V} \right)^{1/2} \frac{P}{(c')^{3/2}} \cdot \frac{1}{(\pi \Omega c')^{1/2}}$$

and the relationship between applied stress and radial crack size then becomes

$$\sigma_a = \frac{K_c}{(\pi \Omega c')^{1/2}} \left[1 - \alpha_r \left(\frac{E}{H_V} \right)^{1/2} \frac{P}{(c')^{3/2} K_c} \right] \tag{5.69}$$

The applied stress can now reach some maximum that the sample can bear, and equation (5.67) has a maximum expressed as $d\sigma_a / dc' = 0$, which is to say

$$\sigma_{max} = \frac{3 K_c}{4 \pi \Omega c'_{max}} \tag{5.70}$$

and

$$c'_{max} = \left(\frac{4 \alpha_r \left(\frac{E}{H_V} \right)^{1/2} P}{K_c} \right)^{2/3} \tag{5.71}$$

These last two equations can be used to express the fracture toughness K_c in terms of the measured strength of the as indented, therefore flawed, ceramic beam

$$\sigma_{max} = \frac{3 K_c}{4 (\pi \Omega)^{1/2} \left(\frac{4 \alpha_r (E/H_V)^{1/2} P}{K_c} \right)^{1/3}}$$

which rearranges to

$$K_c = (\sigma_{max} P^{1/3})^{3/4} \left(\frac{E}{H_V}\right)^{1/8} [\tfrac{256}{27}(\pi\Omega)^{3/2}\alpha_r] \qquad (5.72)$$

Extensive comparisons of K_c as determined by conventional techniques and from equation (5.72) using glass, glass ceramics, Si_3N_4, and Al_2O_3 enables a value to be put on the last constant term in equation (5.72) as 0.59 ± 0.12. Thus the important final equation is

$$K_c = 0.59(\sigma_{max} P^{1/3})^{3/4} \left(\frac{E}{H_V}\right)^{1/8} \qquad (5.73)$$

The following points are worth noting

- There is no need to know the size of the radial crack and so careful surface polishing is avoided.
- σ_{max} is the measured strength of the as indented beam which will be *less* than the normal beam strength by at least a factor of two.
- The elastic–plastic parameters must be known; that is, hardness and Young's modulus must be measured. This can be achieved by using the Knoop indent method as already described in Section 5.4.3. However, if they are not known it has been estimated that removal of the E/H_V term and the 0.59, to be replaced by 0.88, will add only 10% to the error of estimation.
- A given peak load P will produce a c' value, but if there is considerable delay before measuring the tensile strength, extensive crack growth can invalidate the analysis since the experimental constants are determined assuming no slow crack growth. Some attempt must be made to restrict this by protecting the indent area with oil and performing the tensile test as soon as possible.
- Samples with compressive residual stresses in the surface will not follow this analysis, and such samples must be annealed to remove the stresses.
- In equation (5.73), since K_c and E/H_V are material constants and 0.59 is an experimental constant, $\sigma_{max}P$ should be constant over a range of indentation loads. This can be used as a test to investigate the applicability of this analysis to any given ceramic specimens.
- Failure in the tensile test must be seen to come from the indentation cracks for this analysis to apply.
- This equation could be useful in predicting strength degradation in ceramics subjected to hits by sharp particles when in normal use.

A recent use of equation (5.73) to determine K_{IC} values as a function of grain size for alumina[25] compares results to notched beam tests. The broken arms of the beams were used for the indentation–strength in bending test (ISB). Thus a good comparative study was possible. Figure 5.16 shows the close correspondence between the ISB results and the earlier results of Rice et al.[26] using a double cantilever beam method.

However, the notched beam results showed the opposite dependence on grain size for K_{IC}. Small grain sizes produced K_{IC} values about 6 MPa m$^{1/2}$ in the NB test. Notch radius effects and stress distribution in NB tests have been the subject of considerable theoretical discussion.[27] Thus the addition of this new technique to fracture toughness determination is contributing to theoretical development of the whole area. For example, one new suggestion is that the total stress intensity factor on an indentation crack of length $2c$ under an applied stress should not be taken as just a two-term expression like equation (5.68), but should have a third term involving the microstructure via grain size and shape, and distance between inclusions, all of which can contribute to crack deflections. If this suggestion is pursued then it has implications with respect to strength predictions for ceramics made from K_{IC} determinations that were themselves made from cracks of large size. Extrapolation to ceramic strengths using the large-crack K_{IC} values will predict strengths that are much too high. Introducing cracks via indentations at varying loads enables this important point to be tested because beam strengths after low-load indentation will reflect the effects of small cracks and vice versa.

Figure 5.17 demonstrates the effect with two regimes separated by the critical load P^*. Above P^*, the curve is a reflection of two terms in equation
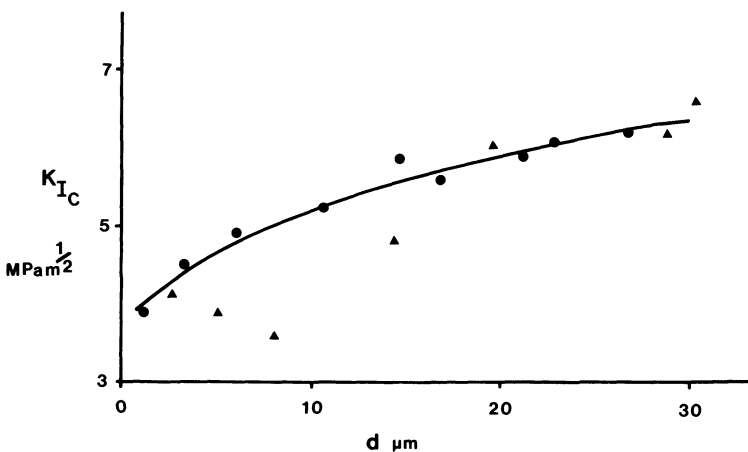
Figure 5.16. K_{IC} as a function of grain size: ●, ISB method; ▲, DCB method. After Rice et al.[26]
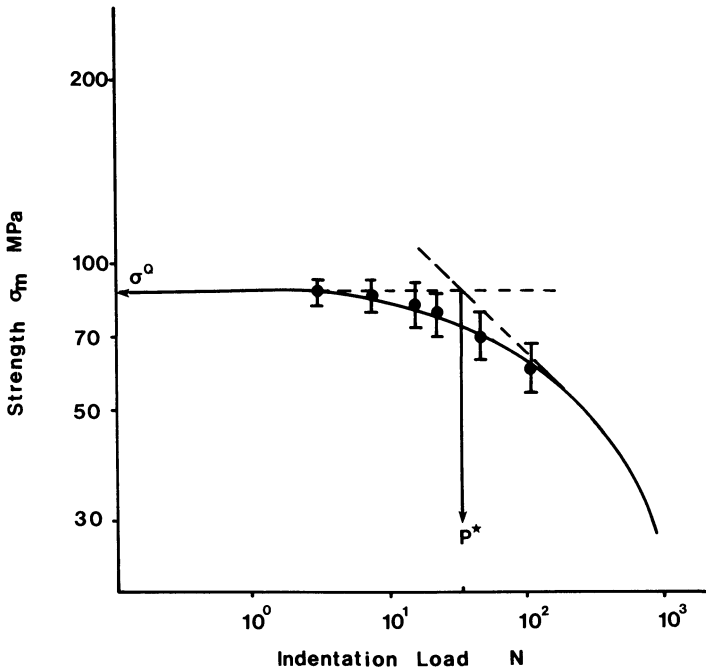
Figure 5.17. Plot of inert strength against indentation load for hot-pressed BaTiO₃.

(5.74) dominating; that is, the applied load driving force and the residual contact field. This is the normally accepted case expressed previously as equation (5.68). Below P^*—that is, for small indentation cracks—the two dominant terms are the applied load driving force and microstructural stress intensity factor $\mu Q/(c')^{3/2}$ in the three-term function

$$K = \sigma_a(\pi\Omega c')^{1/2} + \alpha_r\left(\frac{E}{H_V}\right)^{1/2}\frac{P}{(c')^{3/2}} + \frac{\mu Q}{(c')^{1/2}} \qquad (5.74)$$

When controlled by the first and third terms on the right-hand side of equation (5.74), the beam strength will no longer depend on the applied indentation load, as is in accord with results like those shown in Figure 5.17 for BaTiO₃. This behavior denotes once again the dominance of microstructural flaws in determining the intrinsic strength characteristics of real ceramics and the fact that these cannot be modeled with certainty from macroscopic flaws. The extrapolated strength value, σ^Q, is a useful design parameter obtained by combining indentation hardness methods allied to

bend strength determinations. The microstructural effect μQ can be estimated from

$$\alpha_r \left(\frac{E}{H_V} \right)^{1/2} P^* = \mu Q \qquad (5.75)$$

when P^* is determined by the extrapolation procedure shown in Figure 5.17.

5.5.2. Hertz Fracture Method

The Hertz method of determining K_c involves the use of an optically flat surface and a blunt—i.e., spherical—indenter. The sphere is pressed with a series of loads P_x until a critical load P_f is found that gives a 50% chance of Hertz ring crack formation. In practice this is found by plotting the fracture probability against applied load for any given indenter radius; a typical plot would look like Figure 5.18.

In order to establish plots like those in Figure 5.18, from which P_f can be found, a large number of indents must be made to measure how many cause ring crack formation. Indenters with radius less than 3.5 cm are chosen and the plots shown in Figure 5.18 are used to verify Auerbach's law, equation (5.33), which is assumed to apply so that the analysis developed by Warren[29] can be used. Such analysis gives P_f as

$$P_f = \frac{9.18 K \gamma}{(1 - \nu^2)} \frac{a_o}{c''} (\phi c'')^{-2} \qquad (5.76)$$
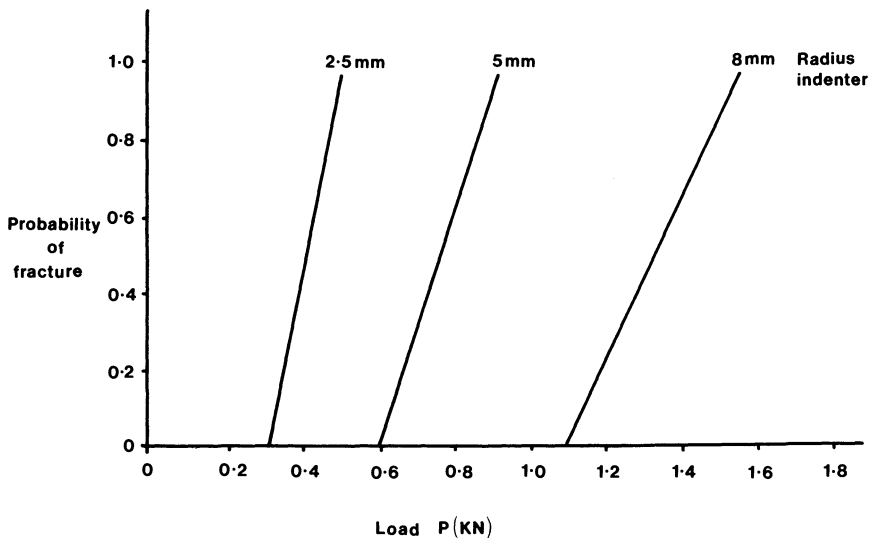
Figure 5.18. Relationship between probability of Hertzian ring crack formation and load for different-sized steel indenters on flat surface of a brittle ceramic.

In equation (5.76), K is a materials constant which can be obtained from the model and shown to be equal to

$$\frac{9}{16}\left[(1 - \nu_S^2) + (1 - \nu_I^2)\frac{E_S}{E_I}\right]$$

where ν is Poisson's ratio and E is Young's modulus with the subscripts S and I referring to surface and indenter respectively. In equation (5.76), γ is the fracture surface energy and a_o is the contact radius, which can be calculated from the applied load, the indenter radius, and the material parameters, by equation (5.30). Also, $(\phi c'')^{-2}$ is an integral function over the crack path of the principal tensile stress perpendicular to the crack path. These values are given by Warren.[29] Finally, c'' is the crack depth as measured after failure.

Thus a knowledge of P_f allows the fracture surface energy to be found, and this is related to fracture toughness via equation (5.77):

$$2\gamma = \left[\frac{1 - \nu^2}{E}\right]K_{IC}^2 \qquad (5.77)$$

This method involves critical load evaluation and crack depth measurement, and has been used in recent years to define fracture parameters in several ceramics, for example, UO_2, SiC, and TiC.[30,31]

5.6. THERMAL STRESS RESISTANCE

Traditionally, ceramics are ranked with respect to their ability to withstand thermal cycling and thermal shock by counting first the number of cycles required to produce visible surface cracks and finally the number required to produce fracture. However, during thermal shocking of ceramics such as occurs when carbide tool tips are used in cutting operations two processes are important: crack initiation and the propagation of pre-existing cracks. Thus the analyses already given in this chapter are quite relevant to characterizing this process more quantitatively.

For crack initiation caused by thermal shock, the appropriate parameter is

$$\text{crack resistance} = \frac{K\sigma_f}{E\alpha} \qquad (5.78)$$

where K = thermal conductivity, σ_f = tensile fracture strength, E = Young's modulus, and α = coefficient of linear expansion. The larger the value given by equation (5.78), the less likely it is that ceramics will have flaws initiated. Clearly this parameter is not particularly related to hardness. However, damage resistance, which is the extent to which flaws propagate by thermal shock, is characterized by the ratio $(K_{IC}/\sigma_f)^2$. Since K_{IC} can be obtained from microhardness measurements, then indirectly the technique can be used to rank ceramics with respect to thermal shock resistance. Undoubtedly the use of these two parameters is more analytical than the traditional method of ranking.

5.7. CERAMIC GRINDABILITY AND EROSION

5.7.1. Grindability

Grindability is a property of some interest in the ceramics industry, for example, where hydraulic cement clinker is made. The clinker is ground to a fine powder using some 38 kWh tonne^{-1} which represents considerable expenditure of energy. Grinding consists of two stages: first, breaking up crystal aggregates and second, breaking down the individual crystal phases. In the second stage, hardness is less important than brittleness and the brittleness index defined as H_V/K_c is a measure of ceramic grindability.

Indentation hardness therefore can be used to grade materials with respect to powder production and energy expenditure. For example, as Table 5.3 shows, Ca_3SiO_5 (C_3S in cement notation) is the most brittle component in cement clinker, requiring the least energy to grind it to satisfactory powders. The table shows magnesia to be almost twice as brittle as the most brittle parts of cement while Al_2O_3 is comparable to an average cement clinker.

Table 5.3. Brittleness Index of Cement Clinker Phases

Phase	H_V (GPa)	K_c (M/Pa m$^{1/2}$)^a	$H_V/K_c \times 10^{-3}$ m$^{-1/2}$
C_3S	7.5	1.7	4.7
C_3A	9.0	3.1	2.9
C_2S	6.7	3.7	1.8
C_4AF	9.0	N.D.	2
Al_2O_3	12.0	4	3
MgO	9.2	1.2	8

^{a}Determined by the post-indentation crack length method, equation (5.41).

5.7.2. Erosion Predictions

In Section 1.4.4, the erosion test was outlined in the list of hardness determination methods and it was concluded that it was of minimal practical importance. However, solid particle erosion is a serious problem in gas turbine operations and in plants where powders are handled and it is of course used as a secondary shaping method in ceramic technology. Therefore it is more useful to consider how a knowledge of ceramic hardness contributes to an assessment of erosion. Figure 5.19 outlines how a knowledge of the process has developed through models taken from the types of indentation test damage already discussed in this chapter.

In the type A approach, applied force and the penetration depth is assessed by converting the kinetic energy of a sharp indenter (representing a sharp particle) into plastic work on the target. The analysis concentrates on the production of intersecting *lateral* cracks and estimates the volume of surface removed per impact by finding the depth of the laterals, h in Figure 5.2(b), and the length of the lateral crack system. We have seen in equation (5.26) that we can calculate the lateral crack length, and so the material removed can be estimated. In practice a simpler expression for lateral crack length is assumed, $c \propto (P_{max}/K_c)^{2/3}$, and material removed is proportional to c^2 times the depth of penetration. Depth of penetration is found from one of the several equations relating applied load and indenter geometry as outlined in Chapter 1. Differences then arise for different shaped particles or the corresponding indenters; for example, model B1 in Figure 5.19 is concerned not with the lateral crack system but with the *median* crack system and model B2 with the size of the ring crack radii as given by equations (5.28) and (5.29).

All models—A, B1, B2—give, for steady state erosion, relationships containing the same material properties of the ceramic surface and contacting particle

$$\Delta w \propto (D^m V^n \rho^q)_p (H_x^a K_c^b)_s \tag{5.79}$$

EROSION MODELS

A   B

QUASI-STATIC   ELASTIC IMPACT

1   2

SHARP   SPHERICAL
PARTICLE   PARTICLE
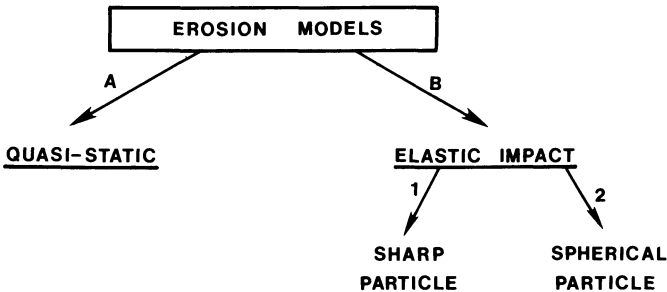
Figure 5.19. Schematic representation of erosion theory development.

Equation (5.79) has been arranged to emphasize the properties of impor-
tance in the particle (first parenthesis) and the material properties of
importance in the surface being eroded (second parenthesis). Δw is the
grams removed per gram of impacting particles. Particle properties are D,
the diameter; V, the velocity; and ρ, the density. Target surface properties
of importance are hardness, H_x, and fracture toughness, K_c. Each of the
models used gives rise to some differences in the values of the exponents
m, n, q, a, and b; equations (1.49) and (1.50) are complete expressions of
equation (5.79) and demonstrate this point. Table 5.4 collects together the
various exponents that can be used with equation (5.79).

By using the same hard powder, for example, Al_2O_3, to erode different
surfaces, the erosion rates can be compared via the hardness and toughness
parameters of the surface material—that is, the second bracket only of
equation (5.79). This is the usual way to use hardness data to make erosion
predictions; first use the cracked indent technique (see Section 5.4) to find
K_c and then use a Vickers indenter to find H_V. Where this has been done
carefully, it is obvious that all the predictions are very subject to variations
in the microstructure of the eroding surface. Data collected for Si_3N_4[33]
emphasize that practical erosion measurements are not capable of distin-
guishing between the various exponents in equation (5.79) and in practice
hardness measurements can be used in any of the several expressions
obtained by using a mixture of the quoted values from Table 5.4. Thus, as
long as the eroding particles are harder than the target material, efficient
erosion will occur and, as shown in Figure 5.20, experimental erosion data

Table 5.4. Exponents for Use in Equation (5.79)

Exponent	Model	Value	Notes
n	A and B	2.4–3.2	The value of n is an experimental one sensitive to particle size
m	A and B	0.66	
q	A	1.06	} Very model-dependent
	B	0.39	
a	A	0.11	
	B(2)	−0.25	Spherical particles
	B(1)	−1.42	Sharp particles
	Experimental	0.48	Practical analysis of available ceramic-only data[a]
b	A	−1.3	
	B(2)	−1.3	
	B(1)	0.16	
	Experimental	−1.9	

[a]From reference (32).
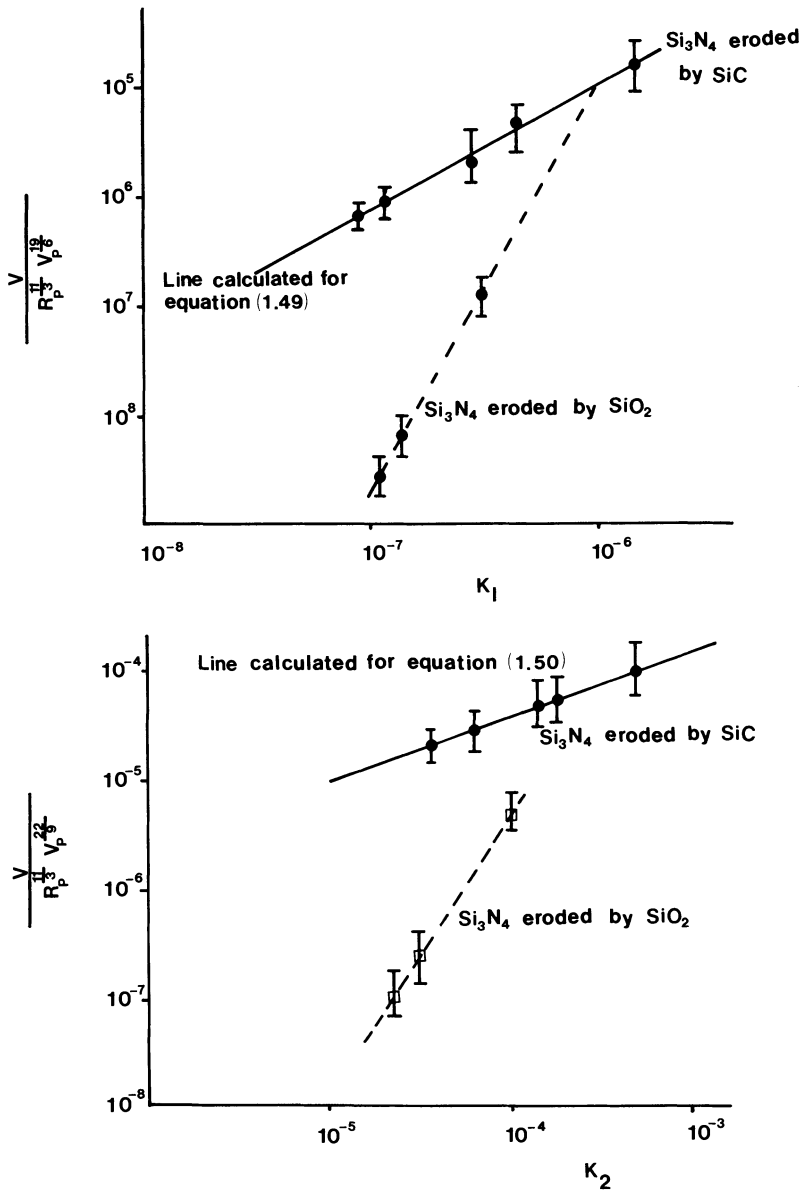
Figure 5.20. Erosion of Si_3N_4 by hard particles (SiC) and soft particles (SiO_2). The functions K_1 and K_2 can be derived from equations (1.49) and (1.50), respectively, where the symbols are described. The data are represented from reference (33).

fit the two types of model equally well and very well indeed and do not allow a distinction to be made between equation (1.49) and equation (1.50). When a soft particle is used to erode a hard surface, the agreement is not good, as Figure 5.20 clearly shows. The erosion of Al_2O_3 surface by Al_2O_3 particles also follows equation (5.79) well, but modifications have to be made when SiC fibers are included in the Al_2O_3 matrix.[34] The SiC imparts substantial erosion resistance as lateral cracks are made to supply fiber pull-out work. This can be modeled into the erosion process resulting in a change in the particle velocity exponent of either equation (1.49) or equation (1.50) to $\frac{14}{9}$ from $\frac{19}{6}$ or $\frac{22}{9}$, respectively, together with a change in the particle radius exponent to $\frac{7}{3}$ from $\frac{11}{3}$. With these changes to equations (1.49) and (1.50) the erosion of the matrix material of a ceramic–ceramic composite can be estimated from these equations given a knowledge of relative hardness among other parameters.

5.8. PREDICTION OF CRITICAL FLAW SIZE IN GLASS OR GLASS-CONTAINING CERAMICS CAUSED BY IMPACT

It is known that striking a glass artifact or a ceramic that is bonded by a glassy phase can cause subsequent strength degradation. This is believed to arise because the sharp impact nucleates flaws beneath the impacted area and the question is, can a knowledge of microhardness enable an estimate to be made of the size of flaws induced this way?

A semi-empirical analysis by Hagan,[35] based on Stroh's hypothesis about dislocation pile-up in polycrystalline material collapsing and coalescing to form a crack with overall decrease in energy if the effective shear stress conforms to equation (5.80), can be used

$$\sigma_s^2 = \frac{3\pi}{8}\left[\frac{\gamma G}{(1-\nu)L}\right] \tag{5.80}$$

In equation (5.80) γ = fracture surface energy, G = shear modulus, ν = Poisson's ratio, and L is the slip length along which shear acts. When radial cracks are formed along with median cracks, $L \leq 1.4a$ where a is, as usual, the half diagonal of the indent impression. Hagan's equations for critical load and the critical flaw length such a load produces are

$$P_{\text{crit}} = 885\left[\frac{K_{IC}}{H_V}\right]^3 K_{IC} \tag{5.81}$$

$$c_{\text{crit}} = 29.5\left[\frac{K_{IC}}{H_V}\right]^2 \tag{5.82}$$

As stated in Section 5.2.1.4, when considering Palmqvist cracks, ceramics can produce shallow radials without prior formation of median cracks, and then a new stress distribution is used to anticipate this situation such that L in equation (5.80) becomes $\leqslant 1.577a$; the result is that equation (5.81) is rewritten as equation (5.83) while the critical flaw size is left as equation (5.82) describes

$$P_{\text{crit}} = 700 \left[\frac{K_{IC}}{H_V} \right]^3 K_{IC} \qquad (5.83)$$

Inserting values for hardness and K_{IC} of glass shows that typically such flaws have a length of about 0.5 μm and that they are situated below the surface, suggesting that failure in glassy phases can result from nonsurface flaws. Common acceptance is that *surface* flaws are responsible for glass failure.[3] This paradox disappears if it is accepted that Palmqvist cracks precede the appearance of the medians during or after impact.

Flaws of the size estimated from equation (5.82) are the median, radial, and lateral cracks caused by indentation, and the questions are where and why do they nucleate in a noncrystalline material? Examination of the deformed zone beneath an indent or an impact shows that a series of intersecting flow lines is produced. Plastic strain is concentrated on the flow lines while the material between them is only strained elastically. Median cracks arise from the need to accommodate strains at the intersections of flow lines in a way analogous to crack nucleation from dislocations on intersecting slip planes in fully crystalline materials.

Lateral cracks are nucleated along the flow lines at the elastic–plastic boundary.

The lines observed in the plastically deformed region are not cracks because, when two cracks meet, for further progress to occur they have to renucleate, and hence the subsequent paths are not predictable while crossing lines can be seen to kink but still continue with the same curvature. Types of line intersection that have been observed are sketched in Figure 5.21.
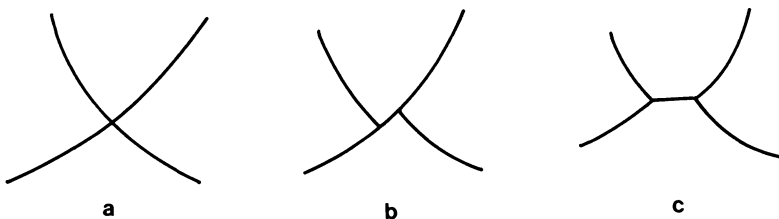
Figure 5.21. Intersecting flow lines observed in the plastically deformed region of glass beneath an indenter with (a) no effect on each other, (b) one line kinked, and (c) both lines kinked.

The kinking of the flow lines can lead to a *hardening effect* as a radial flow line in its progress meets another and is caused to kink, as shown in Figure 5.21(b); this requires an increase in propagation energy, and before this is reached another flow line can be nucleated elsewhere, absorbing more energy in total and limiting the penetration—i.e., increasing the hardness.

5.9. TECHNIQUES TO INVESTIGATE SURFACE LAYERS

It is more common to use a hardness versus load study to investigate surface features of ceramic systems, and this is dealt with in Chapter 4. However, since hardness determinations made at loads greater than the critical one needed to produce cracks around the indent are made, it is possible by applying the foregoing analyses to gain insights into the nature of surface layers by studying the crack lengths and patterns.

5.9.1. Determination of Compressive Stress in Tempered Glass

Equation (5.38) gives the stress intensity factor for driving forward cracks nucleated by the indentation technique. In the case now to be considered where the material has a compressive stress present in the surface layers, the driving force, equation (5.38), will be opposed by the compression

$$K_{\text{measured}} = K_{\text{extension}} - K_{\text{compression}}$$

$K_{\text{extension}}$ is given by equation (5.38) and $K_{\text{compression}}$ is proportional to the mean compressive stress over the crack volume and the crack length

$$K_{\text{compression}} = 2B\bar{\sigma}_c \left(\frac{c'}{\pi}\right)^{1/2} \tag{5.84}$$

The constant B is a dimensionless modification factor accounting for free surface effects and stress gradients along the crack depth as the compressive surface stress diminishes into the bulk. For the depths of compressed zones encountered in toughened glass, B is approximately unity, but it must be emphasized that this is not true for chemically tempered glass where the stress profile is very steep.[3]

During growth the crack is stable if K_{measured} is equal to K_c and is therefore a material constant

$$K_c = K_{\text{extension}} - 2\bar{\sigma}_c \left(\frac{c'}{\pi}\right)^{1/2} \tag{5.85}$$

and, writing in equation (5.38) for $K_{\text{extension}}$

$$K_c = \frac{AP}{(c')^{3/2}} - 2\bar{\sigma}_c \left(\frac{c'}{\pi}\right)^{1/2} \tag{5.86}$$

In equation (5.86), a general contact constant A has been used in place of the specific constant $\pi^{-3/2}$ shown in equation (5.38).

From equation (5.86) we get

$$\frac{P}{(c')^{3/2}} = \frac{K_c}{A} \left(1 + \frac{2\bar{\sigma}_c (c')^{1/2}}{\pi^{1/2} K_c}\right) \tag{5.87}$$

Since K_c / A is a material-experimental constant, a plot of $P/(c')^{3/2}$ against $(c')^{1/2}$ will be a straight line whose slope contains the $\bar{\sigma}_c$ term, and hence the mean compressive stress can be extracted.

The correct A term must be found experimentally by making cracked indents at various loads in a piece of the glass that has been annealed to remove the surface compression. Extrapolation to zero crack length in Figure 5.22 gives a working value for K_c / A, and since K_c can be calculated
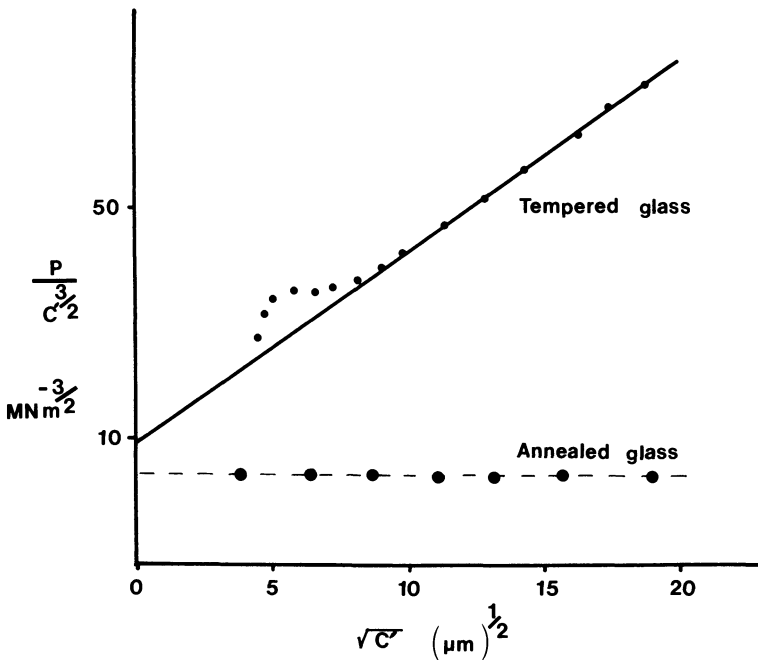
Figure 5.22. Typical crack length–load relationship for Pyrex glass.

from any of the equations (5.40) or (5.45) to (5.60) from the hardness and crack length data at the various loads chosen, A can be found. For example, the results shown in Figure 5.22 lead to K_c/A for the Pyrex glass used of 9.8 MN m$^{-3/2}$ and, since K_c is typically 0.75 MN m$^{-3/2}$ for this type of glass, $A = 0.076$ and a value of $\bar{\sigma}_c$ of around 130 MPa results for the tempered glass.

Opaque materials and not just glasses can be investigated using this technique.

The results in Figure 5.22 suggest that reliable data are limited to loads that produce c'/a values greater than 2. It must be remembered that although this is a nondestructive test the sample cannot safely be used again under stress because the induced cracks weaken it.

5.9.2. Estimation of Critical Load Required to Produce Surface Layer Flaws

As derived, the equations in this chapter can be used to *estimate* the magnitude of the minimum load required to produce a flaw beneath the impact zone when a particle hits a toughened glass screen. Using equations (5.86) and (1.6) we can first replace the applied load P with a Vickers hardness term

$$K_c = \frac{Aa^2 H_V \sin 136°}{0.2(c')^{3/2}} - 2\bar{\sigma}_c \left(\frac{c'}{\pi}\right)^{1/2} \tag{5.88}$$

There will be a threshold load that will produce a cracked indent such that we can imagine the situation where this is reached and the crack is just equal in size to the diagonal of the impression $2a$. Thus we can rewrite equation (5.88) using a_t as the threshold indent diagonal size

$$K_c = \frac{Aa_t^2 H_V \sin 136°}{0.2a_t^{3/2}} - 2\bar{\sigma}_c \left(\frac{2a_t}{\pi}\right)^{1/2}$$

which becomes

$$K_c = \frac{A \sin 136° H_V a_t^{1/2}}{0.2(2)^{3/2}} - 2\bar{\sigma}_c \left(\frac{2a_t}{\pi}\right)^{1/2} \tag{5.89}$$

Thus the limiting-sized indent that can be generated without producing the flawed specimen is, from equation (5.89), equal to

$$a_t = \left[\frac{K_c}{\dfrac{A \sin 136° H_V}{0.2(2)^{3/2}} - \dfrac{2\bar{\sigma}_c}{(2/\pi)^{1/2}}} \right]^2$$

which simplifies to

$$a_t = \left[\frac{K_c}{1.22AH_V - 1.6\bar{\sigma}_c}\right]^2 \qquad (5.90)$$

Now, using equation (5.90) to find a_t, it is possible to use equation (1.6) to estimate the threshold load P^*

$$H_V = \frac{0.2P^*}{a_t^2 \sin 136°}$$

$$P^* = H_V \frac{\sin 136°}{0.2} \left[\frac{K_c}{1.22AH_V - 1.6\bar{\sigma}_c}\right]^4 \qquad (5.91)$$

As equation (5.91) shows, the threshold load can be estimated from a knowledge of H_V, K_c, and $\bar{\sigma}_c$, all of which are found by the indentation hardness technique. In the case just considered, with $K_c = 0.75 \text{ MN m}^{-3/2}$, $H_V = 6 \text{ GN m}^{-2}$, $\bar{\sigma}_c = 130 \text{ MN m}^{-2}$, and $A = 0.076$, an estimate for P^* is 0.43 N. This small load over the area represented by a_t is of course a large local stress, but the estimate does emphasize that small particles can generate critical flaws beneath the surface. The effect of the surface compression layer can be seen by removing the $-1.6\bar{\sigma}_c$ term from equation (5.91) when the critical load decreases to 0.068 N for this glass.

These estimated values are of the same order of magnitude as those listed in Table 5.1 for glassy materials like silica when no surface compression exists and equal to those of MgO when one does. Equation (5.91) is in fact quite analogous to equation (5.11), showing a fourth-power dependence on the fracture toughness parameter, but the determination is somewhat simpler.

5.10. PREDICTION OF FRACTURE SURFACE ENERGY

The fracture surface energy γ is usually found by using the double cantilever beam and double torsion test methods and so fracturing the samples in the process. It is possible to obtain values for γ for ceramic systems that are only up to 30% in error without breaking a sample if the Knoop indentation method is used with a range of loads that produce cracked indents. Loads in the range 6–30.5 N are required for SiC and Si_3N_4, as shown in the collected results for these materials in Chapter 6. Table 6.7, which records crack depths, median or radial trace lengths, and

indent long and short axis lengths for Knoop indentations on SiC and Si_3N_4, shows that a load greater than 15.7 N is needed to cause "pop-in" in Si_3N_4 but one of less than 6 N will suffice for SiC. The results also show that the radials are in fact very close to the halfpenny shape assumed for much of the theory developed in Section 5.4.

The relevant equation to use is

$$\gamma = \frac{(1 - \nu^2)(1 - 2\nu^2)P^2}{8E\pi^3 c' z^2 Q} \tag{5.92}$$

In equation (5.92), ν is Poisson's ratio, P is the indenter load, E is Young's modulus, c' is the crack depth, z is the depth of the indentation zone where no tensile stress component is present, and Q is a term required to convert a straight edged crack to a semielliptical geometry. Q is defined by the expression

$$Q = \int_0^{\pi/2} \left[\sin^2 \theta + \left(\frac{\text{crack depth}}{\text{radial trace}} \right)^2 \cos^2 \theta \right]^{1/2} d\theta$$

For a Knoop diamond, z can be taken as equal to the short axis length of the Knoop indent.

To use equation (5.92), the crack depth must be measured, and in order to do this the sample must be broken in four point bend and the fracture surface scanned to identify and then measure crack depth. However, if c' is assumed to be equal to the indent trace long axis then the sample can be left intact and equation (5.92) gives γ correct to ±30%; this is sufficient in many cases for subsequent calculations. When fracture in three point bend follows Knoop indentation the relevant parameters from the fractographic analysis can be used in equation (5.92) to get good results; for example, SiC gave 18 J m^{-2} at 5.9 N load, 17 J m^{-2} at 2.1 N, and 25 J m^{-2} at 3.0 N which compare reasonably well with the double cantilever beam result of 16 J m^{-2}. A single crystal of 6H-type SiC yielded average γ values of 23 J m^{-2} for the (0001) surface as found by Vickers and Berkovich methods.[36]

5.10.1. Prediction of Grain Boundary Fracture Surface Energy and Strength

The fracture energy value that often features in theoretical discussions on ceramic strength for normal polycrystalline material is the specific fracture energy of the grain boundaries γ^{gb}. Unfortunately, γ^{gb} is hard to measure directly and so almost no experimental data exist. It is common to see γ^{gb} approximated to lattice fracture energy γ^L as a fraction ranging

from 0.1 to 0.33 of γ^L. An analysis of the crack path of radials and laterals produced by Vickers indentation[37] leads to an equation from which γ^{gb} can be reasonably estimated. The general argument is as follows: First, the grain-boundary strength is determined by K_{IC}^{gb} and the size of microflaws. Then, for grain boundaries perpendicular to the tension causing the radial cracks, propagation of the crack will be along the boundary, in (say) the x direction. Small kinklike displacements of grains still allow the crack to travel in the grain boundary at small angles from the x direction; if, however, the crack travels too far along a particular grain boundary of, say, a larger grain at an angle to the x direction, then the crack may pass through the next grain instead of around it because the driving force in the x direction, K_I^x, would be a maximum. Whether the crack goes transgranular or continues following a boundary will depend on the direction of the next boundary. This is expressed as

$$K_I^a = K_I^x \cos^2 \alpha \qquad (5.93)$$

In the above equation, K_I^a represents the crack driving stress intensity in any general direction, K_I^x is the driving force in the x direction, and α is the angle of inclination of the crack direction to the x direction.

When α is small, $K_I^a \approx K_I^x$ and therefore K_I^a will exceed the low grainboundary strength at low applied load so that K_I^x is still far below K_{IC}^L, the critical stress intensity for transgranular crack growth. When α is large the opposite result follows from equation (5.93).

Where $K_I^a = K_{IC}^{gb}$, α_o is defined as the grain-boundary orientation. Following from this, two cases emerge.

For $0 \leq \alpha < \alpha_o$, grain-boundary crack growth occurs since $K_I^x < K_{IC}^L$ if

$$K_I^a = K_{IC}^{gb} \quad \text{for } \alpha < \alpha_o \qquad (5.94)$$

And for $\alpha_o < \alpha \leq \pi/2$, grain cleavage occurs in the next grain the crack encounters as $K_I^a < K_{IC}^{gb}$ if

$$K_I^x = K_{IC}^L \quad \text{for } \alpha > \alpha_o \qquad (5.95)$$

α_o can be evaluated by determining experimentally the percentage of intergranular fracture (PIF), given by equation (5.96)

$$\frac{\text{PIF}}{100} = \frac{\alpha_o}{90} \qquad (5.96)$$

Combining equations (5.75), (5.94), and (5.96) leads to

$$K_{IC}^{gb} = K_{IC}^L \cos^2 \left(\frac{\pi}{2} \frac{\text{PIF}}{100} \right) \qquad (5.97)$$

Thus, from a knowledge of the average lattice stress intensity factor for the material and a measurement of PIF from an SEM micrograph, K_{IC}^{gb} can be found. The specific fracture energy of the grain boundary is then given as

$$\gamma^{gb} = \frac{(K_{IC}^{gb})^2}{2E} \tag{5.98}$$

or if necessary the grain boundary strength may be found by measuring the average size boundary flaw a_m^o from

$$\sigma_f^{gb} = 0.886 \frac{K_{IC}^{gb}}{(a_m^o)^{1/2}} \tag{5.99}$$

5.10.2. Estimation of Matrix–Fiber Frictional Stress in Ceramic Composites

A Vickers indenter can be used to selectively push a fiber through a matrix and in a sense generate a circumferential crack which can be used to find the frictional binding stress that contributes to increased toughness in fiber composites.[38] The method requires that a thin section of the composite be cut perpendicular to the fiber direction, polished, and mounted on a plasticene base. By trial a small load is selected such that when an indent is made on the circular cross-section of a fiber it is completely contained in the fiber and no depression of the fiber through the matrix is observed, but corners of the indent are just in the matrix. This process allows the hardness of the fiber to be obtained in the usual way from equation (1.6) and gives an apex indentation diagonal a_1 to be used in equation (5.100)

$$\tau = \frac{a_1^4 H_V}{\pi^2 x r^2 E_f} \tag{5.100}$$

Equation (5.100) can be obtained from a force–balance equation of the situation that occurs when a large load is applied to the indenter and the fiber is pushed through the matrix and into the plasticene for a distance l, the slipping distance. In the equation τ is the frictional stress, a_1 has been defined above, H_V is the Vickers hardness derived from a_1, r is the fiber radius, E_f is the fiber's Young's modulus, and x is related to the slipping distance l. (It is in fact the depth below the surface that the apex of the indenter reaches while the prism faces are supported by both the fiber and surrounding matrix.) For the correct load that produces an apex diamond

a_1 and just causes slippage such that the pyramid just rests on the matrix; i.e., the secondary diamond shape has $a_2 = r$

$$x = (r - a_1) \cot \psi \qquad (5.101)$$

where ψ is the usual interfacial angle of the diamond chosen. Hence the final equation for this method is

$$\tau = \frac{a_1^4 H_V}{\pi^2 (r - a_1) \cot \psi r^2 E_f} \qquad (5.102)$$

The model used to arrive at equation (5.102) is based on a constant shear stress approximation for transfer of stress across the interface between matrix and ceramic fiber, and this is often interpreted as the flow stress of the matrix or as the friction stress at the interface. Such a model leads to the view that the average fiber stress varies linearly as a function of distance along the fiber which is proportional to shear stress. Thus the shear stress at the interface is expected to equal the frictional stress only over a specific part of the fiber and then to decrease steadily with distance along the interface. A more detailed model concentrating on the transfer of load across a frictional interface between elastic solids is reported by Dollar and Steif,[41] which suggests that the results obtained by using equation (5.102) are approximations because the constant shear stress approximation overestimates the extent of slip. Furthermore, the error increases as the coefficient of friction in the interface increases and as the load increases. Nevertheless this hardness indentation procedure does lend itself to obtaining much useful comparative data for one type of ceramic fiber say, in a series of matrices. Thus the technique is in line with how hardness indentation methods are most commonly used.

5.11. INDENTATION MICROCRACKS AS A ROUTE TO STRESS-CORROSION SUSCEPTIBILITY COEFFICIENTS

It is accepted that ceramics under load fail as a result of *subcritical* crack growth from preexisting flaws, and as shown in Sections 5.9.2 and 5.2 and Table 5.1 these are relatively easily generated. Hence ceramic lifetime predictions require evaluation of crack growth rates when subjected to an applied stress just as much as estimations of the initial flaw sizes.

The idea that cracks will grow longer under the influence of subcritical loads in particular environments is crucial to a correct use of the equations in Section 5.4 to estimate ceramic fracture toughness, although it was not

then emphasized. Clearly each toughness equation in Section 5.4 has a c' term and, if crack length can increase before it is measured after unloading because of the *residual* stress field, or if there is a delay in measuring c' (if, for example, an SEM is used), then a method of determining c'_o, the true load-determined crack length, is essential.

The microhardness indentation method can be useful in this important area of ceramic science because as Section 5.2 shows it is a way to introduce controlled cracks by "pop-in" and then to study their growth. It is more common in accurate work to try to prevent crack growth by working at liquid nitrogen temperatures or under dry oil, but these modifications to the technique can make crack detection difficult. If we are prepared to let the cracks grow it is possible to use the growth rate to determine c'_o for more accurate K_{IC} determinations.

In general, most ceramics show a slow crack growth which is dependent on the applied stress intensity factor K_I and the test environment. And as a result growth is not simple, as Figure 5.23 shows with its three distinct regions of behavior. Region I is generated by chemical control of the process, region II by diffusion control, and region III is not well understood but may represent control by transformation in an excited state, as in Section 4.2. In region III, K_I is rapidly approaching K_{1C} when catastrophic extension will occur; hence entry into this region is undesirable. For design purposes region I, because it is much longer than region II, is considered to be most important, and for this region a simple power function can be
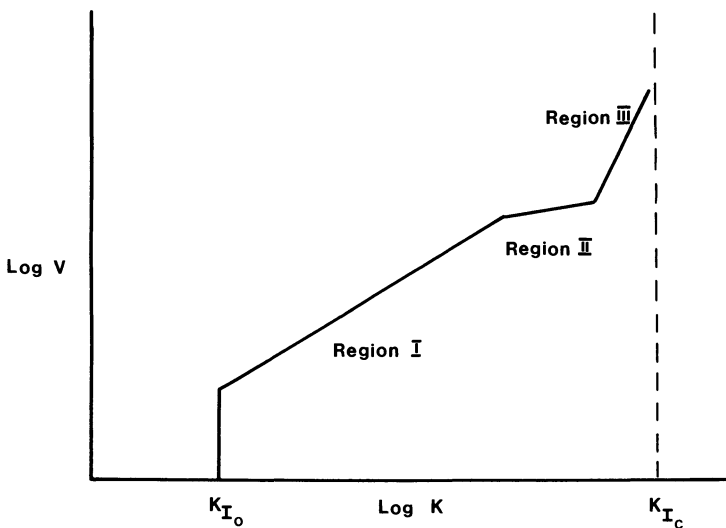
Figure 5.23. The three regions of subcritical crack growth.

used to relate crack velocity and stress intensity factor

$$V = BK_I^n \qquad (5.103)$$

In equation (5.103), V is the crack velocity, K_I the stress intensity coefficient, and B and n are constants dependent on the material and its environment. The constant B is sometimes written as V_o to signify that it represents the critical velocity of crack growth at failure. The exponent n is an important parameter known as the *stress-corrosion susceptibility coefficient* of the ceramic.

Thus equation (5.103) is alternatively expressed as equation (5.104), which involves the residual stress intensity factor K_r.

$$V = \frac{dc'}{dt} = V_o \left[\frac{K_r}{K_{IC}} \right]^n \qquad (5.104)$$

We have seen in Sections 5.2–5.4 how after indentation there is a residual stress with a *residual stress intensity* factor already given in equation (5.44), and this can be used to substitute for K_r in equation (5.104)

$$(c')^{3/2} \frac{dc'}{dt} = V_o \left[\frac{\beta_r P}{K_{IC}} \right]^n \qquad (5.105)$$

Rearranging and integrating we can obtain

$$(c')^{(3n+2)/2} - (c'_o)^{(3n+2)/2} = \left(\frac{3n+2}{2} \right) V_o \left[\frac{\beta_o P}{K_{IC}} \right]^n t \qquad (5.106)$$

Fracture toughness K_{IC} is given as

$$K_{IC} = \frac{\beta_r P}{(c'_o)^{3/2}}$$

and this can be substituted into equation (5.106) with some rearrangement to get

$$\frac{c'}{c'_o} = \left[1 + \left(\frac{3n+2}{2} \right) \frac{V_o t}{c'_o} \right]^{2/(3n+2)} \qquad (5.107)$$

If slow crack growth is a serious problem with the ceramic and atmospheric combination of interest, then $V_o t/c'_o \gg 1$ and equation (5.107) approximates to

$$\frac{c'}{c'_o} = \left[\left(\frac{3n+2}{2}\right)\frac{V_o t}{c'_o}\right]^{2/(3n+2)} \tag{5.108}$$

Taking logs of equation (5.108) and using $K_{IC} = \beta_r P/(c'_o)^{3/2}$ to replace c'_o

$$\ln c' = \frac{2}{3n+2}\ln t + \frac{3n}{3n+2}\ln\left(\frac{\beta_r P}{K_{IC}}\right)^{-3/2} + \frac{2}{3n+2}\ln V_o$$

$$+ \frac{2}{3n+2}\ln\left(\frac{3n+2}{2}\right) \tag{5.109}$$

which tells us that $\ln c'$ should be linearly dependent on $\ln t$ and a measurement of indent crack length with time can be used to find n. Extrapolation to time $t = 0$, when the indenter diamond was lifted, enables c_o to be found, and this can be used in more precise determinations of the fracture toughness coefficient.

Returning to equation (5.107), we can see that if crack growth is very small then $(3n+2)V_{ot}/2c'_o \gg 1$ and the exponent in equation (5.107) can be ignored to give

$$\frac{c'}{c'_o} = 1 + \frac{3n+2}{2}\left(\frac{V_o t}{c'_o}\right)$$

Thus

$$c' = c'_o + \left(\frac{3n+2}{2}\right)V_o t \tag{5.110}$$

This shows that crack extension is directly proportional to time and the intercept is the required value of crack length for refined determinations of K_{IC}. The slope cannot be used directly to find n in this case.

Values of n for soda–lime glass in water and air environments gave average n values of 15.7 and 23.3, respectively, which are typical of values found by less convenient methods.

5.12. INDENTATION MICROCRACKS AS A WAY TO
FIND ADHESION CHARACTERISTICS OF THIN FILMS

Industries concerned with the production of thin films on substrate materials have for some time sought routine methods to monitor the quality of adhesion between film and substrate. The characteristics of the indentation test, and in particular its ability to develop cracks beneath the surface, present a way to do so.

Figure 5.2 shows the *lateral cracks* as nucleating near the base of the plastic zone and then running somewhat parallel to the surface. It is not necessary, as stated already, for the laterals to nucleate at the base, but to nucleate at an appropriate flaw. In one sense the interface between deposited layer and substrate is a flaw because bonding across this region cannot be as efficient as within the substrate or within the film. Thus the lateral crack may well be expected to nucleate in this interface. If it does not, the general path of the crack will meet the interface and then continue along it. This being so, some of the models and equations already developed in this chapter will be adaptable to find K_{IC}. This approach has been proposed by Chiang *et al.*[39] and results in equation (5.111) from a model in which the stored energy of the plastic zone acts as a *lateral* crack opening force. The representation of the model is shown in Figure 5.24.

Application of the treatment in Section 5.2.1.3 gives

$$c' = \alpha_1 \frac{h^{3/4} H_V^{1/4}}{(K_{IC}^{int})^{1/2}} \left[1 - \frac{P^*}{P} \right] P^{1/4} \qquad (5.111)$$
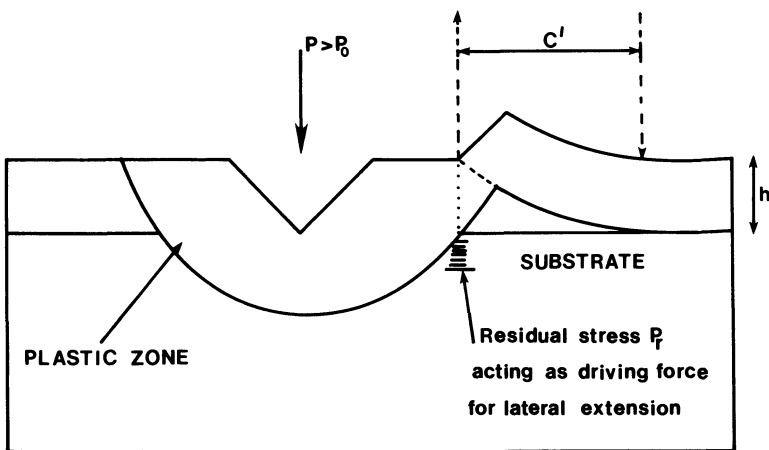
Figure 5.24. Representation of the residual stress associated with the plastic zone driving a lateral crack to peel off the deposited film, thickness h.

α_1 is a material indent coefficient obtained by calibration using glass and found to be 6.4×10^{-8}. The c' value is measured as the ring radius shown in Figure 5.2(c), film thickness is measured microscopically, P^* is determined by making indents at increasing loading, and H_V by the usual measurement of indent diagonal. Hence the fracture toughness parameter of the interface can be found and this is a measure of adhesion.

5.13. INDENTATION MICROCRACKS AS MODEL FLAWS IN CERAMIC SYSTEMS

Indentation hardness testers have been used for some considerable time as adjuncts to conventional three and four point bend test equipment. Indentations have been made in specimen beams at loads greater than the critical load (see Section 5.8) so that median and lateral cracks have been developed from which subsequent failure in the macroscopic strength test occurs (see Section 5.5.1). Such testing procedures relate strength to crack dimensions but do not contribute to resolving the continuing argument concerning the relationships of crack geometry and ceramic strength. There are two schools of thought.

First is the blunt crack school by whom the laws of stress concentration at the tips of rounded cracks are believed to apply. As a result, great attention is focused on the blunt tip radius. This model is easily used in the interpretation of increased strength on aging because corrosion effects are seen to increase the tip radius and so decrease the stress concentration.

The second model assumes that cracks are atomically sharp and tip radius is not a variable. The driving force for fracture is expressed as an applied stress intensity factor proportional to $c'^{1/2}$. Thus crack length is important in controlling the strength. This theory, based as it is on the idea of spontaneous instability of constant radius cracks, on achieving a critical length seems unable to account so easily for strength increases on aging. However, it has recently been demonstrated[40] that observations of median and lateral crack lengths as a function of time can be used to provide an explanation for strength increases on aging in glass specimens. Such an explanation invokes the concept of *residual stress* beneath an impacted zone (see Section 5.4) after the indenter is removed. Clearly if the strength is measured soon after the indenter is removed the applied stress in the breaking experiment is assisted by the residual stress and an experimental value for stress is found. However, as the sample is aged some of the residual stress is used in increasing the median lengths, so that a subsequent breaking test requires a larger load to cause fracture. Thus a decline in the residual stress is responsible for antifatigue in glass and is not necessarily a crack blunting mechanism. Further, it was shown that annealed indented speci-

mens, although still cracked, did not show the antifatigue effect because the residual stress was removed prior to fracture and could not therefore be diminished by postindent crack extension.

Since most natural flaws have a contact as their cause it is thought that they behave like the indentation induced flaws. This reappraisal stemming from hardness indent crack observations is important in that it suggests that atomically sharp cracks are constant features in ceramics and that their consideration should be centered on the basic laws of crack growth as related to stress intensity coefficients in Section 5.11.

REFERENCES

1. I. J. McColm and N. J. Clark, *Forming, Shaping and Working of High Performance Ceramics*, Blackie, Glasgow (1988).
2. R. Stevens, *An Introduction to Zirconia*, Magnesium Elektron Ltd., Twickenham (1988).
3. I. J. McColm, *Ceramic Science for Materials Technologists*, Blackie, Glasgow (1983).
4. S. Palmqvist, *Jernkontorets Annalen* 167, 208 (1963) and 141, 300 (1957).
5. B. R. Lawn and M. V. Swain, *J. Mater. Sci.* 10, 113 (1975) and 10, 1049 (1975).
6. D. B. Marshall, B. R. Lawn, and A. G. Evans, *J. Amer. Ceram. Soc.* 65, 561 (1982).
7. R. Mouginot and D. Mangis, *J. Mater. Sci.* 20, 4354 (1985).
8. A. G. Evans and E. A. Charles, *J. Amer. Ceram. Soc.* 59, 371 (1976).
9. S. S. Chiang, D. B. Marshall, and A. G. Evans, *J. Appl. Phys.* 53, 298 (1982).
10. B. R. Lawn, A. G. Evans, and D. B. Marshall, *J. Amer. Ceram. Soc.* 63, 574 (1980).
11. A. G. Evans, *ASTM-STP* 678, (1979) p. 112.
12. K. Niihara, R. Morena, and D. P. H. Hasselman, in *Fracture Mechanics of Solids V*, R. C. Bradt, ed., Symp. Penn State College (1981), p. 97.
13. G. R. Antis, P. Chantikul, B. R. Lawn, and D. B. Marshall, *J. Amer. Ceram. Soc.* 64, 539 (1981).
14. D. G. Bhat, *J. Amer. Ceram. Soc.* 64, C-165 (1981).
15. J. L. Henshall and C. A. Brookes, *J. Mater. Sci. Letters* 4, 783 (1986).
16. D. K. Shetty and I. G. Wright, *J. Mater. Sci. Letters* 5, 365 (1986).
17. K. Niihara, R. Morena, and D. P. H. Hasselman, *J. Amer. Ceram. Soc.* 65, C-116 (1982).
18. P. Mirazano and J. S. Moya, *Ceram. Int.* 10, 147 (1984).
19. C. T. Peters, *J. Mater. Sci.* 14, 1619 (1979).
20. M. T. Laugier, *J. Mater. Sci. Letters* 6, 897 (1987).
21. J. T. Hagan, *J. Mater. Sci.* 14, 2875 (1979).
22. D. B. Marshall, T. Noma, and A. G. Evans, *J. Amer. Ceram. Soc.* 65, C-175 (1982).
23. E. Breval and N. H. MacMillan, *J. Mater. Sci. Letters* 4, 741 (1985).
24. P. Chantikul, G. R. Anstis, B. R. Lawn, and D. B. Marshall, *J. Amer. Ceram. Soc.* 64, 539 (1981).
25. B. Mussler, M. V. Swain, and N. Clausson, *J. Amer. Ceram. Soc.* 65, 566 (1982).
26. R. W. Rice, S. W. Freiman, and P. F. Becher, *J. Amer. Ceram. Soc.* 64, 345 (1981).
27. S. N. Bandyopadhyay and H. K. DeSarker, *Eng. Fract. Mech.* 14, 373 (1981).
28. R. F. Cook, B. R. Lawn, and C. J. Fairbanks, *J. Amer. Ceram. Soc.* 68, 604 (1985).
29. R. Warren, *Acta. Met.* 26, 1759 (1978).
30. J. L. Routbort and Hj. Matske, *J. Mater. Sci.* 18, 1491 (1983).
31. Hj. Matske, T. Inoue, and R. Ward, *J. Nucl. Mater.* 91, 205 (1980).
32. S. M. Weiderhorn and B. R. Lawn, *J. Mater. Sci.* 18, 766 (1983).

33. M. E. Gulden, *J. Amer. Ceram. Soc.* **64**, C-59 (1981).
34. M. T. Sykes, R. O. Scattergood, and C. R. L. Routbort, *Composites* **18**, 153 (1987).
35. J. T. Hagan, *J. Mater. Sci.* **15**, 1417 (1980).
36. J. L. Henshall and C. A. Brookes, *J. Mater. Sci. Letters* **4**, 783 (1985).
37. A. Krell, J. Woltersdorf, E. Pippel, and D. Schulze, *Phil. Mag.* **A51**, 765 (1985).
38. D. B. Marshall, *J. Amer. Ceram. Soc.* **67**, C-259 (1984).
39. S. S. Chiang, D. B. Marshall, and A. G. Evans, *Mater. Sci. Res.* **14** (Surf. Interfaces Ceram. Ceram.-Met. Systs.), 603 (1981).
40. D. H. Roach and A. R. Cooper, *J. Amer. Ceram. Soc.* **68**, 632 (1985).
41. A. Dollar and P. F. Steif, *Int. J. Solid Struct.* **24**, 789 (1988).

Ceramic Systems

Bonding, Microstructures, Hardness Values, and Hardness-Derived Properties

The materials of particular interest in this book have already been defined and listed in Section 1.2, and they are now considered in relevant detail in this chapter. Because ceramics encompass all main bonding types—ionic, covalent, and metallic—it is convenient to divide this chapter into sections on covalent engineering ceramics, ionic engineering ceramics, electronic ceramics, and special hard-metal ceramics.

6.1. COVALENT ENGINEERING CERAMICS

In current order of importance this heading encompasses SiC, Si_3N_4, B_4C, BN, silicon dioxide and glasses, carbon, silicon, and boron.

6.1.1. Silicon Carbide

Although several methods for the production of silicon carbide are available, there are only two main engineering grades:

1. Artifacts obtained by reaction bonding in a process known for over 15 years as the REFEL process, which is basically still that developed by British technologists. "Green" products are pressed from silicon carbide powders usually made by the Aecheson process from silica and carbon heated to in excess of 2200°C, with excess graphite present. Molten silicon then infiltrates the connected pores where, on further heat treatment, reaction with the extra graphite produces SiC in the interpore space. This secondary SiC is referred to as "reaction sintered." The final body has about 12% free unreacted silicon.

2. Pressureless sintered SiC bodies made from ultrafine SiC powders which are themselves highly milled Aecheson powders or are made from vapor-phase reactions of silanes with hydrocarbons. Such ultrafine powders are usually mixed with carbon and boron sintering aids in order to achieve the necessary high densities.

   Articles made this way have high thermal conductivity and high hardness and are resistant to chemical corrosion. This combination of properties combined with high strength has already led to the development of heat exchangers, wear-resistant sliders, and turbocharger rotors. Surfaces are usually diamond ground to obtain final dimensions, or vapor deposits of SiC are added to produce high-quality finishes. It is these products that require testing to provide hardness values and to gain insight into toughness through K_{IC} measurement.

While REFEL or conventionally sintered (CS) materials are the common forms, hot pressed material (HP) of almost theoretical density is also available. The HP artifacts are usually obtained at 2100°C and 50 MPa pressure with either aluminum or boron carbide, B_4C, added as a sintering aid. Hot pressing with up to 1.5% aluminum produces equiaxed microstructures with grains about 2 μm in diameter, but a different microstructure, with elongated grains 20–40 μm long, is produced in the presence of B_4C.

There is also available reaction sintered (RS) material made by shaping a Si + C powder and heating it so that dissolution of the graphite by molten silicon occurs; this is then followed by precipitation of SiC in the cooler regions of the specimen.

Several forms of chemically vapor deposited (CVD) SiC can be obtained, usually based on methylchlorosilanes heated and deposited onto SiC, graphite, or silicon. This produces a columnar morphology in which the close-packed atomic planes of the deposited grains align at 90° to the direction of the condensation reaction.

Finally, single-crystal SiC has frequently been obtained for experimental purposes.

Thus there is a wide range of SiC types in existence, and hardness results do not always specify the type used or make clear the microstructure or composition of the sample. Furthermore, as Section 6.1.1.2 shows, the real situation in any sample can be much more complex on a microscopic scale.

6.1.1.1. Bonding, Polytypism, and Epitaxy

Silicon with a groundstate electron configuration $1s^2 2s^2 2p^6 3s^2 3p^2$ and carbon with $1s^2 2s^2 2p^2$ inevitably interact via (sp^3) hybrid orbitals to produce a tetrahedral arrangement of bonding orbitals. Distribution of these in three

dimensions gives the fourfold coordination of each component, and within this distribution puckered, six-membered rings formed from corner-sharing SiC_4 and C_4Si tetrahedra can be discerned, arranged as layers throughout the structure. These layers are not graphitic and planar, because they are connected by strong covalent bonds between the layers and bond angles are near to the ideal tetrahedral angles, but discerning them allows the structure to be described as a stacking sequence of such layers (see Figure 6.1). Hexagonal or α-SiC is in the simple sequence ABAB . . . , and cubic or β-SiC is in the usual ABCABC . . . sequence.

The α and β forms are known to coexist metastably in an epitaxial relationship, but conventional X-ray methods do not always reveal the intergrowth. Thus the role that this intergrowth plays in determining hardness may not be apparent but may account for some of the variation in reported values on otherwise well characterized samples.

Intergrowths do give rise to a very large series of SiC polymorphs, each characterized by a sequence of stacking reversals. As long ago as 1951 epitaxial coexistence of different polytypes was first observed by Baumhauer,[1] who noted that "single" crystals varied in structure along the c-axis.

The stacking sequence at a coherent twin boundary in β-SiC is

$$\downarrow$$
$$\ldots ABC \quad ABC \quad ACB \quad ACB \ldots$$
$$ \underset{1\ 2\ 3}{} \quad \underset{4\ 5\ 6}{} \quad \underset{7\ 8}{}$$
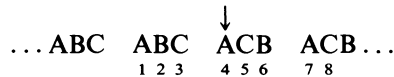
$\downarrow$
The layer A is a coherent twin boundary layer with the layers on either side being in twin relationship to each other.

Polytypes are identified by the sequence of repeat layers in the numbers shown above

layer sequence 1–7	polytype 6H = α
layer sequence 1–6	polytype 15R
layer sequence 2–7	polytype 15R
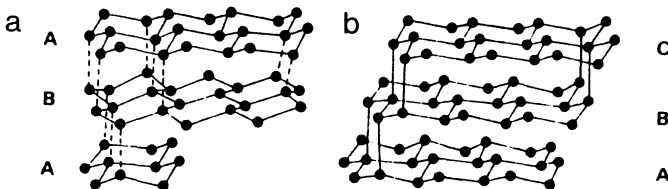
Figure 6.1. Pseudolayer representation of (a) Wurtzite form of SiC (the α-form in which horizontal six-membered rings have a chair configuration and vertical puckered hexagonal rings have a boat configuration) and (b) β or zinc blende structure of SiC containing all chair-form rings.

layer sequence 2-6   polytype 4H
layer sequence 1-8   polytype 21R
layer sequence 1-3   polytype 3C = β

A coherent twin boundary in the β-phase such as that shown above is by its stacking sequence an incipient α hexagonal nucleus. Because of their low stacking fault energy, such faults are present in abundance in the β-phase. The tendency of complex epitaxial structures in SiC to persevere at temperatures where β is metastable with respect to α is attributed to the small free energy difference between α- and β-SiC and the low energy of the epitaxial β-α interface.

Both these factors result in a low driving force for the elimination of the coherent interface. Microsyntaxy usually involves 3C, 4H, 15R, 6H, and 21R in various admixtures and truly polytype pure crystals of α-SiC are extremely rare. When a regular repeat occurs, then a long-period polytype results. This is true for all ways that SiC is prepared and hardness can be affected by stress-induced polytype changes beneath an indenter. In practice one is often measuring the hardness of a β-α composite and transformation processes are important.

Transformation is by a two-stage process when thermal energy alone is involved

Dense β-SiC annealed above 1800°C $\xrightarrow{\text{FAST}}$ Fine-grained β recrystallizes
onto α-plates

SLOW

α-Plates grow as β-transforms
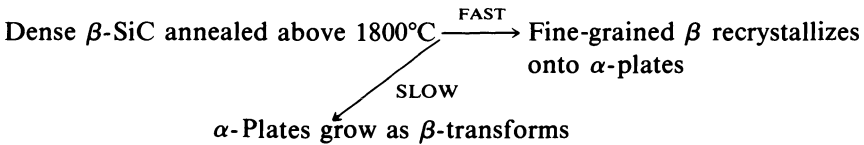
The simultaneous processes outlined above produce a continuous, fully coherent β envelope around each α-SiC plate. These composites change quite quickly as the fine β-SiC grains are consumed by rapid growth parallel to the coherent boundary. Further $\beta \rightarrow \alpha$ transformation occurs as the α-plates thicken at the expense of the now large grain coherent β envelopes. Hence the nature of the β-α interface, nucleation of α in β, and the role of β-twin boundaries are all important features of the mechanism. Combined effects of slip, atmosphere, and stress under an indenter can affect these features and lead to polytype changes during measurement of hardness. There seems to have been no real consideration of these possibilities in hardness studies even though the results in Table 6.1 do show that unusual reverse transformations can be affected by N_2, pressure, and stress.

From Knoop hardness anisotropy measurements on single crystals of 6H-SiC, discussed in Chapter 3, the following slip systems have been identified in experiments from ambient to 600°C: $(0001)\langle 1\bar{2}10\rangle$, $(0001)\langle 0\bar{1}10\rangle$,

Table 6.1. Phases Identified in SiC (10–15 μm Grain Size) Following Annealing in N_2 and Argon[a]

Temperature (°C)	Atmosphere	Pressure (MPa)	Phases (%)	
			α-SiC	β-SiC
1800	N_2	0.1	100	0
1800	N_2	3	90	10
2000	N_2	0.1	93	7
2000	N_2	3	39	61
2250	N_2	0.1	75	25
2250	N_2	3	6	94
1800	A	1	99	1
2000	A	3	97	3
2250	A	3	100	0

[a]After Jepps.[2]

$\{30\bar{3}8\}\langle1\bar{2}10\rangle$, and $\{10\bar{1}0\}\langle1\bar{2}10\rangle$. The first two are basal slip systems; the $\{10\bar{1}0\}$ are prismatic systems.

6.1.1.2. Microstructure

At low preparation temperatures, cubic β-SiC dominates in products but α–β composites occur in all preparations unless high-temperature annealing is used for long periods to achieve a basic α-hexagonal form. Thus in many specimens several boundaries exist: α–α, β–β high-energy grain boundaries; β–α incoherent high-energy interface boundaries; epitaxial β–α low-energy composite grains. In general CS and HP SiC have similar microstructures which are quite different from RS and CVD sample microstructures.

6.1.1.2a. CS and HP material. Fabricated materials contain 5–10% α-SiC either inherited from the starting powder or formed by the $\beta \to \alpha$ transition during densification. The α-SiC crystals are elongated plates with the flat faces of the plates parallel to (0001) basal planes. Such plates are surrounded by a coherent β-SiC envelope with $(0001)_\alpha \parallel \{111\}_\beta$. The coherent β-envelope is surrounded by a fine-grained β-SiC matrix. Annealing causes the α-plates to grow in elongated fashion accompanied by simultaneous recrystallization of the fine-grained β-SiC matrix onto the α-plates until the microstructure is one of *large composite* grains of α-plates in the middle of β-envelopes. High aspect ratios for the hexagonal phase are common and all α–β interfaces are coherent.

Table 6.2. Single-Crystal Silicon Carbide

Method/ Plane	Indent diagonal orientation	Crystal type	Hardness (GPa)	K_{IC} (MPa m$^{1/2}$)	Crack trace	E (GPa)	Notes
Vickers (0001)	$\langle 11\bar{2}0\rangle$ and $\langle 1\bar{1}00\rangle$	—	36.5[1] 28.7[2]	—	$\langle 11\bar{2}0\rangle$[3] and $\langle \bar{1}100\rangle$		
(0001)	(4)	6H	33.0[5] 29.0 25.0 28.5[7] 29.4[8]	3.4[6] 3.1 3.2	—	460	
Knoop (0001)	$\langle 11\bar{2}0\rangle$[9] $\langle 10\bar{1}0\rangle$[9]	— —	27.3[10] 30.6[10]				

[1] Dry surface
[2] H$_2$O on same surface
[3] Suggests preferred cleavage planes $\{10\bar{1}0\}$ and $\{11\bar{2}0\}$
[4] Orientation given as angle between indenter faces and the [11$\bar{2}$0] direction
[5] 15° angle; re-note (4) values correspond to 4.90, 9.81, and 19.61 N loads
[6] Equation (5.40) used
[7] Indenter face along [11$\bar{2}$0]
[8] 15° angle (note 4)
[9] Direction of long axis of indent
[10] Load = 2.75 N

(0001)	⟨11$\bar{2}$0⟩	6H	19.6–5.89[11]	—	—	[11]Hardness unaffected by temperature up to 800°C but falls rapidly to 5.89 GPa at 1300°C (load = 4.91 N)
	⟨10$\bar{1}$0⟩	6H	21.6–3.92[12,13]	—	—	[12]Almost linear decrease from RT (21.6) to 1300°C (3.92)
Berkovich (0001)	(4)	6H	36.0[14] 30.6 25.8 25.5	3.1[15] 3.3 3.3 3.3	—	[13]Hardness independent of loading time at 45°C but slow softening at 400°C; activation energy for creep 527 KJ mol^{-1}
($1\bar{1}$00)	(16)		32.0[14] 27.1 25.9	3.5[15] 3.0 3.1	—	[14]Face along [11$\bar{2}$0] load 2.94 to 19.61 N show decreasing hardness
		6H	29.9	3.1	—	[15]Equation (5.50) used [16]90° between indenter face and [11$\bar{2}$0]
Scratch[17] (0001)	⟨11$\bar{2}$0⟩	—	—	—	[11$\bar{2}$0][18]	[17]60° conical diamond with 2.94 N load [18]Cracks only on one side of groove; dislocation arrays localized 1 μm below groove (because of this etch pit experiments do not work).
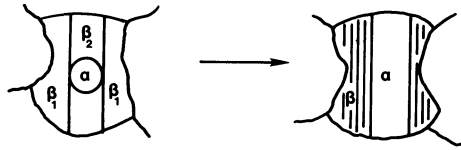
Figure 6.2. Development of principal microstructure of RS silicon carbide.

6.1.1.2b. RS material. As stated above this is made by dissolving graphite in molten silicon followed by precipitation of SiC in cooler regions. In this process thick layers of epitaxial β-SiC form on α-SiC seed grains while β-SiC is deposited in the large pores of the compact. The former structure is the major part of the microstructure. Figure 6.2 sketches the way the initial microstructure changes.

As Figure 6.2 shows, the final microstructure of RS silicon carbide is like the morphology of CS and HP forms after stage 1 of their development, but in this case the α-plates are not so elongated in the final microstructure. α is seen to extend by consuming β_2, and therefore β_2 gives way to the same polytype as the α-seed, but β_1 can become other polytypes depending on nucleation at the twin boundaries.

6.1.1.2c. CVD material. In this material the microstructure is one of columnar grains of cubic β-SiC composed of stacks of {111} microtwins because {111} forms the solid-vapor interface during deposition. Each grain is a mosaic of subgrains with small misorientations. At 1800°C the sample is totally β-SiC, but heating above this produces a series of β-α composites.

All of these microstructures can be prepared for hardness testing by using the usual polishing diamond pastes down to 1 μm with surface etching if required by using a boiling saturated solution of Murakami's reagent for 3 to 10 minutes.

6.1.1.3. Hardness Values and Properties Derived from Them

The data collected in Tables 6.2–6.24 and some of the conclusions drawn therefrom come from many sources, most of which are collected into the references at the end of the chapters and are not further acknowledged.

6.1.2. Silicon Nitride and Sialons

To the engineer the three forms available of both silicon nitride and its alloys with alumina and other oxides, the sialons, are:

1. Reaction sintered (RS) material made from silicon fired in nitrogen.

Table 6.3. Reaction Bonded and Sintered SiC

Method/ Commercial symbol	Si free (%)	Microstructure	Hardness (GPa)	E (GPa)	ν	ρ (kg m^{-3})	K_{IC} (MPa m$^{1/2}$)	γ (J m^{-2})	Notes
Vickers NC 430	10.6	50% large SiC grains in matrix of small Si + SiC	27.7[1] ± 2	383	0.24	3100	1.9[2]	4.3[2]	[1]Hardness is load independent, 0.98–3.92 N
SC-1	20	Random agglomerates of Si	25.7 ± 3	403	0.19	3030	3.0[2]	11.0[2]	[2]From Hertz method, equation (5.77)
SC-2	13	Same as SC-1	24.3 ± 1.6	404	0.19	3100	2.8[2]	9.6[2]	
NC-203	—	—	—	455	0.27	—	—	18.25[3]	[3]Value depends on load used
GEC-Commercial	0	Some large tabular grains of α-SiC, porosity 4.1%	23.9	395	0.17	3120	2.8[4]	—	[4]Equation (5.45) used
Knoop[5]	—	—	19[6]	—	—	—	4.0[6]	—	[5]Load range 0.59–30.4 N to produce cracks
REFEL	—	—	19.62[7]	—	—	3100	—	—	[6]Critical load from equation (5.11) = 7.85 N but 0.79 N from equation (5.85); acoustic emission gives $P^* = 0.98$ N; critical flaw size from equation (5.12) = 1.84 μm
GEC-Commercial	0	Submicron β + large α grains	20.9	395	0.17	3120	2.8	—	
TiB$_2$ particle composite	—	15% TiB$_2$	27.5	—	—	—	4.2	—	
Brinell	—	—	27.5	—	—	3100	5.0	—	[7]The n value from equation (4.2) is 1.92

Table 6.4. Hot Pressed SiC

Sample	Grain size (μm)	Crack path	Hardness (GPa)	E (GPa)	$K_{IC}^{(1)}$ (MPa m$^{1/2}$)	$K_{IC}^{(2)}$ (MPa m$^{1/2}$)	Notes
SiC (0.3% Al)	2	Intergranular			3.1–5.2	—	[1]Vickers indent using equations (5.40) and (5.45)–(5.59), hence the range of values
SiC (1.5% Al)	2	Intergranular			3.0–6.5	—	[2]Hertz ring crack method, equation (5.77)
SiC–B$_4$C	20–40 Elongated	(3)			2.9–4.6	—	[3]Crack hard to distinguish
SiC	15 Elongated	(3)			3.0–5.8	—	
SiC	—	—			—	3.8	[4]$\beta = 2.8$ from equation (1.16)
SiC	—	—	19.3	420	4.0$^{(4)}$		

Table 6.5. CVD SiC

Method	Hardness (GPa)	E (GPa)	K_{IC} (MPa m$^{1/2}$)	Notes
Vickers	32.3[1]	450		[1]Load used 4.91 N
			3.0–6.6[2]	[2]Range of values depends on which of equations (5.40), (5.45)–(5.59) is used
	24.5–32.4[3]			[3]When deposited at 900°C H_V = 24.5 rising to 32.4 at 1100°C deposition temperature
	32.4–29.43[4]			[4]Independent of load from 2.45 N to 9.81 N then falls to 29.43 GPa at 19.6 N load
	32.43–21.10[5]			[5]Almost linear fall in this range from room temperature to 1300°C

2. Hot pressed (HP) Si_3N_4, preformed mixtures of α and β polymorphs sintered to high density using high pressures.

3. Pyrolytically deposited Si_3N_4 formed from $SiCl_4$ vapor and NH_3.

From an early stage in the development of these ceramics useful artifacts have involved the sealing of the surfaces of sintered or hot pressed articles with pyrolytic material to make use of its very high hardness and high density. The relative hardness of the three forms is shown in Figure 6.4.

Deposition on to RS or HP silicon nitride shapes can be achieved at rates up to 0.25 mm h^{-1} producing strong, void-free interfaces. Depending on the conditions of deposition and in particular the temperature of deposition, the growing layers are either amorphous or crystalline and, as later seen in Table 6.9, greater hardness is achieved with the crystalline deposit. If freestanding CVD Si_3N_4 articles are needed they are made by depositing onto carbon preforms which can then be oxidized away, but *only* the crystalline form is satisfactory for such a process.

When Si_3N_4 artifacts have their surfaces sealed by the CVD method they are particularly suited to applications in which hot corrosive environments are encountered; one notable example of this is in gas turbine components where fuel absorption is eliminated and if necessary less-pure fuel can be used without severe chemical degradation from combustion products.

As Figure 6.4 shows there is virtually no load dependence of hardness for all forms of silicon nitride after a load of 1.96 N. Furthermore cracked indentations do not become apparent until loads in excess of 9.81 N are applied, which is in sharp contrast to the case of SiC. Sliding hardness determinations with a load of 4.9 N produces only plastic grooves and small
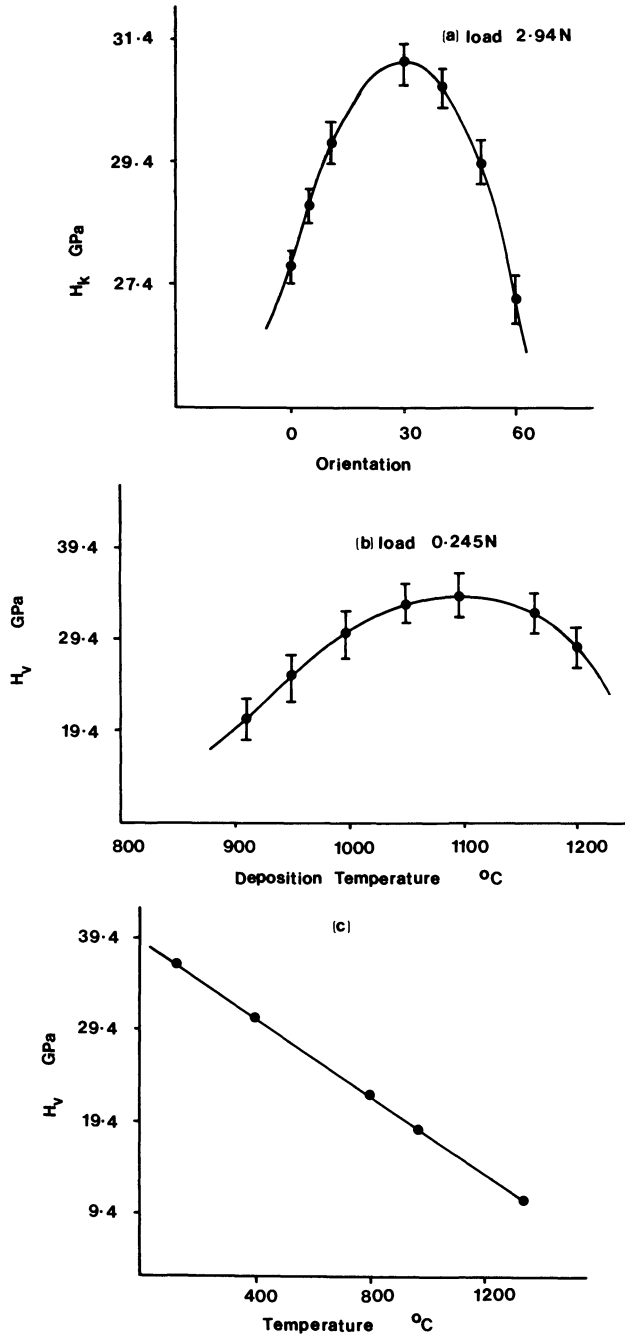
Figure 6.3. (a) Knoop hardness values for single-crystal SiC as a function of indenter long-axis orientation. At 0° the long axis is parallel to $\langle 11\bar{2}0 \rangle$; at 60°, to $\langle 11\bar{2}0 \rangle$; and at 30°, to $\langle 10\bar{1}0 \rangle$. (b) Vickers hardness of CVD SiC as a function of deposition temperature. (c) Effect of temperature on Vickers hardness of CVD layer deposited at 1000°C for 24 hours.
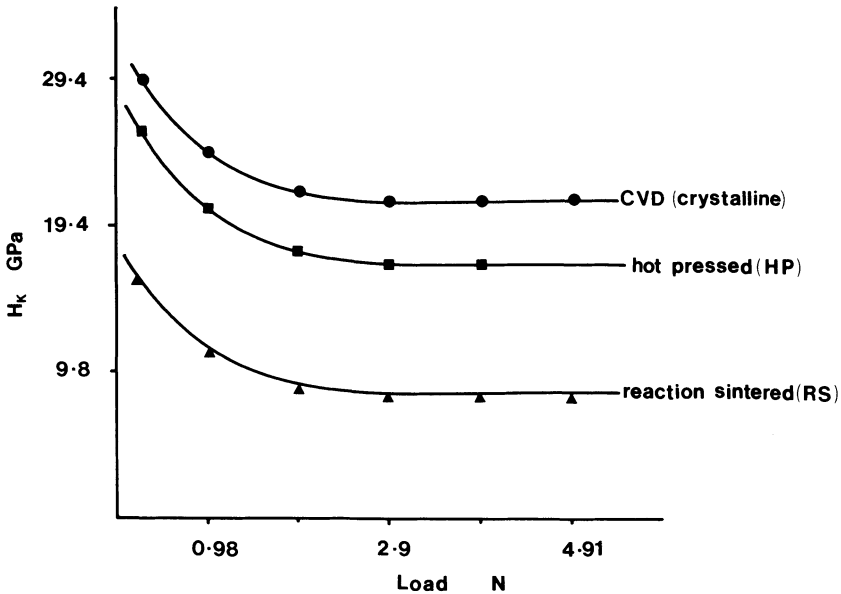
Figure 6.4. Load dependence of Knoop hardness for various forms of silicon nitride.

rounded pieces of groove debris. Once again these features are markedly different from the behavior of SiC (Section 6.1.1), which is frequently considered to be a rival to Si_3N_4 in areas of application.

6.1.2.1. Bonding and Polymorphism

As usual for silicon-based ceramics, the silicon in Si_3N_4 is seen as bonding via an excited electron state sp^3 configuration to produce a tetrahedral array of valence orbitals. Thus, as for silicates, the structural unit is a tetrahedron but these are SiN_4 building units in a three-dimensional network, each corner being shared by three other SiN_4 tetrahedra in contrast to oxygen atoms in silicate tetrahedra which are shared between only two tetrahedra. Two main advantages accrue from this fact: the greater rigidity of the bridging atoms in silicon nitride, which gives rise to the outstanding properties of the material; and only limited polymorphism, as the structural weakness of the Si—O—Si bridge in silicates is not present.

Two polymorphs are encountered, α and β, of which β is the more stable and the more commonly encountered.

While sp^3 hybridization of silicon realizes SiN_4 tetrahedra to form the structure, nitrogen with a ground-state electron structure of $1s^2 2s^2 2p^3$ must have a filled p orbital perpendicular to the plane of the sp^2 hybridized valence orbitals necessary to produce the planar Si_3N groups that are the

second type of linking polyhedron needed to form the macrocovalent structure. Because the p^2 pair on each nitrogen atom is perpendicular to the Si_3N group, it can with a slight tilting of the group produce some π bonding into the empty silicon $3d$ level, thus producing stronger bonds and contributing to the advantageous properties of Si_3N_4. The result of this is some puckering of the Si_3N groups perpendicular to the (001) plane. In this way the structure can be viewed rather like that discussed for SiC in Section 6.1.1.2, as superimposed layers of linked, puckered rings formed by joining six almost unstrained SiN_4 tetrahedra.

Overall β-Si_3N_4 has hexagonal symmetry with $a = 0.760$ nm and $c = 0.2908$ nm and space group $P6_3/m$. β-Si_3N_4 is more symmetrical and less strained than the α-polymorph and as a result is more stable. The $\alpha \rightarrow \beta$ transformation is commonly observed but the reverse $\beta \rightarrow \alpha$ transformation has never been reported.

The α-Si_3N_4 structure has been described as two distorted β-Si_3N_4 type layers rotated with respect to each other and covalently joined in the c-axis direction. As a result of this operation the Si_3N groups are definitely nonplanar, having a pyramidal aspect. Like the β-form, the overall symmetry is hexagonal, with $a = 0.7748$ nm and $c = 0.5619$ nm in the space group P31c. The distorted structure produces internal strains that make the α form less thermodynamically stable, but there are features in the mechanism of formation of Si_3N_4 that make α kinetically the favored species in many preparation conditions. Once formed it is slow to transform to the β-polymorph because this involves quite large reconstruction of the whole covalent structure.

Two mechanisms leading to formation of both types of Si_3N_4 are postulated, depending on whether nitrogen reacts with silicon as a molecule or as nitrogen atoms:

$$4N + 3Si \rightarrow Si_3N_4 \tag{6.1}$$

$$2N_2 + 3Si \rightarrow Si_3N_4 \tag{6.2}$$

If equation (6.1) applies, the atomic nitrogen will be mobile and the more symmetrical $p\pi$-$d\pi$ bonded β-structure results.

If equation (6.2) applies, then silicon diffuses via a liquid or gaseous state towards the N_2 molecule and steric hindrance from $N\equiv N$ may result in the more strained α-form. Impurities which reduce the likelihood of atomic nitrogen being present—i.e., O_2, H_2, and H_2O, which scavenge N atoms—lead to a preponderance of α-Si_3N_4 in powder preparations of silicon nitride.

Thus some samples of Si_3N_4 can be of two phases, α-β, which may affect hardness determinations. However, in general when any sample of

Si_3N_4 is raised to high temperature to hot-press shapes, etc., it transforms to the β-form. In general, though, it is rare to encounter a pure single-phase β-Si_3N_4 sample because densification aids are commonly used in the ceramic shaping processes. Above 1700°C the outer surface layer of silica that is inevitably present becomes glassy and viscous, but before its viscosity becomes low enough to assist the sintering process it reacts with Si_3N_4 to produce a crystalline silicon oxynitride.

Thus even "pure" samples of β-Si_3N_4 have grain-boundary phases that are not Si_3N_4. Technology has advanced by assisting the SiO_2 to remain liquid long enough for it to aid the sintering process. Densification occurs by three stages:

1. Particle rearrangement.
2. Solution of α-Si_3N_4 and reprecipitation of β-Si_3N_4.
3. Coalescence.

Potential additives are assessed in terms of these three needs.

Magnesia is a widely used additive because it reacts with SiO_2 to give a silicate liquid near the $MgSiO_3$–SiO_2 eutectic when amounts near to 2% by weight are used. The eutectic liquid dissolves Si_3N_4 to produce a Mg–Si–N–O glass capable of fulfilling all the three requirements listed above. From this it is clear that an intergranular glassy phase becomes part of the final microstructure and this can influence hardness measurements; some values of the hardness of this glass are given in Table 6.10.

Yttria, Y_2O_3, is another common aid which fulfills the requirements but in this case produces a crystalline intergranular phase. Unfortunately this yttrium-containing phase is not stable in the presence of oxygen at high temperatures.

Zirconia is the third common sintering aid encountered. It is used at the 5% by weight level to give high density products and grain-boundary crystals of Si_2N_2O and ZrO_2.

Elucidation of the role of sintering aids and uncertainty about the existence of α-Si_3N_4 as a true binary ceramic has led to the development of ternary, quaternary, and higher-level ceramics known as the sialons, an acronym formed from the elements present: Si, Al, O, and N.

6.1.2.2. Sialons

Realization that the atomic arrangements in β-Si_3N_4 are the same as in silicates like Zn_2SiO_4 and Be_2SiO_4 soon suggested that the principles of silicate crystal chemistry should apply. In particular, because the AlO_4 tetrahedron is the same size as the SiO_4 tetrahedron, one can replace the other in silicate structures as long as valence compensation is made elsewhere in the structure; the same should apply with SiN_4 and AlN_4 tetrahedra. It was soon shown to be the case that two-thirds of the silicon in β-Si_3N_4

can be replaced by aluminum without changing the structure provided an equivalent amount of nitrogen is replaced by oxygen. This material became known as sialon for the reasons stated above. Because sialon has the same atomic arrangement as β-Si_3N_4, its mechanical and physical properties are similar to those of the nitride. It has some of the advantages found for solid solutions; in particular, it has a lower vapor pressure and forms more liquid at lower temperatures with sintering additives, thus making pressureless sintering more feasible. Hence lower-temperature densification leads to finer-grained material and higher strength. The solid solutions $Si_3N_4 + Al_2O_3$ carry the designation β'-sialon, and artifacts based on these solid solutions are inevitably sintered with additives which produce microstructures containing grain-boundary phases as was the case for β-Si_3N_4 itself; these are either the nitrogen–oxygen glass or yttrium–aluminum garnet.

While there are sialons based on the β-Si_3N_4 structure known as the β'-sialons, there are others based on the α-Si_3N_4 structure. They usually contain up to two cations from Li, Ca, Y, and the lanthanides per X-ray unit cell. The structural principle involved in these materials is that found in the "stuffed" quartz silicate minerals in which Al^{3+} replaces Si^{4+} and compensating cations occupy appropriately sized interstitial sites in the structure.

As mixtures of the α and β polymorphs usually arise in the preparation of Si_3N_4, in sialon preparation it is common to find mixtures of α' and β' sialons. Vickers hardness determination can be used to assess the amount of α' and β' in a preparation because a linear correlation between H_V and β' content appears to exist, as Figure 6.5 shows. The hardnesses of some β' and α' sialons are given in Table 6.10.

A third family of sialons is based on the Si_2N_2O structure, and these are known as the o'-sialons.

All the sialon families are the subject of intensive research work, but currently commercial materials and artifacts are restricted to two grades supplied by Lucas Cookson Syalon Ltd: a general purpose wear grade known as Syalon 101 which is a β'-sialon with grain-boundary glassy material, and a high temperature grade, Syalon 201, also a β'-phase with yttrium aluminum garnet (YAG) boundary material.

More interest has recently centered on the nature of the glassy grain-boundary phases because glasses containing substantial amounts of nitrogen are quite novel and crystallization of such phases is seen as a way to improve the high-temperature mechanical properties of sialons in general. Typical Mg–Si–Al–O–N glass compositions are listed in Table 6.10, along with some hardness, and hardness-derived data. General equations relating H_K, E, and K_c to nitrogen content have been experimentally derived[4]:

$$H_K = 0.549 \, N + 6.58 \, GPa \qquad (6.3)$$
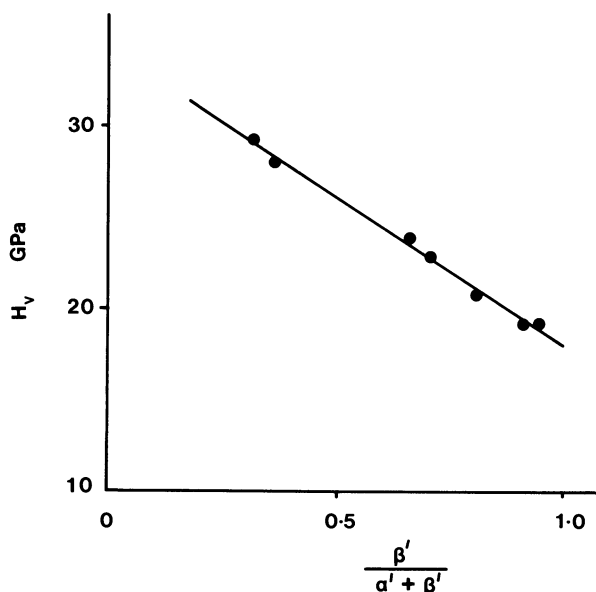
Figure 6.5. Linear dependence of Vickers hardness on the β'-sialon content of sialon preparations. After Babini et al.[3]

$$E = 9.2\,N + 65.4\,\text{GPa} \tag{6.4}$$

$$K_c = 0.0328\,N + 0.82\,\text{MPa m}^{1/2} \tag{6.5}$$

Equations (6.3)–(6.5) can be used for Mg–Si–Al–O–N glasses when N is measured in % by weight.

These equations are statements of the general trend found in all this work with nitrogen-containing glass, that hardness and elastic modulus all increase with increasing N content.

Even more recently a new family of solid solution ceramics based on SiC, Al_2OC, and AlN have been prepared and investigated. The acronym for these materials is sicalon, and they have to be prepared by hot pressing appropriate mixtures of SiC, AlN, sialons and aluminum oxycarbide at temperatures in excess of 1800°C.

All of the forms of Si_3N_4, sialons, and sicalons can be prepared for hardness testing by polishing with the commercial diamond pastes down to 1 μm. If surface etching is needed, a rather harsh treatment is required by boiling in a three-to-two mixture of sulphuric and orthophosphoric acid for four hours.

Table 6.6. Reaction Sintered Si_3N_4

Method	Microstructure	Hardness (GPa)	K_{IC} (MPa $m^{1/2}$)^a	Density, ρ (kg m^{-3})	Notes
Vickers					
—	25% porosity, 0.5–7.0 μm grains	7.5	2.2	—	
—	25% porosity, 2–50 μm grains	5.0	2.2	—	
—	21%α, 79%β	—	3.4	2590	
—	13%α, 87%β	—	2.4	3410	
—	8%α, 92%β	—	2.2	2310	
Knoop					
—		14.2	—	—	0.49 N load 0.98 N load
—		8.83	—	—	4.50 N load
—		8.83	—	—	
Brinell					
—		9.81	2.0	2500	From 3 point bend

^{a} From equation (5.40).

6.1.2.3. Hardness Values and Data Derived from Them

Data for the different types of silicon nitride and sialons can be found in Tables 6.6 to 6.10.

6.1.3. Boron Carbide

Boron carbide, B_4C, is mostly used for its hardness and wear resistance. It is, after diamond and cubic boron nitride, the third hardest material for

Table 6.7. Critical Load and Crack Size for Si_3N_4 from Equations (5.11) and (5.12)

Sample	Load (N)	Crack depth (mm)	Median or radial (mm)	Indent long axis (mm)	E (GPa)	γ (J m^{-2})	P^* (N)	c^* (mm)
HS-130	5.9	0.0305	0.0634	0.0675	310	25	15.7	
	10.1	0.0405	0.0960	0.106				
	15.7	0.0494	0.120	0.1205				
	20.6	0.0640	0.140	0.1398		35		
	25.5	0.0700	0.170	0.1578				
	30.4	0.0800	0.188	0.165		45		
CVD	4.91				310			0.142

Table 6.8. Hot Pressed Si$_3$N$_4$

Method/Sample	Microstructure	E (GPa)	Hardness (GPa)	K_{IC} (MPa m$^{1/2}$)^a	Density ρ (kg m^{-3})	Notes
Vickers	Zero pores 2-μm grains α-Si$_3$N$_4$[1]	—	16	5		[1]$\beta = 2.8$; see equation (1.16)
NC-132		300	18.5	6.6	3200	
		320	14.1	4.9		[2]Rockwell A = 92.8, $\nu = 0.233$
		287[2]	17.86	9.4	32370	[3]Temp = 1000°C
			11.48[3]			[4]30 N load
Composite	SiC whiskers		17.67[4]			
Knoop			24.03			0.49 N load
			19.17			0.98 N load
			14.72			4.9 N load
Composite Si$_3$N$_4$/BN	Acicular grains 2 × 10 μm in fine grained BN		13.5–14.2			1.96 N load
Brinell			17.65	5	3200	From 3 point bend
Scratch			24.7			Load = 50 N using equation (1.52)

^{a} From equation (5.40).

Table 6.9. Chemically Vapor Deposited Si_3N_4

Method	Microstructure	Hardness (GPa)	K_{IC} (MPa m$^{1/2}$)^a	E (GPa)	Notes
Knoop	Crystalline	29.4	—	—	0.49 N load
		25.2			0.98 N load
		19.6			4.9 N load
	Amorphous	20.71	—	—	0.98 N load
Vickers	—	34.4	2.1–5.0	310	0.99 N load; indent with 19.2 μm cracks

^{a}Values dependent on which Equation of (5.40), (5.45)–(5.59), is used.

industrial use. Within its structure it combines a low density, 2510 kg m^{-3}, with a high Young's modulus of 441 GPa, and this leads to its use as lightweight personnel and aircraft armor as well as strong neutron moderator rods in nuclear reactors. For body armor the boron carbide is hot pressed into hexagonal tiles 6 mm thick which are then mounted on a backing of glass-fiber-reinforced epoxy resin. On impact with a projectile, even one made from the hardest, most piercing material such as tungsten carbide, the B_4C shatters but absorbs so much energy in the process that the missile then cannot penetrate the fiber-reinforced underlay.

Industrial production of B_4C is based on fusion of boric oxide and carbon in electric furnaces operated around 2500°C. This process leads to lumps of coarse-grained material of high purity which has to be milled for sinter powders. Finer powders are obtained by magnesiothermic reduction of the boric oxide at lower temperatures around 1750°C:

$$2B_2O_3 + 6Mg + C \rightarrow B_4C + 6MgO \qquad (6.6)$$
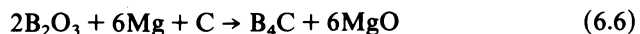
6.1.3.1. Bonding, Composition, and Structure

The covalent bonding in B_4C in both the structural B_{12} icosahedra and the intericosahedra bonds is the same as that occurring in the element boron (Section 6.1.8), and not unexpectedly the rigid three-dimensional structure of B_4C resembles that of boron itself. Two structural units can be discerned, B_{12} icosahedra and C_3 carbon chains. The structure can then be viewed as a face-centered cubic lattice with a B_{12} icosahedron and a C_3 chain occupying the lattice points with the B_{12} at what would be the Na$^+$ sites in the NaCl structure and the C_3 chains being centered on the Cl$^-$ ion sites. Boron is bonded to carbon through *sp–sp* orbital interaction, and three interatomic

Table 6.10. Sialon Hardness Data

Method/sample	Microstructure	Hardness (GPa)	K_{IC} (MPa m$^{1/2}$)	Notes
Vickers				
Syalon	Hot pressed	19.13[1,2]		[1]9.81 N load
	Zero porosity	15.31[1,3]		[2]25°C
	—	12.26[1,4]		[3]500°C
				[4]1000°C
Sandvik cc680	—	13.05	[5,6]	[5]Surface bombarded
			19.3 at 6 μm	with Al_2O_3
			17.6 at 12.3 μm	particles[a] at 140 m s^{-1}
			10.3 at 23.2 μm	[6]Equation (5.49) used
			5.4 at 44.1 μm	with E/H = 23, P = 2.94 N
β'-sialons:				
Si_3N_4–10% CeO_2		17.31		
–5% Al_2O_3	$\beta'/(\alpha' + \beta')$ = 0.31 grains 0.6 μm	29.53		
–5 wt% Al_2O_3	$\beta'/(\alpha' + \beta')$ = 0.87 grains 1.0 μm	21.22		
Mg Sialon Glass				
$Mg_{13.7}Si_{21.6}$ $Al_{3.9}O_{56.9}N_{3.9}$	Zero porosity E = 80.9 GPa	8.90[7] 7.97[8]	0.84	[7]Load = 0.98 N [8]Load = 9.81 N
$Mg_{18.75}Si_{16.67}$ $Al_{6.25}O_{52.08}N$ $N_{6.25}$	E = 108.1	11.46[7] 9.76[8]	1.10	
$Mg_{14.3}Si_{18.4}$ $Al_{8.2}O_{51.0}N_{8.2}$	E = 113.3 GPa	11.64[7] 9.57[8]	0.95	
Sicalon	Hot pressed 90–95% SiC, 4.1–2.1% Al_2O_3 5.9–2.9 Al_4C_3	20.5–21.4	4.1–4.3	
Knoop	Glass zero	7.16[9]		[9]0% N
Y-Al-O-N glass	porosity	7.95[10]		[10]5% N
		9.12[11]		[11]10% N
		9.86[12]		[12]15% N
Mg sialon glass, composition as above				
$N_{3.9}$		7.66[7] 6.22[8]		
$N_{6.25}$		9.27[7] 7.00[8]		
$N_{8.25}$		9.47[7] 7.42[8]		
Y sialon glass	Zero porosity			
at % N = 6.3	ρ = 3820 kg m^{-3}	9.01[7]	0.95	E = 141 GPa
13.3	ρ = 3920 kg m^{-3}	10.37[7]	1.44	E = 157 GPa
15.0	ρ = 4000 kg m^{-3}	10.37[7]	1.25	E = 186 GPa
Brinell	—	19.62	8–10[13]	[13]Determined by
Syalon				3 point bend, not hardness.

[a]The results showing a very high K_{IC} value at the surface after erosion with fine Al_2O_3 particles are a strong indication that engineering ceramics may have much tougher surfaces than first thought.

distances are important: B–B = 0.174 to 0.180 nm, B–C = 0.164 nm, and C–C = 0.139 nm. A section of the structure is shown in Figure 6.6 indicating how the C_3 chains are bonded to the boron icosahedra.

From Figure 6.6 it is easy to see that B_4C is likely to be an idealized composition because excess boron can be accommodated by replacing the central of the three carbon atoms by boron, which would then form a stronger sp–sp bond with neighboring boron atoms in the icosahedra. Thus it is possible to get a composition range from $B_{12}C_3$ to $B_{13}C_2$ and, even though this happens, the general hardness data for boron carbide do not reflect the possibility with investigators quoting B_4C as the composition each time. However, detailed hardness values and those for hardness-related properties are not plentiful as Section 6.1.3.2 shows.

6.1.3.2. Hardness Values and Data Derived from Them

Data derived from the hardness values of sintered B_4C can be found in Table 6.11.

6.1.4. Boron Nitride

Principally two forms of BN, differing markedly in their hardness, are commercially available. The hexagonal form because of its chemical inertness, its electrical insulating properties, and its low coefficient of friction
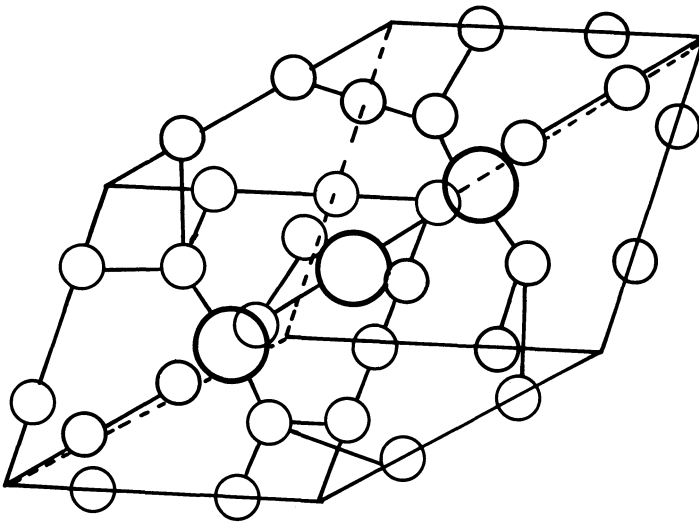
Figure 6.6. Part of the structure of B_4C. Large atoms are carbon; small atoms are parts of boron icosahedra.

Table 6.11 Hardness of Sintered B_4C

Method	Microstructure	Hardness (GPa)	E (GPa)	γ (J m^{-2})	Notes
Vickers		44.15	460[a]	3.27	load = 0.98 N
	Fine polycrystalline	32.2	500		K_{1_c} = 6.0 MPa m$^{1/2}$
Rockwell C					
	Porosity range 0–30%, grains 2 μm	30–90[b]			

[a] $E = 460[1 - \theta/1 + 2.99\theta]$ GPa, where θ = fractional porosity.
[b] $H_R = H_o(1 - \theta^2)^2 \exp(-B\theta)$, where $B = 0.35$ for boron carbide.

is encountered mostly as crucible material for molten metals and as high-temperature insulation. In these uses it is usually fabricated by the hot pressing route.

At temperatures around 2300°C and high pressures, around 6.3 GPa, the hexagonal form can be converted to a cubic diamond structure form. The cubic modification is known as borazon and is finding application now in wear-resistant parts and in the cutting tool industry.

A third form of BN exists that is also a high pressure polymorph, with the wurtzite, structure and it is not always clear whether borazon samples contain both the cubic and this hexagonal form.

Although borazon requires fierce conditions for its manufacture, the precursor hexagonal BN powder is made by a relatively low-temperature reaction from boric oxide. An inert filler is used to disperse the B_2O_3 and prevent it from forming large, slow-to-react lumps; calcium phosphate is a common filler material stable at the 600–800°C at which the reaction is carried out. Ammonia is used to convert the B_2O_3 to BN at these temperatures. Acid leaching leaves an impure product that is upgraded by heating in ammonia to 1100°C and nitrogen to 1800°C.

A chemical vapor deposited material is made by pyrolyzing trichloroborazine and plating the vapor formed BN onto substrates:

$$B_3N_3H_3Cl_3 \xrightarrow[1300°C]{} 3BN + 3HCl \qquad (6.7)$$
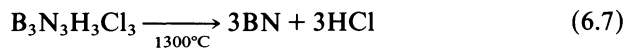
At temperatures around 1000°C the product is amorphous and up to 1200°C it is polycrystalline with little orientation. When prepared above 1800°C by this method the product is highly oriented with resultant obvious anisotropy of mechanical properties. This feature can affect the values of hardness found in the literature. All forms are chemically very inert, but

surfaces can be etched with sodium nitrate at 530°C and slip traces revealed on {111} if not {001} surfaces.

6.1.4.1. Bonding, Composition, and Structure

Carbon and BN are isoelectronic and not surprisingly, therefore, the two structures found for carbon, diamond, and graphite are found for the main polymorphs of BN. The common hexagonal "white graphite" form is shown in Figure 6.7. Hexagonal layers of alternating B and N arise from covalent bonding between half-filled sp^2 hybrid valence orbitals. Each atom in the layers has a p_z orbital perpendicular to the plane of the hexagonal rings but, while the boron orbital is empty, each nitrogen p orbital is full; π-interaction between these orbitals is minimal because of the preclusive energy differences. Thus there is no delocalization as is the case with hexagonal carbon layers, and so BN is not metallic in behavior. The presence of the lone pair on each nitrogen atom does assist the direct alignment of a N atom above a B atom in successive layers, as Figure 6.7 shows. The hexagonal unit cell has $a = 0.2504$ nm and $c = 0.661$ nm and a density of 2270 kg m^{-3}. Planar B–N bonds are 0.145 nm long and interlayer B–N bonds are 0.333 nm long, providing obvious anisotropy in mechanical behavior.

The cubic, very hard form borazon is difficult to produce from the hexagonal structure shown in Figure 6.7 because to obtain the cubic F unit
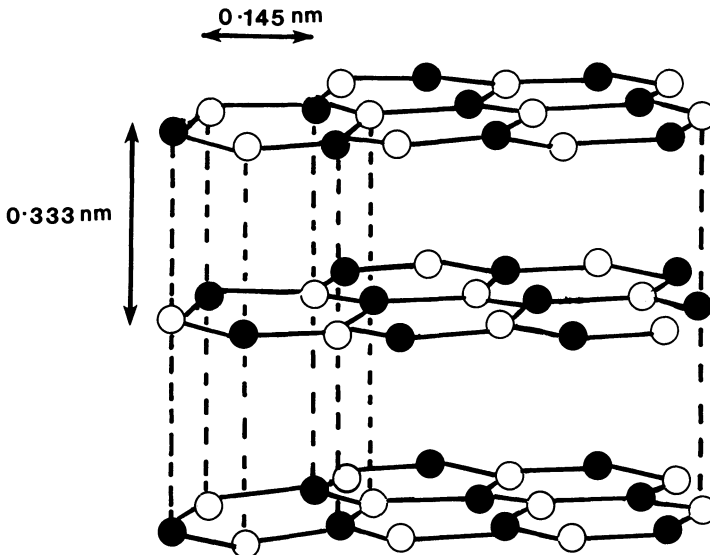
Figure 6.7. The layer structure of hexagonal BN. Dark circles are boron atoms and white circles are nitrogen.

cell with tetrahedrally distributed 4-coordinate B and N atoms, bonding has to be changed to sp^3 hybrid bonding from the sp^2 arrangement.

6.1.4.2. Hardness Values and Data Derived from Them

Few data exist, but some are collected in Table 6.12.

The results for aggregated BN cubic crystals shown in Figure 6.8 demonstrate a surprisingly high rate of indentation creep (see Section 4.4) at such a low homologous temperature—i.e., $\sim 0.2 T_m$.

Table 6.12. Hardness of Sintered BN

Method/sample	Microstructure	Hardness (GPa)	Notes
Vickers			
Hexagonal	—	1.96 ⎫	Loads in the range 0.245–1.47 N
Cubic Borazon	—	46.11 ⎭	
60% cubic	3 μm grains in a	35.33	
85% cubic	binder of TiN, AlN, and WC	42.20	
Knoop			
Hexagonal BN	Polygonal grains of 2 μm in Si$_3$N$_4$ matrix	6.87	Load = 1.96 N
Cubic	3–9 μm grains in binder phases TiN and TiB	33.35 ⎫	
Cubic	1–5 μm grains in TiN, TiB binder	34.35 ⎪	
Cubic	1–3 μm grains in TiN binder	39.2 ⎬	Load = 4.91 N
Cubic	2.5 μm grains in cobalt and WC binder	39.2 ⎭	
Cubic	Single crystals 200–500 μm edge length, (001) plane long axis [100], (001) plane long axis [110]	43.0 ⎫ 30.0 ⎭	Load = 4.91 N; consonant with $\{111\}\langle 1\bar{1}0 \rangle$ being the active slip system
Cubic	Aggregate of 10 μm crystals	55	Load = 0.98 N
		39.5	Load = 1.96 N
		35	Load = 2.94 N
		30	Load = 4.91 N, then no further load effect on hardness; n in equation (4.2) = 1.7
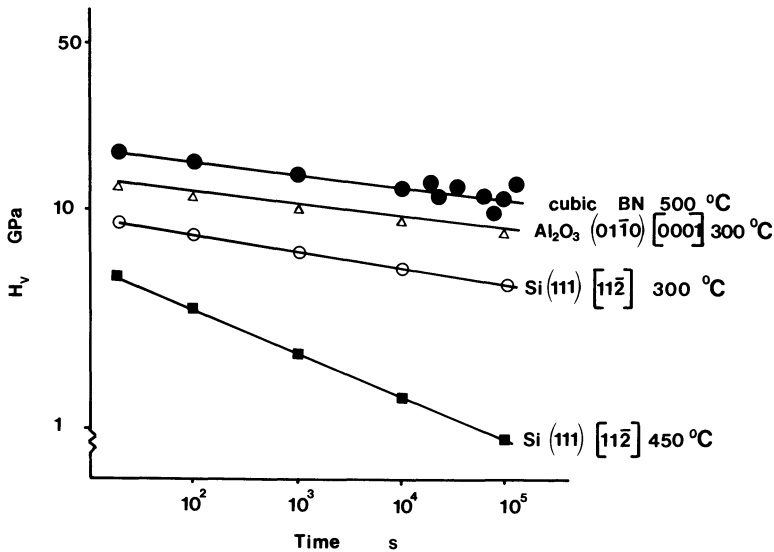
Figure 6.8. Hardness of cubic BN at 500°C showing an indentation creep effect and comparing it to some single crystal data for alumina and silicon.[5]

6.1.5. Silicon Dioxide, Silica, Glasses, and Glass Ceramics

There are three main reasons why a considerable amount of work in the hardness field has been done with this class of materials. First, on the theoretical front, there is the fact that glasses have been considered to be ideal brittle materials and have been used to test theoretical ideas; the fact that conventional, soda-based glasses could be indented without cracking was an early step in the reappraisal of this class of materials. Marsh[31] used the presence of indentations in glass surfaces and the appearance of sliding hardness grooves to suggest that glasses had a plastic component in their mechanical behavior. Naturally this became a source of controversy and fueled many indentation hardness studies.

A second obvious reason why glasses have been studied so much is the fact that they are transparent and the generation of cracks below the surface can be seen and measured.

The third main reason why hardness methods have been used is technical in the sense that crystallization of the glass to produce whole new families of materials—the glass ceramics—can be followed. Glass ceramic systems are becoming increasingly important in applications as high-temperature, high-strength, 100% dense bodies.

Most recent and careful observation of the deformation zone below an indent in glass shows that it consists of a series of flowed areas separated by areas in which elastic deformation has taken place (see Section 5.8). All

deformation between the elastic zones is concentrated into a series of intersecting flow lines. Median, radial, lateral, and Palmqvist cracks appear to be nucleated by the strains at the intersection of these flow lines or along them where they have boundaries with the elastic-only deformed regions. Observations such as those summarized above do show that genuine slip occurs and not just compaction of the open network structures of the glass.

6.1.5.1. Silicon Dioxide

The various forms of SiO_2 are based on complete corner sharing of the four oxygen atoms in SiO_4 tetrahedra, and the large degree of polymorphism arises from the competing structural requirements outlined below. First consideration must be given to the covalent bonding present in the "isolated" SiO_4 unit; silicon with a groundstate electron configuration $1s^2 2s^2 2p^6 3s^2 3p^2 3d^0$ requires less energy to form four valency orbitals via the excited state $1s^2 2s^2 2p^6 3s^1 3p^3 3d^0$ than does the archetypal atom carbon. Hence these four valency orbitals are formed and are directed to the corners of a tetrahedron with no involvement of the empty, relatively low lying $3d$ orbitals. To match these valency orbitals of silicon it is possible for oxygen atoms to be hybridized also to produce four sp^3 hybrids from the ground state $1s^2 2s^2 2p^4$, and resonance between the Si and oxygen hybrids would produce a tetrahedral unit, as observed, but bonding of two or more of the SiO_4 units through an oxygen atom would result in Si-O-Si angles of 109°. However, in this orientation none of the oxygen $2p$ orbitals containing wave pairs are directed toward the empty $3d$ orbitals on the silicon atom and so no π-bonding with resultant strengthening of the Si-O bonds can occur. If, however, the oxygen atoms are hybridized only to the sp state then linear Si-O-Si bridging would result and the $2p^2$ orbitals on the oxygen atom would be able to interact with the empty $3d$ orbitals of silicon producing stronger Si-O bonds. Thus SiO_2 and glasses based on SiO_2 can have Si-O-Si bridging angles between the structural SiO_4 building units that vary from 109° to 180°, giving rise to polyhedral variation. Put another way, it is possible to say that oxygen orbital hybridization can alter to accommodate the requirements of other groups bonded to the silicon or to meet the coordination requirements of charge balancing cations that are found in silicates and glasses.

A second structural feature of linked SiO_4 tetrahedra leading to polymorphism is the rotating of tetrahedra about the common oxygen atom to give configurations ranging from eclipsed to staggered. This feature was not possible for SiN_4 tetrahedra in Si_3N_4 (see Section 6.1.2).

A third possibility is relative tilting of tetrahedra about triad axes. These variations do give rise to polymorphs, and it is not outside the bounds of possibility that the large hydrostatic pressures beneath an indenter can

cause some of them to occur locally with corresponding energy absorption and apparent increases in hardness. Structural analysis of the material in the immediate vicinity of an indent is not often encountered and so this possibility is not considered.

All SiO_2 structures are described as frameworks and have "open" appearances with large interstitial spaces. The structures are a compromise between the conflicting requirements of tetrahedral shape, the ideal tetrahedra linking angle of 180°, and the symmetry demands of the structure. The main polymorphs are described below.

6.1.5.1a. Quartz. This is stable up to 870° when it transforms to tridymite, but because substantial rearrangement of oxygen hybridization is required the transformation is very slow to occur. At 573°C quartz undergoes a rapid phase change between the α (low-temperature) form and the β (high quartz) structure with the transformation just involving a small amount of rotation by SiO_4 groups about diad axes. The β-form of quartz appears to be stronger than the α-form and has a zero to slightly negative thermal expansion coefficient up to 1400°C. The fact that it does exist up to such a high temperature reflects the sluggish nature of the quartz $\rightleftharpoons$ tridymite change. Both forms of quartz are common raw materials of the ceramics industry. When pure, quartz is colorless and transparent, commonly exhibiting conchoidal fracture.

Both structures are based on a hexagonal lattice containing three formula units per unit cell with $a = 0.49$ nm and $c = 0.539$ nm.

6.1.5.1b. Tridymite. This form of SiO_2 exists in the temperature range 870°C–1470°C before transforming to cristobalite, but again the transformation is extremely slow. A consequence of the sluggishness of the transformations is that tridymite is commonly encountered at room temperature where it has an extremely large hexagonal unit cell with $a = 3.008$ nm and $c = 4.908$ nm, containing 864 formula units; this is α-tridymite. At 250° there is a rapid phase transformation to the β-form which has a much smaller hexagonal unit cell with $a = 0.503$ nm, $c = 0.822$ nm. This simpler structure can be described in the pseudolayer manner already used for SiC and Si_3N_4 and some correlation with SiC can be seen, making it likely that SiC is protected to give it environmental protection by a thin layer of tridymite rather than the other forms of SiO_2.

6.1.5.1c. Cristobalite. This is the high-temperature form of SiO_2 from 1470° to the melting point at 1730°C, but it can be encountered down to ambient temperatures as once again the kinetics of transformation are dominant. The idealized structure is cubic; $a = 0.705$ nm with Si–O–Si linear groups in the diamond structure. When found at room temperature it is

actually tetragonally distorted; this is the α-form. Once again there is rapid transformation to the cubic β-form at 220°C as the Si–O–Si bond angles open out to 180°. The β-form has negligible thermal expansion because increase in the Si–O–Si angles causes a shortening of the Si–O bonds while the rising temperature increases their length, tending to a null situation.

Both α- and β-cristobalite can be described by the pseudolayers of puckered hexagonal rings of SiO_4 units, and when this is done it is possible to see that tridymite and cristobalite are related in the way the zinc blende and wurtzite structures are.

The increasing openness of these polymorphs is reflected in decreasing density from quartz (2655 kg m^{-3}) to cristobalite (2330 kg m^{-3}).

Perhaps significantly in the context of this book there are three rare polymorphs of silicon dioxide all found after the application of high pressure: coesite, keatite, and stishovite. The possible production of these in the zone immediate to the indenter and the energy this would absorb do not appear to have been considered.

6.1.5.2. Silica and Glass

Silica is the name given to fused SiO_2 that has become rigid without crystallizing and is therefore the glass formed from the polymorphs described in Section 6.1.4.1. Being a glass it conforms to the definition: a noncrystalline elastic solid with viscosity $> 10^{12.5}$ Ns m^{-2}. To be noncrystalline we conceive it to be a solid with areas of 2.0 nm maximum order. Within this constraint for order there have been many attempts to describe structural models for silica and other glasses; there are too many to review and consider the various features of, but this information can be found in Chapter 3 of reference (6). Sufficient to say that the commonly accepted random network model based on the disordering of the crystalline structures of SiO_2 may be neither correct nor the most helpful when considering the behavior of glasses in general.

It must be emphasized, however, that when glasses based on silica are formed by adding other oxides such as CaO and Na_2O then substantial changes to the bonding must occur with the introduction of a varying degree of ionic bonding making these solids mixed covalent and ionic in character.

None of the models for glass structure allow interpretation of behavior via dislocation generation and glide which, in the area of hardness and mechanical properties, is a drawback as most of the work in the preceding chapters demonstrates. Interpretation is heavily dependent on flaw generation and propagation and on chemical bond interpretations involving dilation effects. For example, it has been shown that dilation of an already compact structure in metallic glasses does lead to flow behavior. Such behavior does reflect an overall structure in which localized structural

variations can control overall mechanical properties. The appearance of
kinked "flow lines" has already been described in Section 5.8 and shown
to produce hardening effects under the point of a pyramid indenter.

The addition of oxides known as network modifiers—that is, Na_2O,
K_2O, CaO, La_2O_3, and many other *ionic* oxides—generally causes a con-
tinuous decrease in hardness, and where this is found not to be true then
it is because precipitation of finely dispersed crystals is taking place. For
example, up to 10% by weight La_2O_3 decreases the Vickers hardness of
silica from 6.87 GPa to 6.38 GPa almost linearly, after which the hardness
rises again as more La_2O_3 is added and $La_2Si_2O_7$ pyrosilicate crystals are
formed. This is a useful outlet for the technique of microhardness indenta-
tion because it can be used to follow nucleation and crystal growth stages
in the preparation of glass-ceramic materials.

While the material remains a glass the hardness decreases on addition
of ionic oxides because the polarizability of all nonbridging oxygen atoms,
those that are not shared by two network elements such as silicon, is
increased. Thus we are not surprised to find that indentation hardness does
have a strong correlation with changes in molar refractivity of glass, the
polarizability of the added cation, and glass softening temperature.

It is through these effects that other mechanical correlations are made—
for example, the relationship between Young's modulus and Vickers hard-
ness which can be expressed as equation (6.8).

$$H_V = C'(\alpha GK)^{1/2} \tag{6.8}$$

In equation (6.8) C' is a constant giving the ratio of the stress to the
resistance to deformation at the time the indentation ceases; α is the ratio
of average single bond strength to Si–O bond strength. G and K are shear
and bulk moduli, respectively, with $G = E/2(1 + \nu)$ and $K = E/3(1 - 2\nu)$.
The Poisson ratio is estimated from the ionic oxide volume fraction com-
pared to the SiO_2 volume fraction. For silica glass with no added modifier,
α must equal 1 and $C' = 0.19$.

Equations (5.11) and (5.12) relate flaw sizes that are produced by
impact on glass to the measured hardness via the fracture toughness
parameter.

Perhaps the most important semi-empirical relationship between
indentation hardness and a mechanical property of glass, namely, flow
stress, has already been introduced in Chapter 1; it is that derived by Marsh
following his original interpretation of indentation shapes in glass. Marsh[31]
was originally interested in finding the yield stress in glass, having postulated
that glasses were not perfectly brittle as generally assumed. Taking a leaf
from the metallurgist's book, he turned to the Tabor relationship, equation
(1.9), which was derived for a flat, rigid indenter and gives two-thirds the

pressure under the indenter as hydrostatic and one-third as shear stress with only the latter able to produce plastic flow. This assumes that elastic deformation is unimportant. However, equation (1.9) leads to values of flow stress well below the observed brittle fracture stress and so flow should be apparent in the fracture patterns of glass. To resolve this dilemma Marsh believed that elastic deformation in glass systems was important and so moved from the Tabor approach to that of a spherical cavity being expanded by the hydrostatic pressure with no material being forced up to the surface. Combining his analysis with hardness and modulus data for a series of glasses, ceramics, and plastics he arrived at equation (1.13), which is similar in form to the more theoretically derived equation of Johnson (1.14). A late small variation in the model changed equation (1.14) to the following

$$H_V = \frac{2}{3}\left[1 + \frac{\ln E \cos \theta}{3(1 - \nu)\sigma_y}\right]\sigma_y \qquad (6.9)$$

Equations (1.13), (1.14), and (6.9) give $H_V \simeq 4.5\sigma_y$ instead of the Tabor relationship and give values of σ_y sufficiently close to σ_{uts} that the phenomena associated with yield and flow are not apparent in macroscopic breaking tests of glass. Nevertheless clearly from the appearance of the area directly beneath an indenter the material can be made to flow as these stresses are reached and exceeded. The intersection of flow lines below the glass surface is the site of flaw generation leading to failure.

That Marsh's instinct was correct regarding the importance of the elastic component of the deformation of glass and ceramics has been much more recently confirmed in the derivation and practical application of a relationship between the residual impression dimensions, hardness and modulus.[7]

The analysis is based on two cycles of a Vickers indenter where first the loading causes elastic and plastic deformation, then unloading allows elastic recovery, and finally reloading is done at the same indent with loads sufficient to bring about various percentages of the original elastic deformation and increase the indent depth to the original depth. This sequence is sketched in Figure 6.9.

In Figure 6.9, the depth of impression L is given by equation (6.10)

$$L = \gamma a \cot \psi \qquad (6.10)$$

where γ is a geometrical factor that takes account of surface deformation around the indent (see Figure 1.6).

Load P is related to hardness through equation (1.6) and elastic recovery is governed by equation (6.11)
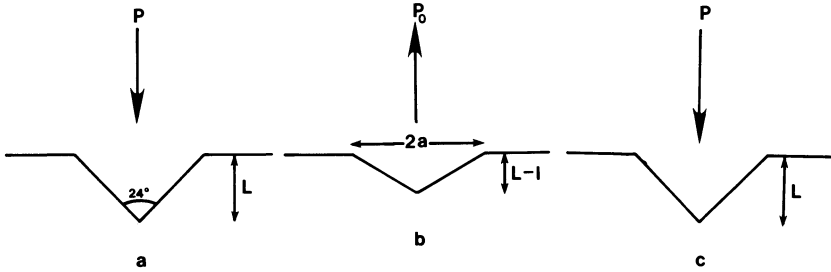
Figure 6.9. (a) Vickers indent made. (b) Elastic recovery of the indent. (c) Reloading to deform to original depth.

$$P_o = \frac{E \cot \psi}{2(1 - \nu^2)} \tag{6.11}$$

Impression depth after unloading divided by the unrecovered depth L is called the residual impression parameter, and this parameter squared is related to hardness and Young's modulus from equations (6.10), (6.11), and (1.6)

$$\left(\frac{L - l}{L}\right)^2 = 1 - \left[2(1 - \nu^2)\left(\frac{\gamma_E}{\gamma_H}\right)^2 \tan \psi\right] \frac{H_V}{E} \tag{6.12}$$

It is not always possible to measure the indent depth directly by focussing on indent bottom and surface, respectively, at the depths required to produce uncracked indentation, but when it is done equation (6.12) is found to be obeyed with respect to a linear dependence between H_V/E and residual impression parameter squared until low values of H_V/E are encountered.

    A closer fit with experimental data over the whole H_V/E range is claimed for the related expression given as equation (5.64) for the reasons given in Section 5.4.3.

    An interesting use of equation (6.12) is as an elasticity–plasticity parameter to classify not only glasses, but ceramics in general. This arises because for ideal elastic behavior $(L - l/L)^2$ = zero and H_V/E is the ratio that brings the bracket in (6.12) to unity. Thus $H_V/E = 0.15$ represents no plasticity, and for perfect plasticity $(L - l/L)^2 = 1$ because $l = 0$, and for this to be true H_V/E must equal zero. The above ratios are found using $\nu = 0.25$, $\gamma_E/\gamma_H = 1$, and $\psi = 74.05$. Data given in Table 6.13 show soda–lime glass not to be least plastic of the range of materials quoted.

    These then are a number of equations and observations that have resulted from using glass to study the processes that generate indentation shapes and cracks around such indents.

Table 6.13. Values of H_V/E as a Plasticity Parameter

Material	Vickers hardness (GPa)	Young's modulus (GPa)	H_V/E
B_4C	44.2	460	0.096
Soda–lime glass	5.6	70	0.080
Pyroceram	8.4	109	0.077
Si	9	168	0.054
SiC (single crystal)	33	460	0.072
SiC (RB)	25.7	403	0.064
SiC (CVD)	32.3	450	0.072
Si_3N_4-α	18.5	300	0.062
Si_3N_4-β	16.0	310	0.052
Al_2O_3	20.1	406	0.050
WC–Co	12.7	575	0.020
ZrO_2 (PSZ)	11.4	170	0.067
MgO	9.3	240	0.039

The nature of glass surfaces and their structure can be investigated by using hardness techniques: One example applied to industrially made flat glass suggests how such glass can be improved.[8] Vickers indents were made on the surface of the glass as received, after various heat treatments and after treatment with boiling water. Following a dwell time of 15 s at loads in the range 0.75 to 1.25 N, the indent corners with cracks emanating were counted 15 seconds after the indenter was withdrawn. The ratio of cracked corners to all corners expressed as a percentage was used for comparisons. After analysis for Na^+ and H^+ content and a consideration of the results it was clear that treatments able to remove surface hydrogen result in more cracks. The H^+-depleted layer was found to be only 100 nm thick but is dominant in its effect on the appearance of indentation traces and the cracks they contain. Depolymerization at the surface of the Si–O–Si network causes Si–OH groups to be in the surface layer. Thus the 100-nm layer is softer and has a lower σ_y and E. This softer layer will yield more easily and produces less cracks as a result. Thus heating the glass to 460°C increases the crack formation on subsequent tests by 50% compared to the as-received glass while treatment with boiling water quickly restores the glass to the as-received condition with few cracked indents being made. A reheat to 550°C reintroduces the propensity for cracked indents with 60–100% of all corners having cracks. This experiment is a visible confirmation of the phenomenon in glasses known as antifatigue: Standing in damp environments in the absence of stress produces an increase in the strength of the material.

Table 6.14. Hardness of SiO_2, Glasses, and Silicates

Material	Form	Microstructure	Vickers hardness (GPa)	Knoop hardness (GPa)	E (GPa)	K_{IC} (MPa m$^{1/2}$)	Notes
SiO_2	Quartz crystal	(001)	12.17[1]	—	—	—	[1]Dry material; when wet, the hardness decreased to 10.80 and 5.40 GPa, respectively
SiO_2	Fused glass	—	7.12[1]	5.73	—	0.7	
Cordierite Al_3Mg_2 $(Si_5Al)O_{18}$	Crystals	Sintered polycrystals	8.2	—	—	—	
Cordierite	Glass	—	6.6	—	—	—	
Pyroceram C9606	Glass ceramic	1 μm grain of cordierite, 5% glass phase	8.4	6.47	108	2.5	Load = 0.98 N
Commercial soda-lime-silica glass	Glass	—	5.6 6.61	—	70	0.75 1.10	
Alkali glass 7.6:92.4 mol %	Glass	—	5.54	—	—	—	Exposure to H_2O reduces hardness to 4.51 GPa
Float glass			4.4	4.51			
Pyrex	Glass	—	5.0	4.12	70	0.75	
Alumina silica glass $Al_2O_3:SiO_2$ 0.9:99.1 mol %			6.08	—	89	0.8	
$La_2O_3:SiO_2$ 1.85:98.5 mol %	Glass	—	6.45				
$La_2O_3:SiO_2$ 5.36:94.64 mol %	Glass ceramic	$La_2Si_2O_7$ crystals in glass matrix	6.87				

Material	Phase	Formula	Value	Conditions
Schott Zerodur			9.32	Load = 4.91 N
B_2O_3	Glass		2.01	Load = 1.96 N
GeO_2	Glass		1.94	Load = 4.91 N
			3.43	Room temperature 1.96 N load
			1.96	400°C
Machinable glass ceramic	Glass + crystals	$KMg_3AlSi_3O_{10}F_2$	1.72–4.62	
Glass ceramic Li_2O-CdO-SiO_2 10-30-60 by weight %	Glass		6.0	
	Glass crystal		8.0	
10-40-50	Glass		6.5 3.5	After anneal at 550°C After 650°C phase separation
	Glass		5.75 7.00	
10-60-30	Glass crystal		6.50 4.50	After anneal at 550°C After 650°C phase separation
	Glass		6.50 5.50	
Glass ceramic SiO_2-Al_2O_3-Y_2O_3-CaO	Glass crystal		6.75 6.0	After anneal at 550°C After 650°C phase separation
	Crystals[10] $Ca_4Y_6O(SiO_4)_6$ hexagonal		6.87	Crystals formed after 2 hours at 1100°C

6.1.5.3. Glass Ceramics

A glass ceramic begins its existence as a glass which at some stage in the manufacturing route undergoes a process that enhances the formation of crystal nuclei by the addition of nucleating agents and controlled changes in the heating cycle. The resultant material contains very small crystals and ideally is 100% crystalline. However, the technical compositions that can in the first instance provide glasses stable enough to be processed by glass technology methods and then later be crystallized are almost impossible to crystallize to zero-glass phase. Hence the properties of these materials are dominated by the residual glassy phase around the crystals.

At present the major restriction in this field is the need for the initial glass, which puts a restriction on the range of crystal composition and the types that can be encountered. The most advantageous aspect is that they are to some extent engineerable in the sense that thermal expansion coefficients can be varied to suit both metal and ceramic systems. This means that they represent good intermediate materials able to bond metals and ceramic systems together. Dependence on the intergranular glass phase means that they have limited refractoriness and poor strength characteristics.

Hardness is used in two areas of their study: first, as a method of monitoring the preparation process through hardness–temperature–time studies; second, to estimate strength and toughness. An example of hardness revealing something about the glass-ceramic process is the results for Li_2O–CdO–SiO_2 glasses before and after heat treatment as given in Table 6.14. These results[9] show broadly that separation into crystals and glass occurs around 650°C and after separation the new glass contains a higher percentage of CdO and is therefore harder than the original glass. In contrast the glass ceramic prior to separation has a decreasing Knoop hardness as the CdO content increases.

A useful property of some of the series—for example, lithium aluminum silicate (LAS)—is that they are transparent and offer an alternative to glass and single crystals for the direct observation of indentation processes and crack formation.

6.1.5.4. Hardness Values of Silicon Oxides, Glass, and Some Glass Ceramics and Data Derived from Them

The limited amount of data in Table 6.14 is sufficient to demonstrate the large decrease in hardness that accompanies glass formation in the SiO_2 system and in the classical silicate system cordierite. They also demonstrate, along with Figure 6.10, the presence of surface softening induced by an aqueous environment. Little variation in the toughness parameter K_{IC} is encountered, which from equations (5.11) and (5.12) implies that only small
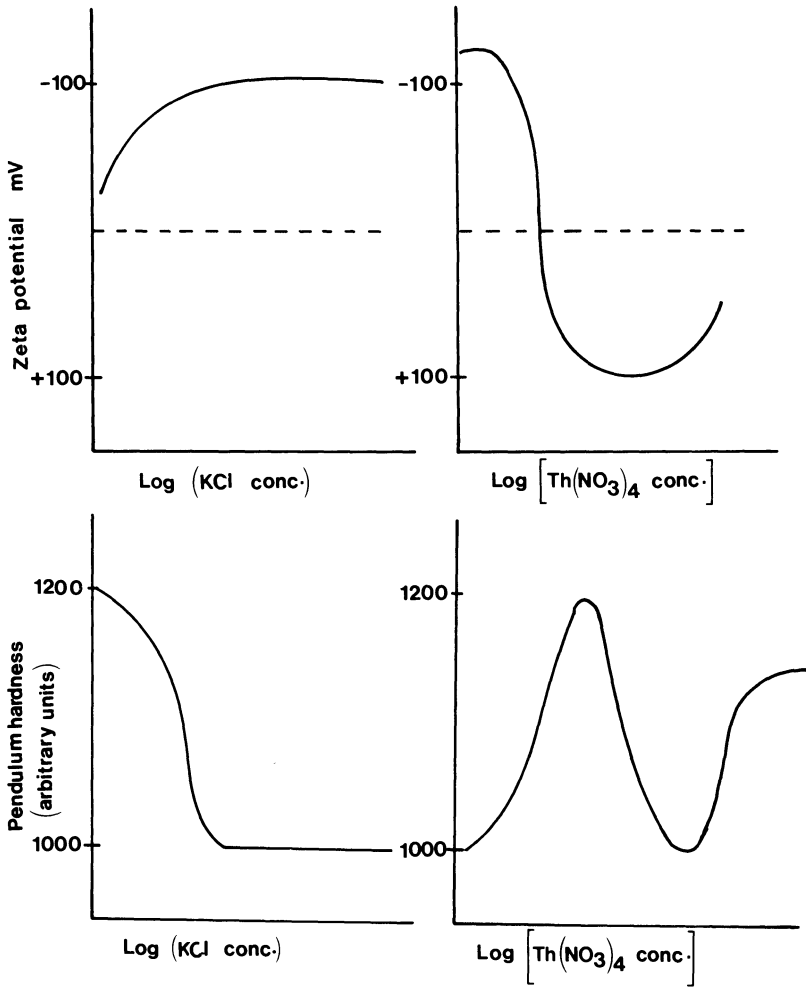
Figure 6.10. Correlation between pendulum hardness and zeta potential at the surface for glass ($Na_2O : CaO : MgO : SiO_2$) = (10.8 : 8.6 : 7.2 : 73.4 mol %). Maximum hardness is achieved when zeta potential is zero.

critical impact loads are necessary to produce the flawed surfaces so dominant in glass mechanics, glass science, and glass usage.

6.1.6. Carbon, Silicon, and Boron

Interest in these covalent ceramics is almost equally divided between potential engineering applications and their use as electroceramics. Carbon

as graphite and as fiber is rapidly gaining in engineering applications; obviously, as a cutting and drilling medium, carbon in its diamond form has always excited interest. The excellent heat-transfer characteristics of diamond give it special applications in electroceramics as a substrate; in this respect recent success in deposition from the vapor phase of diamond-type films could be very significant.

Silicon as whisker material is entering the area of engineering application, but the dominant area of interest is the use of silicon and doped silicon as semiconductor materials. The use of hardness measurement as a probe of the properties of specially prepared silicon crystals for semiconductor device use has been attempted several times but as some of the data presented below show, doping at the levels used in the device industry does not show up as change in hardness even through etch-pit rosette studies in the area around indentations show some dependence of dislocation movement on concentration and type of dopant.

Boron is a major fiber for engineering applications in such areas as reinforcement of aluminum but has not been examined by the hardness technique to any substantial extent.

Despite the multitude of applications of these materials, it is true to say that most of the interest shown in their hardness properties is purely theoretical because of the controlled way in which experiments can be carried out involving them, as well as the ready availability of well-characterized single crystals. Thus data on diamond and single-crystal silicon is reasonably easily found while information on other polymorphs is frequently not available. This latter point brings us to a consideration of bonding, polymorphism, and microstructure of these materials.

6.1.6.1. Carbon

Crystalline carbon exists in natural deposits in three crystalline modifications: α and β-graphite and diamond. Synthetic graphites contain only the α-form, from which the β can be made by mechanical working. This introduces the possibility of the transformation $\alpha \to \beta$ during a hardness test. Localized transformation from diamond to a metallic carbon β-graphite could also be considered, but in this case a radical rearrangement of covalent bond hybridization would be required from sp^3 to $sp^2 + p$ such that time would be a problem.

6.1.6.1a. Diamond. Classically the groundstate carbon electron structure hybridizing to produce four sp^3 valency orbitals explains the tetrahedral coordination, the constant C–C bond lengths of 0.1555 nm, and the three-dimensional picture of a structure consisting of puckered hexagonal rings.

The layer sequence of the carbon atoms is (AA')(BB')(CC')(AA'), etc., where A and A', etc. denote the different orientations of layers. The brackets show the overall sequence ABC... which indicates the cubic overall sequence. Thus diamond has a cubic structure of high symmetry such that any section through it cuts large numbers of strong sp^3-sp^3 bonds so that no easy cleavage exists.

6.1.6.1b. Graphite. The α-form has an hexagonal stacking sequence of layers caused by the turbostratic arrangement of new neighbor layers when the layers are rotated by 60° on ascending the c axis in order to minimize delocalized π-bond repulsion. All layers are planar because the carbon atoms have hybridized sp^2 orbitals producing very strong covalent bonds at 120° in the plane of the layers. Sideways overlap of the p_z orbitals produces the π bonds delocalized in the plane of the layers and bestowing the metallic properties, as well as the gross anisotropy evident in all properties of graphite.

When the layer stacking has a smaller turbostratic angle such that the position repeats after every fourth layer—i.e., there is an ABC ABC... stacking sequence while maintaining the sp^2 hybridization—then β-graphite results. If the layer sequence were maintained but the hybridization changed to sp^3 then a transformation of β-graphite to cubic diamond would result.

Graphite is a generic term for a wide range of carbonaceous materials made by high-temperature pyrolysis of a range of organic precursors ranging from coal through hydrocarbon gases to polymer fibers such as polyacrylonitrile. Such products have a variety of crystal and microstructures ranging from the nearly perfect crystalline material known as pyrolytic graphite to the amorphous phases known as carbon black or glassy carbon. All manufactured graphites in fact consist of microcrystalline graphitic regions in an amorphous carbon matrix. Frequently there is no simple stacking sequence of carbon layers in the graphitic regions so that intergrowths of α and β exist.

Until recently, chemical vapor deposition of cracked hydrocarbons was a source only of pyrolytic carbon with a graphite structure but when deposited in a glow discharge produced by a radio frequency generator of 0.5–1.0 kW from a gas pressure of 0.5–3 kPa and at 950°C, microcrystals of diamond have been deposited.[10] The diamond film is formed from {111} and {100} crystal faces and has a high hardness as shown in Table 6.15.

6.1.6.2. Silicon

This element crystallizes with the diamond structure involving covalent bonds formed from sp^3 hybrid silicon atoms. A molecular orbital description of bonding based on the sp^3 hybrid orbitals shows that the gap between

Table 6.15. ISE Effect for
Silicon (111)
in $[1\bar{1}0]$

Temperature (°C)	n
25	1.54
100	1.73
200	1.80
300	1.82
400	1.83

the filled valence band and the empty conduction band is only 1.09 eV which means that at 1000°K about one electron in 700 can cross the gap to the conduction band, bestowing intrinsic semiconductivity of about 10^{-2} ohm^{-1} cm^{-1}. The energy levels vacated in the valence band by the promoted electrons bestow intrinsic "hole"-type conductivity. Manipulation of the hole concentration and the insertion of discrete energy levels in the band gap by the alloying of Si has been the basis of the semiconductor device industry.

The fact that hardness does not appear to vary with dopant concentration or type—that is, n-type, with excess electrons, or p-type, with electron deficiencies—suggests that electron transfer across the gap during hardness determination is not seriously involved in the mechanism. However, the dislocation motion is affected by dopants as the etch-pit rosette technique shows, and this suggests that the hardness should be related to the dopant. This in turn implies that the room temperature mechanism responsible for plastic deformation leading to an indent impression is dominated by a nondislocation glide mechanism. Of the several possibilities, a structural phase change involving twinning seems possible allied with a microcracking process. For example, shear at every third layer along $\langle 111 \rangle$ in the cubic structure can produce a double hexagonal stacking sequence (AA')(BB') (AA') .... This would involve bond rearrangement to a metallic hexagonal form of silicon and could be brought about by a multiaxial compressive stress similar to that available beneath an indenter. The magnitude of the energy required to bring about the transition is approximately γ/c where γ is the intrinsic stacking fault energy of the cubic structure and c is the axial length of the wurtzite cell arising from the cubic diamond structure. With a wurtzite cell around 0.63 nm, about 10 GPa are required for the conversion. Such a stacking fault sequence can lead to twin formation with a preferred interface between cubic and hexagonal forms on (115) cubic planes.
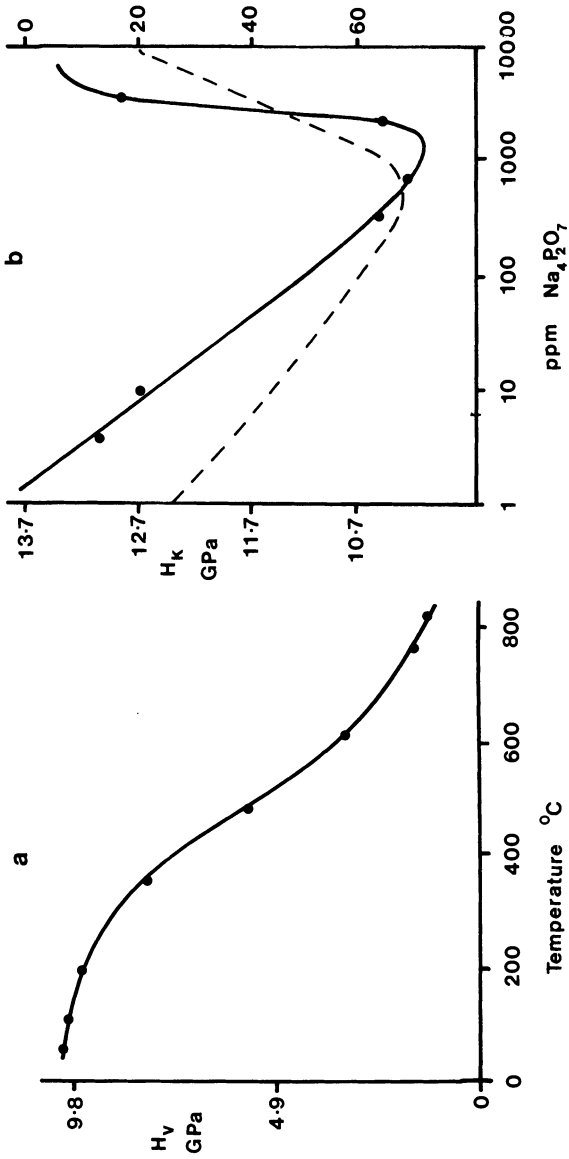
Figure 6.11. (a) Vickers hardness of Si{111} with diagonals along ⟨110⟩ and ⟨1̄1̄2⟩ as a function of temperature. (b) Knoop hardness, solid line, and zeta potential, dotted line, at surface of silicon under $Na_4P_2O_7$ solution.

This mechanism is in accord with the fact that silicon hardness is only a weak function of temperature up to about 380°C, after which it is strongly temperature dependent as Figure 6.11(a) shows. The temperature dependence is reflected in the ISE effect with the n values approaching 2 above 300°C as Table 6.15 and Table 4.3 show for silicon in comparison to some other ceramic systems. Above the transformation at 380° deformation occurs through a combination of dislocation glide and thermally activated dislocation creep, and such hardness values would then be expected to reflect doping effects as dislocation movement involves interaction between band gap and dislocation atmosphere as outlined in Section 4.4 and Figure 4.8. Hardness in the outermost layers of silicon is affected by the zeta potential, as Figure 6.11(b) shows, which indicates a minimum hardness for p-type silicon at a zeta potential of -60 mV as controlled by sodium pyrophosphate solutions.

Indentation twinning and possible structure change are the only indications that exist for any forms of silicon other than the cubic diamond modification which is in contrast to the polymorphism of carbon. Chemically deposited silicon films from the vapor phase are frequently encountered that are amorphous to X-radiation.

6.1.6.3. Boron

As a structural ceramic this element appears as fibers grown from the vapor phase onto thin substrate wires, usually of tungsten. As a result of this central core and the W–B interface they have not yet achieved anything approaching their intrinsic capabilities. To make fiber, the boron is deposited at 1100°C onto the 10-μm wire from the reaction of BCl_3 with H_2 which gives polycrystalline fiber of average crystallite diameter 2–3 nm. The boron is in the tetragonal or mixed tetragonal, α-rhombohedral polymorphic modification.

Both the abovementioned boron structures are unusual in that they are made up of 12-boron-atom icosahedral units linked at each apex to another such unit. One structural description regards the close packing of the B_{12} units; e.g., for the tetragonal polymorph the packing is of the cubic type. A more useful structural description is obtained by considering the molecular orbital arrangement on the B_{12} icosahedron: Each boron atom is considered to center two sp hybridized orbitals and two p orbitals. One of the sp hybrids is directed outward from the icosahedron and forms the basis for overlap and covalent bond formation with similar valence orbitals on other icosahedra, thus providing the strong, three-dimensional network of bonds. The second sp hybrid and the p_x, p_y orbitals on each boron are directed toward the inside of the icosahedron and, depending on symmetry, there is a polycentered molecular orbital consisting of 36 levels. Only 13 of

the inner levels are bonding, but since $12 \times 3 = 36$ electrons only need be allocated, and 12 of them are in the outward sp hybrids, the remaining 24 electrons can be accommodated in the bonding level leaving two "holes" to bestow semiconductor behavior and some inherent chemical reactivity. As with diamond, any section through the structure cuts large numbers of strong covalent bonds, so no easy cleavage exists. This time, however, the bonds are mainly sp–sp and not as strong therefore as the diamond sp^3–sp^3.

6.1.6.4. Hardness Data and Properties Derived from Them

As well as information for C, Si, and B, a few data are given in Table 6.16 for germanium for comparison purposes with the other group IV members even though it has no engineering applications. It does, however, have important electroceramic properties.

The relative ease with which hardness studies of silicon can be made and the ready availability of well characterized single crystals is reflected in the number of results and the figures that involve this material. Figure 6.8, for example, shows the indentation creep effect and Figure 6.11 shows the chemomechanical effect on the Knoop hardness. Figure 6.12 shows the effect that temperature and load have on the radial cracks; several studies have both derived and measured the critical load necessary to produce such cracks, with good agreement being achieved at the small load of 0.02 N which implies that such cracks, so easily produced, play a dominant role in applications. The dominant role played by dopants of both n and p type in the electronic properties of silicon has recently been shown to be negligible when hardness above 400°C is measured. Hardness is found to be independent of doping at any load,[11] but significantly, the dislocation rosette length does vary systematically with the dopant. Growth of the rosette is easier with n-type dopants present than with p-type.

In order to reveal the dislocation etch pits a vigorous etchant has to be used: 1 part 0.25 M $K_2Cr_2O_7$ solution to 4 parts 40% HF. Etching times from 10 to 90 seconds are needed. At a 0.98 N load the rosette length is 9 μm at 1.96 N for a dopant concentration of 10^{12} atoms cm^{-3} and, as the impurity level is raised to 12×10^{18}, the rosette arms are 15 and 66 μm at the above loads, respectively.

The load–hardness effect in the diamond structure is shown in Figure 6.13.

6.2. IONIC ENGINEERING CERAMICS

Here one encounters some of the traditional refractory ceramic materials that have been used for generations but are now receiving much

Table 6.16. Vickers and Knoop Hardness Values for Carbon, Silicon, Germanium, and Boron

Material	Microstructure	H_V (GPa)	H_K (GPa)	E (GPa)	K_{IC} (MPa m$^{1/2}$)	Notes
Carbon diamond	(100)	115.8[1]	—	—	—	[1]H_2O on surface
		129.5[2]				[2]Dry surface
Carbon diamond TYPE-II	{111}⟨1$\bar{1}$0⟩	—	103[3]			[3][100] on (001)
			91[4]			[4][110] on (001)
Carbon CVD	Polycrystalline {111} + {100}	0.687[5]–1.18	—	—	—	[5]Load = 0.98 N
Carbon graphite		35		14.35	0.5–1.8	
Silicon	Single crystal	9.0[6]	—	168	0.7	[6]β = 2.65; see equation (5.51): P^*crit = 0.04 N
Silicon	Single crystal (111)	8.15[1]				
		11.0[2]				
Silicon p-type			12.76–9.81[7]			[7]Depends upon the pH of solution on the surface
Silicon[12] n-type	Doped with 5×10^{14} Sb	9.81[8,9]				[8]Diagonals along ⟨110⟩, ⟨112⟩
		4.9[10]				
	(111)	1.2[11]				

Material	Form / orientation			
Germanium	Crystal	9.0[13]	140	0.5
Germanium	(111)	5.89[1], 7.46[2]		
GaAs	Single crystal 10^{18} n cm^{-3}			
	(111)Ga face	6.0		
	($\bar{1}\bar{1}\bar{1}$)As face	5.85		
	(111)	3.0[14]		
	($\bar{1}\bar{1}\bar{1}$)	2.4[14]		
GaAs	Single crystal 10^{18} p cm^{-3}			
	(111)Ga face	6.0		
	($\bar{1}\bar{1}\bar{1}$)As face	6.3		
	(111)	2.6[14]		
	($\bar{1}\bar{1}\bar{1}$)	2.2[14]		
Boron	Polycrystal hot pressed	35.09[15]		

[9] Room temperature
[10] 500°C
[11] 800°C
[12] Cracks form along 3 of the (112) on (111) at critical load of 0.02 N
[13] β = 2.5 critical load = 0.02 N
[14] 350°C
[15] Load = 2.94 N
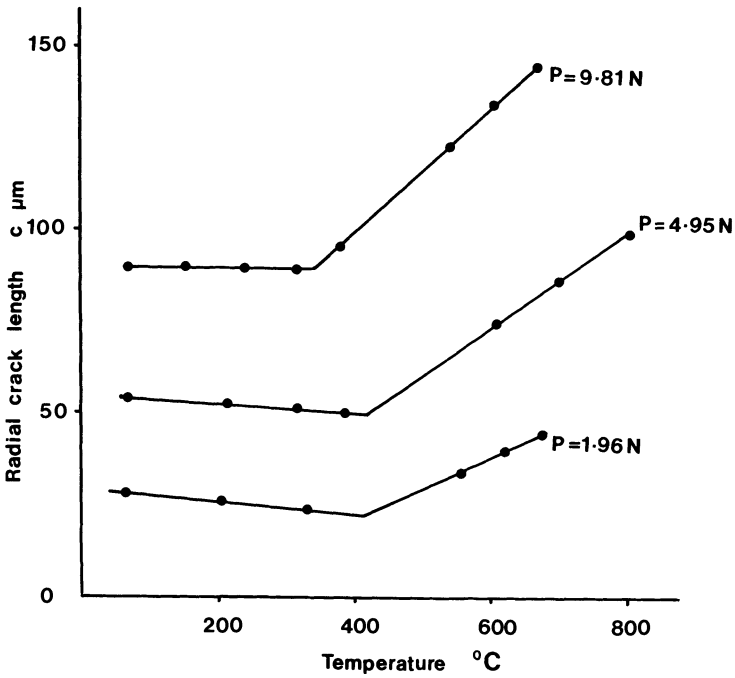
Figure 6.12. Radial crack length on {111} silicon as a function of temperature.
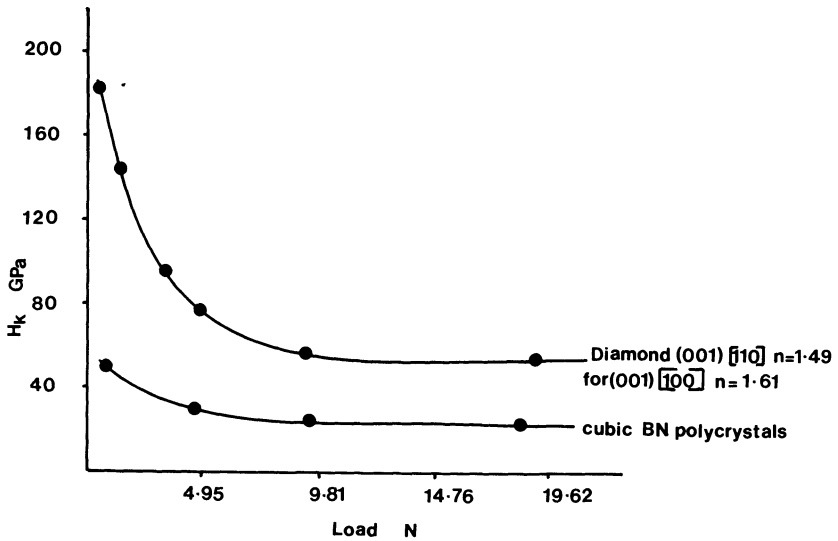
Figure 6.13. Load–hardness effect in the diamond structure.

reappraisal as fabrication routes to very high densities become available, new routes to achieving toughness are being sought, and production routes to fibers are pioneered.[12] This section contains data on Al_2O_3, MgO, ZrO_2, BeO, and alloys of these and other oxides.

6.2.1. Alumina

Worldwide there has been a large trade in alumina and high-alumina ceramics for many years which is currently valued at approximately $821 × 10^6; they completely dominate the engineering ceramics market. Some of the types, additives, and uses are listed below:

1. Purity > 99.7% Al_2O_3 available at high densities and dependent on the dopant can be translucent with zero porosity. Such material has grain sizes of 3–30 μm and is used as machine tool tips, crucibles, and high pressure sodium vapor lamp tubes. In these purest grades the small amount of impurity is MgO or Y_2O_3.
2. Grades around 99% Al_2O_3, usually doped with MgO, SiO_2, and CaO, have a variety of uses for mechanical components and high-temperature tubing.
3. 93–99% Al_2O_3 with the same general dopants because of their high acid resistance have many mechanical outlets including pumps, tool tips, and insulators.
4. 75–93% Al_2O_3 doped with MgO, SiO_2, ZrO_2, and TiC are strong and tough, finding uses in tool tips, mechanical mills, and erosion protection sheaths.

The general processing route is sintering, not often hot pressing, which is another advantage alumina systems possess.

As well as the commercial interest in the material, scientists have found the ready availability of good single crystals, corundum and sapphire, a great incentive for hardness studies and anisotropy studies.

The nomenclature of aluminas, α, β, and γ, suggests that polymorphism is common with this material. However, if one considers only the undoped, pure form of the material, it exists in only one crystalline form throughout the entire temperature range to the melting point at 2050°C. This form, α-Al_2O_3 is the pure form with a hexagonal structure, D_{3a}^6 space group, and two Al_2O_3 units per unit cell. In this structure, even at room temperature, slip occurs on $\{0001\}\langle11\bar{2}0\rangle$ systems. As for the other forms, β-Al_2O_3 has been shown to be a ternary oxide with general composition $Na_2O.11 Al_2O_3$ and will be discussed fully in Section 6.3.1. The nomenclature γ-Al_2O_3 is used to describe a number of phases produced by incomplete dehydration of gelatinous $Al(OH)_3$, which leads to Al_2O_3 containing impurity protons.

The structure of this material is a cubic form of defect spinel. Thus in this section we will consider only the common form of alumina, α-Al_2O_3.

It is common when considering ionic oxides to visualize the structure in terms of close-packed layers of the large O^{2-} ions generating the packing sequence for cubic or hexagonal symmetry and then to see the cations as occupying octahedral or tetrahedral interstices in the close-packed layers. This picture produces a too symmetrical view because when the small cations with large charges occupy the interstices, polarization is a consequence and a series of unequal M^{n+}-O^{2-} distances are generated. In α-Al_2O_3 such distortion causes 3 oxygen ions to be closer to each Al^{3+} and the structure then is formed from highly distorted AlO_6 octahedra. These distorted poly-hedra and the overall hexagonal symmetry lead to a large anisotropy of hardness for alumina. Grain sizes commonly in the range 0.1 to 300 μm contribute to variations in reported hardness values, fracture toughness, and strength, while impurity phases, often glassy, at grain boundaries add further to the variations in behavior and reported results.

Thermal etching between 1200 and 1500°C for 5 minutes is often sufficient to reveal grain boundaries after polishing. Careful polishing to 0.1 μm diamond is usually needed to get good Vickers and Knoop data. Because of the availability of such a wide range of samples and the impor-tance of alumina as a ceramic material many reports exist where the anisotropy, the effect of grain size, and the effect of grain-boundary material and surface treatments have been examined by the hardness techniques. Before tabulating hardness and other data it is worthwhile examining a few examples of these effects.

6.2.1.1. Grain Size Effect

Theoretical calculations for noncubic oxides point to a grain size-K_{IC} relationship. The essence of the relationship arises because below a critical grain size no microcracks arise from thermal expansion anisotropy on cooling, but above the critical grain size the presence of spontaneous microcracks is reflected in the measured K_{IC} value, and this could appear directly in a hardness–grain-size relationship. High-purity hot-pressed Al_2O_3 is available with grain sizes in the range 6-60 μm and such material can be tested by the Vickers method and the toughness parameter measured using loads from 5-200 N and the Evans and Charles equation, equation (5.41). The data shown in Figure 6.14 indicate a slight hardening effect with grain size increase, probably reflecting the relative weak bonding in grain-boundary regions, and a sharp decrease in fracture toughness above 15 μm grain size until 25 μm grains are reached. Indent sizes are around 20 μm, but because microcracks arising from the thermal anisotropy are located in grain boundaries, development of indentation radial cracks is hindered.
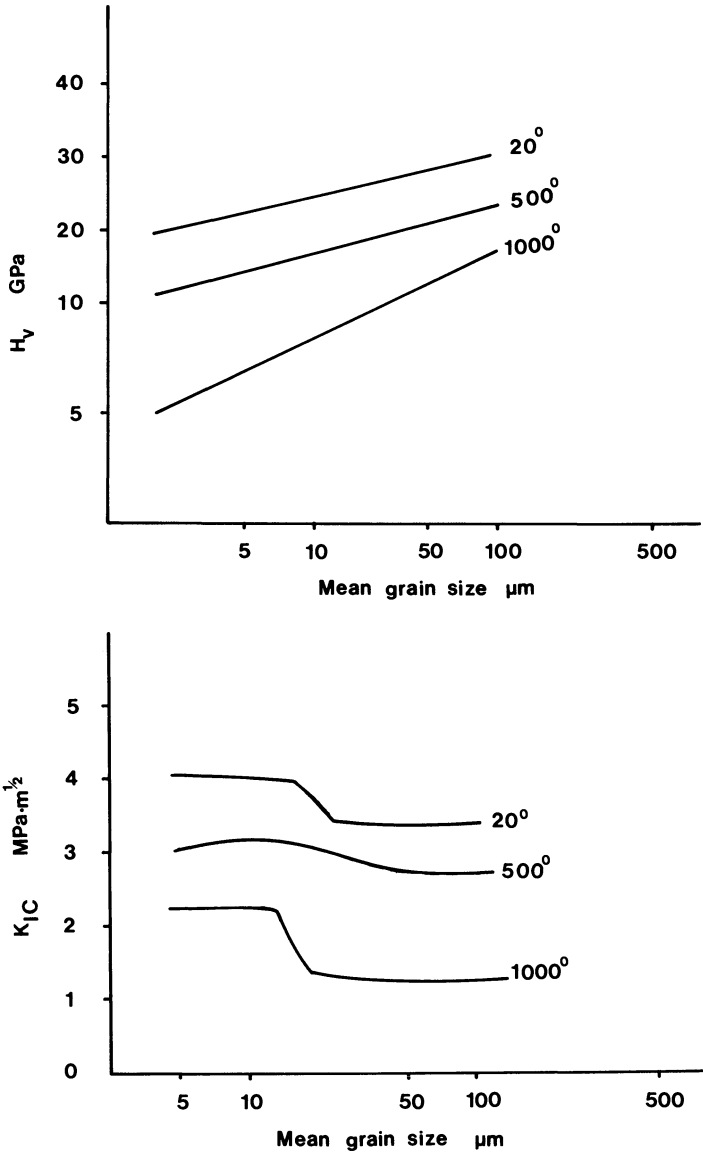
Figure 6.14. Grain size effect on Vickers hardness and toughness of Al_2O_3.

However, above 25 μm grain size the indent is essentially in the crystal and radial crack development is unhindered and therefore the sample is less tough as determined by the indentation technique. When cubic Y_2O_3 is tested this way there is no grain-size effect on K_{IC} because Y_2O_3, being cubic, has no spontaneously produced grain-boundary microcracks.

6.2.1.2. Grain Boundary Effect

An indentation method has been developed to measure one of the three quoted measurements of grain-boundary strength: K_{IC}^{gb}, the critical stress intensity required to propagate a crack along a grain boundary; γ^{gb}, specific fracture energy; and σ_f^{gb}, local microscopic fracture stress. The obvious parameter is K_{IC}^{gb}, which is related to single-crystal fracture toughness K_{IC} and the percentage intergranular fracture (PIF) by

$$K_{IC}^{gb} = K_{IC}^2 \cos^2\left(\frac{\pi}{2}\frac{PIF}{100}\right) \tag{6.13}$$

The other measures of grain-boundary strength then follow:

$$\gamma^{gb} = \frac{(K_{IC}^{gb})^2}{2E} \tag{6.14}$$

$$\sigma_f^{gb} = \frac{0.886 K_{IC}^{gb}}{(a_m^o)^{1/2}} \tag{6.15}$$

where a_m^o is the average original size of the grain-boundary microflaws that initiate grain-boundary fracture.

To find PIF, scanning electron micrographs are used to study the appearance of radial cracks from an indent made at 91.8 N load. Such cracks show no preferential cleavage fracture of larger grains, no significant change in PIF along a macrocrack, and average grain boundary inclination to the macrocrack in the range 38°–47°. Typically, Al_2O_3 of 99.5% theoretical density and 11.9 μm average grain diameter has a PIF of 65% and therefore a grain boundary K_{IC} of 0.68 MPa m$^{1/2}$ which is much lower than values for K_{IC} given in Tables 6.17 and 6.18 and shows the importance of the grain boundaries. Of course, when the alumina is of lower purity the grain boundary region becomes a sink for the impurity with obvious effects then on σ_f^{gb} and K_{IC}^{gb} and overall K_{IC} values. It is by changing the content and crystallinity of the grain-boundary phase that reported heat treatments have their observed effects on toughness and strength of alumina specimens. For example, when an Al_2O_3 sample with a 10% (by volume) boundary phase consisting of Al_2O_3, MgO, and SiO_2 close to the eutectic at 7.5:20.5:62% (by weight) is sintered at 1600°C, the toughness determined by use of equation (5.46) increases from the as received value of 3.0 up to 5.1 MPa m$^{1/2}$. Microscopy reveals that the improvement stems from turning the grain-boundary phase from a glass to a crystalline silicate.

Table 6.17. Hardness and Hardness-Derived Data for Single Crystal Al_2O_3

Type	Orientation	H_K (GPa)	H_V (GPa)	E (GPa)	K_{IC} (MPa m$^{1/2}$)	ISE n value	Notes
Sapphire	Diagonal $\langle 0\bar{2}21 \rangle$	39.26	—	—	1.6[a]	—	Load = 0.245 N
Sapphire	$\{0001\}$	28.46	21.8		2.5		Load = 0.92 N
		20.61					Load = 2.94 N
	and						
	$\{11\bar{2}0\}$	31.9					Load = 0.92 N
		23.55					Load = 2.94 N
Sapphire	(0001)	—	—	—	1.08[a]		Load = 1.69 N
					1.69[a]		Load = 9.8 N
α-Al_2O_3	(0001)	—			3.0[a]		Load = 0.49 N
α-Al_2O_3	—	—	23.0	400	2.2[a]		
α-Al_2O_3	$(0001)/[10\bar{1}0]$	15.0				1.80	
	$(11\bar{2}0)/[0001]$	3.5				1.88	
	$(1\bar{1}00)/[0001]$	11.0				1.87	Room temperature 1020°C
	$(1\bar{1}00)/[11\bar{2}0]$	3.5				1.72	Room temperature 1020°C
α-Al_2O_3	—	—	12.0	—	4.0[a]		Critical load $P^* = 0.25$ N, $C^* = 4$ μm

[a] Equation (5.46) used.

Table 6.18. Hardness and Hardness-Derived Data for Polycrystalline Al$_2$O$_3$, Both Pure and Polyphase

Composition (% by volume)	Density (% theor.)	Preparation or type	Grain size (μm)	H_V (GPa)	E (GPa)	K_{IC} (MPa m$^{1/2}$)	ISE n value	Notes
99.9	99.7	Hot pressed and HIP	6	19.0	406	3.5		Load = 2.0 N;
			60	23.0		3.0		$^{(1)}T = 1000°C$
				5.0$^{(1)}$				
99.7	—	Sintered	—	24.04				Wet surface
				26.5				Dry surface
99.7	—	ALCOA-16SG	—	10.45				Load = 294 N; radial crack 392 μm; depth of crack = 390 μm; good halfpenny shape
99.5	98.5	—	—	20.1	406	4.1^a		
99.9	—	Hot pressed	—	20.1	406	—		
		Sintered	—	12	393	4.1^a	—	Critical load P* = 0.4 N, C* = 3 μm
99.7 + 0.3 MgO	99.5	Sintered	11.9			0.68^b		
	98.0	Sintered	3.5			0.40^b		
99.5 + 0.5 silicate glass	—	—	—	13.74	—	—	—	Load = 1 N
				12.75				Load = 2.5 N
				12.27				Load = 10 N
90 + 10(Al$_2$O$_3$ + MgO + SiO$_2$ eutectic)	95.3	Sintered at 1600°C	5.0	11.0		3.0^a		After long anneal at 1200°C to crystallize grain boundary phase, loads 4.5-180 N
						4.0^a		
						5.1^a		
88 + 12 silica glass phase				9.81				Load = 1 N; Rockwell 45 N = 84
				9.32				Load = 2.5 N; Rockwell 15 N = 92
				8.34				Load = 10 N
87 + 13 glassy phase		—	—	25.1			1.76	At load chosen to make 10 μm indent; for last, $^{(2)}T = 800°C$
				3.67$^{(2)}$			1.88	

	Density	Processing	Grain size	Hardness	E (GPa)	K		Comments
74 + 26 glassy phase	—	—	—	22.3 / 2.91[2]	—	—	1.41 / 2.02	Very sensitive to depth of indent
97 + 3ZrO$_2$	—	Sandvick CC620	—	15.89	370	3.8–15.4	—	
58 + 42ZrO$_2$	—	Hot pressed	—	15	264	—	—	
58 + 42ZrO$_2$ monoclinic ZrO$_2$	—	Directionally solidified	—	9.8	—	9.0[c]	—	Perpendicular to grain growth direction
						6.8[c]		Parallel to grain growth
58 + 42ZrO$_2$ tet + cubic ZrO$_2$	—	Directionally solidified	—	16.19		5.2[c]		Perpendicular to grain growth direction
						4.8[c]		Parallel to grain growth
95 + 5Cr$_2$O$_3$	3940 kg m^{-3}	Hot pressed	—	22.57				Load = 1.96 N
90 + 10Cr$_2$O$_3$	4050 kg m^{-3}	Sintered in air at 1700°C	—	23.06				
70 + 30Cr$_2$O$_3$	4470 kg m^{-3}		—	23.95				
50 + 50Cr$_2$O$_3$	4240 kg m^{-3}		—	23.26				
Al$_2$O$_3$/TiC	—	Hot pressed	—	20.9 / 7.63[3]	373	4.3	—	[3]Value at 1000°C
Al$_2$O$_3$ [4]	—	Hot pressed	—	18	380	4.2	—	[4]Scratch hardness from equation (1.47) (see Fig. 1.9) = 12.8 GPa at 50 N
Al$_2$O$_3$/ZrO$_2$	—	Hot pressed	—	17.08	—	—	—	
Al$_2$O$_3$/ZrO$_2$/ SiC whiskers	—	Hot pressed	Al$_2$O$_3$ (1.6 μm) ZrO$_2$ (0.65 μm)	18.65	—	—	—	Load = 30 N
Al$_2$O$_3$/ZrO$_2$ 92:8	99 — 4090 kg m^{-3}	Sintered at 1570°C for 10 hours		14.0	—	5.9[d]	—	
Al$_2$O$_3$/ZrO$_2$/TiO$_2$ 91.5:8:0.5	99 — 4110 kg m^{-3}	Sintered at 1570°C for 10 hours		12.9	—	4.8[d]	—	

[a] Equation (5.40) used.
[b] This is the grain boundary toughness from equation (5.97).
[c] Equation (5.53) used because cracks are Palmqvist.
[d] Mirazono equation (5.55) used.

6.2.1.3. Anisotropy Effect

It has already been stated in Section 3.5 that, although it is known to exist, the anisotropy effect has not been fully investigated. Figure 3.12 shows the anisotropy of hardness on (0001) and ($1\bar{1}00$) in alumina and Table 4.3 in Section 4.1.2 has the different ISE effects on the different planes and directions. Clearly the effect of hardness anisotropy is more marked on the prism planes than on the basal planes, as is not unexpected in view of the distorted nature of the AlO_6 octahedra in the structure. Knoop hardness shows that the anisotropy effect decreases rapidly with test temperature increase as shown in Figure 6.15.

6.2.1.4. Surface Treatment Effect

Studies involving sapphire single crystals and sintered polycrystals show that large variations in reported hardness arise from variations in surface treatment because they produce different degrees of work hardening, as shown in Figure 6.16(a), (b). Reaction with aqueous environments to produce forms of γ-Al_2O_3 also occur, and the effect pH has on varying the surface hardness is shown in Figure 4.10. Ion implantation experiments show that initially the hardness can be increased substantially by solid
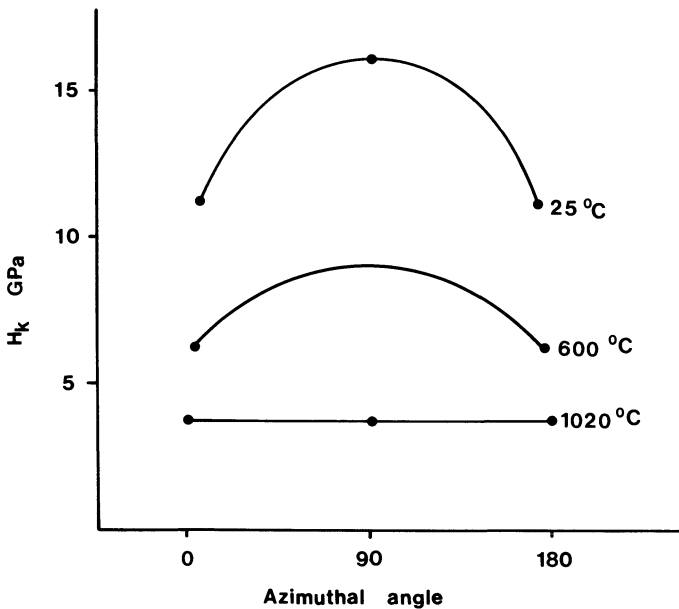
Figure 6.15. Knoop hardness as a function of long axis orientation: $0° = [11\bar{2}0]$, $90° = [0001]$, $180° = [11\bar{2}0]$ on Al_2O_3 ($1\bar{1}00$). From Brookes.[13]
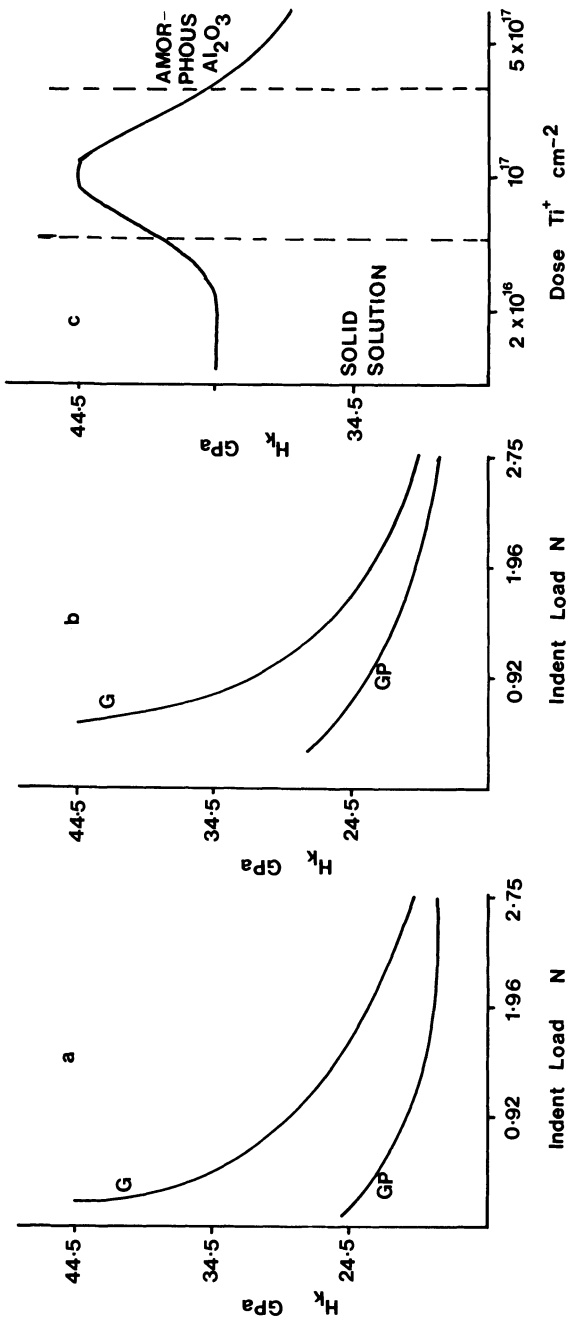
Figure 6.16. Effect of surface finish on sapphire hardness (a) (0001) (b) (11$\bar{2}$0), with GP = gas polish, G = dry grinding. (c) Effect of Ti$^+$ dose on Al$_2$O$_3$ surface and its hardness. After Becher.[14]

solution formation and the production of a compressive surface layer before being reduced as higher ion doses produce the amorphous layer analogous to some of the γ-Al_2O_3 phases. Figure 6.16c shows an example of the variation in effect that surface treatment can have, especially when induced by the vigorous quenching technique of ion implantation.

6.2.1.5. Hardness Data and Properties Derived from Them

Collected measurements for single-crystal Al_2O_3 and polycrystalline Al_2O_3 can be found in Tables 6.17 and 6.18.

6.2.2. Magnesia

Magnesia has the advantages of being abundant, refractory, and resistant to basic melts, but because of its structure it has relatively low strength and is reactive with acidic components. Thus the outer surface of a crystal or a significant portion of fine powder is the carbonate or hydroxide, not the oxide. This is reversion to the raw material, for most magnesia is derived from either magnesite, $MgCO_3$, or dolomite, $MgCa(CO_3)_2$, by calcination. Powders made this way require hot pressing to achieve theoretical density. Large crystals of MgO can be obtained from the melt at 2450°C. These crystals cleave easily along {100} planes bestowing as a result the common name for single-crystal MgO: namely, periclase.

The radius ratio of Mg^{2+}/O^{2-} falls comfortably in the octahedral polyhedron range and so one simple rock-salt structure is all that occurs in which Mg^{2+} ions occupy the octahedral interstices of a close-packed O^{-2} structure. Polarization from Mg^{2+} is not a problem, and as a result one is dealing here with one of the most ionic of all ceramic systems.

The structure is undeformed *fcc* with four formula units per unit cell. Within the rock-salt structure slip is easy on {110} even though dislocation models suggest that slip on {100} in ⟨110⟩ might be more favorable because {100} planes are the most densely packed and have the widest spacings. However, for such a slip system the ionic nature intervenes because at half the translation the Mg^{2+} ions are juxtaposed; this would require extra high energies to overcome. Thus only at high temperatures is the "obvious" slip system {100}⟨110⟩ available. Known slip systems are the primary, {110}⟨110⟩; the secondary (800–1600°C), {100}⟨110⟩; and, above 1600°C, {111}⟨110⟩. In all cases the directions are ⟨110⟩, which connect ions of same sign without involving a juxtaposition of like ions during the movement; ⟨100⟩ glide would result in such juxtaposition en route.

Above 1600°C all systems can operate, conferring ductility on MgO, and under the high stresses of point indentation such plasticity at room temperature makes this ceramic relatively soft. Fracture is also not difficult and appears to be well understood. Common types of fracture involve

cleavage on {100}; fracture on {100} is caused by dislocation interactions on intersecting orthogonal {110} slip planes, as, for example, $\frac{1}{2}a[0\bar{1}1] + \frac{1}{2}a[0\bar{1}\bar{1}] = a[0\bar{1}0]$; fracture on {110} is initiated by dislocation interactions on obliquely intersecting {110} slip planes, such as $\frac{1}{2}a[0\bar{1}1] + \frac{1}{2}a[10\bar{1}] = \frac{1}{2}a[1\bar{1}0]$; and fracture on a (110) plane parallel to a deformed surface. Such well-documented information on this structure and ready availability of single-crystal material have made this a source of hardness research often involving the dislocation etch-pit rosette technique as outlined in Section 3.1 and shown in Figure 3.3.

Flat, smooth surfaces of polycrystalline MgO are not easy to prepare because of the easy pull-out arising from the slip and fracture systems outlined. Careful polishing with $\frac{1}{4}\mu$ diamond paste is needed. Etchants as mild as saturated NH_4Cl solution at room temperature or 0.5 M $AlCl_3$ at 50°C will reveal surface structure; 15 s are needed to see grain boundaries and 1 minute to see etch pits. More vigorous reagents for etch-pit revelation are nitric acid at 90°C for 15 s on {100} or phosphoric acid, H_3PO_4, at 60°C for 1 minute on {110}.

Microstructure and purity can have considerable influence on the measured hardness of magnesia artifacts while a degree of hardness anisotropy also leads to variations. The plethora of slip systems can also lead to work hardening in such a structure. The following abstracted studies highlight these effects.

6.2.2.1. The Influence of Microstructure

This is most clearly seen when a specific microstructure is prepared and varied in a controlled way such as directionally solidifying to produce a lamellar eutectic of $MgO-MgAl_2O_4$ in which the interlamellar spacing of MgO and spinel can be varied. Results shown in Figure 6.17 demonstrate a straight-line relationship between hardness and interfiber spacing when the MgO lamellae are indented with a Knoop diamond and a load of 2.94 N. The almost linear relationship between $d^{-1/2}$ and hardness shows a Petch-type relationship between increasing hardness with decreasing "grain" size. Since the values for microhardness for "pure" MgO are around 8.5 GPa, the considerable hardening effect brought about by this specific microstructure and by producing finer microstructures is also clear from Figure 6.17. Indents were made only in the MgO areas and not over the $MgO-MgAl_2O_4$ interface boundaries, so these data show the important role such boundaries must play in determining overall hardness and strength of samples with this fibrous microstructure.

6.2.2.2. The Effect of Work Hardening

As already stated, several slip systems have been proven for the MgO structure, and so dislocation movement is relatively easy and varied. Such
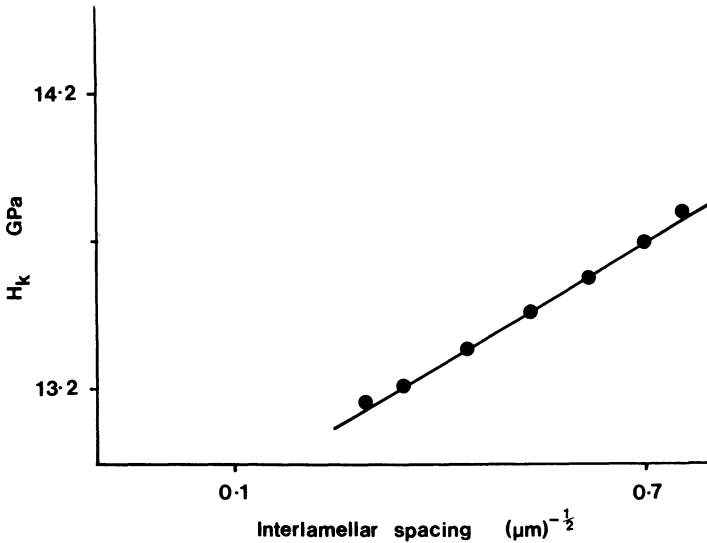
Figure 6.17. Knoop microhardness of MgO lamellar in directionally solidified MgO–MgAl$_2$O$_4$ eutectic versus square root of reciprocal lamellar spacing. After Kennard et al.[15]

a situation would lead one to expect a work hardening contribution to observed hardness values for magnesia unless it is specified that care has been taken to anneal the samples. Brookes has shown that even contact with soft pointed sliders on well lubricated MgO surfaces can lead to work hardening as long as the material of the slider can itself work harden to produce an ultimate hardness sufficient to cause slip on critical resolved shear planes in magnesia. The maximum hardness achieved by the work hardening is a function of the slider ultimate hardness

$$H_K = H_o + \alpha H_u \qquad\qquad (6.16)$$

In equation (6.16) H_K is the Knoop hardness at a load of 0.98 N of the area directly beneath the slider; H_o is the annealed hardness of the MgO crystal before contact; H_u is the ultimate Knoop hardness of the slider material after it has been made to flow; and α is a constant = 0.5 for magnesia. Figure 6.18 demonstrates this work hardening effect.

The work hardening demonstrated by the slider experiments clearly shows the effect of dislocation mobility on this rock-salt-structure material, and it is not unexpected to find much evidence for a load hardness effect with a range of n values at room temperature depending on plane and direction; this is shown in Table 4.3. Dislocation mobility under the influence of the stress fields found in indentation hardening also manifests itself as an indentation creep effect as shown in Figure 4.11.
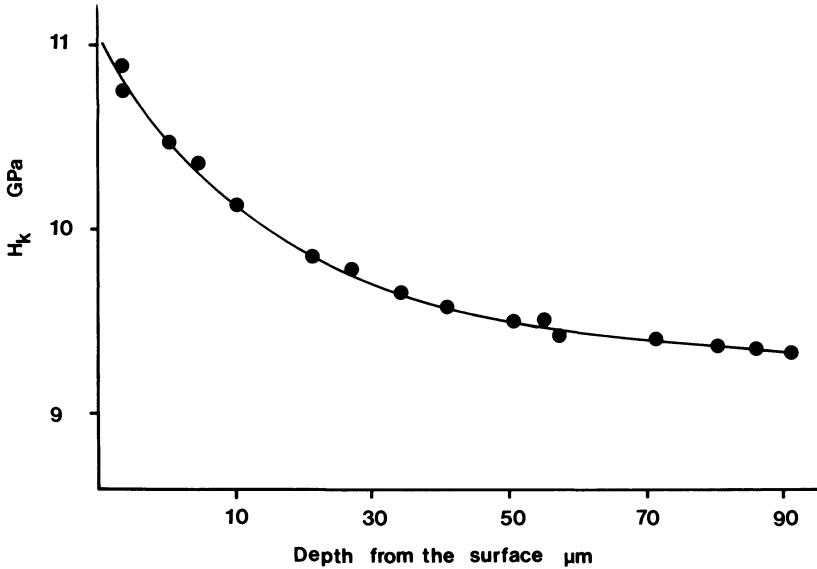
Figure 6.18. Knoop hardness of MgO in area over which a copper slider has passed, as a function of depth below surface. After Brookes.[16]

6.2.2.3. Hardness Anisotropy

Rickerby and Brookes, in independent studies, have reported anisotropy with the softest direction being the one in which the Vickers indent diagonals lie along [110] on (001) planes, as shown in Figure 6.19 and discussed in Section 3.3. More recent investigation[17] claims that such anisotropy is an artifact arising from the fact that the indent shape on the surface is not square after removal of the diamond which leads to a 15–20% variation in H_V. Furthermore there is extensive cracking along $\langle 110 \rangle$ at loads above 0.49 N.

The Giberteau results in Figure 6.19 are plotted when the indentation area is calculated from the observed nonsquare shape of the indent. Interestingly, when they are recalculated using just the observed indent diagonal, $2a$, to calculate H_V, a distinct anisotropy is observed in agreement with the earlier work. In an attempt to resolve this problem the dislocation etch-pit rosette lengths were considered following earlier analysis, which gives a dislocation velocity $V \propto \tau^m$ where τ is the resolved shear stress. Then l, the dislocation rosette length, is proportional to load and time

$$l \propto P^{m/(2m+1)} t^{1/(2m+1)}$$

or

$$l = K P^{m/(2m+1)} t^{1/(2m+1)} \tag{6.17}$$
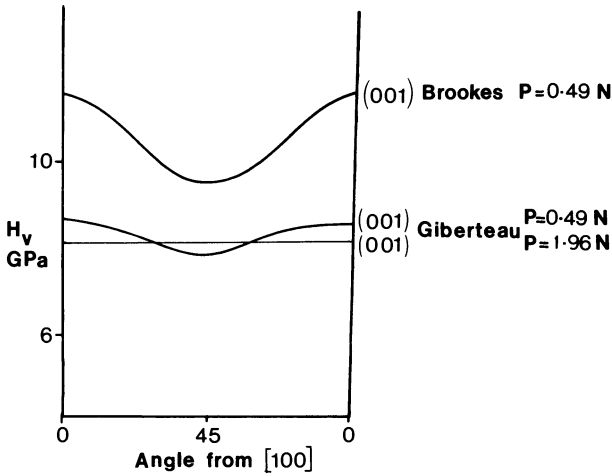
Figure 6.19. Vickers hardness of (001) MgO as a function of indenter diagonal orientation. After Giberteau.[17]

Since large values of m characterize ionic solids, the rosette length will be proportional to $P^{1/2}$ and independent of time. Furthermore l/a is a constant, so if H_V is anisotropic then l will be anisotropic in the opposite sense. Experimental observations show this not to be the case even though the relationship l against $P^{1/2}$ is clearly demonstrated, but great care now has to be exercised in interpreting rosette lengths since they may show no simple correlation with hardness data, as the work with GaAs and silicon discussed in Section 3.6.2 shows.

6.2.2.4. Hardness Data and Properties Derived from Them

Data not already discussed from various sources for MgO are given in Table 6.19.

6.2.3. Zirconia

Until a decade ago, zirconia would not have been considered a candidate to be developed as an engineering ceramic because its polymorphism can lead to such large strains that it is self-fracturing. It has always been used in the refractories and glass industry in amounts approaching three-quarters of a million tonnes per year. A detailed study of the crystallography of zirconia, and in particular the mechanism of the phase changes, has

Table 6.19. Hardness Data from Various Sources for MgO

Form	Orientation or microstructure	H_V (GPa)	H_K (GPa)	E (GPa)	K_{IC} (MPa m$^{1/2}$)	Notes
Single crystal	(100)	—	10.8			$P = 0.98$ N
	(100)		10.2			
	(001)/[100]		4.41			
	(001)[100]	9.05	3.93			
	(001)[110]		7.35			
	(001)[110]	7.51	7.65			
	(100)	7.6				$P = 0.49$-1.96 N
	(110)	7.8				
	(111)	9.85				
	(100)	5.8-7.19				Hardness is dependent on indenter orientation
	(110)	7.19-8.35				
	(111)	7.93-8.58				
Single crystal	—	9.3	—	240	1.2	β in equation (1.16) = 3.0
	—	9.2		—		
Polycrystalline eutectic	Solid solution containing Al^{3+}, grain size 4 μm	—	12.6			

placed this material in the forefront of ceramic potential. A result of recent research is a new generation of zirconia-based materials prepared by sintering ultrafine powders prepared by special chemical processes. Because high densities can be achieved at moderate temperatures, the solid artifact contains large amounts of the metastable tetragonal modification which results in very high toughness and modulus of rupture and even more significantly bestows an excellent resistance to crack initiation. The fine powders needed to ensure metastability lend themselves well to forming by cold isostatic pressing or to conventional slip casting. As a lightweight material with a low coefficient of friction, it is being used in wire drawing dies, in diesel engines as cylinder liners, as complete turbocharger components, and as a toughening agent in other ceramic systems.

6.2.3.1. Bonding and Structure

The radius ratio of $Zr^{4+}:O^{2-}$ is 0.57; this is close to a boundary value, indicating some polymorphism between structures with metal–oxygen octahedra and metal–oxygen cubes as structural units together with O^{2-}–Zr_4^{4+} tetrahedra. This is the case with a low-temperature structure containing distorted octahedra as the Zr^{4+} induces polarization and partial covalency. The structural consequence of the polarization is a monoclinic phase stable to about 1170°C, but the actual transformation is dependent on several parameters as indicated in Section 6.2.3.2. When the transformation is accomplished, the Zr^{4+}–O^{2-} polyhedra show eightfold coordination of the Zr^{4+} but do not reach the ideal cubic structure because there are two Zr^{4+}–O^{2-} distances of 0.207 nm and 0.247 nm in the polyhedron. The overall symmetry is higher when tetragonal but the unit cell volume shows a sharp decrease variously given as 4–9% depending on the form and purity of the sample. It is this sharp decrease that subjects ZrO_2 artifacts to large strains and very large tensile stresses sufficient to break up a single crystal. It has been a physical barrier to its use in the past. More thermal energy eventually overcomes the polarization distortion, and at about 2300° the deformed polyhedra become truly cubic and zirconia then has the fluorite structure.

It has been necessary in the past to counteract the effect of the monoclinic to tetragonal change, and this has been achieved mainly by alloying with a cubic oxide in which the metal cation is larger than Zr^{4+}. These solid solution materials were of either cubic or tetragonal symmetry and became known as *stabilized zirconia*. More recent investigation has shown that sufficient alloying oxide to not completely produce the tetragonal form is desirable because there are gains in toughness and strength (see Section 6.2.3.2); these materials are partially stabilized zirconias, PSZ for short. Common additives that lead to these forms are MgO, CaO, Y_2O_3, La_2O_3,

and CeO_2. With the exception of CeO_2, stabilization cannot be achieved with these oxides without introducing some other form of lattice defect: a combination of oxide ion vacancy and cation vacancy with or without variable valency charge compensation.

The occurrence of the three polymorphs is also a function of particle size; as the crystallites are reduced in size, a critical size is reached when the tetragonal form is more stable than the monoclinic form, and at even finer grain sizes the cubic is the stable form. An explanation for this is given in terms of the surface energy of the three polymorphs by suggesting a decrease $\gamma_{mono} > \gamma_{tet} > \gamma_{cubic}$; so as the total surface area increases, the monoclinic form becomes metastable relative to the tetragonal. Following that argument through to hardness via Johnson's development of Hill's expanding cavity equation, equation (1.14), and putting σ_y in that equation equal to the Griffith–Orowan value $(E\gamma/\pi c)^{1/2}$, then the hardness would be predicted to follow the order monoclinic > tetragonal > cubic. This, however, is the reverse of the experimental data. However, an examination of the theoretical hardness equation, equation (1.46), provides some explanation because the tetragonal form has a molar volume V_m which is 4–9% smaller than that of the monoclinic form and the hardness of the tetragonal form should then be greater than that of the monoclinic. Indentation of the tetragonal form would cause pressure-induced transformation of the monoclinic form in the plastic zone and then it would appear to be softer than expected. Hence the order would be cubic > tetragonal > monoclinic. A microscopic examination of hardness-tested monoclinic ZrO_2 shows (100) and (110) twinning on a scale as fine as 10 nm in two orthogonal directions; it is this that provides for multiaxial, nearly continuous plastic deformation and the unexpected softness of the monoclinic form. The softness of the tetragonal form relative to the cubic form is revealed by the microscope to be due to the postulated stress-induced transformation to the monoclinic form. Because ZrO_2 powders contain a range of particle sizes it is common to find samples containing variable percentages of all three forms.

A less well documented transition which occurs in the ZrO_2 system may be an important consideration in hardness studies because it is brought about by the application of modest hydrostatic pressure in excess of 3.2 GPa.[18] Experiments have shown that monoclinic ZrO_2 transforms at room temperature to a metastable high-pressure form which has orthorhombic symmetry; the transformation is very rapid, having the characteristics of a martensitic transformation and hence an important shear contribution. Above 16.6 GPa yet another transformation occurs to a second type of orthorhombic structure. However, it is the relatively low pressure transformation with glissile elements that is of some interest for hardness considerations. Indeed, it may be this transformation that contributes to the anomalous softness of monoclinic ZrO_2 just discussed above in terms of

surface energy and twinning. Transformation at these pressures and the fact
that low temperature annealing around 350°C can have marked effects on
the retention of the high pressure phase at ambient pressures lead to the
view that it is a surface nucleation phenomenon. Hydrostatic environment
and particle size are factors that influence the retention of the high pressure
tetragonal form down to room temperature. However, it is the reverse
transformation to the smaller volume orthorhombic form under the influence
of the large shear beneath an indenter that is relevant here.

6.2.3.2. Transformations in Zirconia

Already it has been stressed that the important phase change is mono-
clinic to tetragonal and the reverse, metastable tetragonal zirconia to mono-
clinic. The ways to achieve this are summarized in Figure 6.20.

All the routes in Figure 6.20 have been successful and widely studied.
The general agreement is that the monoclinic to tetragonal transformation
and its reverse is a first-order heterogeneous change involving the movement
of a glissile boundary between phases. It is therefore extremely rapid,
occurring by a martensitic type of shear transformation involving large shear
strains. When the monoclinic phase transforms to the tetragonal, twins
are produced in the tetragonal phase: An interface moves parallel to
$(100)_{mono}$ leaving twins on the $(\bar{1}12)_{tet}$ or $(1\bar{1}2)_{tet}$. Thus when a twinned
tetragonal phase transforms back twins are produced on the $(110)_{mono}$
and $(001)_{mono}$ planes with topotactical relationships $(100)_{mono} \| (110)_{tet}$
and $[001]_{mono} \| [001]_{tet}$. The twinning mechanisms are responsible for

Monoclinic ⇌ Tetragonal ⇌ Cubic

1   TEMPERATURE ——————INCREASE——————→

2   GRAIN SIZE ———DECREASE———→

3   STRESS ←————————————from metastable grains

4   ELASTIC CONSTRAINT ————————————→
    IN MATRIX OF OTHER
    CERAMIC

5   ALLOY OXIDE ———INCREASE %———→
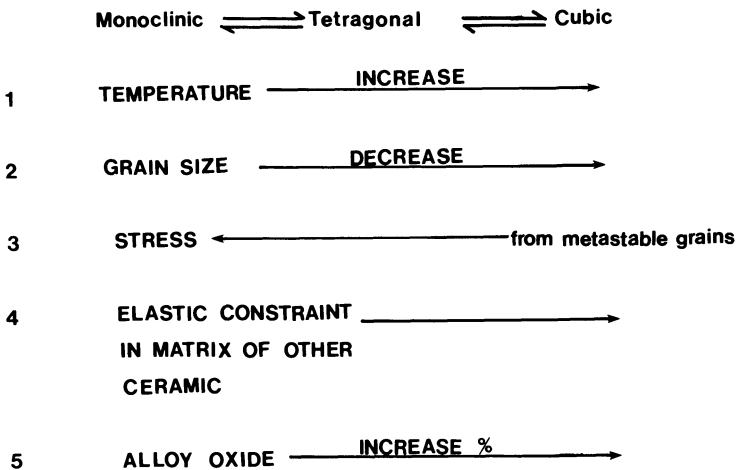
Figure 6.20. Physical ways to effect the zirconia transitions.

the softness of the monoclinic form, and the occurrence of the transformation, because it is dependent on the sample grain size, leads to variations in observed hardness.

While for many years the occurrence of the martensitic change was thought to be very bad with respect to the usage of zirconia, it now gives ceramic engineers three mechanisms for improving zirconia itself as well as many other ceramics containing zirconia: microcrack, transformation, and agglomerate toughenings. These are outlined below.

Stable microcracking in brittle materials generally results from large localized stresses, and in the past this has been caused by thermal contraction anisotropy; now, however, the unusual volume effect in transforming from tetragonal to monoclinic zirconia can be utilized. The zirconia should have a particle size large enough to transform to the monoclinic form in the matrix in which it is placed, and the elastic strain so produced should be greater than the matrix can stand allowing radial cracks to form at the monoclinic ZeO_2-matrix interface. A growing macrocrack will then encounter a *process zone* of microcracked material, and toughening will occur as the macrocrack encounters the microcracks and is caused to bifurcate and then extra loading is needed to generate further growth as extra surface energy γ is required. The toughening will be proportional to the process zone's size and the density of microcracks. The density of microcracks will depend on the volume fraction of monoclinic zirconia, and clearly there must be some lower volume limit because too few particles will not generate sufficient transformation strain to crack the matrix interface. However, too many particles will produce an interlocking network of microcracks that will effectively increase the macrocrack length greatly when the tip reaches such a tangle of microcracks; in this case the ceramic strength will be seriously degraded. Even if the microcracks do not form by a spontaneous mechanism, either because the particle sizes are not correct or because the volume of zirconia is too small, a process zone can be generated by application of an external strain interacting with the transformational strain. Modeling the steps in the energy processes has enabled some interesting features of this type of microcrack toughening to be deduced. Steps in the process are as follows:

1. Calculate dilatational strain energy for a tet → mono transformation. This is $e^{trans}\sigma_p V_p$ where e^{trans} = dilatational strain, σ_p = stress within the particle, and V_p = volume of the particle.
2. Consider the applied tensile stress which produces a dilatational strain that lessens the effect of Step 1 but produces interacting stress fields.
3. There is a third stress field that arises from the mismatch in E values for the ZrO_2 particles and matrix. This contributes to the strain energy.

4. The transformed particle increases in size and therefore has a larger surface energy which is included in an energy balance allowing an estimate of applied stress necessary to produce a process zone to be made.

5. ZrO_2 particle size is important in the above steps, and there is a minimum size, r_{min} necessary to induce a microcracked zone when stress is applied:

$$r_{min} = \frac{17\gamma_i}{E_m(e^{trans})^2} \tag{6.18}$$

where γ_i = interfacial energy, E_m is the matrix is Young's modulus, and e^{trans} is the dilatational strain. Thus particle size can have a noticeable effect on hardness of zirconia and zirconia-containing ceramic only when r_{min} is exceeded.

In order to need no applied stress to generate a process zone (spontaneous microcracking), the critical particle size r_c is

$$r_c = \frac{40\gamma_i}{E_m(e^{trans})^2} \tag{6.19}$$

Particle sizes in excess of this produce greater toughness in the matrix, but not much greater, because a narrow distribution around r_c is needed with a wide distribution, reducing the toughening effect because resistance to crack extension is shown to be directly proportional to V_f^2—that is, the volume fraction of ZrO_2 above r_{min}—and to be inversely proportional to $r_c/\bar{r} - 1$ where $\bar{r}$ is the distribution of particle sizes. Thus a volume fraction over 0.3 is needed, and only when this is achieved is a marked improvement in toughness noted.

This volume dependence shows how the microstructure of zirconia and partially stabilized zirconia or zirconia-containing ceramics can influence hardness values quite markedly.

Figure 6.20 indicates that either a small enough particle size or a sufficiently constraining matrix can hold a zirconia particle in a metastable tetragonal form down to room temperature. When this occurs, strengthening and toughening can be achieved because the stress field that is always moving ahead of a propagating crack releases the elastic constraint and allows the tetragonal → monoclinic change to occur. The effect of the transformation is the usual volume expansion, and so a compressive stress field is set up which is in opposition to the macrocrack stress field, and growth is inhibited. Similarly the stress field set up during a hardness test would be opposed by this mechanism, and the hardness of the material would be

registered as greater than expected. This effect is decreased as earlier discussion suggests because the twinned monoclinic crystals have a ductile mechanism for deformation (Section 6.2.3.1).

A corollary to this strengthening and toughening mechanism arises at the surface where there is a lack of hydrostatic elastic constraint and it is not possible to prevent tetragonal → monoclinic transformation on cooling. Thus the surface layer undergoes a volume expansion leading to compressive stresses in a surface "skin" that restrict the development of surface flaws. Mechanical abrasion can develop the depth of the surface-compressed layer until it is larger than the size of a critical flaw but still small compared with the cross section of the artifact. Thus failure from the surface is inhibited and strength improvements result.

Until recently, to utilize transformation toughening ZrO_2 powders of small particle size have been well distributed in the chosen matrix to prevent grain growth by sintering. For each matrix there will be a critical mean ZrO_2 particle diameter that is capable of contributing to transformation toughening. For example, the critical size reported in the literature[29] for ZrO_2 in Al_2O_3 composites is around the 0.6 μm diameter range. It must be stressed, however, that the particle size distribution is just as important because the population of transformable sized particles is important, not the mean particle size of the zirconia; recent results by Osendi and Moya,[30] summarized in Table 6.18, support this observation. Recently, improvements have been noted when agglomerates of zirconia containing many small particles are kept as such. The whole agglomerate is kept in the metastable state by the combined effect of self and matrix constraint. The macrocrack tip enters such an agglomerate and then causes transformation leading to growth hinderance and the concept of *agglomeration toughening*.

6.2.3.3. Hardness Values and Data Derived from Them for Zirconia and Zirconia-Containing Materials

Despite their potential commercial importance, zirconia and zirconia-containing ceramics have not been as extensively studied with respect to hardness as might be expected. This is apparent from the few data in Table 6.20.

The grain size effect and the range of K_{IC} values is demonstrated in a recent investigation of CeO_2 stabilized ZrO_2 which may become an important form of PSZ more common than other stabilized zirconias because of its resistance to sulphurization in high temperature uses. CeO_2 stabilized zirconia samples contain from 20-100% of the tetragonal form when 8-16 mol% CeO_2 is used. Figure 6.21 shows the effect of grain size and monoclinic content.

Table 6.20. Hardness and Related Data for Zirconia and Alloyed Zirconia Samples

Material	Form	Density (kg m^{-3})	H_V (GPa)	E (GPa)	K_{IC} (MPa m$^{1/2}$)	Notes
ZrO_2	Monoclinic single crystal	—	6.5	—	1.1	—
ZrO_2	Monoclinic 1.0 μm grains	—	9.8	—	—	—
ZrO_2	Monoclinic 2.5 μm grains	—	7.3	—	—	—
ZrO_2-Y_2O_3 3 mol%	Single crystal tetragonal	—	11.0	—	—	—
ZrO_2-Y_2O_3 10 mol%	Single crystal cubic	—	15.0	—	—	—
ZrO_2-Y_2O_3 9 mol%	Tetragonal, 0.3 μm grains	5990	11.7	—	5.8[a]	P = 19.6 N
	Tetragonal + cubic	5990	12.0	—	5.85[a]	
	Tetragonal + cubic, 0.68 μm grains	5993	11.6	—	6.25[a]	
ZrO_2-Y_2O_3 (PSZ)	Tetragonal	—	11.3	170	6.9	Knoop at 0.24 N = 16.7 GPa
ZrO_2-MgO (PSZ)	Cubic	—	15.5	—		
	Monoclinic	—	6.5			
	Cubic 66%, tetragonal 33%	—	11.5	210	—	ν = 0.31, H_k = 16.7 GPa
	Cubic 66%, monoclinic 33%	—	8.3	—	—	
ZrO_2-CeO_2 11 mol%	70% tetragonal 30% monoclinic				5.0–7.0	Grain size 0.5–2.5 μm;
ZrO_2-CeO_2 7 mol%	20% tetragonal 80% monoclinic				11.0–16.0	Niihara equation (5.53) used; P = 490 N

[a]Evans and Charles equation (5.41).
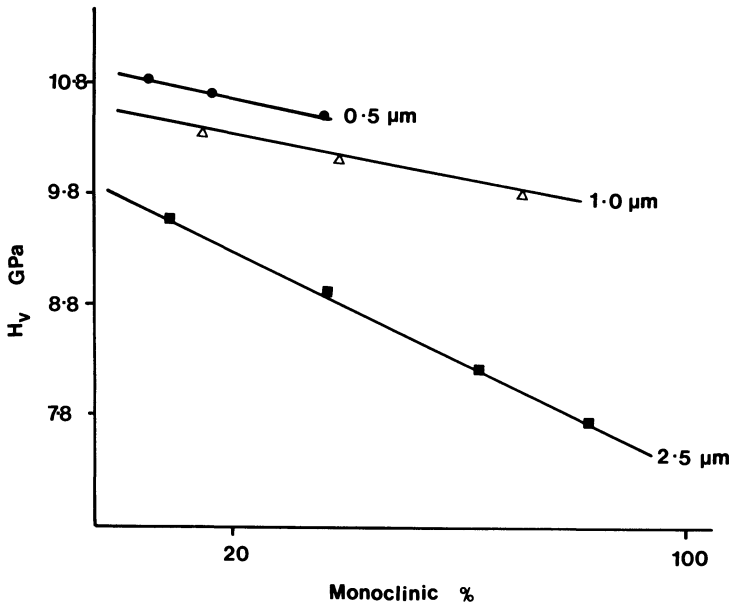
Figure 6.21. Grain size effect on Vickers hardness of CeO_2 partially stabilized ZrO_2. After Tsukuma and Shimada.[19]

Samples containing only 7 mol% CeO_2 contained mostly the monoclinic form, and K_{IC} values determined at 490 N loads to produce cracks and analyzed by the Niihara equation, equation (5.53), were high, in the range 11–16 MPa m$^{1/2}$. High tetragonal content produced by 11 mol% CeO_2 had K_{IC} values in the range 5–7 MPa m$^{1/2}$ which demonstrates that the tetragonal → monoclinic toughening mechanism was not as effective as the controlled microcrack process zone method, but both represent improvement on the reported value of 1.1 MPa m$^{1/2}$ for single crystal ZrO_2. Further support for the greater efficacy of the monoclinic microcracking route to toughness is seen in Figure 6.22 where the greatest toughness values for directionally solidified Al_2O_3–PSZ ceramic are shown in the region containing monoclinic ZrO_2. The fiberlike morphology shows some anisotropy of toughness and produces shallow radial Palmqvist-type cracks with loads in the range 5–100 N; because of the type of crack the Niihara equation, equation (5.53), was again used to determine K_{IC}.

Microscopic examination of the surface crack lengths and their depths below the surface for two stabilized and partially stabilized zirconias[20] available as commercial products, after indentation at 294 N, shows that the cracks do not often have the geometry of the halfpenny (see Section 5.2) but are usually of the shallower Palmqvist radial type with $d/c' \to 0$, where d is the crack depth and c' is the surface trace.
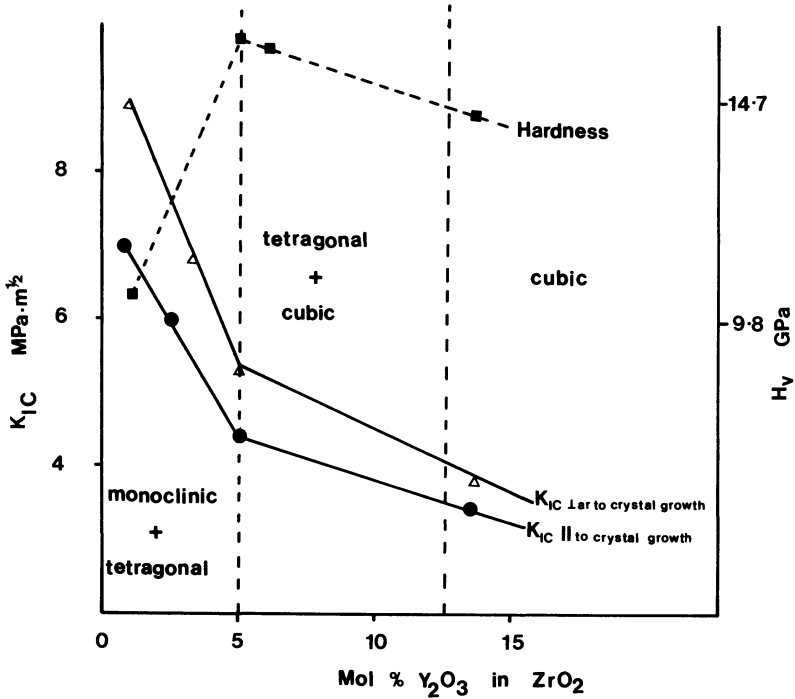
Figure 6.22. Fracture toughness by indentation method and Vickers hardness of Al_2O_3 containing PSZ.

Porosity affects the hardness of zirconia and PSZ perhaps more markedly than nontransformable ceramics because b in equation (6.20) is 8, whereas most other ceramics conforming to equation (6.20) have a b value of 7.

$$H_{measured} = H_o \exp(-bp) \qquad (6.20)$$

In equation (6.20), H_o is the hardness at zero porosity, b is a constant (usually 7), and p is the fractional porosity. For the Vickers hardness of tetragonal zirconia, the equation arising from equation (6.20) is given in GPa as

$$H_V = 12.27 \exp(-8p) \qquad (6.21)$$

When substantial porosity is present, even in a sintered ceramic such as the β-Al_2O_3-ZrO_2 composite shown in Figure 6.23 (top), the hardness is determined by a compaction mechanism. In Figure 6.23 (top) the indented area has almost no dark pores compared to the surrounding area and shows
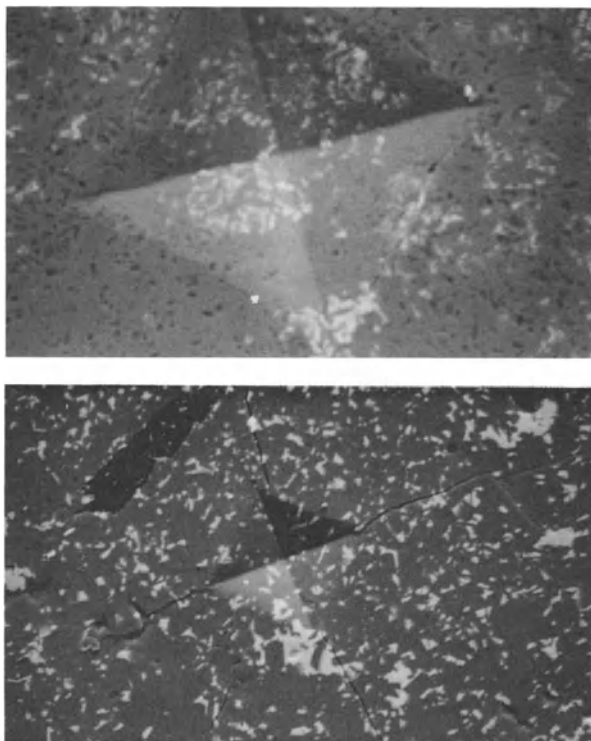
Figure 6.23. Vickers indentations made on the surface of β-Al$_2$O$_3$ infiltrated with Zr(NO$_3$)$_4$ solution and sintered at 1400°C. (top) Magnification of 760× of indent made at 4.9 N after one infiltration. (bottom) Magnification of 340× of indent made at 19.6 N after ten infiltrations. After Inwang.[21]

cracks along the indent edges arising from grainboundary fracture and grain rearrangement in the compacted area. When the same sample is more fully pore filled with ZrO$_2$ from the decomposition of zirconium nitrate solution, as shown by the greater abundance of white areas in Figure 6.23 (bottom), the sample is much harder and shows the characteristic corner cracks (see Section 5.2) of a brittle ceramic subjected to a large indentation load, in this case 19.6 N. The presence of the ZrO$_2$ increases the toughness parameter of the β-Al$_2$O$_3$ by 42% in the example shown in Figure 6.23 (bottom).

6.3. ELECTRONIC CERAMICS

Data for some very important electronic ceramics have already been given and discussed in Section 6.1. The electroceramics of importance, when

these covalent semiconductor materials have been removed, are all ionically bonded and are usually ternary oxides. The first has already been referred to in the section dealing with alumina and is the potentially important β-Al_2O_3.

6.3.1. Beta-Alumina

Fast ion conduction in the planes separating the spinel blocks present in this structure is responsible for the deep interest in using this ceramic as a solid electrolyte in advanced battery design. The term β-alumina encompasses an ever growing series of ternary oxides $M_xO_y \cdot 11Al_2O_3$ with the best known being $Na_2O \cdot 11Al_2O_3$, the one most people associate with the name β-alumina. The structure has overall hexagonal symmetry with each unit cell containing two very important mirror planes perpendicular to the c-axis. These planes are separated by four close packed layers of O^{2-} ions containing Al^{3+} in octahedral and tetrahedral sites, distributed so as to have spinel composition and structure. Each spinel block is linked through O^{2-} ions on the mirror planes that are joined to Al^{3+} ions in the spinel blocks above and below the plane. The Al–O–Al links so formed have considerable covalent character through sp hybrid bonding. In the mirror planes these linking oxygen atoms form an open hexagonal array of negative ions able to coordinate M^{n+} cations on the plane. Two sites for M^{n+} ions are available, each type forming an hexagonal array, one known as the Beevers–Ross site lying beneath a trigonal interstice in the spinel oxide layer; the second site, known as an anti-Beevers–Ross site, lies directly beneath an oxide ion in the spinel layer. Partial occupancy of the Beevers–Ross sites, and the availability of the antisites, is responsible for the easy ionic conduction in the plane of the O^{2-} ions forming the mirror plane. The overall unit cell has a large, 2.26 nm c axis, because it contains two of the spinel blocks related by a twofold screw axis.

Nonstoichiometry is the rule in this class of material together with obvious anisotropy and considerable polymorphism. The polymorphism arises from one, or a combination of, the following mechanisms: variation in the number of close-packed O^{2-} layers constituting the spinel block, change in the screw axis relationship of the blocks, increase in the number of blocks along the c-axis, and replacement of Al_2O_3 in the spinel blocks by other M_2O_3-type oxides. Examples of all these variations are known and the nomenclature has extended to β', β'', β'''-Al_2O_3, etc., to accommodate them.

Anisotropy in mechanical properties, as well as electrical properties, is associated with the presence of the mirror planes. Easy cleavage on (00.1) conduction planes is observed. The microhardness method has been found convenient for probing this mechanical anisotropy and producing data that

can be used in calculations to find the critical current density above which strength damaging flaws are generated in β-Al_2O_3 battery membranes. A critical current density at which a crack is nucleated can be estimated from

$$i_c = AK_c^4(c')^{-n} \tag{6.22}$$

In the above equation, c' is the flaw length, A is a constant, and n is a model-derived constant varying between 1.0 and 3.0 depending on the model used. When K_c values as derived from macroscopic tests on polycrystalline samples are used, i_c values several orders of magnitude too high are predicted from those observed to produce cracks in the β-Al_2O_3 membrane.

The hardness indentation technique is able to distinguish (00.1) cleavage planes from prismatic planes, all of which can be investigated by the methods described in Chapter 5. In this way E values in x and y directions have been found on different planes as well as K_{IC} values for the various planes. Clearly, E values need to be determined that are relevant to the planes of interest, whichever of the K_{IC} equations in Chapter 5 are used. Data obtained with indenter loads in the range 19.6–49.0 N using both Vickers and Knoop indenters show, in Table 6.21, the considerable variation in E for the structurally important planes. Using the E values obtained this way, K_c values were calculated for cracks running along [00.1], i.e., perpendicular to the mirror planes, which are in agreement with values from macroscopic methods with values around 1.98 MPa m$^{1/2}$. However, K_c values for cracks running in the basal plane were only 0.162 MPa m$^{1/2}$, and if this value is used in equation (6.22) critical current densities are predicted that are around those found practically. Thus it appears that current overload initiates failure by nucleating small cracks running across (00.1) planes in the β-Al_2O_3 grains. Basal plane hardness and toughness were seen to be load dependent up to 50 N according to equations (6.23) and (6.24) which relate hardness and toughness to load P

$$H_V = 13.5 - 3.37 \times 10^{-5}P^3 \quad (GPa) \tag{6.23}$$

$$K_{IC} = 0.916 - 6.42 \times 10^{-7}P^3 \quad (MPa\ m^{1/2}) \tag{6.24}$$

Attempts to improve K_{IC} values so that greater current densities can be used are concentrated on the inclusion of zirconia as a toughening agent (see Section 6.2.3.2), and results given in Table 6.21 and Figure 6.24 indicate some success from this route. Most of the improvement is thought to arise from a compressive surface stress which can be estimated from Figure 6.24 and equation (6.25):

$$K_{IC}^a = K_{IC}^i - \sigma_c A(c')^{1/2} \tag{6.25}$$

In equation (6.25), K_{IC}^i is the intrinsic fracture toughness (i.e., the value

Table 6.21. Hardness Values and Hardness-Derived Data for Some Electroceramics

Ceramic	Microstructure	H_V (GPa)	H_K (GPa)	E (GPa)	K_{IC} (MPa m$^{1/2}$)	Notes
β-Al$_2$O$_3$(Na$^+$)	Basal plane (00.1)	13.59^a	14.38	215^b	0.162^c	Cracks in [0001]
	Prismatic (11$\bar{2}$0)	8.1		174^b	1.98	
β''-Al$_2$O$_3$(Na$^+$)				207	2.8	
β''-Al$_2$O$_3$(Na$^+$) + 15 wt% ZrO$_2$					5.0–8.0	K_{IC} depends on load in range 14–90 N; equation (5.53) used
β-Al$_2$O$_3$(K$^+$)			13.3			
β-Al$_2$O$_3$(Ag$^+$)			12.95			
β-Al$_2$O$_3$(NH$_4^+$)			8.83			
β-Al$_2$O$_3$(Tl$^+$)			12.95			
β-Al$_2$O$_3$(H$_3$O$^+$)			10.06			
MgAl$_2$O$_4$		14.72	11.53			Load = 0.98 N
			16.68			Load = 24.5 N
FeFe$_2$O$_4$	Single crystal	11.78				Load = 0.98 N
	(111)	5.28				
	(100)	5.14				
	(110)	4.95				
Fe(Mn, Zn, Fe)$_2$O$_4$	(111)	5.79	5.69 [211]			
			5.89 [011]			
	(100)	6.18	6.18 [100]			
			5.50 [110]			
	(110)	6.33				
γ-Fe$_2$O$_3$		4.04			1.9^d	Defective inverse spinel, load = 0.98 N
BaFe$_{12}$O$_{19}$	95% theor. density	4.80			2.0^e	
BaFe$_{12}$O$_{19}$	90% theor. density contain 5% density by weight grain boundary glassy phase	4.74			2.1^d	
					2.3^e	

Material	Form					Comments
ZnGa$_2$S$_4$	Single crystal with chalcopyrites structure	3.88				
ZnSc$_2$S$_4$	Spinel	3.93				
CaLa$_2$S$_4$	Th$_3$P$_4$ structure	5.71				
YBa$_2$Cu$_3$O$_{7-x}$	Sintered	2.2				Load = 29.4 N produced no cracks; rose to 3.1 GPa at 77 K
	Sintered with additive	2.5				
TiO$_2$	Rutile (100)	12.7	283	2.5		Load = 0.98 N, diamond polished surface
		9.42				Load = 4.9 N, diamond polish
		8.83				Load = 4.9 N, gas-etched surface
						Rockwell 45 N = 70
ReO$_3$	Polycrystals					
	(001)(100)				5.45	
	(001)(110)				5.65	
Na$_{0.15}$WO$_3$		7.06[f]			4.66	(001)[100]
					6.94	(001)[110]
Na$_{0.75}$WO$_3$		8.16[f]				
Na$_{0.75}$WO$_3$	(001)(100)	10.8			4.88	Load = 4.9 N
		5.74				Load = 4.9 N
	(001)(110)	7.84				Load = 4.9 N, diamond polish
						Load = 4.9 N
					8.28	Load = 4.9 N, gas-etched surface
BaTiO$_3$	Sintered 7 μm grains	5.25				Load = 1.96 N
WO$_3$	Large twinned crystals	5.20	1.05		1.05	
V$_2$O$_5$	Single crystals					Very large anisotropy; see Table 3.5.
	(100)				2.96	
	(010)				2.40	
	(001)				2.16	

[a] Hardness is load dependent; see equation (6.23).
[b] Equation (5.65) used.
[c] Load dependent; see equation (6.24).
[d] From equation (5.40).
[e] From equation (5.53); P in range 20–100 N.
[f] Random indenter.
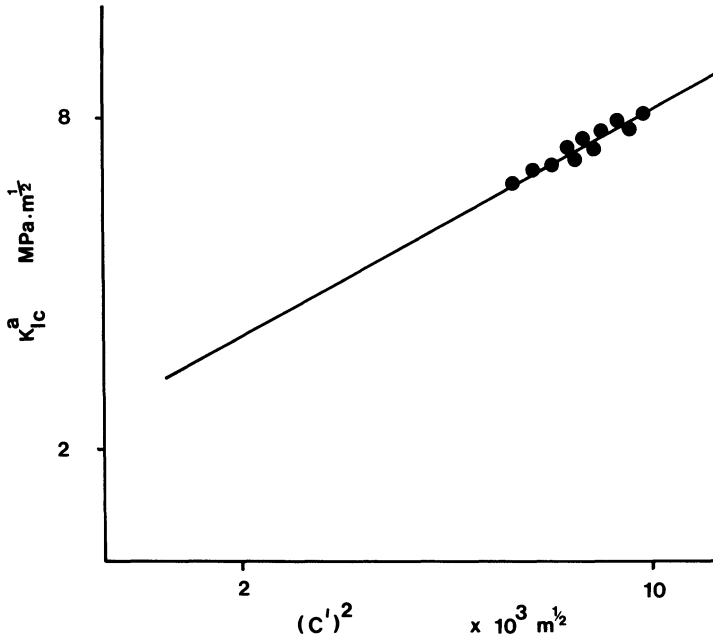
Figure 6.24. Fracture toughness calculated for a polished surface of β-Al_2O_3 + 15 by weight of % tet ZrO_2 plotted against square root of indentation crack length.

for pure β-Al_2O_3), A is a constant $(\pi^{1/2})$, σ_c is the residual stress, compressive and therefore negative, and c' is the indent crack length.

Results from a more specific examination of hardness anisotropy using the Knoop indenter have been given in Section 3.5.1, which shows that the direction of maximum hardness in the basal, (00.1) plane depends on the M^+ cation in the mirror plane: active slip systems are $(00.1)\langle11\bar{2}0\rangle$ for Na^+-β-Al_2O_3 and $(00.1)\langle10\bar{1}0\rangle$ for Ag^+, K^+, and Tl^+-β-Al_2O_3, which suggests some differences in local structure in the conduction planes.

6.3.2. Spinels

This class of ceramic is named after the mineral $MgAl_2O_4$ and many members have been fabricated because of the sensitive dependence of their electrical and magnetic properties on composition and temperature. Such a dependence arises from the variations in cation site occupancy that can be engineered. Spinels containing iron are particularly useful because of their magnetically soft properties that led to their application in computer hardware, memory devices, high-frequency transformers, and phase shifters.

Discussion and differentiation of spinels is based on the X-ray revelation that the basis of the structure is cubic close-packed layers of oxygen

ions with variable occupation of the octahedral and tetrahedral sites by A and B cations that such packing generates. The unit cell contains $32\,O^{2-}$ ions in the close packed array which leads to the structural composition $A_8B_{16}O_{32}$. Since a close-packed arrangement of 32 anions generates 64 tetrahedral and 32 octahedral sites and only 24 cations have to be accommodated, there is great scope for structural variation.

Anion charge neutralization can be achieved with different combinations of cation valency: $A^{2+} + 2B^{3+}$, known as two-three spinels; $A^{4+} + 2B^{2+}$, known as four-two spinels; and $A^{6+} + 2B^{+}$, the six-one spinels. Two-three spinels constitute 80% of the class.

Very few cations can occupy the tetrahedral sites without distorting the oxygen anion packing, so many spinels are less symmetrical than cubic. The structure is described as normal or inverse. When all 8 A-type ions occupy tetrahedral sites and all 16 B cations are in octahedral sites, the spinel is known as *normal* even if the oxygen site distortion does not result in cubic symmetry. When half the B cations occupy the tetrahedral sites and the other half plus the A cations occupy octahedral sites, the substance is called an *inverse* spinel. Obviously degrees of inversion can be encountered depending on the mechanisms that allow inversion to occur. Many of the important uses of spinels arise from the degree of inversion. For example, consider Fe_3O_4, which is a completely inverse spinel, $(Fe^{3+})_{tet}(Fe^{2+},Fe^{3+})_{oct}O_4^{2-}$, because of the strong octahedral site tendency of Fe^{2+}. Such a structure produces a random array of Fe^{2+} and Fe^{3+} ions in equivalent octahedral sites which leads to "hopping charge" semiconduction via $Fe^{2+} \rightleftharpoons Fe^{3+}$. Substitution of Zn^{2+} with its dominant tetrahedral site characteristic eventually leads to $Zn^{2+}_{tet}Fe_2^{3+}O_4^{2-}$ with complete suppression of electrical conductivity.

Closely related to the spinel structure is that of the hexagonal, magnetically hard ferrites characterized by the commercially important $BaFe_{12}O_{19}$. In this structure the oxygen anions are hexagonally close-packed and, because Ba^{2+} cations are of a similar size to oxide ions, some are incorporated into the oxygen layers, too. This has the effect of defining a greater number of sites than the octahedral and tetrahedral ones found in spinels. Among the five distinct sites so produced the Fe^{2+} and Fe^{3+} cations are distributed. Because the structure is hexagonal, the magnetic properties are markedly anisotropic, and we might expect this to be true for hardness measurements, especially since Table 3.1 shows that cubic manganese zinc ferrite demonstrates hardness anisotropy. However, definite measurements do not seem to have been made on single crystals of $BaFe_{12}O_{19}$. Improvements in the fracture toughness of sintered $BaFe_{12}O_{19}$ have been made by mixing in a low melting glass phase, and here the indentation technique has proved useful in confirming the toughness improvements made to these ceramic magnets.[22]

In the search for newer electroceramics, a series of spinel and spinel-related sulphides have been prepared and examined.[23,24] The hardness of these materials shows a general trend related to the cation coordination: the softest are like $ZnGaS_4$ which have the defect chalcopyrites structure and are tetragonal with 4-4 coordinated cations; the spinels like $ZnSc_2S_4$, with 6-4 coordination, are intermediate in hardness; while the 8-8 coordinated materials like $CaLa_2S_4$, that have the Th_3P_4 structure, are hardest. Some hardness values are given in Table 6.21. A particularly unusual feature of the defect chalcopyrites structure is the decreased hardness at low loads so that the hardness versus load curve in Figure 6.25 is in marked contrast to the normal behavior sketched in Figure 1.3; according to the analysis of indentation size effect given in Section 4.1, the n exponent in equation (4.2) is greater than 2 for these sulphospinels.

6.3.3. Perovskites

The ideal perovskite structure derives from the mineral $CaTiO_3$, which is cubic with a unit cell around 0.39 nm containing one formula unit. The
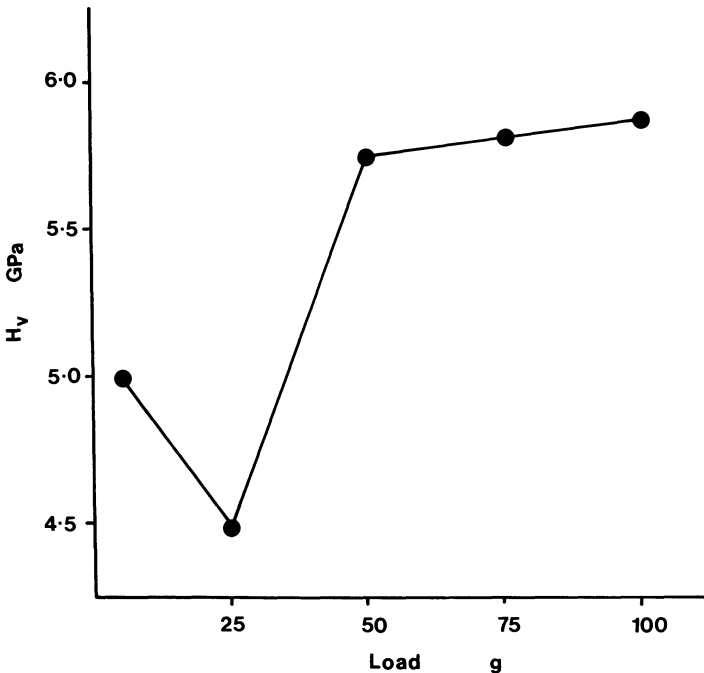
Figure 6.25. Unusual softening effect at low loads for $ZnGa_2S_4$ single-crystal hardness. After Vengatesan *et al.*[24]

structure is most commonly viewed as corner-sharing BO_6 octahedra along the cube axes. This regular, well ordered arrangement is then seen as generating a series of interstitial sites one of which has 12-fold O^{2-} coordination and is available for the large A^+ cations. When all 12 coordinate sites are vacant, an interesting electroceramic ReO_3 results which has excellent metallic electrical conductivity in the [001] direction. When all the A sites are occupied by, say, Na^+ another unusual metallic conductor, $NaWO_3$, whose golden color closely resembles ReO_3, results. Variation from Na_0 to $Na_{1.0}$ in Na_xWO_3 produces a wide range of conducting ceramics known as the tungsten bronzes. Semiconductor-to-conductor transitions occur in the series at critical compositions, but pressure can also cause such transitions at a given composition. The size of the octahedral site at which B cations reside is large, and often the B cations are displaced from the center of symmetry. If all such displacements are cooperative so that the dipoles are aligned, a spontaneous polarization occurs like that found in $Pb(ZrT_i)O_3$ along $\langle 001 \rangle$. Hence ferroelectric ceramics frequently occur in this class of material and, since ferroelectric perovskites are piezoelectric, they are used to convert electrical pulses to mechanical oscillations and vice versa. When the B octahedral cations are transition elements, a wide variety of magnetic properties can be found as the d orbitals on the B ions interact along [001] through the p_z orbitals of the O^{2-} ions. When the B site contains iron, the ceramics are known as orthoferrites and possess high coercivity.

Although the ideal structure is cubic, it is found only infrequently because polarization of the O^{2-} by the small B cations causes considerable covalency. Deviation from the cubic structure is defined by the tolerance factor

$$t = \frac{(r_A + r_{O^{2-}})}{[2(r_B + r_{O^{2-}})]^{1/2}} \qquad (6.26)$$

r_A and r_B are the cation radii and $r_{O^{2-}}$ the oxide anion radius. When t is 1.0 the cubic structure is found, but usually t is in the range 0.75–1.0. At the low values of t, tetragonal and orthorhombic structures are encountered.

Variation of composition and structure have made it possible to engineer materials with specific properties, and this has led to the development of many perovskite ceramic sensors: for example, $BaTiO_3$ has a large positive temperature coefficient and is used as a current limiter or as a temperature measuring device; $BaTiO_3 + BaSnO_3$, known as BTS, has been developed into fast, stable, and sensitive detector systems for temperature change, relative humidity meters, and the detection of small amounts of organic gases as the decrease in resistance of the system is monitored. The effectiveness of BTS sensors depends upon development of three types of pore system within the material: micropores $< 2\,nm$, mesopores 2–$5\,nm$,

and capillary pipe macropores >50 nm. In addition, $LaTaO_3$ and $PbTiO_3$ have been developed as pyrometer materials and optical sensors because the current output is proportional to the total incident radiation energy and $Pb(ZrTi)O_3$ converts mechanical to electrical energy and finds uses in igniter systems, bleepers, resonators, and strain gauges.

Hardness, like the electrical properties, is related to the concentration and type of A atoms in the structure; this is demonstrated in Figure 6.27 which shows that the hardness of the $\langle 110 \rangle$ and the degree of anisotropy increases as the sodium content of Na_xWO_3 increases. The fact that A-type cation–lattice interactions are dominant in determining hardness with the concentration of conduction electrons being unimportant is demonstrated by the lack of anisotropy and the relative softness shown by ReO_3 crystals in Figure 6.27. ReO_3 has all A sites vacant but by virtue of the Re^{7+} valency, compared to W^{6+} in Na_xWO_3, it has a filled conduction band.

Hardness in these materials may be related to the size of the band gap; as A^{m+}–BO_3 interactions lower the energy of the bonding states then as the concentration of A cations rises, the band gap is increased. Thus, when bonds are broken during a hardness test, electrons need to be excited to the nonbonding or conduction levels, a process that becomes more difficult as the composition of the A sites is varied.

The active slip system has been determined by the RSSM approach (see Section 3.6.1) to be $(110)\langle 1\bar{1}0 \rangle$, and the slip lines shown around the indents in Figure 6.26 support a (110) assignment.[25]
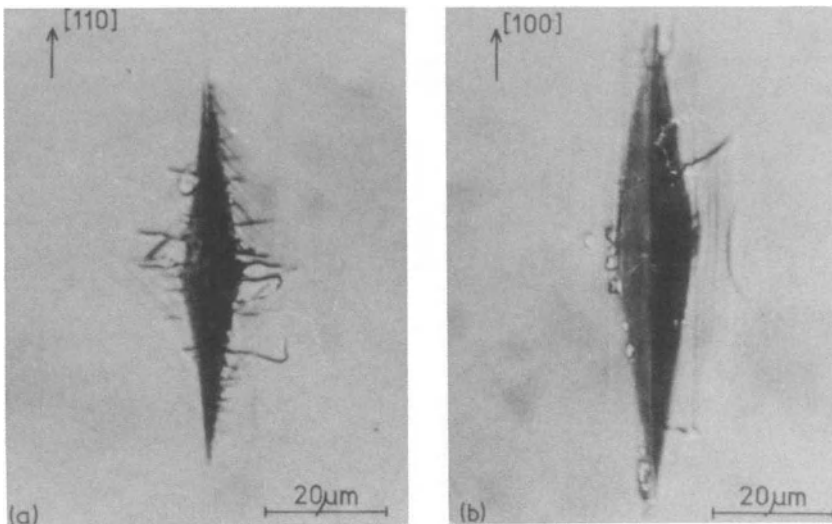
Figure 6.26. Knoop indents produced by a 1.96 N load on a (001) crystal face of $Na_{0.75}WO_3$ (a) along [110] and (b) along [100].
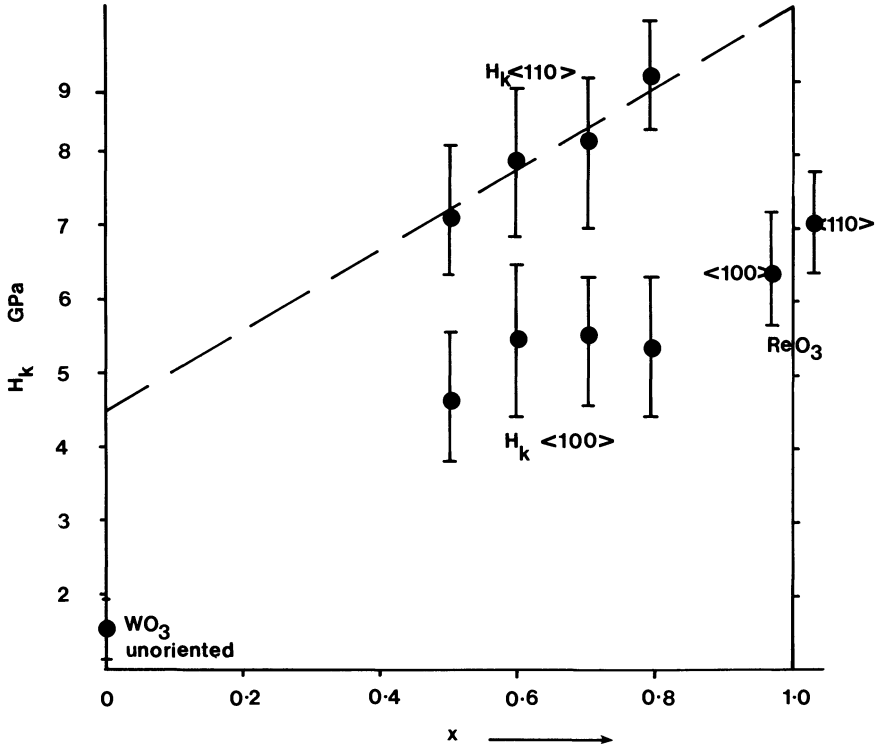
Figure 6.27. Knoop hardness of (001) faces of Na_xWO_3 and ReO_3 crystals and of unoriented WO_3 crystals.

6.3.4. Ceramic Superconductors

The perovskite structure can, like almost all oxide ceramics containing transition elements, be made defective, and when this was achieved for yttrium–barium–copper perovskites a startling development was reported that has the potential to alter our way of life; high-temperature superconductivity was discovered. The phenomenon was first reported for material of compositions $YBa_2Cu_3O_7$, the structure of which can be described in several equivalent ways centering on the basic K_2NiF_4 structure. One description refers to the structure as possessing a sequence of Ba–Y–Ba ions along the c-axis separated by two-dimensional CuO_2 planes leading to a tripled unit cell in the c-direction. Thus the formula would be $YBaCu_3O_{9-x}$ implying considerable numbers of vacancies in the oxygen sites to bring the overall composition to O_7. Other descriptions of the structure emphasize the defect-perovskite-layered nature according to which there are ordered oxygen vacancies in the CuO_2 planes separating the planes containing Ba^{2+} ions. This description leads to the $YBa_2Cu_3O_{7-x}$ formulation. Structural features

thought to be essential for the occurrence of superconductivity in a perovskite are: an ordered array of vacancies, mixed valence Cu^{2+} and Cu^{3+} states (although the existence of Cu^{3+} is disputed), and pyramidal and square-planar coordination of copper ions.

The attainment of superconductivity is very dependent on the annealing conditions used because the structure is so easily able to intercolate oxygen and also pertectically decomposes at 1040°C. There appears to be an optimum oxygen stoichiometry for high temperature superconductivity related to the content of oxygen in the copper plane that will allow "perfect" CuO_2 chains to be created by oxygen vacancy ordering in the basal plane of the structure.

Changes in oxygen content are, however, not without structural consequences and, as oxygen is removed, the orthorhombic distortion of the cubic perovskite structure is altered. Thus above a critical temperature the unit cell can lose oxygen such that the oxygen content reaches $O_{6.5}$, at which point a transition to tetragonal symmetry occurs. This tetragonal phase will not show the superconductivity around the 90K mark which makes the orthorhombic phase so exciting. As the oxygen leaves the Cu–O–Cu chains in the orthorhombic phase, the O^{2-} ions disorder between sites in the basal plane along the a and b axes which effectively makes them equivalent axes and produces the tetragonal symmetry.

In order to realize the potential of these ceramics they must be fabricated, and with such a low decomposition temperature sintering to high strength is proving a problem. Hardness determinations will prove useful in characterizing the mechanical properties of these and other ceramic superconductors, but as yet little has been reported. Table 6.21 contains hardness values obtained for the $YBa_2Cu_3O_{7-x}$ superconductor at room temperature and at liquid N_2 temperatures (77 K). As expected, the Vickers hardness rises to 3.1 GPa at 77 K and some success with sinter additives is achieved because the standard material hardness is raised from 2.2 to 2.5 GPa after sintering in their presence. Indentation hardness techniques have been used to establish the K_{IC} value of 1.1 MPa m$^{1/2}$.

6.3.5. Hardness Data and Properties Derived from Them

Some of the collected data, most of which was obtained from single crystal experimentation, are given in Table 6.21.

6.4. SPECIAL CERAMICS (REFRACTORY HARD METALS)

This class of ceramics contains some of the hardest materials available for exploitation, and the types encountered have such ranges and combina-

tions of properties that they cannot be described easily by one form of chemical bonding. Components of ionic, metallic, and covalent bond models are obvious in their behavior, their structure, and the theoretical descriptions encountered. Consideration is made a little easier by grouping the ceramics formed from the small nonmetal atoms carbon, nitrogen, and oxygen and calling them interstitial alloys, then grouping together the borides and silicides because the large nonmetal atoms in these systems form chains, sheets, and network structures through s-p covalent bonding into which metal atoms are intercalated.

Composites of interstitial alloys and metals are encountered in this class of ceramic, in particular the system sintered tungsten carbide–cobalt, which is used in metal cutting tools.

Many of the interstitial carbides are cubic and as a result of this have been examined in detail by the hardness technique with respect to anisotropy of behavior. As in the work with perovskite oxides (Section 6.3.3), there have been many studies made to investigate the relationship between composition and hardness because one of the fascinating aspects of these materials is the tremendously wide ranges in stoichiometry that are encountered, and the large changes in physical properties these introduce.

Within the classes of silicide and boride a much wider range of structural types is encountered.

6.4.1. Interstitial Carbides

All interstitial carbides have high melting points, and indeed the solid of highest melting point known is an alloy of 80% $TaC_{0.93}$ + 20% $HfC_{0.93}$ which melts above 4050°C. All are brittle and have high hardness values and high strengths maintained to high temperatures. All have a metallic luster and electrical and thermal conductivities of the same order as those found for metals. Thermodynamically they are expected to be easily oxidized and corroded but surface protective layers of oxidized material are often adequate to allow their use in ambient and, in many cases, to high temperatures. Such an unusual admixture of properties suggests that the bonding forces in these ceramics cannot adequately be interpreted on any one model. The best explanations offered for their intrinsic properties involve models that have ionic components, covalent overlap of bonding orbitals, and broad overlapping bands of molecular orbitals.

The technically important interstitial carbides usually exhibit three distinct phase ranges dependent on M:C ratio. First M takes up carbon in solid solution to produce the α-phase with an expanded metal structure. When the solubility limit is passed in the range 5–10%, conversion to the β-phase occurs which is a nonstoichiometric phase around $MC_{0.5}$ composition. The width of the composition variation is temperature dependent and

arises from carbon deficiency, not metal excess. The β-phase inevitably has an hexagonal symmetry. Extra carbon brings about a transformation of the metal structure to cubic and the carbon occupies octahedral sites in the cubic structure to produce the γ-phase. The γ-phase is always widely nonstoichiometric from $MC_{0.55}$ to $MC_{1.0}$, but it must be stressed that it is unlikely that the M:C ratio of 1:1 is ever achieved. Modern bonding theory suggests that maximum electron stability is achieved when x in MC_x reaches a maximum in the range 0.83–0.97. Samples that are supposedly $MC_{1.0}$ must be carbide and graphite eutectics. Since all octahedral sites in the rock-salt structure of metal atoms are not occupied by carbon atoms, there is considerable scope for ordered occupation and the existence of series of superstructure phases; VC_x is a classic example of this behavior.

The general mechanical behavior of the cubic carbides is similar to that of carbon and silicon (Section 6.1.5), with the slip systems, elastic behavior at room temperature, and plastic behavior at elevated temperatures being the same. Mechanical properties show a marked composition dependence not least hardness, for example, the hardness of $TiC_{0.82}$ is 19.63 GPa, and this rises to 26.99 GPa for $TiC_{0.97}$. In contrast, the Vickers hardness of $TaC_{0.82}$ is 26.99 GPa, but this *decreases* to 13.74 GPa at $TaC_{0.96}$. A plausible explanation for this behavior for two materials that have almost identical structures has to be sought in the bonding arrangements.[26] Titanium in group IV and Ta in group V differ only in the number of valence electrons they contribute to MC_x and CM_6 octahedra molecular orbitals. Addition of electrons from carbon in the titanium case is to metal d–carbon $p\pi$ bonding bands, but these are full in the case of the CM_x octahedra in TaC_x; thus, carbon electrons are moving into antibonding levels in the M–C d–$p\pi$ bands.

The slip mechanism at temperatures up to 1500°C have been probed[27] for crystals of $NbC_{0.8}$, $VC_{0.88}$, and a range of less well defined samples of TiC_x and TaC_x by using the indentation creep technique (see Section 4.3) as well as by oriented Vickers and Knoop studies. The results, shown in Table 6.22 with m values in the range 3.7–4.3 and activation energies around the value expected for carbon diffusion, indicate that a common slip mechanism exists, governed by carbon diffusion and dislocation climb. The activation energy for indentation creep of WC is 460 kJ mol^{-1} which is higher than values in Table 6.22, but this reflects the fact that γ-WC is hexagonal not cubic.

Hardness is quite anisotropic at room temperature, becomes less so as the temperature rises, and shows a reversal beyond a critical temperature. Figure 6.28 demonstrates these features for TiC indented on (001). This is indicative of a change in the operative slip system with temperature.

Although there are growing uses for this type of carbide as crucibles, pump linings, heating elements, electrode materials, and in the case of UC_x

Table 6.22. Hardness Creep Data

Material	Crystal arrangement	m^a	Q (kJ mol^{-1})
TiC$_x$	(100)[001]	3.85	336
	(110)[001]	4.05	339
	(111)[110]	3.73	322
VC$_{0.88}$	(100)[001]	4.27	358
	(110)[001]	4.07	348
	(111)[110]	3.79	333
NbC$_{0.8}$	(100)[001]	3.91	378

$^a m$ and Q are from the relationship $B = H_V^m \exp(-Q/RT)$.

nuclear fuels, by far the commonest application is in the field of cemented hard-metal cutting tools. These tools are a successful attempt to minimize the problems associated with brittleness when using the desirable high hardness of the ceramic to provide cutting faces for tools. A ductile metal
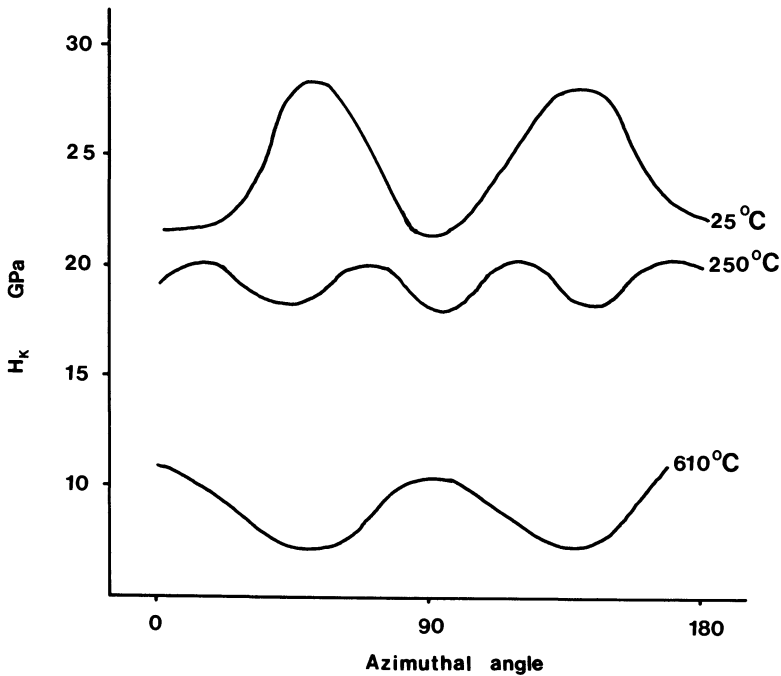
Figure 6.28. Knoop hardness anisotropy as a function of temperature for TiC on (001), $0° = [100]$, $45° = [110]$, $90° = [010]$, $135° = [1\bar{1}0]$, and $180° = [100]$.

is used to cement the interstitial carbide crystals. A suitable metal has to
fulfill several criteria:

- It should wet the carbide when molten so that good bonds can be
  formed on cooling.
- It must not itself be a carbide former.
- It should have little solubility in the carbide phase.
- It should be ductile.
- It should be resistant to oxidation.
- It should have good self-sintering characteristics.

The metal found to satisfy these criteria best is cobalt, and in particular it
fulfills them best with γ-WC, so the literature is heavily weighted toward
WC–Co systems.

Because WC is oxidized to WO_3 at high cutting speeds and this oxide
is volatile, in order to cut hard steels, substantial amounts of TiC_x are added
to some WC–Co grades. Some hardness data for cemented carbides is given
in Table 6.23 along with other carbide data, and equations (5.51), (5.52),
and (5.55) can be used to determine fracture toughness parameters from
indentation hardness measurements.

6.4.2. Ionic Ceramic Carbides

The term "ionic" is, in most of cases, an oversimplification because
the carbides in this class usually have metallic sheen and solid-state electrical
conductivity similar to those of a metal, so some delocalized bonding is
involved. Furthermore, these properties usually occur when the carbon-to-
metal ratio exceeds 1.0. Examples are Ln_2C_3 and UC_2. Many such carbides
contain C_2 units and, because of the enhanced reactivity with water or water
vapor, it is thought that the C_2 unit carries two negative charges, hence the
ionic classification. A molecular orbital analysis of two carbon atoms can
be used to demonstrate that the C_2 unit has two holes in the bonding level
with energy lowering for the system when the electrons are provided by a
metal atom. Further stabilization is then achieved by ionic bonding between
the metal cations and the C_2^{2-} anions. A third component of the total bonding
can then arise as the antibonding $2p_\pi^*$ orbitals on the C_2^{2-} unit are favorable
for overlap with metal d or f orbitals. The result of this is a refractory,
hard material with some potential uses as long as the system is protected
from water vapor.

For UC_2 the system can be represented as $U + C_2 \rightarrow U^{4+}C_2^{2-} + 2e^-$ in
the $7s$-$6d$-$2p_\pi^*$ band.

If the metal is a lanthanide, then the carbide would contain $Ln^{3+}C_2^{2-}$
and only one electron per metal is available for the covalent $6s$-$5d$-$2p_\pi^*$
band. In this way the decreased stability on going from UC_2 to LaC_2 is

anticipated. The presence of C_2^{2-} units in the octahedral sites of the close-packed metal structure brings about a tetrahedral distortion as the C_2^{2-} ions are aligned with their long axis along [001]. Nonaligned C_2^{2-} units can lead to overall cubic symmetry, and so all such carbides are polymorphic, exhibiting brittle martensitic phase changes when subjected to raised temperature or pressure.

The hardness, both pendulum and Vickers, of a series of lanthanide carbides LnC_2 is most easily interpreted on the bond model outlined above. Figure 6.29 shows the pendulum hardness of the lanthanide dicarbide series alongside the f electron character of the delocalized electrons, and the notable feature is that the softer dicarbides contribute a higher f-electron character to the band, so the $2p_\pi^*$ metal band will be more diffuse. After SmC_2 the hardness appears constant, while the f-orbital contribution is zero from SmC_2 onward. The hardness of YC_2 and ScC_2, which are isostructural with the lanthanides but in which the $4f$ levels are too far above the Fermi surface to allow any $4f$ character in the band electrons, have hardness values close to LuC_2 and the other heavy lanthanide dicarbides. A sharp change in hardness values as indicated in Figure 6.29 is not to be expected from other contributions to the bonding since the lanthanide contraction
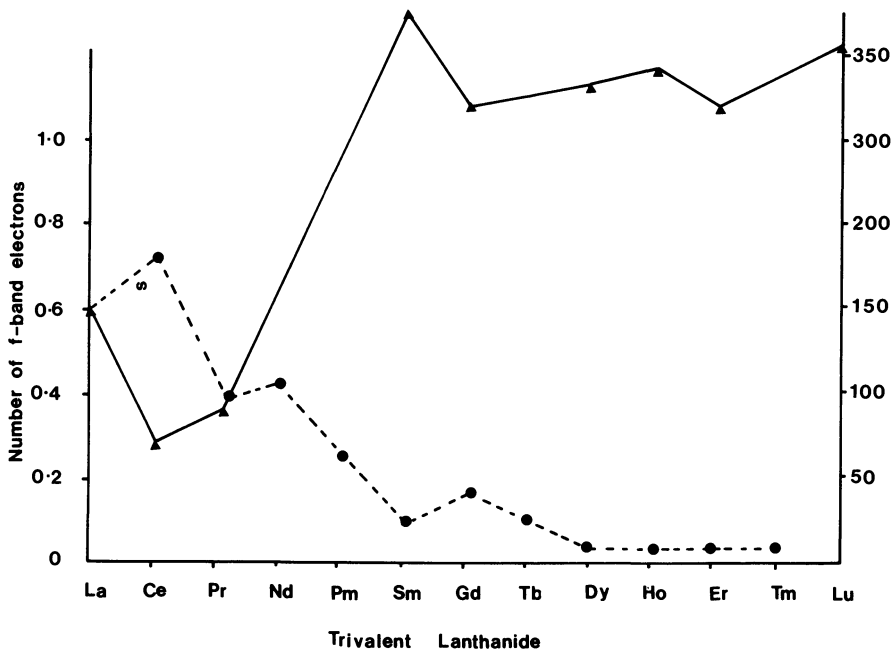
Figure 6.29. Correlation between f-band electron concentration for Ln^{3+} and pendulum hardness (———). Also shown is the number of f-band electrons (– – –). Pendulum hardness for LnC_2. After McColm.[28]

of 14% from LaC_2 to LuC_2 leads to an expectation of gradually increasing hardness across the series.

Since these substances are isostructural, solid solution formation is easy across the whole series, and the hardness of 50 mol% alloys, $Ln_{0.5}Ln_{0.5}C_2$, can be considered alongside the observed depression of the cubic-to-tetragonal phase transformation on cooling. It has been shown[28] that the depression in transformation temperature, ΔT_t, is related to cell volume difference ΔV and the shear modulus G for such solid solutions when the dicarbide of smaller cell volume is considered as the solvent and the dicarbide of larger cell volume is dissolved in it; the relationship is

$$\Delta T_t = AG(\Delta V)^2 \qquad (6.27)$$

A direct linear dependence like that shown in Figure 6.30 between hardness and ΔT_t for these solid solutions demonstrates the relationship between hardness and shear properties.

6.4.3. Interstitial Nitrides

There are great similarities between carbides and nitrides, and the same bond models are used when rationalizing their properties. The overall uses
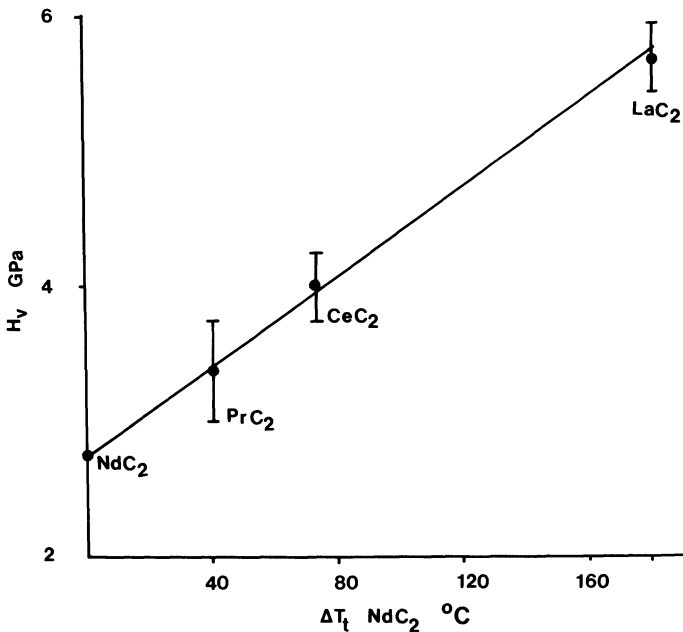
Figure 6.30. Relationship between Vickers hardness and the depression of the transformation temperature for NdC_2 50:50 mol % solid solutions.

as crucibles, pump parts, and components in cermet cutting tools parallels the carbide phases. Crystal structures and packing sequences through α, β, and γ phases are like those for carbides, but the heavier metals such as TaN and NbN are not able to achieve a cubic form, existing only as hexagonal polymorphs. However, the application of high pressure to TaN results in a cubic modification, which as Table 6.24 shows is almost three times harder than the hexagonal form. In the cubic form the extra covalent contributions to bonding more than offset the easier slip that is available in the more symmetrical structure with the result that the extremely hard material, cubic TaN, $H_V = 31.4$ GPa, is achieved.

As a general rule the nitrides appear to be more stable than the carbides and do not have nonmetal-rich phases, similar to MC_2, or any other other nitrogen-rich phases. Once again for all compositions wide stoichiometric ranges are encountered as a result of nitrogen vacancies. It is doubtful if $MN_{1.0}$ exists.

Because of their fine golden color, high hardness, and extreme corrosion resistance, TiN films deposited by CVD techniques are becoming common in both electronic and mechanical applications.

6.4.4. Borides

Like the carbides and nitrides, these materials have all the characteristics of covalent and metallic materials, so their properties are interpreted according to a number of mixed bonding models. For any one system, MB_x, more than one bond model is encountered because compared to the carbides and nitrides the nonmetal–metal ratio is very large, ranging from 0.2 to 12. Several metals form as many as six distinct boride phases, most of which are very stable, usually more so than the carbides or nitrides. Their availability and lower cost mean that borides are the most commonly used special ceramics. Diborides, in particular TiB_2 and ZrB_2, are commonly encountered now as linings on rocket nozzles and rocket nose cones and in turbine applications as well as sintered pump parts. Their resistance to scratching and abrasion sees their use as sliding contacts in electrical systems because of course their unusual bonding behavior gives many of them electrical resistivities similar to those of metals. Higher borides such as LaB_6 are used as stable refractory sources of electrons in several types of electronic application.

The stability of borides, as the fact that so many exist attests, is a reason for their not appearing as components in cermet systems; few, if any, metal matrices will not react with boride powders or fibers to form ternaries that lead to matrix degradation. Indeed, when boron fibers are to be used they have to be coated, usually with carbon, to prevent matrix interactions.

Fortunately, aluminum is one of the few metals that does not readily form borides, so it is used as a matrix for boride or boron fibers.

The size of the boron atom means that it cannot be accommodated in tetrahedral or octahedral interstices in close-packed metal structures, which was the convenient model used to discuss the carbides in Section 6.4.2. Furthermore, the large size of boron together with its $1s^2 2s^2 2p^1$ electronic structure, easily hybridized to $(1s^2 2(sp^2))^*$ arrangements, means that overlap of the sp^2 planar orbitals is frequently achieved, leading to the evolution of chains and networks of covalently bonded boron atoms throughout many of the structures found in metal borides. It is convenient to use the composition MB_2 as a pivot point in any discussion of structure: From M_4B to MB_2 the structures are viewed as being intact metal lattices which define M_6 trigonal prisms capable of being occupied by boron atoms; that is, different degrees of boron vacancy concentration can exist in complete metal structures. Above MB_2 up to MB_{12} the structures are regarded as three-dimensional boron networks within which combinations of metal atoms and vacant metal atom sites are perceived. The pivot composition, MB_2, is generally a widely nonstoichiometric phase with deficiency in both sublattices, but more often the boron network is most affected. Diborides are hexagonal and consist of alternate two-dimensional planar layers of boron atoms and metal atoms. The filled trigonal prism model that leads to the interpenetrating networks can be seen in Figure 6.31.
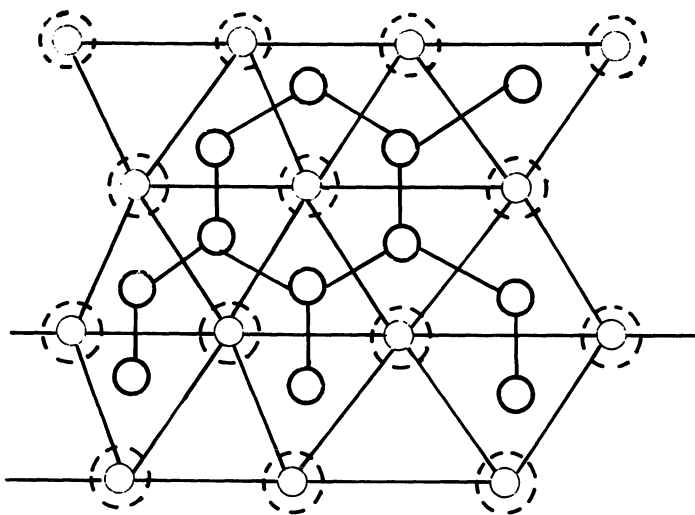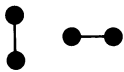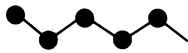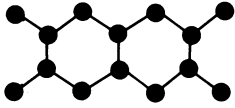
Figure 6.31. Condensed M_6 trigonal prisms of metal atoms at $Z = 000$, ◯, and $Z = 001$, ◌, each prism sharing all three faces. Hexagonal network of sp^2 hybridized boron atoms —●— are at $Z = 00\frac{1}{2}$. These two-dimensional networks compose the structure of MB_2 phases.

Other boron linking patterns found in borides are summarized in Table 6.23. Several bonding theories have been developed, starting from the recognizable networks of boron found in these compounds. For example, NMR and conductivity measurements on diborides suggest that the boron network has a π bonding component which could be achieved if some electron transfer from metal to boron took place. The model would then be $M^{n+}(B_2)^{n-}$ with an ionic contribution to bonding. The extra electron density on the boron network would provide p orbital character above and below the boron planes rather similar to that found in graphite. Such an arrangement would favor a metal atom d_z orbital covalent contribution to bonding via $B(2p)-M(4$ or $5)d_z$ overlap. Calculations show that the bonding level from the $B(2p)-M(4$ or $5)d$ orbitals lie just below the Fermi surface while the antibonding level lies above the Fermi surface. This fact would account for the weaker bonding in group V diborides (NbB_2, TaB_2) which have greater electron density in the antibonding level compared to group IV diborides (TiB_2, ZrB_2, HfB_2). In terms of hardness the group IV diborides are harder than those of group V, which supports this model.

Diborides have a large homogeneity range as a result of the structure containing metal vacancies plus excess borons at $\frac{1}{3}$ and $\frac{2}{3}$ O sites; both

Table 6.23. Boron Units Encountered in Borides

Composition	Boron unit	B–B distance (nm)
$\left\{\begin{array}{l} M_4B \\ M_3B \\ M_2B \end{array}\right.$	△ Isolated B atoms 	 0.33
M_3B_2	B₂ pairs	0.179
MB	Single chains	0.177
M_3B_4	Double chains	0.177
MB_2	Layer network, see Figure 6.27	0.175
$\left\{\begin{array}{l} MB_4 \\ MB_6 \\ MB_{12} \end{array}\right.$	Three-dimensional frameworks of B_6 octahedra	0.174

occurrences will lead to a decrease in electrons in the antibonding level with increased stability. Figure 6.32 reflects this by showing a sharp increase in hardness for NbB_2 of 0.29 GPa (at % boron)$^{-1}$.

Summarizing, for diborides the total bonding forces come from strong covalent sp^2 hybrid interactions in the boron planes, strong metal d orbital interactions in the planes of metal atoms, ionic bonding following metal → boron electron transfer, and bonding and antibonding contributions from boron $(2p)$–metal (d_z) orbitals.

These last two contribute to holding the two-dimensional networks together. The nature of the bonding, strong in planes and weaker between planes, together with the hexagonal symmetry, leads to considerable anisotropy, not least in hardness values.

The bond models for the boron-rich borides such as MB_6 have a common feature with the ionic carbides discussed in Section 6.4.2, in that a mechanism exists for a favorable transfer of electrons from the metal atoms to the boron framework to add a considerable ionic character to the overall bond character. Molecular orbital calculations for isolated units such as B_6, using $2s$ and $2p$ boron orbitals, reveal that the molecular orbitals can be divided into two sets: one group of six outward pointing at an energy
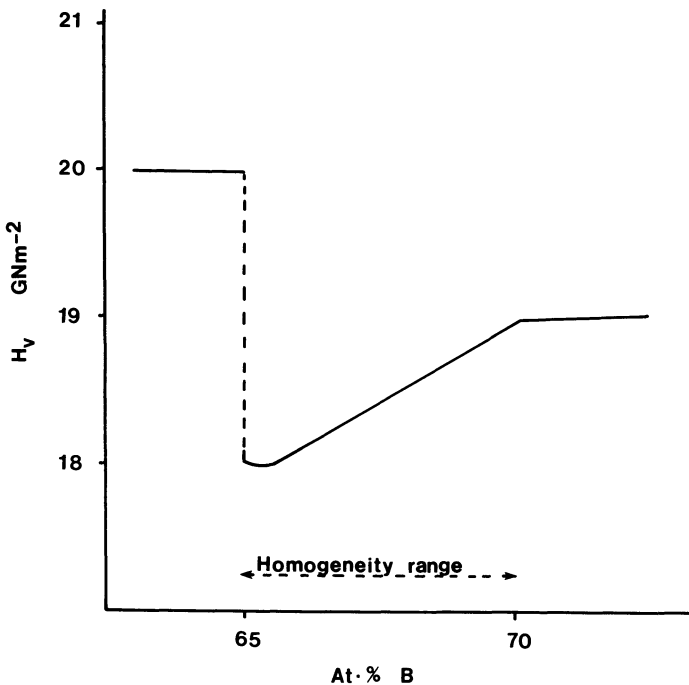
Figure 6.32. Vickers hardness as a function of composition for the nonstoichiometric NbB_2 phase.

value approximately nonbonding. Half occupancy of each of these will involve six electrons per B_6 unit and provide the basis for establishing the boron three-dimensional network by covalent interaction of these wave functions with near-neighbor B_6 units. A second set of 18 molecular orbitals is inwardly directed to the B_6 octahedron, the energies of which make seven levels bonding and the remainder antibonding. The 12 remaining electrons fully occupy six of the bonding levels contributing to the B6 stability and leave two holes in a bonding level. It is the presence of the two holes that encourages ionization of the metal atom to allow full occupancy. Metallic or semiconducting properties arise from the narrow gap between the intra-B_6 bonding and antibonding levels. Calculations involving groups of B_6 octahedra show that some of the molecular orbitals are broadened into bands. CaB_6 is a semiconductor because the two electrons from $Ca \rightarrow Ca^{2+} + 2e^-$ just fill the B_6 bonding level, and there is still a gap before the antibonding set. LaB_6 is ionized to $La^{3+} + 3e^-$ which places one electron per La atom in the antibonding level and relatively easy to remove from the solid. These materials are good sources of electrons and electrode materials.

6.4.5. Silicides

Silicides follow the discussion so far given for borides with two notable exceptions. First, phases with ratios greater $1:2$ for $M:Si$ are very rarely encountered. Second, the oxidation of a silicide leads to $M_xO_y + SiO_2$ producing substances which are themselves frequently glasses. Hence, surface coatings on these ceramics are glasses which provides considerable high-temperature protection with the result that WSi_2 and $CrSi_2$, for example, can be used at temperatures above 1700°C for many hours in the air.

The metal-rich silicides do not have such predictable structures from just knowledge of their composition, as the borides do; for example, CrSi, FeSi, and CoSi contain isolated Si atoms and not zig-zag chains as might be expected from boride phases of the $1:1$ composition. Furthermore, the composition MSi_2 is variable in structure type: $FeSi_2$ contains isolated Si_2 pairs and $ThSi_2$ has a three-dimensional Si atom framework while $MoSi_2$, among others, has the two-dimensional layer structure of Si networks and metal networks close packed like those found in MB_2 phases.

6.4.6. Some Hardness and Hardness-Related Data for Special Ceramics

Hardness methods are commonly used to gain a measure of yield stress, σ_y, of this class of materials and particularly as a function of temperature.

Table 6.24. Hardness Values and Hardness-Derived Data for Some Refractory Hard Metals and Special Ceramics

Ceramic	Microstructure	H_V (GPa)	H_K (GPa)	K_{IC} (MPa m$^{1/2}$)	Notes
W_2C	Fused	26.99			
WC	Fused	22.08			
WC–Co	7.6% cobalt	20.0		10,[a] 15[b]	$P = 100$ N
		10.45		8,[a] 7[b]	$P = 400$ N
WC–Co	6.0% cobalt	12.76–15.7			$P = 200$–400 N
WC–Co	5.0% Co	19.84		7.1[a]	Load = 294 N
	0.6 μm			5.1[c]	
	10.0% Co	17.46		10.5[a]	Load = 294 N
	0.5 μm			6.4[c]	
	16.0% Co	15.70		15.4[a]	Load = 294 N
	0.5 μm			6.4[c]	
	24.0% Co	13.30		21.9[a]	Load = 294 N
	0.7 μm			10.2[c]	
	12.0% Co	14.27		15.2[a]	Load = 294 N
	1.1 μm			9.3[c]	
Cr_3C_2	Fused	17.2			$E = 373$ GPa
Mo_2C	Fused	18.65			
UC	Fused	19.63			
TiC	Single crystal				
	(110)[100]	25.92	20.01		
	(110)[110]	28.62	26.95		
TaC		20			$E = 285$ GPa
VC	Single crystal				
	(111)[100]	18.03	13.52 ⎱		$T = 300°C$
	(111)[110]	16.61	10.78 ⎰		
$VC_{0.88}$	Single crystal				
	(100)[100]	30.4			
	[110]	32.39			
	(110)[100]	26.99			$P = 1.96$ N
	[110]	27.0			
	(111)[100]	26.5			
$NbC_{0.8}$	Single crystal				
	(100)[100]	29.93			Load = 1.96 N
	[110]	27.93			
CrB_2	Sintered	17.67			
	Fused	24.55			
	(001)	22.47–20.37			
Cr_3B	Fused	10.80			
TiB_2	Hot pressed		26.6		
MoB_2	(100)	24.24–21.30			
WB_2	(100)	22.18–20.51			
CrB	{010}	19.23–22.96			
CrB_4	{010}	20.90–22.96			Load = 0.98 N
Cr_3B_2	{010}	20.71–24.04			
Cr_2B_3	{010}	20.31–22.47			

Table 6.24. *Continued*

Ceramic	Microstructure	H_V (GPa)	H_K (GPa)	K_{IC} (MPa m$^{1/2}$)	Notes
BeB$_2$	Dynamically compacted $\rho = 2420$ kg m^{-3}		31.21		
BeB$_6$	Dynamically compacted $\rho = 2350$ kg m^{-3}		25.32		
Mo$_5$Si$_3$	Polycrystals		11.68–13.05		Load = 0.98 N, variation is evidence of anisotropy
MoSi$_2$	(100)[010]		8.93		
	[011]		9.91		Load = 0.98 N
	[001]		10.89		
	(001)[010]		12.27		
	[011]		12.76		
	[100]		10.89		
	(101)[010]		11.09		
	[101]		11.38		
	[100]		12.46		
WSi$_2$	(100)[010]		11.48		Load = 0.98 N
	[011]		12.56		
	[001]		15.70		
	(001)[010]		13.54		
	[011]		14.43		
	[100]		12.66		
	(101)[010]		13.50		
	[101]		13.74		
	[100]		12.17		
TiN		20.61			$P = 1.18$ N
			23.65		$P = 0.98$ N
AlN	Dynamically		7.29		$\rho = 90\%$ theor.
	compacted		10.27		$\rho = 95\%$ theor.
TiC	Single crystal				
	(001)		28.95		
	(110)		26.50		
	(111)		27.28		
ZrC$_{0.89}$	(001)		24.63		
	(110)		22.96		
	(111)		23.55		
H$_f$C	(001)		25.12		
	(110)		22.67		
	(111)		23.65		
VC$_{0.91}$	(001)		26.79		
	(110)		23.55		
	(111)		21.79		
NbC$_{0.94}$	(001)		27.09		
	(110)		20.81		
	(111)		19.92		

Table 6.24. *Continued*

Ceramic	Microstructure	H_V (GPa)	H_K (GPa)	K_{IC} (MPa m$^{1/2}$)	Notes
TaC	(001)		22.08		
	(110)		19.14		
	(111)		18.45		
TaN		31.4			Cubic structure made by explosive forming
		11.08			Normal hexagonal form
TiB$_2$	(0001)	26.90–38.27			
VB$_2$	(0001)	26.20–28.76			
VB$_2$	Polycrystals		24.04		
NbB$_2$	Polycrystals		26.01		
	(0001)	23.95–29.44			
TaB$_2$	(0001)	28.95–30.23	28.56		
	(10$\bar{1}$0)		25.03		
	(10$\bar{1}$2)		24.04		
H$_f$B$_2$	(0001)	19.63–24.54	24.83		
	(10$\bar{1}$0)		23.75		
	(10$\bar{1}$2)		22.18		
ZrB$_2$	(0001)	19.63–25.51	28.95		
	(10$\bar{1}$0)		26.60		
	(1012)		27.68		
LaC$_2$		2.40			
CeC$_2$		0.98			
PrC$_2$		1.37			
NdC$_2$		2.36			
SmC$_2$		6.38			
GdC$_2$		4.63			
DyC$_2$		5.71			
HoC$_2$		5.61			
ErC$_2$		4.48			
LuC$_2$		5.89			
ScC$_2$	Arc cast	5.84			
YC$_2$		5.01			
UC$_2$		7.75			Load = 0.98 N
UTaC$_2$		19.82			
UMoC$_2$		12.86			
UWC$_2$		12.66			
UCrC$_2$		13.45			
URuC$_2$		6.77			
UMnC$_2$		7.36			
UFeC$_2$		7.65			Load = 0.24 N

[a] Antis equation (5.48).
[b] Palmqvist equation (5.51).
[c] Laugier equation (5.59).

The general trend of data show that σ_y decreases some ten times faster than for other covalent solids such as Si and Ge (see Section 6.1.5.4), thermal softening coefficients, that is B in $H = H_o \exp(-BT)$, for diborides lie in the range $1.6-2.1 \times 10^{-3}$ deg^{-1}. Figure 6.28 gives an indication of the thermal softening encountered in interstitial carbides and demonstrates a common feature, namely, that slip systems change from $\{110\}\langle 1\bar{1}0\rangle$ to $\{111\}\langle 1\bar{1}0\rangle$ as the temperature is increased. This fact, coupled with the very rapid decrease in hardness with temperature, suggests that covalent binding between M and C is rapidly reduced. At lower temperatures the high directionality of the covalent bonds inhibits slip on close-packed $\{111\}$ as the strength of the bonds results in low dislocation mobility. The temperature affects sp^x hybridization through introducing s orbital mobility which means that only modest temperature rises are needed to induce metal-like hardness. Some of the available data are collected in Table 6.24.

REFERENCES

1. H. Baumhauer, *A. Krist.* **55**, 249 (1915).
2. N. W. Jepps and T. F. Page, *J. Amer. Ceram. Soc.* **64**, C177 (1981).
3. G. N. Babini, A. Bellosi, R. Chiara, and M. Bruno, *Adv. Ceram. Mater.* **2**, 146 (1987).
4. J. Mukergi, P. K. Das, and D. Chakrabarty, *Ceram. Bull.* **66**, 1616 (1987).
5. C. A. Brookes, in *Science of Hard Materials*, R. K. Viswanadham, D. J. Rowcliffe, and J. Gurland, eds., Plenum, New York (1983), p. 181.
6. I. J. McColm, *Ceramic Science for Materials Technologists*, Leonard Hill, Glasgow (1983), p. 132.
7. B. R. Lawn and V. R. Howes, *J. Mater. Sci.* **16**, 2745 (1981).
8. G. Soraru, R. Dal. Maschio, and G. Della Mea, *Glass Tech.* **27**, 69 (1986).
9. J. M. Rincon, J. M. Gonzalez Pena, and V. A. Bosch, *Amer. Ceram. Soc. Bull.* **66**, 1124 (1987).
10. S. Matsumoto, *J. Mater. Sci. Letters*, **4**, 600 (1985).
11. S. G. Roberts, P. Pirouz, and P. B. Hirsch, *J. Phys. Colloq.* **44**, C4-75 (1983).
12. I. J. McColm and N. J. Clark, *Forming, Shaping and Working of High Performance Ceramics*, Blackie, Glasgow (1988).
13. C. A. Brookes, in *Science of Hard Materials*, R. K. Viswanadham, D. J. Rowcliffe, and J. Gurland, eds., Plenum, New York (1983) p. 181.
14. P. F. Becher, *J. Amer. Ceram. Soc.* **57**, 107 (1974).
15. F. L. Kennard, R. C. Bradt, and V. S. Stubican, *J. Amer. Ceram. Soc.* **59**, 160 (1976).
16. C. A. Brookes, *Proc. R. Soc. London*, to be published.
17. F. Giberteau, A. Dominguez-Rodriquez, R. Marquez, and J. Castaing, *Rev. Phys. Appl.* **17**, 777 (1982).
18. J. A. H. Da Jorriada, G. J. Piermarini, and S. Block, *J. Amer. Ceram. Soc.* **70**, 628 (1987).
19. K. Tsukuma and M. Shimada, *J. Mater. Sci.* **20**, 1178 (1985).
20. J. D. Sullivan and P. H. Lauson, *J. Mater. Sci. Letters* **5**, 247 (1986).
21. I. Inwang, Ph.D. Thesis, University of Bradford (1988).
22. E. Lucchini and O. Sbaizero, *J. Mater. Sci. Letters* **6**, 1098 (1987).
23. D. L. Chess, C. A. Chess, and W. B. White, *Mater. Res. Bull*, **19**, 1551 (1984).
24. B. Vengatesan, N. Kanniah, and P. Ramasamy, *Phys. Stat. Sol.* (a) **104**, K93 (1987).
25. T. W. Button, I. J. McColm, and S. Wilson, *J. Mater. Sci.* **14**, 159 (1979).

26. I. J. McColm, *Ceramic Science for Materials Technologists*, Leonard Hill, Glasgow (1983), p. 326.
27. Y. Kumashiro and E. Sakuma, *J. Mater. Sci. Letters* **15**, 1321 (1980).
28. I. J. McColm, *J. Less-Comm. Metals* **78**, 287 (1981).
29. A. H. Heuer, N. Claussen, W. M. Kriven, and M. Ruhle, *J. Amer. Ceram. Soc.* **65**, 642 (1982).
30. M. I. Osendi and J. S. Moya, *J. Mater. Sci. Letters* **7**, 15 (1988).
31. R. D. Marsh, *Proc. Roy. Soc. London, Ser. A* **279**, 420 (1964).

Index